Signalling dependent regulation of the fission yeast actomyosin cytoskeleton.

Thesis submitted to the University of Kent
for the degree of Doctor of Philosophy (Ph.D.)
in the Faculty of Science, Technology and Medical Studies

2016

Karen Baker

Declaration.

No part of this thesis has been submitted in support of an application for any degree or qualification of the University of Kent or any other University or Institute of learning.

Signed:

Karen Baker.

Acknowledgements.

I would firstly like to thank my supervisors Dr. Dan Mulvihill and Professor Mike Geeves for their invaluable support and guidance throughout this project. I would also like to thank past and present members of the Mulvihill and Geeves laboratories for their assistance, friendship and motivation.

In addition I would like to thank all individuals and groups with whom I collaborated during this project, in particular, Cairn Research Ltd, Janni Petersen and her research group, Justin Molloy, Gregory Mashanov, and Steve Tovey.

Finally I would like to thank all my family and friends for their support and cooperation during the course of my study.

Abstract.

The actomyosin cytoskeleton is a highly dynamic complex of proteins which facilitate diverse processes within the cell. It is regulated by a network of signaling pathways to coordinate growth and division in response to changes in the extracellular environment. A wide range of actin binding proteins control the organization and dynamics of the actin network within eukaryote cells. This study explored the function of signaling dependent phosphorylation events on two *S. pombe* actin binding proteins, the actin capping protein, Acp1, and the class I myosin, Myo1.

Disruption of the TOR-signaling complex, TORC2, results in defects in the formation and constriction of the cytokinetic actomyosin ring (CAR). This study explores the localisation of TORC2 to the CAR, and the function of TORC2-dependent phosphorylation of Acp1. Data shows that phosphorylation of Acp1 functions to regulate the stability and cellular organization of the actin cytoskeleton. This allows a cell to couple growth and division with changes in the environment.

Similarly, phosphorylation of a conserved serine residue lying between the two IQ motifs of the neck region of the class I myosin, Myo1, was shown to be TORC2-dependent. Fission yeast express two calmodulin-like light chains, Cam1 and Cam2, which are capable of associating with the IQ domains in the neck region of Myo1 *in vitro*. The location of this phosphorylation site, between the two IQ motifs, provides a potential mechanism of determining which light chain associates with Myo1. This study provides evidence that this TORC2 dependent phosphorylation event is cell cycle dependent, and may result in a switch between Cam1 and Cam2 binding.

These potentially conserved mechanisms of regulating the organization of the actomyosin cytoskeleton provide an important insight into the system of control networks that regulate cell growth and division in response to changes in the extracellular environment.

Contents

Chapter 1: Introduction

Chapter 2: Materials and Methods

Chapter 3: Calmodulin association with IQ motifs of Myo1 and Myo52.

Chapter 4: Effect of the second *S. pombe* calmodulin-like protein, Cam2, on *S. pombe* myosins.

Chapter 5: Effects of phosphorylation of Myo1 at serine-742.

List of figures and tables:

Abbreviations.

[ ] : Denotes concentration.

ADF: Actin depolymerising factor.

APC : Anaphase promoting complex.

CaM : Calmodulin

Cam1-ACE : Acetylated *S. pombe* Cam1.

CAR : Cytokinetic actomyosin ring.

CD : Circular dichroism.

dH_20 : Deionised water.

EGTA : Ethylene glycol-bis(β-aminoethyl ether)-N,N,N',N'-tetraacetic acid

F-actin : Filamentous actin.

F_{max} : Fluorescence maximum (at saturation).

FRET : Fluorescence Resonance Energy Transfer.

G-actin : Globular actin.

GFP : Green Fluorescent Protein.

IAANS : 2-(4'-(Iodoacetamido)anilino)Naphthalene-6-Sulfonic Acid, Sodium salt.

IgG : Immunoglobulin G (antibody).

K_d : Dissociation constant.

MOPS : 3-(N-morpholino)propanesulfonic acid.

MTOC : Microtubule organizing centre.

Myo1IQ12 : Denotes the two IQ domains of *S. pombe* Myo1.

Myo1-S742 : Denotes the serine-742 residue of *S. pombe* Myo1.

NA : Numerical Aperture.

NETO : New end take-off.

Nt-acetylation : N-terminal acetylation.

OD_{280} : Optical density at 280 nm.

OD_{600} : Optical density at 600 nm.

PBS : Phosphate buffered saline

RCF : Relative centrifugal force.

RT : Room temperature.

SDS-PAGE : Sodium dodecyl sulfate polyacrylamide gel electrophoresis

SCPR : Search, capture, pull, release.

SIN : Septation initiation.

SPB : Spindle pole body.

STORM : Stochastic optical reconstruction microscopy.

TIRFM : Total internal reflection fluorescence microscopy.

TOR : Target of Rapamycin.

TORC1 : TOR Complex 1.

TORC2 : TOR Complex 2.

TRIS : Tris(hydroxymethyl)aminomethane

WT : Wild Type.

YFP : Yellow Fluorescent Protein.

Chapter 1: Introduction.

1.1. Cells and cell growth.

All organisms alive today are evolved from a common ancestral cell that lived 3-4 billion years ago (Starr et al. 2015). These simple free-living cells have evolved into the complex multi-cellular animals we recognize today, formed of specialised tissues and organs. Preservation of life over this period of time has relied on the ability of cells to grow and divide, accurately passing on their genetic information, with only rare mistakes in this process driving evolution.

No matter how complex the organism they form part of, all living cells share fundamental molecules and processes essential for life. All cells contain genes, organised onto one or more chromosomes; DNA molecules made from a defined sequence of nucleotides. Cells are able to accurately duplicate and segregate this genetic material between two daughter cells during cell division. The genetic code is interpreted by a set of cellular machinery, able to transcribe and translate this sequence into new cellular protein components, essential for further growth and cell division. All of these cellular components must be surrounded by an effective boundary, which regulates exchange of substances with the environment and allows the cell to respond to external signals (Morgan et al. 2007).

Prokaryotes are amongst the simplest of known organisms; bacteria and archaea have no internal membrane bound organelles, and a single circular chromosome of DNA which is replicated and divided during simple binary fission. Eukaryotic cells are larger, more complex, and contain characteristic membrane bound organelles. They are defined by the presence of a nucleus that encloses DNA organised into linear chromosomes. While animal cells have only a plasma membrane composed of lipids and proteins, fungi and bacteria have an additional cell wall made of polysaccharides. This provides unicellular organisms with the extra support and protection required for survival in direct contact with the external environment (Morgan et al. 2007).

Unicellular organisms grow and divide at a rate that is generally only limited by the availability of nutrients in the environment. By contrast, cells making up a multi-cellular organism must grow and divide in a controlled manner, dependent on the requirement for tissue growth, via signals from neighboring cells. Defects in the response to these environmental signals, for example in cancer cells, results in uncontrolled growth and proliferation (Fededa & Gerlich 2012).

1.2. The Eukaryotic cell cycle.

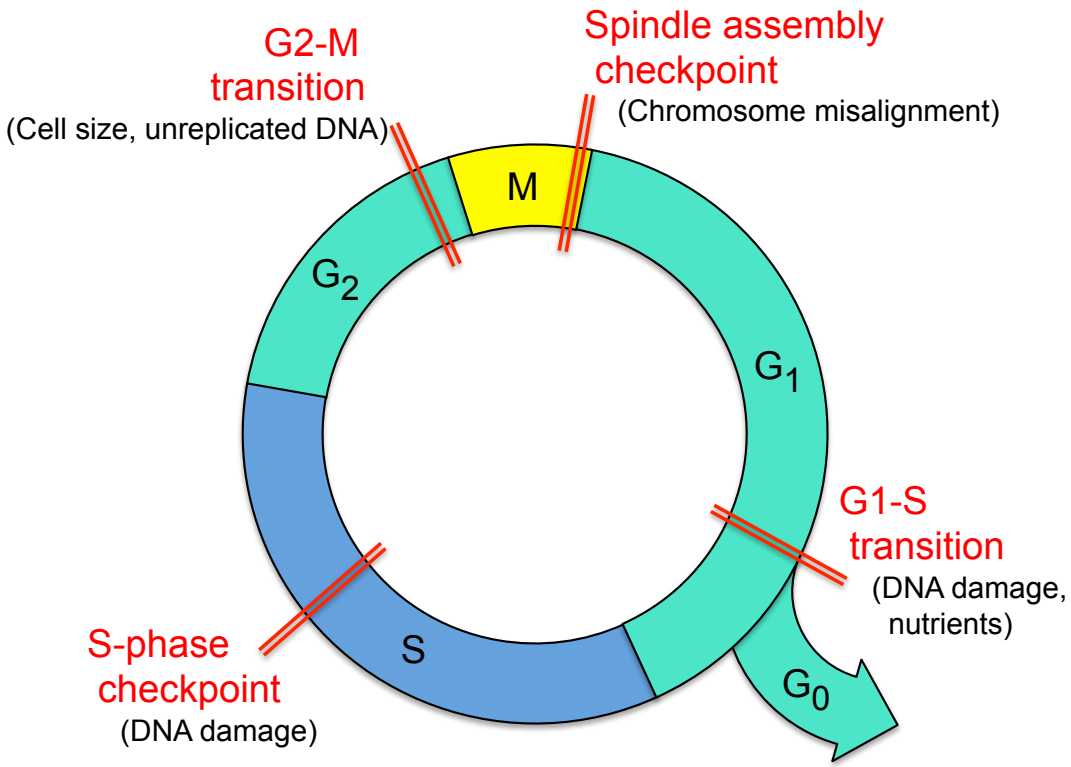

Figure 1.1. Stages of the cell cycle.

Mitosis (M) occupies a small fraction of the total cycle. M is flanked by gap phases, G1 and G2. Synthesis of DNA occurs in S-phase and in the absence of nutrients or non-dividing cells, exit the cell cycle into G0 – a quiescent stage. Checkpoints at which the cell cycle can be arrested are also shown. Adapted from (Alberts 2006).

The cell cycle defines the life of a cell, and is a series of highly regulated events which result in two identical daughter cells. The cell cycle is composed of four stages: Interphase, comprising of G1, S, and G2, and mitosis (Figure 1.1) (Norbury & Nurse 1992). During interphase, cell growth occurs continuously, with the cell accumulating new internal organelles, proteins and membrane material, sufficient to sustain the two daughter cells. Replication of the chromosomes is restricted to S-phase, which is flanked by gap phases, G1 and G2, allowing the cell to grow and assess internal and external factors. Following successful chromosome replication, the cell enters the mitotic phase, and the two sister chromatids are separated (Vermeulen et al. 2003).

Mitosis occupies only a small fraction of the total cell cycle and includes both nuclear division (mitosis) and cell division (cytokinesis). The typical lengths of mammalian cell cycle stages are 12 hours for G1, 6 hours for S-phase, 6 hours for G2, with mitosis lasting around 30 minutes. However, there is huge variability in these lengths depending on cell type, for example a yeast cell can divide every 2 hours, while a liver cell can survive for more than a year. These longer cell lifetimes are usually due to cells exiting the cell cycle from G1 and entering a quiescent G0 state (Cooper 2000).

Figure 1.2. shows the key stages of mitotic cell division, beginning with prophase, where chromosomes condense and the nuclear envelope breaks down (although this is not the case in yeast). Centrosomes, (spindle pole bodies in yeast) organise the formation of microtubules into a mitotic spindle, to which chromosomes attach via their kinetochores. During metaphase, sister chromatids attach to microtubules from opposite poles and line up at the cell equator. When the linkage between sister chromatids is broken down, anaphase begins, and chromatids separate to opposite poles. Cell division is completed by cytokinesis, the physical division of the cell by formation and constriction of an actomyosin ring (Murray 1993).

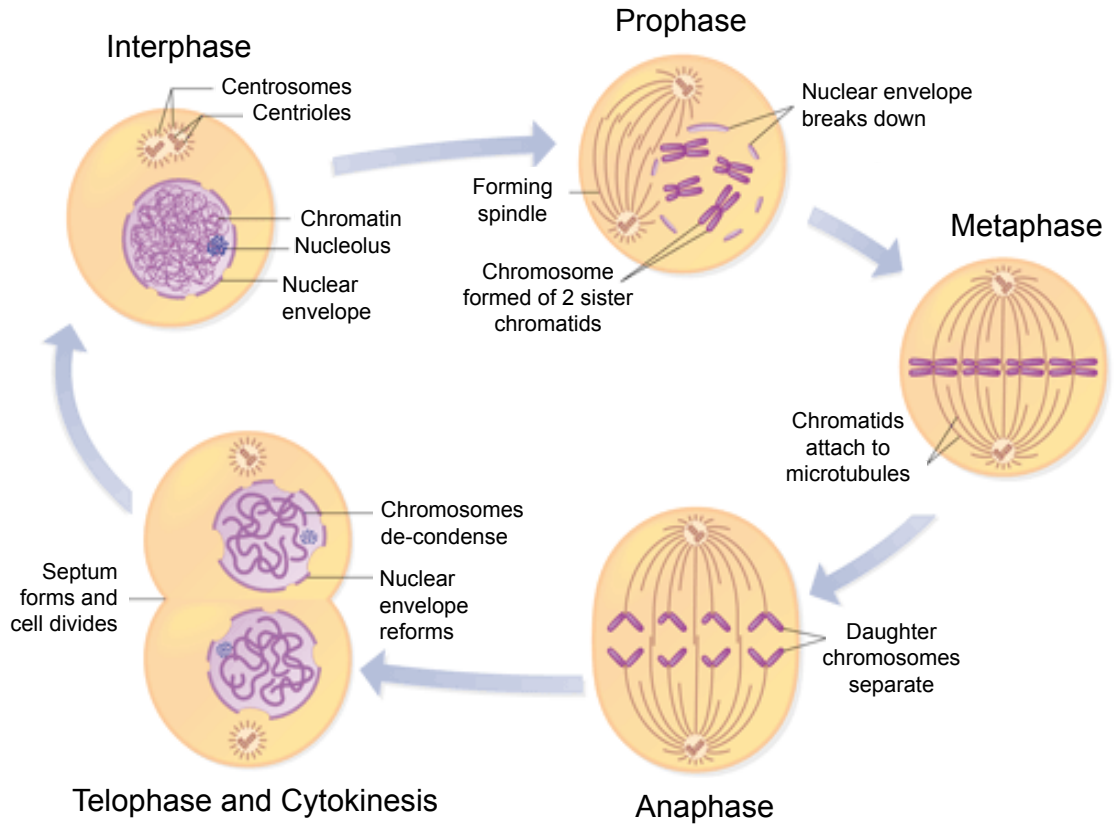

Figure 1.2. Stages of mitosis.

Diagram showing chromosomes and spindle assembly during the stages of mitosis. Chromosomes condense and the nuclear membrane breaks down during prophase. In metaphase sister chromatids align at the cell equator, attached to microtubules from opposite centrosomes. At the onset of anaphase, the linkage between chromatids is broken down and chromosomes separate to opposite poles. Two identical daughter cells are formed following cytokinesis. Adapted from (Pearson Education 2004).

1.3. Cell cycle regulation.

The coordinated levels and activity of key cellular proteins, tightly controls progression through the cell cycle. Control is established through a series of phosphorylation events, that regulate the activity of proteins throughout the cycle (Rhind & Russell 2012). A major family of kinases involved in catalysing these phosphorylation events, are called Cyclin-dependent kinases (Cdks), due to their

partial control by Cyclin regulatory subunits. Different Cdk-Cyclin complexes regulate different stages of the cell cycle (Figure 1.3) (Vermeulen et al. 2003).

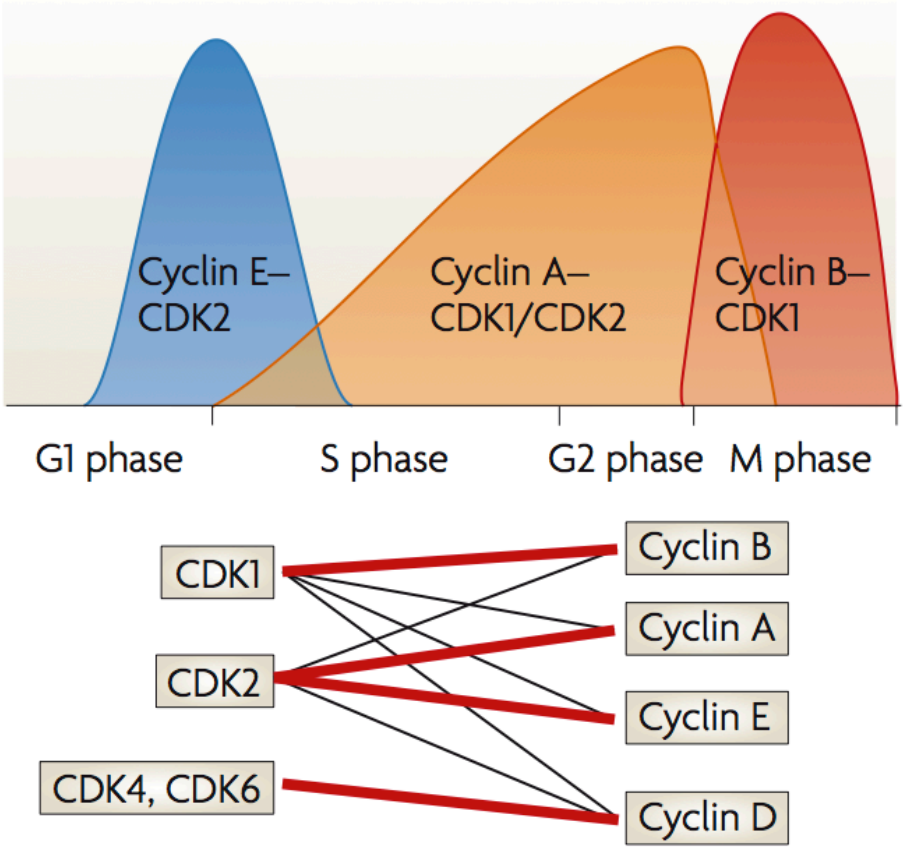

Figure 1.3. Cdk-Cyclin complexes.

Diagram showing the levels of different Cdk-Cyclin complexes throughout the cell cycle. Although interchangeable, red lines show the preferred binding partners of Cdk and cyclin proteins. Cdk2-Cyclin E complex is required to initiate S-phase, and Cdck1/2-Cyclin A required for further progression. Entry into mitosis is cataylsed by Cdk1-Cyclin B complex. Adapted from (Hochegger 2008).

Cdk1 (Cdc2 in yeast) is essential for entry into mitosis and is highly conserved (~65 %) in all eukaryotes. During G2, the concentration of Cyclin B gradually increases, with the levels of Cdk1-Cyclin B complex peaking at the onset of mitosis. During interphase, the kinase activity of Wee1 retains this complex in an inactive, phosphorylated form (Russell & Nurse 1987). At the onset of mitosis, via

polo-like kinase signalling (Roshak et al. 2000; A. Seki et al. 2008), the activity of the phosphatase, Cdc25, is increased over 10 fold (Kovelman & Russell 1996). Increased Cdc25 activity rapidly activates the Cdk1-Cyclin B complex by removing the phosphate groups (Figure 1.4). This active 'Maturating promoting factor' (MPF) promotes entry of cells into mitosis, by causing chromosome condensation, breakdown of the nuclear envelope and spindle formation. This G2-M transition point ensures that cells reach a critical size before entering mitosis. The activity of the Wee1 kinase is maintained to prevent activation of the Cdk1-Cyclin B complex, until cells have reached a threshold size, (Nurse 1975; Kellogg 2003).

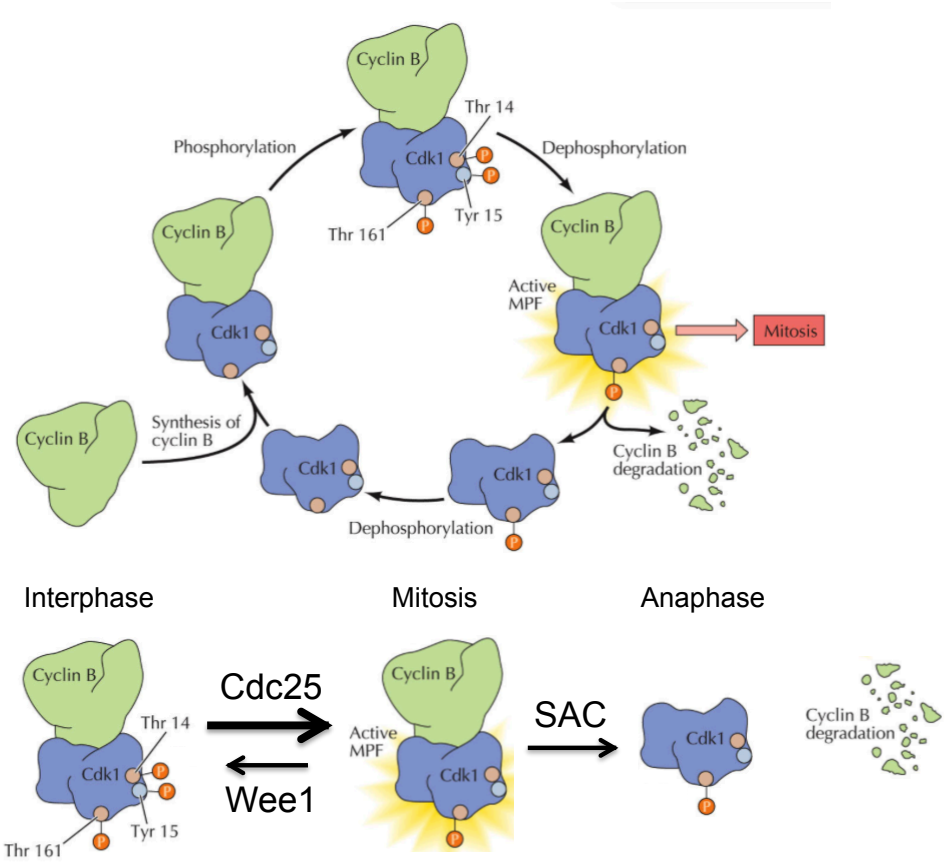

Figure 1.4. Activity of Cdk1-Cyclin B complex.

Cyclin B is synthesized during G2, forming Cdk1-Cyclin B complex which is kept in an inactive, phosphorylated form by the kinase, Wee1. At the onset of mitosis, Cdc25 phosphatase activity increases, resulting in active, dephosphorylated Cdk1-Cyclin B complex. After passing the spindle assembly checkpoint (SAC), Cyclin B is rapidly degraded, while Cdk1 is recycled. Adapted from (Alberts 2006)

To complete mitosis, all chromosomes must align correctly, for the cell to pass the Spindle-Assembly Checkpoint (SAC), and proceed through anaphase. While the kinetochores of chromatids are unattached from the spindle, a 'mitotic checkpoint complex' retains the 'anaphase promoting complex' (APC) in an inactive form (Figure 1.5). Once all chromosomes are correctly aligned, the E3 ubiquitin ligase activity of the APC is activated (Fededa & Gerlich 2012). Ubiquitination of Cyclin B and Securin, targets these proteins for degradation. Degradation of Securin releases Separase, an enzyme which cleaves the cohesin holding sister chromatids together. Meanwhile, degradation of Cyclin B leads to inactivation of Cdk1, and exit from mitosis (Lara-Gonzalez et al. 2012).

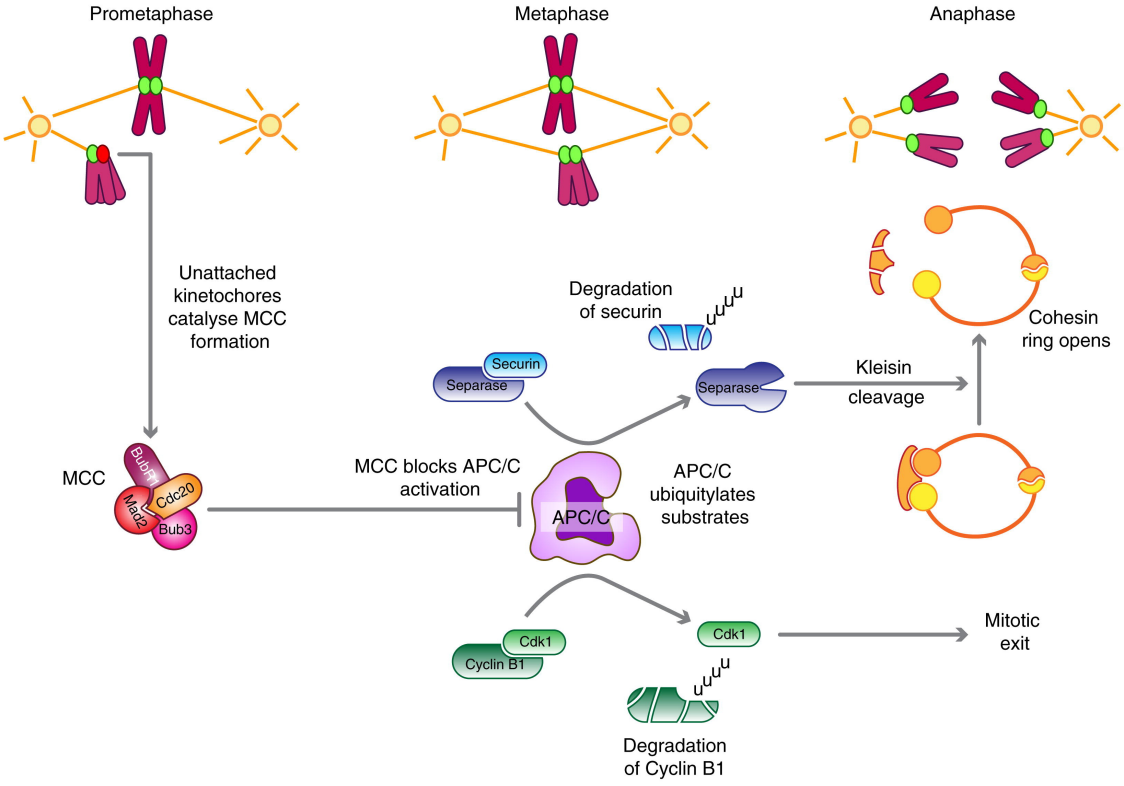

Figure 1.5. The spindle assembly checkpoint (SAC).
Until all chromosomes are aligned, the anaphase promoting complex (APC) is kept inactive. Once chromosomes are aligned, APC ubiquitinates Cyclin B and securin for degradation. This results in degradation of the cohesin holding sister chromatids together, allowing their separation, and inactivation of Cdk1, allowing exit from mitosis. Adapted from (Lara gonzalez 2012).

Cells also arrest at other points in the cell cycle, dependent on the signals they receive. The G1-S transition prevents activation of DNA replication machinery, if the DNA is damaged or the growth conditions are unfavourable. Active Cdk2-Cyclin E and Cdk2-Cyclin A are required for entry into, and progression through S-phase (Vermeulen et al. 2003).

1.4. Cell signalling.

All cells must coordinate cellular processes, including growth, with signals received from the external environment or from neighboring cells. Signalling molecules, such as hormones, growth factors or nutrients, interact with receptors on the cell surface. Three major classes of transmembrane receptor molecules, are ion channels, G-protein-linked and enzyme-linked receptors (Uings & Farrow 2000). These receptors transduce external stimuli via a series of molecular 'switches', predominantly through exchange of nucleotides or addition and removal of phosphate groups. Downstream effector molecules influence multiple cellular processes including gene expression, metabolic reactions and cytoskeletal organization (Hall & Nobes 2000).

In multicellular organisms, the large numbers, and specificity, of receptor molecules expressed on the cell surface, ensures that individual cell types respond appropriately to certain stimuli. The complex network of signalling molecules in the cell is integrated into coordinated signalling pathways through common adaptor proteins (Figure 1.6) (Volinsky & Kholodenko 2013). Two abundant second messenger signalling molecules, produced following activation of receptor molecules, are cyclic AMP (cAMP) and inositol 1,4,5-triphosphate (IP_3). Synthesis of these small molecules allows rapid amplification of signalling cascades. cAMP molecules activate protein kinase A (PKA), leading to up-regulation of many metabolic processes. While IP_3 mediates calcium levels in the cytosol, activating both protein kinase C (PKC) and calmodulin-mediated cellular processes.

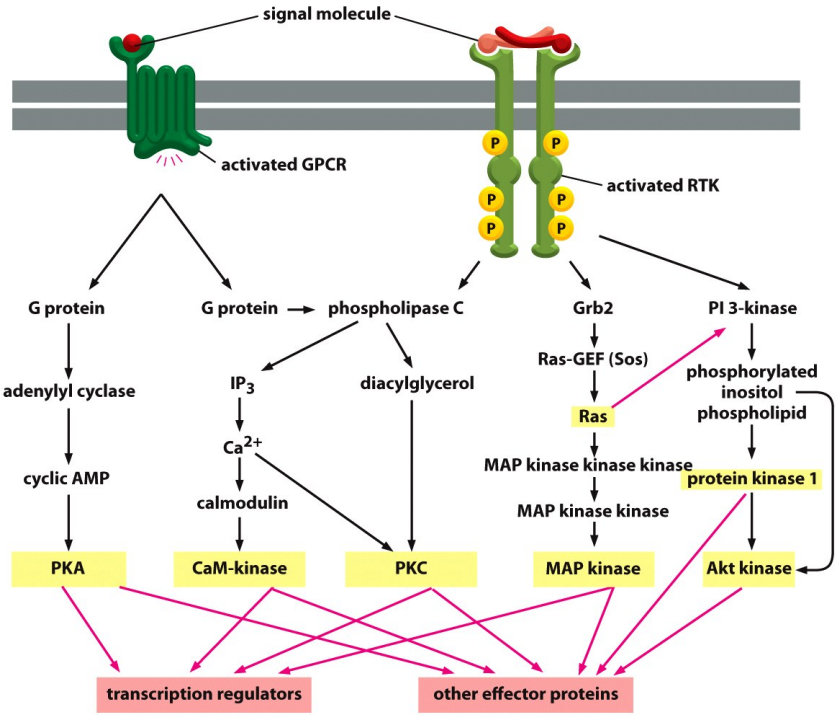

Figure 1.6. Cellular signalling pathways.

A simplified diagram of some of the major signalling pathways in cells. Signals are received from outside the cell via G-protein linked receptors (GPCR) and receptor tyrosine kinases (RTK). These transmembrane receptors initiate overlapping but tightly controlled signalling cascades which result in regulation of cellular processes. From (Alberts, B. 2004)

Signalling in response to growth factors and cell-cell interactions, result in changes in polarized cell growth through remodeling of the actin cytoskeleton (Fededa & Gerlich 2012). Integrins are a specialised type of receptor involved in attachment of cells to the extracellular matrix (ECM). The signalling function of integrins is mediated through non-receptor tyrosine kinases, focal adhesion kinase (FAK) and Src. In response to growth factors, members of the Rho-family of small GTP-binding proteins (Rho, Rac, and Cdc42) play important signalling roles in cytokinesis, formation of cell adhesions and control of actin binding proteins such as myosin and cofilin (Ma & Poon 2011; Das et al 2015).

1.5. TOR signalling.

The Target of Rapamycin (TOR) signalling pathway acts as the 'master switch' of cellular processes, regulating cell growth and metabolism, in response to external stimuli (Zhou & Huang 2010). *Tor* genes were first identified in budding yeast as mediators of cellular toxicity caused by the bacterial macrolide, Rapamycin (Cafferkey et al. 1993). Tor is a serine/threonine kinase from the (PI3K)-related kinase family. Mammals have a single Tor protein, mTor, while yeast express two, Tor1 and Tor2. mTor is a large, 290 kDa protein, containing numerous functional domains (Figure 1.7), including a C-terminal kinase domain, and HEAT repeats which create multiple sites for protein-protein interactions (Zhou & Huang 2010).

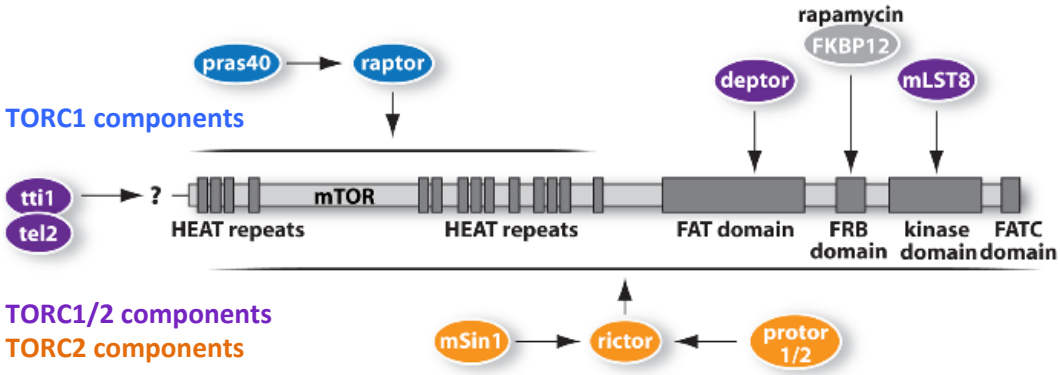

Figure 1.7. Domain structure of mTor protein.
Domain structure of mTor protein, with location of interactions with subunits of the TORC1 and TORC2 complexes. Adapted from (Laplante 2012).

mTor associates with multiple proteins, to form two functionally distinct complexes, TORC1 and TORC2. More is known about the function of TORC1 and the upstream signalling pathway (Figure 1.8). TORC1 responds to multiple upstream regulators, including growth factors such as insulin, amino acids (in particular leucine), oxygen and energy levels (Wullschleger et al. 2006). The kinase activity of mTor is strongly activated by the Ras GTPase homologue, Rheb. mTor directly phosphorylates eIF4E binding protein 1 (4E-BP1) and S6 kinase 1, which leads to increased protein synthesis. TORC1 signalling is also implicated in many other cellular processes, including cell growth, ribosome biogenesis and autophagy (Laplante & Sabatini 2012).

TORC1 signalling, through the stress response mitogen-activated protein kinase (MAPK) pathway, controls the entry of cells into mitosis, in response to poor nutrient conditions (Petersen & Nurse 2007). Under poor nutrient conditions, or Rapamycin inhibition of TOR signalling, increased Sty1-MAPK phosphorylation of Polo-kinase, increases its recruitment to the spindle pole body (SPB). Polo kinase at the SPB promotes the onset of mitosis by activating Cdc25. Therefore TOR signalling allows cells to regulate their size at division according to nutrient availability.

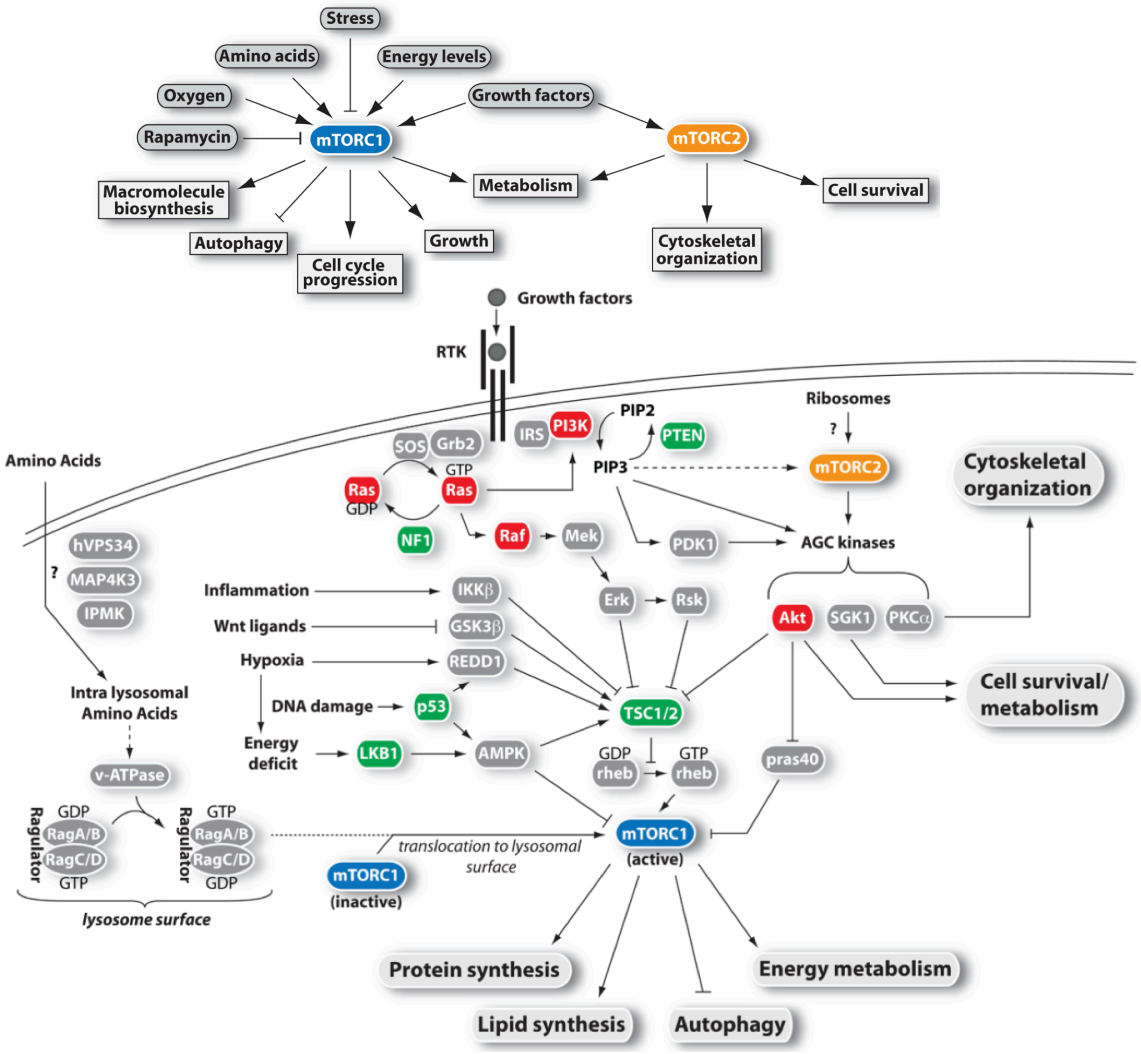

Figure 1.8. Signalling pathways of TORC1 and TORC2.

Diagram showing the upstream regulators of TORC1 and TORC2, and the signalling pathways leading to alteration of cellular processes. Adapted from (Laplante 2012).

The activation and functions of TORC2 are less well characterised than TORC1. However, TORC2 is known to function in response to growth factors, although the signalling pathway is unclear. TORC2 directly phosphorylates Akt, an AGC kinase which influences metabolism, cell cycle progression and apoptosis. TORC2 also plays a role in regulating the actin cytoskeleton through another AGC kinase, PKC-α (Sarbassov et al. 2004) along with Rho GTPases (Jacinto et al. 2004). TORC2 deficient cells show actin polymerization and cell polarity defects, with a loss of cell motility in a variety of cell types(Liu & Parent 2011).

Yeast express homologues of the main TOR signalling components, which are summarised in Table 1.1. The two Tor proteins expressed in *S. pombe* cells are incorporated into distinct complexes. Tor2 is incorporated into TORC1, while TORC2 consists predominantly of Tor1. However in the absence of Tor1, Tor2 can restore TORC2 function (Hartmuth & Petersen 2009; Matsuo et al. 2007). The Rictor homologue, Ste20, named due to *ste20*Δ cells being sterile, specifically abolishes the function of TORC2.

Table 1.1. Components of mammalian and *S. pombe* TOR complexes.

Mammalian	*S. pombe*	Function
mTor	Tor1 or Tor2	Serine/threonine kinase
Raptor	Mip1	Scaffold protein, regulating localisation, assembly and substrate binding
LST8	Wat1/Pop3	Unknown
mTor	Tor1	Serine/threonine kinase
SIN1	Sin1	Scaffold protein
Rictor	Ste20	Scaffold protein, regulating localisation, assembly and substrate binding
LST8	Wat1/Pop3	Unknown

1.6. Schizosaccharomyces pombe as a model organism.

Schizosaccharomyces pombe (fission yeast) is a unicellular eukaryotic organism, first isolated from African millet beer in 1893. Over the past 60 years it has been developed as an experimental organism, resulting in important scientific breakthroughs, particularly in revealing elements of cell cycle regulation (Nurse 1975; Nurse et al. 1976; Thuriaux et al. 1980). Since the full genome sequence was published in 2002, (Wood et al. 2002) *S. pombe* has become an established model for many areas of research, including cell cycle control, DNA replication, as well as the study of the actin and microtubule cytoskeletons.

Its genome is arranged on three chromosomes and encodes around 5000 genes, many of which are homologous to those found in higher eukaryotic organisms. Many structural components of the cytoskeleton have significant sequence homology to protein equivalents found in humans, and are also thought to share similar pathways of regulation. *S. pombe* provides an elegant model in which to study the actomyosin cytoskeleton, in part due to the small number of genes encoding actin binding proteins, and ability to explore protein interactions and localisation using live cell imaging.

Further advantages of using *S. pombe* as a model organism is its ability to grow quickly – with an average generation time of four hours in minimal media. *S. pombe* is also genetically tractable; during the vegetative life cycle, laboratory strains can be cultured in a haploid state, making mutations easy to characterise. Under starvation conditions, these haploid cells can be forced to mate and enter meiosis, where homologous recombination occurs frequently and efficiently. This ease of genetic manipulation allows gene deletions and fluorescent tags to be easily incorporated into the genome.

S. pombe cells can pass through either the mitotic or meiotic division cycles dependent on the availability of nutrients in the surrounding environment. These cycles are summarised in Figure 1.9:

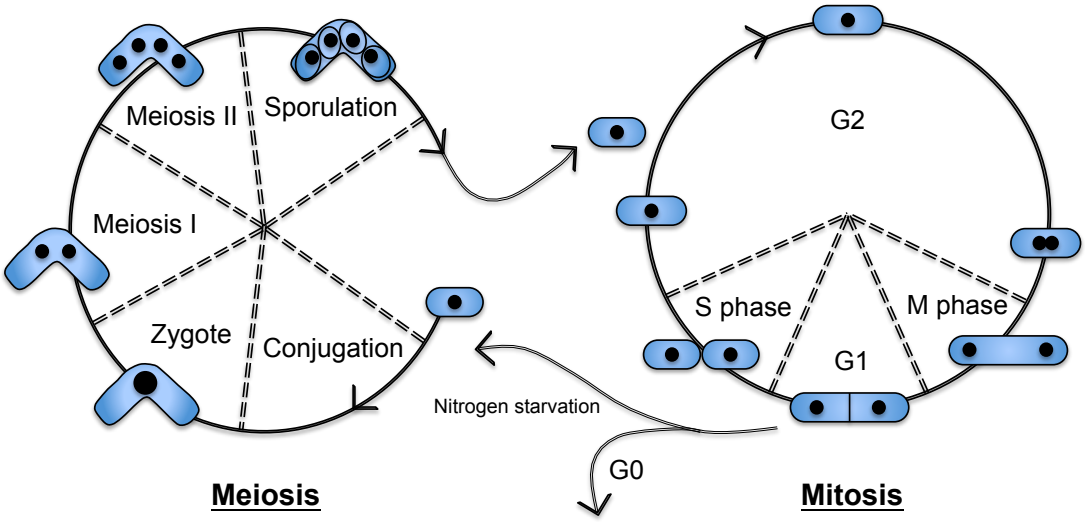

Figure 1.9. *S. pombe* mitotic and meiotic cell cycles.
Under favourable growth conditions, cells proceed through cycles of mitotic growth and division. In conditions of nitrogen starvation, cell growth arrests in G1. In the presence of appropriate mating factors, cells enter the meiotic cell cycle. This begins with conjugation with a cell of opposite mating type, and results in four haploid spores with can germinate and re-enter the mitotic cell cycle. Adapted from (PombeNet Forsberg lab)

1.6.1. Mitotic cell cycle.

Wild type fission yeast have a typical diameter of 3-4 μm, and grow by elongation to between 7 and 14 μm. Cells divide by deposition of a cell wall at the equator at the end of mitosis. *S. pombe* has a conventional eukaryotic cell cycle and nuclear division, however unique to fission yeast is the length of each of these phases: A short S-phase commences immediately after nuclear division and almost simultaneously with septum formation, resulting in a particularly long G2 phase. The reason for rapid DNA replication is largely due to the haploid state of the cells. Without a second copy of the DNA sequence, it is more difficult to repair damage, replicating the DNA early reduces the opportunity for damage to occur (Hoffman et al. 2015).

As described in section 1.3 the G2-M cell cycle transition point ensures cells reach a threshold size before division. As *S. pombe* grow only by tip extension, and divide by medial fission, they provide a simple model for the study of polarised cell growth, and the regulation of cell division. Medial localisation of the division site is essential to form two daughter cells of equal size. Cdr2 is a kinase which negatively regulates Wee1, the kinase retaining Cdk1-Cyclin B inactive. A polar gradient of Pom1, (a DYRK-family kinase), inhibits Cdr2, and confines its activity to the cell equator. As cells grow in length, the concentration of Pom1 at the middle of the cell falls, allowing activation of Cdr2 and entry of the cell into mitosis (Figure 1.10). This mechanism couples the cell cycle to polarized cell growth (Ullal et al. 2015).

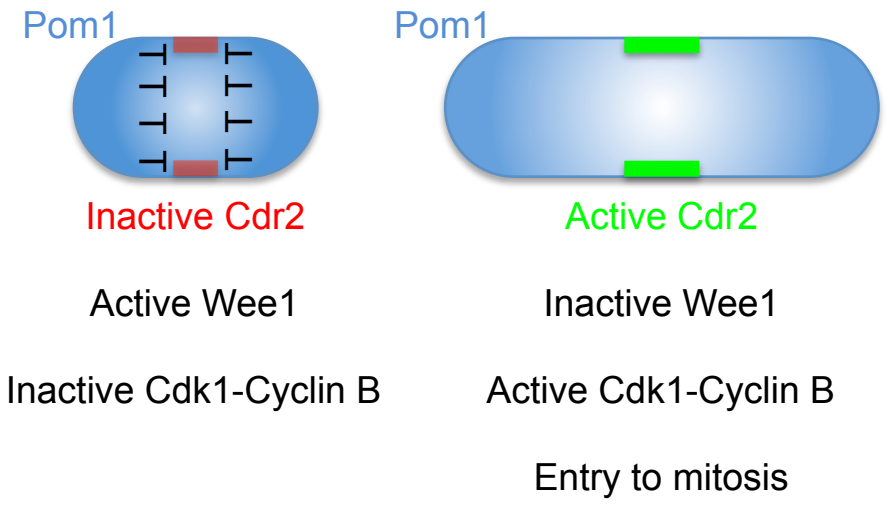

Figure 1.10. A Pom1 gradient regulates cell division.
A polar gradient of Pom1, ensures that Cdr2 remains inactive until the cell reaches an appropriate length. Cdr2 inactivates Wee1 kinase allowing entry into mitosis. This Pom1 gradient also regulates the positioning of Mid1, ensuring the CAR is positioned at the middle of the cell. Adapted from (Martin 2009).

Newly divided cells exhibit biased polarized cell growth during G2, observed as an asymmetric distribution of actin at the cell poles (Marks et al. 1986). Later in G2 and at a cell length of ~ 9.5 µm, 'New End Take Off' (NETO) occurs and growth

becomes bipolar (Figure 1.11) (Mitchison & Nurse 1985; Grallert et al. 2012). These regions of cell growth are marked by the presence of many proteins involved in new membrane and cell wall deposition, including endocytic patch proteins, actin and actin nucleating factors. Delivery of these proteins to sites of cell growth rely on transport by motor proteins such as Myo52 (Martín-García & Mulvihill 2009), and an intact network of actin cables (Pelham & Chang 2001). Initiation of growth and assembly of actin at this new cell end is dependent on regulation by microtubules (MT). Tea1 and Tea4 proteins associate with the plus ends of MT and are responsible for the recruitment of the actin nucleating formin protein, For3 (Martin et al. 2005)

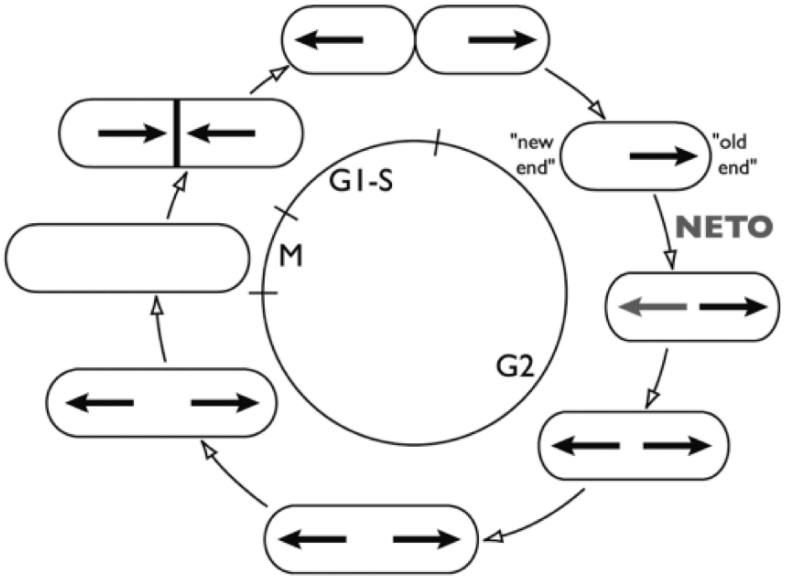

Figure 1.11. *S. pombe* regions of cell growth.
Arrows indicate the direction of cell growth in *S. pombe* cells at each stage of the cell cycle. Immediately after cell division growth is monopolar at the 'old end'. New end take off (NETO) results in establishment of bipolar growth. During mitosis, deposition of new cell membrane and cell wall material must occur at the septum. From (Martin 2014).

1.6.2. Meiotic cell cycle.

The mating type of *S. pombe* cells is determined by the expression of different alleles at the mating type (*mat1*) locus. Cells are either h^+ or h^-, expressing P factor or M factor respectively. Cells can also be homothallic, or h^{90}, meaning that

they are constantly switching between mating types. Therefore a colony contains cells of both h^+ and h^- and so can mate with itself.

Under conditions of nutrient depletion, particularly nitrogen starvation, expression of genes at the mating locus are induced (Yamamoto, M. 1997). Expression of mating pheromones and their receptors allows communication with cells of opposite mating type. TOR signalling also functions to regulate gene transcription in response to nitrogen starvation. TORC1 is down-regulated in response to nitrogen starvation (Matsuo et al. 2007), resulting in translocation of transcription factors to the nucleus (Laor et al. 2015), up-regulating expression of proteins such as Ste11 and Mei2, required for progression through meiosis (Kaur et al. 2006).

Polarised cell growth towards a cell of opposite mating type results in formation of a projection tip, allowing cells to conjugate, creating a diploid zygote that immediately enters meiosis (Nielsen & Davey 1995). During meiosis polarized cell growth and therefore cortical actin patches are located at specific structures (Petersen et al. 1998). Figure 1.12 shows the re-organisation of the actin cytoskeleton at multiple stages of meiosis. The four resulting haploid asco-spores can enter the vegetative cell cycle on return to favourable conditions.

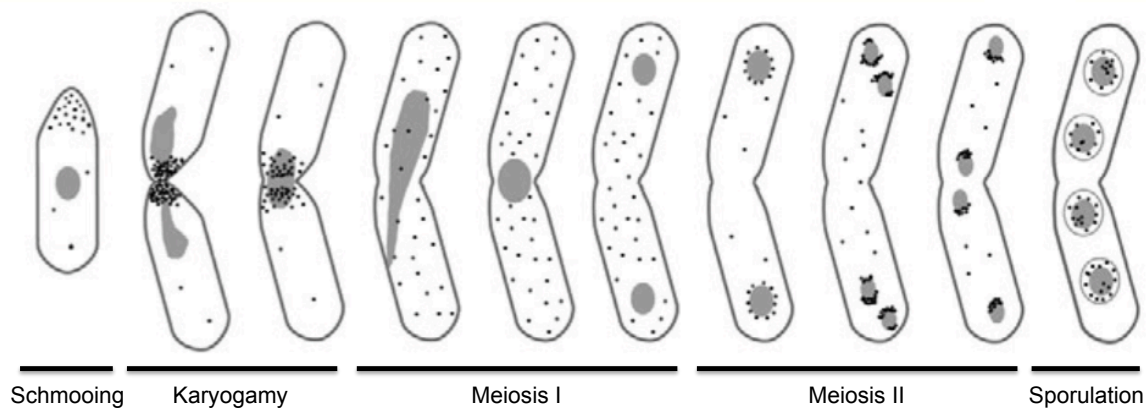

Figure 1.12. Actin distribution in *S. pombe* cells during meiosis.
Actin patches localise to the projection tip during conjugation, but absent from the exact fusion point. Actin is then evenly distributed until metaphase of meiosis II, where it is concentrated at the nuclei. Actin is then concentrated within spores once the spore wall is formed. Adapted from (Doyle 2009).

1.7. The cytoskeleton.

All cells contain some form of cytoskeletal structures, which play essential roles in maintaining cell shape, polarity and cell division. The cytoskeleton is also important for movement of cargoes within the cell and in some cases whole cell motility. Cytoskeletal structures are dynamic protein polymers often extending over long ranges within the cell, formed of actin filaments, intermediate filaments and microtubules.

Bacteria were initially thought to lack a cytoskeleton, but structures similar to those found in eukaryotic cells have since been identified. (Shih & Rothfield 2006) The structural and functional equivalents of actin and tubulin, MreB and FtsZ respectively, have a low sequence identity to their eukaryotic homologues. This suggests considerable divergence in function and regulation (Erickson 2007; Carballido-Lopez 2006). The functions of actin and tubulin-like polymers have been interchangeable during evolution. One example of which is during cell division, where mammalian cells form an actin based contractile ring, while bacteria utilise the tubulin homologue FtsZ at the Z-ring (Figure 1.13). This amongst other examples, indicates the shared characteristics of the cytoskeleton filament components. (Gunning et al. 2015).

As the size of organisms increased during eukaryotic evolution, as did the need for mechanisms to strengthen cells against greater physical stresses. These selection pressures drove the development of a more extensive cytoskeleton, resulting in complex mechanisms to regulate its formation, dynamics and disassembly. Subsequently families of motor proteins, nucleating factors and binding proteins have evolved to regulate the expanding eukaryote cytoskeleton (Wickstead & Gull 2011).

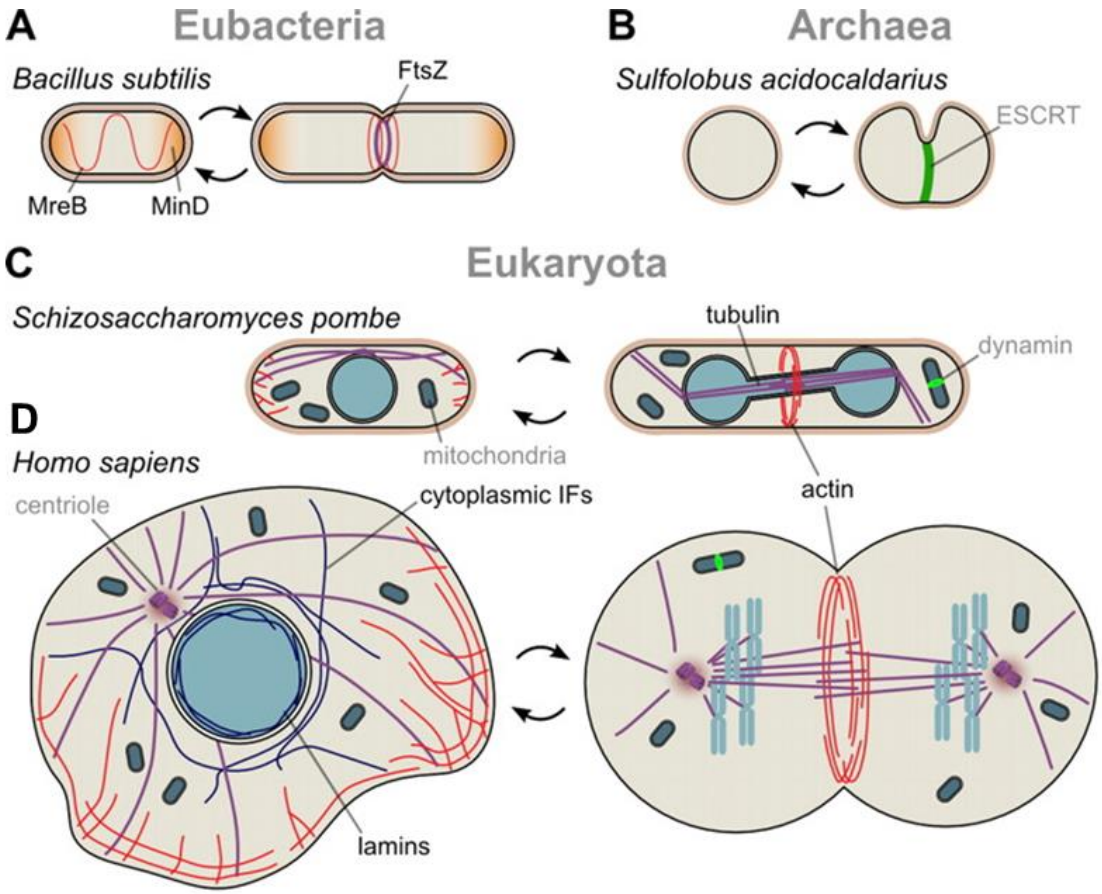

Figure 1.13. Cytoskeletal structures of prokaryotes and eukaryotes. Typical cytoskeletal structures in prokaryotic cells (A-B), and eukaryotic cells (C-D). Actin-like filaments (actin and MreB) are coloured red, with microtubules and FtsZ coloured purple. Intermediate filaments (blue) are only present in cells of multicellular organisms. The diagram shows a typical non-dividing and dividing cell for each organism. Adapted from (Wickstead 2011)

1.7.1. Microtubules.

Microtubules are highly dynamic structures composed of tubulin subunits. Heterodimers of α-tubulin and β-tubulin assemble end-to-end to form protofilaments, which then pack laterally to form a cylindrical tube. Each turn of the pseudo-helix is composed of 13 alternating α-β-tubulin subunits. This end-to-end arrangement of tubulin heterodimers means microtubules have polarity, with the free α-subunit end referred to as the *minus* end, and the exposed β-subunit being the *plus* end.

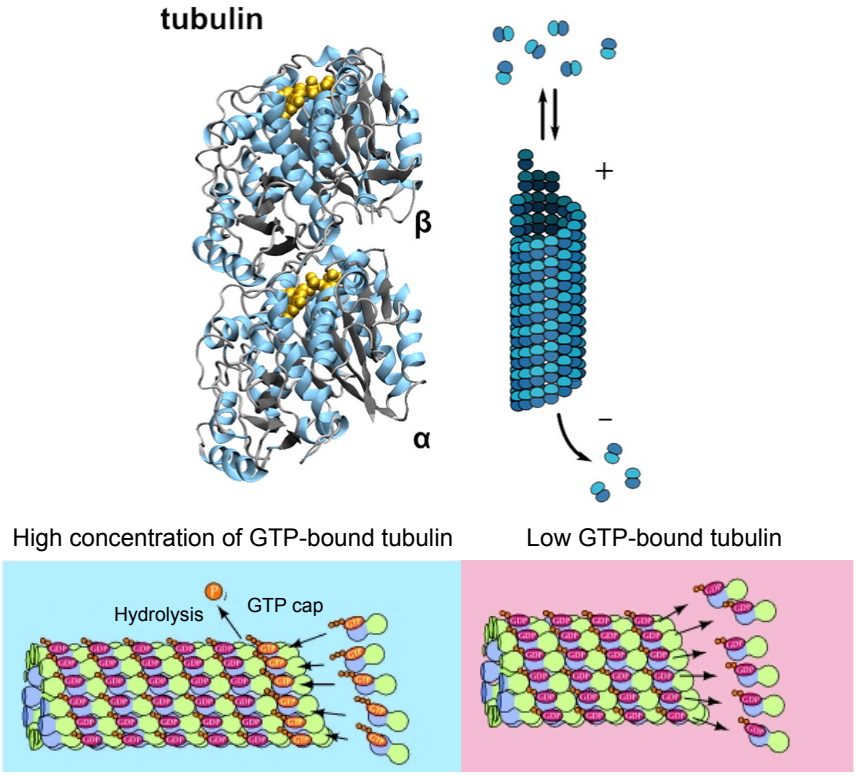

Figure 1.14. Structure and assembly of microtubule.

Crystal structure of an αβ-tubulin dimer, and diagram showing dimers assembling into a polarized microtubule. In the presence of GTP-bound tubulin, microtubules grow at the plus end by maintenance of a GTP cap. In the absence of GTP-bound tubulin, GDP-tubulin dissociates from the plus end. Adapted from (Wickstead 2011 and Cooper 2000).

Microtubules constantly grow (rescue) and shrink (catastrophe) from the highly dynamic plus end. GTP-bound tubulin is incorporated into the growing microtubule, where the GTP is hydrolysed to GDP. While the rate of GTP-bound tubulin addition is greater than GTP hydrolysis, the microtubule retains the GTP cap, and continues to grow. If the relative rate of hydrolysis increases, the more weakly bound GDP-tubulin heterodimers disassemble, and the microtubule shrinks (Figure 1.14).

Microtubule minus ends are anchored at microtubule organizing centres (MTOCs), the centrosome in animal cells, and the spindle pole body (SPB) in yeast. MTOCs contain γ-tubulin which nucleates new microtubules (Paoletti & Tran 2007). During interphase, microtubules are responsible for maintaining polarized cell growth and are major components of cellular structures such as cilia and flagella. During mitosis, the microtubule network is reorganised, with a large array of microtubules extending from the duplicated centrosomes to form the mitotic spindle. This mitotic spindle is responsible for orientating chromosomes for separation into daughter cells (O'Connell & Khodjakov 2007).

Numerous groups of microtubule-associated proteins (MAPs) regulate the dynamics and function of microtubules. These include kinesins, a class of processive motor proteins, which transport cargo along microtubules, towards the plus end. Dynein motor proteins move in the opposite direction, and play an important role in the movement of cilia and flagella (Mandelkow & Mandelkow 1995).

1.7.2. Intermediate filaments.

Intermediate filaments are polymers of fibrous protein only found in multicellular organisms, and largely function to maintain cell rigidity. Intermediate filaments are formed of extended alpha helical proteins such as keratin and lamin, which are packed into coiled-coil structures (Qin et al. 2009). Intermediate filaments form around the inner surface of the nuclear membrane, and throughout the cytoplasm to stabilise the nucleus and other organelles. Intermediate filaments also act to stabilise the epithelial layer by connecting adjacent cells at cell-cell junctions (Garrod & Chidgey 2008).

1.8. Actin.

Actin is one of the most highly conserved and abundant proteins in all eukaryotic cells, and is involved in cell growth, intracellular transport, endocytosis, cytokinesis and many other functions (Dominguez & Holmes 2011). Humans have six actin genes, four of which are expressed differentially between skeletal, cardiac and smooth muscle. The remaining two genes, ACTB and ACTG1 encode cytoplasmic isoforms. Actin is a 42 kDa protein, consisting of four subdomains with a nucleotide binding pocket in the cleft between subunits 1 and 3. (Kabsch & Holmes 1995). In cells, actin molecules are either found as globular actin monomers, G-actin, or polymerized into helical actin filaments, F-actin (Figure 1.15).

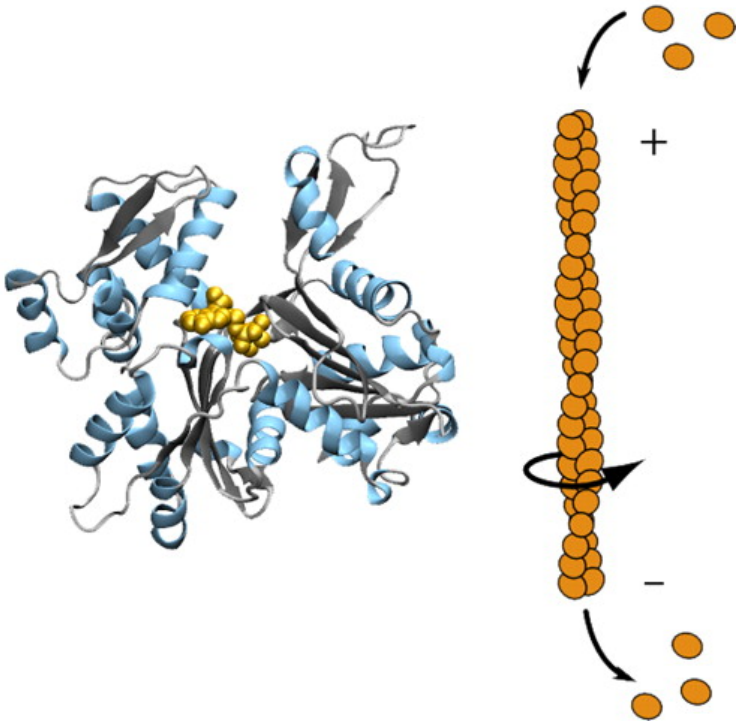

Figure 1.15. Structure and assembly of actin filaments.
Crystal structure of an actin monomer, and diagram showing formation of a helical F-actin filament. Adapted from (Wickstead 2011).

Polymerization of actin filaments occurs by addition of ATP-bound G-actin monomers predominantly to the barbed end, requiring the ATPase activity of actin to hydrolyze the bound nucleotide and stabilise the growing filament. (Pardee & Spudich 1982). At a critical concentration, actin is able to self-assemble into

growing helical filaments, however this process is limited by energetically unstable dimeric and trimeric intermediates. To overcome this initially unfavourable reaction, the nucleating activity of Arp2/3 and formin proteins is required for actin polymerization (Chhabra et al. 2007).

From this basic actin filament unit, a wide variety of larger actin structures can be formed. Figure 1.16. summarises some of the actin structures found in metazoan cells, each specialised to perform distinct functions. Structures such as lamellipodia and filopodia are required for protrusion of the leading edge of motile cells. Other structures such as phagocytic pits are formed for the specialised function of macrophage cells. Actin structures are also required for many common cellular processes, including cell-cell adhesions, endocytosis and cell division (Chhabra et al. 2007).

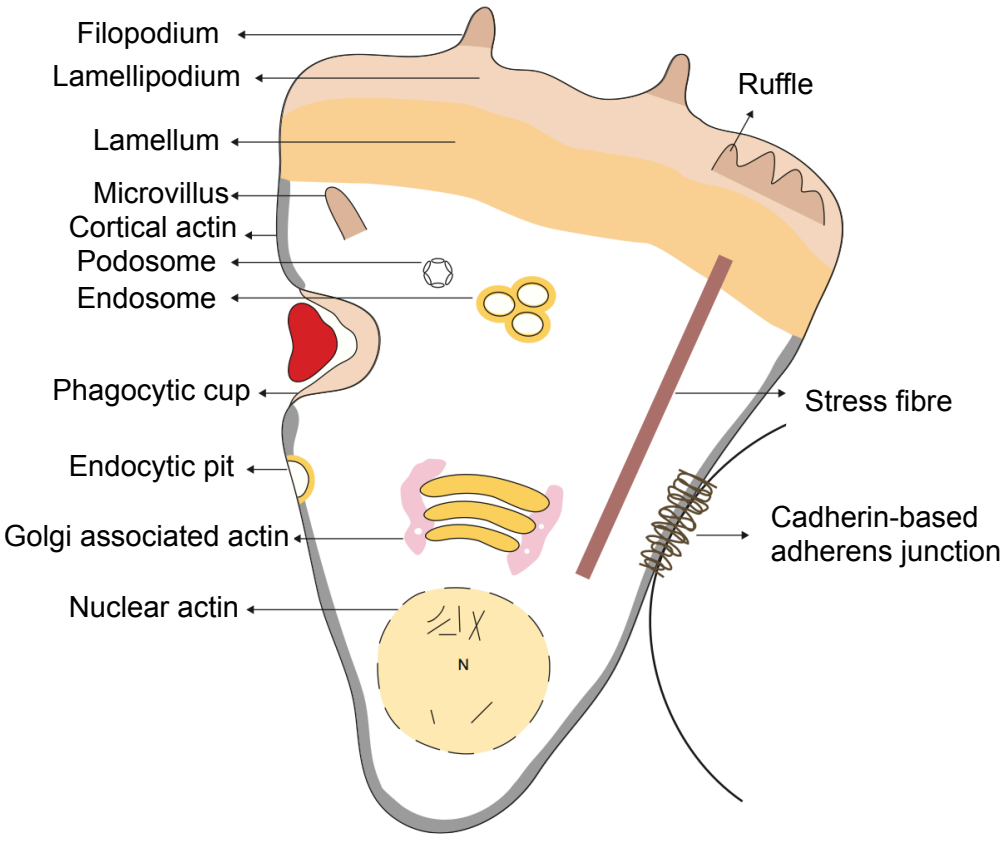

Figure 1.16. Actin based structures in metazoan cells.
Diagram of a hypothetical metazoan cell, migrating with a leading edge at the top and attachment to an adjacent cell on the right. Cellular structures known to contain actin are labelled. Adapted from (Chhabra 2007).

1.9. Actin binding proteins.

In order to form and maintain this array of dynamic actin structures, the cell expresses a large range of actin binding proteins. These actin binding proteins are involved in three major processes, actin polymerization, stabilization and depolymerisation. A specialised group of actin binding proteins required for force generation and transport along these actin filaments, are myosins, discussed later in this chapter.

Polymerisation:

1.9.1. Arp2/3

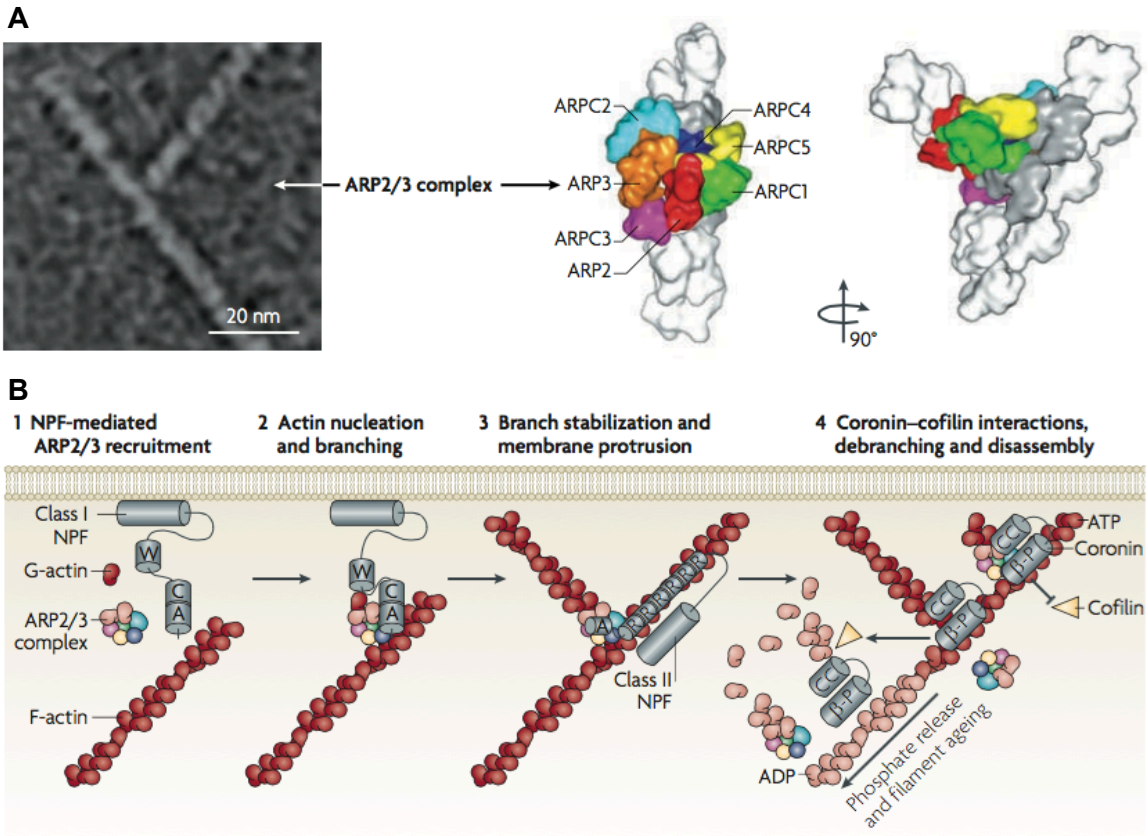

Figure 1.17. Actin nucleation by the Arp2/3 complex.

(A) Electron micrograph of an Arp2/3 branched actin filament, and structural models of the Arp2/3 complex. Class I NPFs recruit and activate the Arp2/3 complex, resulting in a branched actin network. Class II NPFs can bind and stabilise the branched filaments. Adapted from (Campellone 2010).

The Arp2/3 complex was the first class of actin polymerization factor to be identified, and is involved in the formation of branched actin networks. The complex is formed of seven conserved subunits, ARPC1-5 and the actin-related proteins, Arp2 and Arp3 (Figure 1.17). The structure of the Arp2/3 complex is thought to mimic an actin dimer, and act as a template for a new branched actin filament, at an angle of 70º to the mother filament (Firat-Karalar & Welch 2011).

The Arp2/3 complex requires the activity of nucleation-promoting factors (NPFs) to initiate the formation of new filaments. There are two major classes of NPFs. Class I NPFs include the Wiskott-Aldrich syndrome protein (WASP) family of proteins, WAVE, CARMIL and Class I myosins, but these vary dependent on the organism (Goley & Welch 2006). The common structures of these proteins are a WASP-homology-2 (WH2) domain, which binds G-actin, and an acidic domain required for binding to the Arp2/3 complex. Class I NPFs present actin monomers to the Arp2/3 complex, which allows the complex to facilitate the formation of an actin nucleus for polymerization. Class II NPFs include cortactin and the yeast proteins, Abp1 and Pan1. These proteins bind and recruit F-actin, which is also a weak activator of the Arp2/3 complex (Campellone & Welch 2010).

The Arp2/3 complex functions in the cell at locations of branched actin networks, including lamellipodia, cell-adhesions and endocytic vesicles. Actin polymerization is also thought to play a role in generating the force required to transport vesicles and organelles within the cell (Goley & Welch 2006).

1.9.2. Formins

Formins are large proteins, which function in a dimer to facilitate addition of actin monomers to the barbed end of actin filaments. Formins remain attached to the barbed end during this processive process, preventing capping, and promoting elongation of the actin filament (Kovar 2006). Each formin is formed of two formin homology (FH) domains. FH1 is required for binding of profilin-actin, while the FH2 domain binds to the barbed ends of actin filaments and is required for the nucleation of actin cables (Figure 1.18). Mammals express 15 isoforms of formins (Campellone & Welch 2010), while *S. pombe* express three.

Formins play a key role in maintaining cell polarity and facilitating reorganization of the cytoskeleton for many cellular processes, including cell movement and division (Young & Copeland 2010). The localisation and activity of formins in the cell is regulated in response to multiple signals, mainly coordinated through the Rho family GTPase, Cdc42 (Etienne-Manneville 2004). Cdc42 is thought to be responsible for the relief of auto-inhibition of formins (Goode & Eck 2007; Martin et al. 2007).

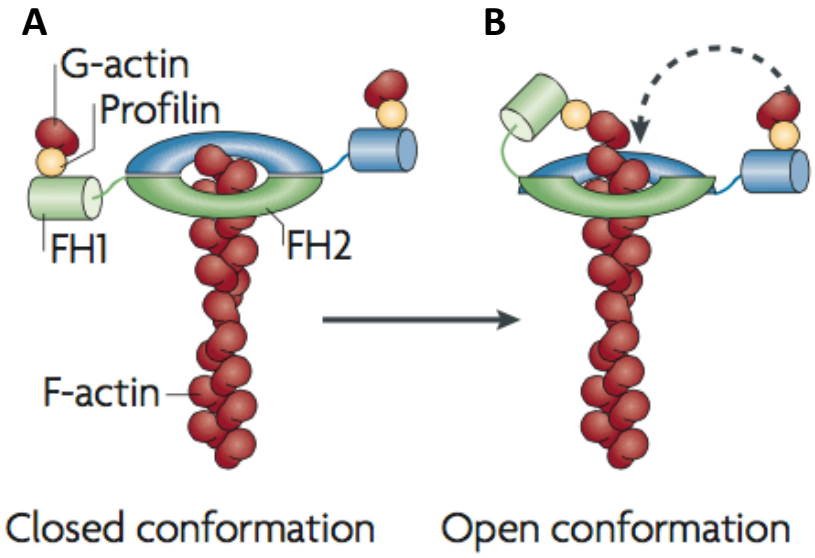

Figure 1.18. Actin nucleation by formins.
A formin dimer binds to the barbed end of an actin filament via the FH2 domains, while the FH1 domains recruit profiling-bound G-actin. The formin facilitates addition of the actin monomer to the barbed end of the filament, where it remains bound. Adapted from (Campellone 2010).

1.9.3. Spire proteins.

A group of proteins identified in *Drosophila* as a third class of actin nucleator, present in metazoan cells (Quinlan et al. 2005). They contain four WH2 domains and an actin binding site, which are capable of nucleating four actin monomers into a tetramer. Spire proteins remain bound to the pointed end of the polymerizing actin filament. Spire also has a capping function, binding to barbed ends of actin filaments, and has also been shown to sever filaments (Bosch et al. 2007).

Stabilisation:

1.9.4. Capping proteins

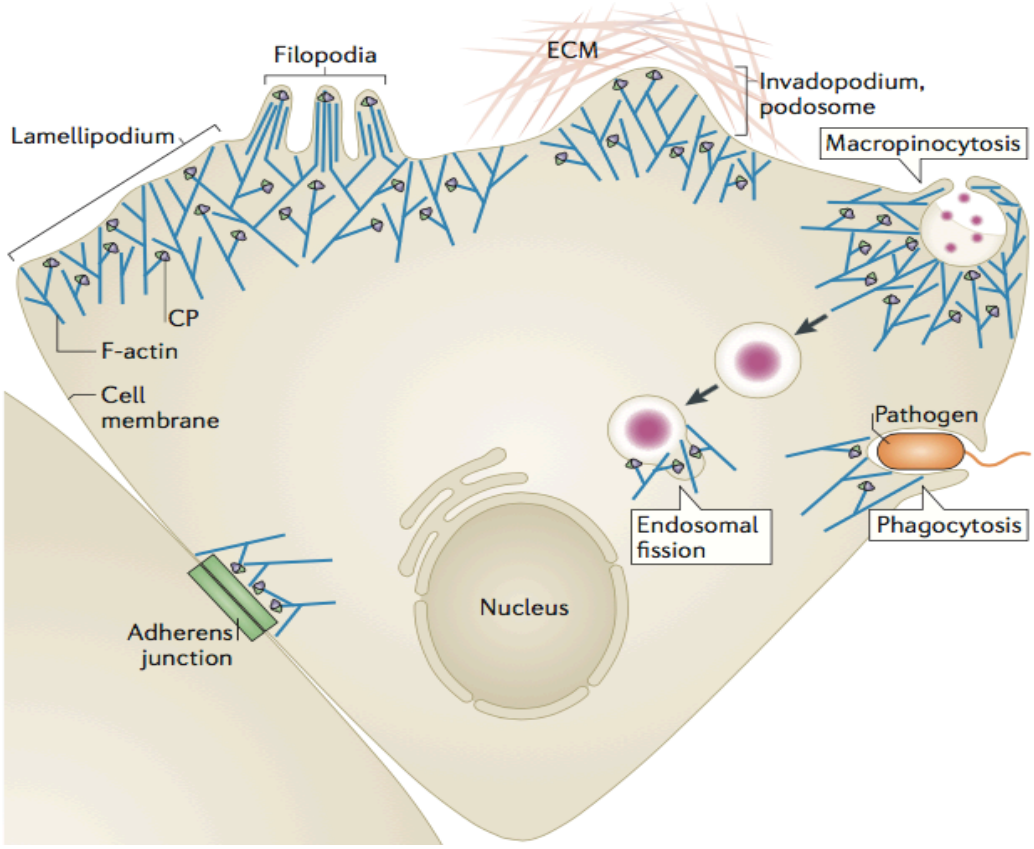

Figure 1.19. Regulation of branched actin networks by capping proteins. Localisation of capping proteins in a hypothetical metazoan cell. Capping proteins regulate Arp2/3 assembled actin filaments at the cellular structures labelled. From (Edwards 2014).

Capping proteins are heterodimers of α and β subunits, found in almost all eukaryotic cells. Capping proteins bind to the barbed end of filaments with a subnanomolar affinity (Wear et al. 2003; T. Kim et al. 2010), blocking the addition or loss of actin monomers. Human capping proteins (CapZA/B) are an essential component of the sarcomere Z-disk (Hart & Cooper 1999). While in non-muscle cells, capping proteins are required for the assembly of cortical actin patches (Cooper & Sept 2008; Ydenberg et al. 2011). Efficient capping of the barbed ends of Arp2/3 nucleated filaments ensures that a dense, highly branched network of actin is formed (Akin & Mullins 2008).

Capping protein binding to the actin filament is regulated by several mechanisms (Edwards et al. 2014). Elongation factors such as formins indirectly regulate actin capping by competing with capping proteins for the barbed ends of actin. The processive nature of actin nucleation by formins, remaining attached to the barbed end, prevents binding of capping proteins. Capping proteins are also directly regulated by binding of molecules such as PIP_2 phospholipids, which inhibit the association of capping protein heterodimers (Heiss & Cooper 1991).

1.9.5. Profilin

Profilin is a highly expressed, small actin binding protein found in almost all eukaryotic cells. Profilin promotes the exchange of ADP for ATP in actin monomers, maintaining a cytoplasmic pool of ATP-actin with a high affinity for the barbed end of actin filaments. Profilin bound actin monomers are required for the nucleation and elongation of actin filaments by formins (Kovar et al. 2003). Profilin also regulates cortical actin patch formation by inhibiting WASP activation of the Arp2/3 complex (Suarez et al. 2015).

1.9.6. Tropomyosin.

Tropomyosin is an α-helical actin binding protein, which forms a coiled-coil dimer. These dimers bind end-to-end to form a continuous polymer that binds in the two grooves of actin filaments. Tropomyosins have a wide range of functions, and in mammalian cells, approximately 40 isoforms are expressed from four genes, by alternative promoters and splicing (Pittenger et al. 1994; Gunning et al. 2005). In humans TPM1 and TPM2 genes encode α and β tropomyosin isoforms respectively, these can form either αβ heterodimers or homodimers.

On activation of muscle fibres, tropomyosin moves on the actin filament, exposing myosin binding sites, allowing muscle contraction. In non-muscle cells, tropomyosin is important for stabilization of actin cables and regulation of actin dynamics. Different tropomyosin isoforms have distinct functions and properties, (Lehman et al. 2000; Coulton et al. 2010) and their distribution within the cell is highly regulated (Bryce et al. 2003; Gunning et al. 2008). For example, Tpm 1.8/9 isoform is found in the lamellipodium of fibroblasts (Brayford et al. 2016) and modulates the Arp2/3 nucleated actin network, regulating cell motility (Blanchoin et

al. 2001; DesMarais et al. 2002). Tropomyosins also play a role in regulating filament elongation by formins (Wawro et al. 2007) and depolymerisation by ADF/cofilin (S. Ono & K. Ono 2002).

1.9.7. Cross-linking proteins

Many types of protein are responsible for stabilization of actin structures. Proteins responsible for crosslinking of actin filaments into parallel bundles are usually small, rigid proteins, with two actin binding sites to link filaments. Proteins such as fimbrin have two adjacent actin binding sites, and bind to actin as a monomer, creating a closely packed bundle (Klein et al. 2004). α-actinin is a larger protein with a single actin binding domain, and is found in actin bundles such as those in the contractile ring. These proteins must crosslink actin filaments through binding as a dimer, resulting in a more loosely packed bundle. These structures allow the interaction of myosin proteins and are capable of contraction (Sjöblom et al. 2008).

Disassembly:

1.9.8. ADF/Cofilin

Mammalian cells express one isoform of ADF, and two of cofilin. Both ADF and cofilin, bind preferentially to ADP-actin, and promote the levels of monomeric actin by filament severing. This family of proteins is responsible for the high rate of actin filament treadmilling, by increasing the rate of actin monomer disassociation at the pointed ends of filaments. These cofilin bound G-actin monomers can be recycled by profilin, ready for incorporation into the barbed end of actin filaments. This process of treadmilling maintains the dynamic nature of actin structures (Remedios et al. 2003).

Studies have shown that cofilin may have a role in modulating the binding of tropomyosin in specific actin networks. It has been shown that Tm1A is excluded from lamellipodia resulting in a densely branched actin network. In the adjacent lamella cofilin is thought to sever the branched actin network, facilitating tropomyosin binding to the pointed actin filament ends created. Tropomyosin binding in the lamellum results in a slower moving, stabilised actin network (Hsiao et al. 2015).

1.10. Actin structures in *S. pombe*.

S. pombe has a single actin gene – *act1*, which encodes an actin protein with 90% sequence identity to both human ACTB and ACTG1. With a single actin gene and a limited subset of associated proteins, yeast presents an attractive model system for study of the dynamics of essential actin structures required for eukaryotic life. Despite its relative simplicity, fission yeast are able to form three distinct actin structures to fulfill the diverse roles of actin within the cell (Figure 1.20).

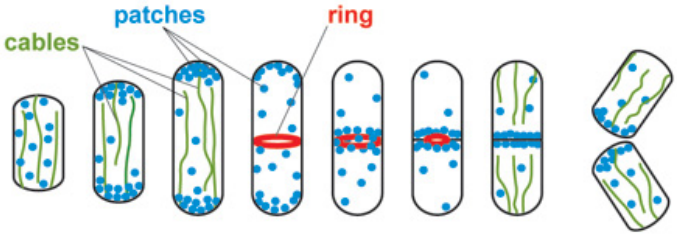

Actin structure	*Nucleation factor*	*Actin organization*	*Myosin motor*	*Cellular role*
cables:	For3p (formin)	long unbranched bundles	Myo52p (type-V)	Intra-cellular transport
rings:	Cdc12p (formin)	short unbranched bundles	Myo2p, Myp2p (-II) Myo51p (-V)	Cytokinesis
patches:	Arp2/3 complex	branched network	Myo1p (-I)	Endocytosis

Figure 1.20. Actin based structures in *S. pombe* cells.

Diagram showing typical localisation of actin structures during stages of *S. pombe* cell growth. For3 nucleated cables are found throughout the cell and are tracks for Myo52 motor proteins. Cdc12 nucleated actin filaments are found in the contractile actomyosin ring. Cortical actin patches are nucleated by the Arp2/3 complex and are found at sites of cell growth. Adapted from (Lord 2010).

1.10.1. Actin Cables.

Unbranched actin filaments are assembled from profilin-actin monomers by formins. *S. pombe* expresses three formins, For3, Fus1 and Cdc12, which have distinct roles in the cell. Fus1 is required to assemble actin during mating (Petersen et al. 1998), and in contrast to For3 and Cdc12, is also able to bundle actin filaments. Cdc12 localises to the cell equator, where it is an efficient nucleator of actin filaments which are incorporated into the contractile actomyosin ring. Formin, For3 is a much weaker nucleator of actin filaments (Scott et al. 2011).

Actin cables are formed of bundled parallel actin filaments, which are nucleated by For3. These cables extend throughout the cell and provide tracks for the movement of actin patches and cargo bound to type V myosins (Pelham & Chang 2001; Motegi et al. 2001). These filaments are polarized, with the barbed ends at the cell cortex during interphase, and contribute to polarized cell growth (Feierbach & Chang 2001).

For3, and activation factors such as Cdc42, are targeted to the cell ends by microtubule plus-end factors, Tea1 and Tea4. For3 is transiently anchored to the cell tip, where it drives actin cable polymerization from the cortex (Martin & Chang 2006). Assembly of actin filaments by For3, specifically results in actin cables decorated with an unacetylated form of Cdc8 tropomyosin (Johnson et al. 2014; Coulton et al. 2010).

1.10.2. Contractile actomyosin ring.

Most eukaryotes assemble a contractile actomyosin ring (CAR) for cytokinesis, formed of a conserved group of proteins (Balasubramanian et al. 2004). The contractile actomyosin ring structure of fission yeast is formed of actin and myosin II along with other cytoskeletal and signalling proteins. Positioning of the contractile ring at the cell equator is dependent on the anillin-like protein, Mid1 (Bähler et al. 1998). Mid1 localisation at the middle of the cell is determined by a polarized gradient of Pom1 (Figure 1.10) (Padte et al. 2006).

There are two independent but complimentary models of ring formation: 'Search, capture, pull, release' (SCPR) based around Mid1 function, and the 'leading cable' model relying on the septation initiation network (SIN) (Figure 1.21).

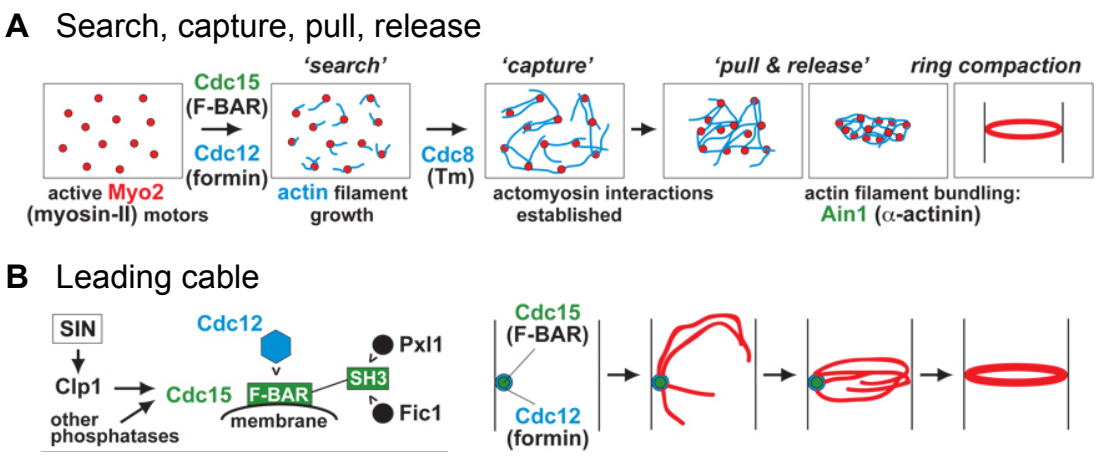

Figure 1.21. Formation of the CAR in *S. pombe* cells.

Summary of the two methods of CAR formation. (A) SCPR involves Mid1 nodes at the cell equator recruiting Myo2, Cdc12 and Cdc8 which nucleate, capture and stabilise actin filaments. These filaments form a ring through the motor activity of Myo2 and bundling by α-actinin. (B) The SIN signalling pathway is responsible for recruitment of Cdc15 and Cdc12 which nucleates actin filaments, which in the absence of the SCPR mechanism are also able to form a ring. Adapted from (Kovar 2011).

Mid1 node formation on the plasma membrane at the cell equator occurs >90 mins before SPB separation (Paoletti & Chang 2000). As SPBs separate, Mid1 recruits CAR components, including the class II myosin, Myo2 and the formin, Cdc12 (Motegi et al. 2000; Wu et al. 2006). Soon after, these nodes are condensed in to a contractile ring, incorporating actin monomers, tropomyosin, Cdc8 and the cross-linking protein, α-actinin (Wu et al. 2003). The SCPR model (Figure 1.21.A) proposes that actin filaments are nucleated, and anchored to nodes, by Cdc12. Elongating filaments 'search' the neighboring space until they are 'captured' by

Myo2. Myo2 movement along these filaments, ‘pulls’ nodes together to form the CAR, until filaments break or are ‘released’ from Myo2 (Vavylonis et al. 2008).

Maturation of the contractile ring occurs over a period of around 25 minutes, the ring diameter remains constant, while additional protein components, such as Myp2, Arp2/3 and capping proteins arrive at the CAR. The SIN pathway coordinates the timing of mitosis and cytokinesis (Gould & Simanis 1997). SIN is a network of protein kinases which associate with the SPB, and are regulated by the GTPase, Spg1 (Schmidt et al. 1997). The SIN pathway is essential for ring stability and maturation, in particular the recruitment of the F-BAR protein, Cdc15 (Hachet & Simanis 2008; Balasubramanian et al. 1998). Cdc15 regulates the recruitment of the formin Cdc12 to the CAR, and therefore subsequent actin assembly (Carnahan & Gould 2003; Willet et al. 2015).

In the absence of Mid1 nodes, cells can form actomyosin rings capable of contraction, although at a reduced efficiency, and are misplaced. The ‘leading cable’ mechanism of CAR formation (Figure 1.21.B) describes an aster-like structure of F-actin cables at the cell equator (Arai & Mabuchi 2002). These are bundled together to form the CAR (Pelham & Chang 2002). However, in the absence of components from both SCPR and SIN, no rings are formed (Hachet & Simanis 2008; Huang et al. 2008; Simanis 2015). This suggests that the leading cable mechanism forms a ‘backup’ for ring formation (Laporte et al. 2010).

Cdc12 requires the presence of profilin, Cdc3, to elongate actin filaments at the barbed end. This profilin-gating means that, in the absence of profilin, Cdc12 acts as a capping protein bound to the barbed end of filaments (Kovar et al. 2003). The capping protein heterodimer, Acp1/2 localises to the cell equator just before CAR constriction. It is thought that Acp1/2 competes with Cdc12 for binding to barbed ends of actin filaments (Kovar et al. 2005). Replacement of the formin for a capping protein, leads to dissociation of actin subunits from the pointed end of the filament. This depolymerisation is required for ring constriction (Wu et al. 2003).

1.10.3. Cortical actin patches.

Cortical patches are dense networks of branched actin filaments that localise to sites of cell growth, where they are required for endocytosis (Mulholland et al. 1994). In fission yeast, actin patch localisation reflects the regions of cell growth - the tips of growing cells and at the cell equator during mitosis. Immediately after division, actin patches are only concentrated at the old end of the cell. After NETO has taken place, actin patches are observed at both ends of the cell (Marks et al. 1986).

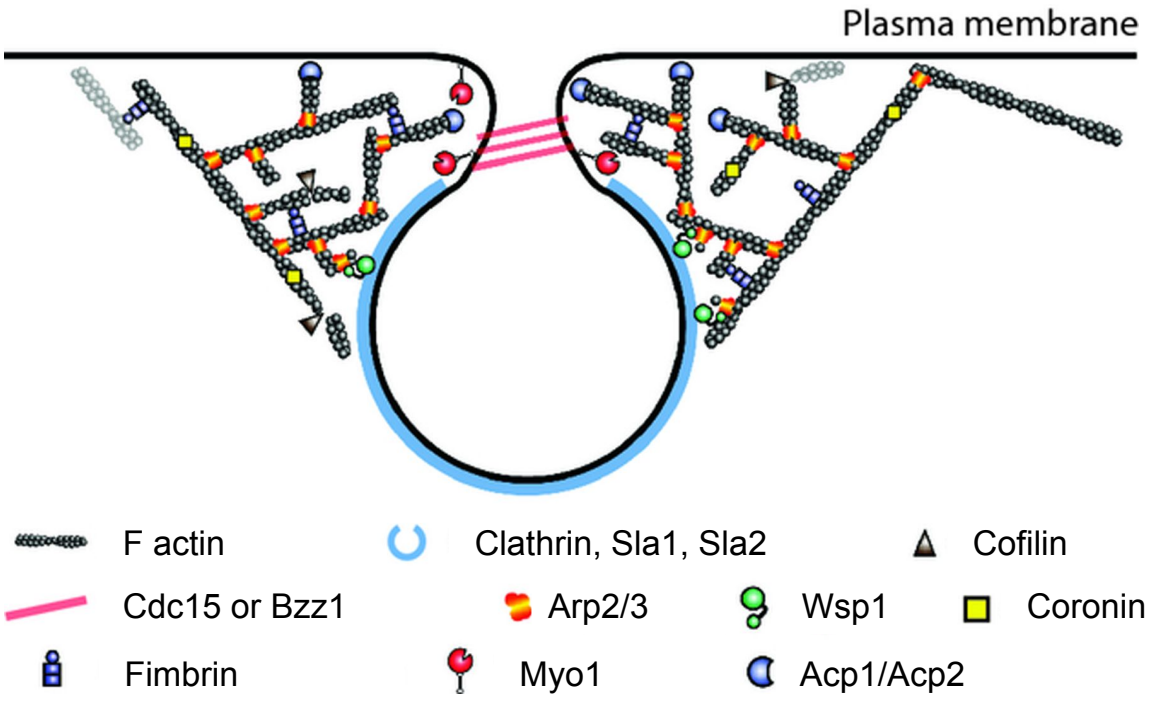

Figure 1.22. Formation of cortical actin patches in *S. pombe* cells.

A cross-section of a cortical actin patch assembled at an endocytic site. Clathrin and adaptor proteins arrive first and form a coated pit. NPFs, Myo1 and Wsp1 recruit and activate the Arp2/3 complex. Arp2/3 nucleates a dense network of branched actin filaments around the forming vesicle. Fimbrin cross-links the actin filaments in the actin patches. Capping proteins limit the growth of actin filaments, which are severed by cofilin. F-BAR-domain proteins, Cdc15 and Bzz1 promote membrane invagination and scission. Adapted from (Mishra 2014)

Actin patches have been shown to consist of a network of up to 150 branched actin filaments (Kovar et al. 2011). These filaments are restricted to a relatively short length of 100-200 nm by rapid association of actin capping protein – a heterodimer of Acp1 and Acp2, which binds the barbed end of actin filaments (Nakano & Mabuchi 2006). Actin patch movement is thought to be directed by actin polymerization and actin cables, and occurs at a velocity of ~0.3 μm s^{-1} (Pelham & Chang 2001).

Arp2/3 requires NPF activity to facilitate nucleation of branched actin filaments. In *S. pombe*, the WASP family member, Wsp1 contains the characteristic WH2 and acidic domains necessary to activate the Arp2/3 complex (Higgs 2001). The class I myosin, Myo1, also has C-terminal acidic domain which is capable of activating the Arp2/3 complex. Myo1 activates the Arp2/3 complex three-fold more weakly than Wsp1, but is enhanced by the WH2-domain containing protein, verprolin, Vrp1, which is recruited by Wsp1 (Sirotkin et al. 2005). Myo1 localises to the neck of the endocytic vesicle, while Wsp1 localises to a more distal region (Mishra et al. 2014).

The Arp2/3 complex arrives at actin patches ~3 seconds after Myo1 and the actin network builds around the forming vesicle. Actin polymerization is thought to extend the endocytic neck region (Kaksonen et al. 2006). The F-BAR proteins, Cdc15 and Bzz1 are required for vesicle scission (Carnahan & Gould 2003; Arasada & Pollard 2011) Actin associated proteins are internalised centripetally with the endocytic vesicle but Myo1 remains at the membrane (Sirotkin et al. 2005).

1.11. Homeostasis of the actin cytoskeleton.

Cells maintain a relatively constant concentration of cytoplasmic G-actin monomers which are available for nucleation into different actin structures within the cell at appropriate stages of the cell cycle (Rotty et al. 2015). This pool of unassembled actin monomers is maintained by G-actin binding proteins such as profilin, and prevented from associating with F-actin structures by capping proteins. While actin polymerization is tightly controlled by multiple GTPase signalling pathways, regulating the activity of actin nucleators (Torres & Rosen 2006; Lai et al. 2009; Ridley 2006).

The competition for this limited pool of actin monomers, by different assembly factors, has been investigated in fission yeast cells. Normally, around 35 – 50 % of the ~1 million actin molecules in each cell are incorporated into cortical patches, with ~15 % in actin cables and ~10 % found in contractile rings (Sirotkin et al. 2010). Disruption of the Arp2/3 complex reduces the numbers of cortical actin patches, but simultaneously increases the amount of formin assembled actin cable structures. Likewise, disruption of formin nucleation, leads to increased actin patch density. This balance in the formation of actin structures, is as also affected by the cellular concentration of actin. Increased actin concentrations favour the formation of Arp2/3 mediated actin patches, while at lower concentrations increase levels of actin cables (Burke et al. 2014). Similar mechanisms of actin regulation are likely to be present in higher eukaryotic cells, with observation of increased cable structures in the absence of Arp2/3, in *Drosophila* and *Dictyostelium* cells (Steffen et al. 2006; Rogers et al. 2003).

1.12. Endocytosis.

Endocytosis involves the internalisation of lipids and proteins of the plasma membrane along with extracellular fluids and molecules. It allows the cell to detect and respond to changes in the environment, uptake nutrients, eliminate pathogens and facilitates cell-cell communication. Mammalian cells have multiple endocytic pathways, (clathrin-mediated endocytosis, caveolar-type endocytosis, macropinocytosis amongst others), each adapted to allow internalisation of fluids and solutes or larger particles (Figure 1.23) (Conner & Schmid 2003). These distinct, and highly regulated pathways mediate the uptake of different types and sizes of extracellular material, and begin the process of targeting the cargo to the appropriate site within the cell (Doherty & McMahon 2009).

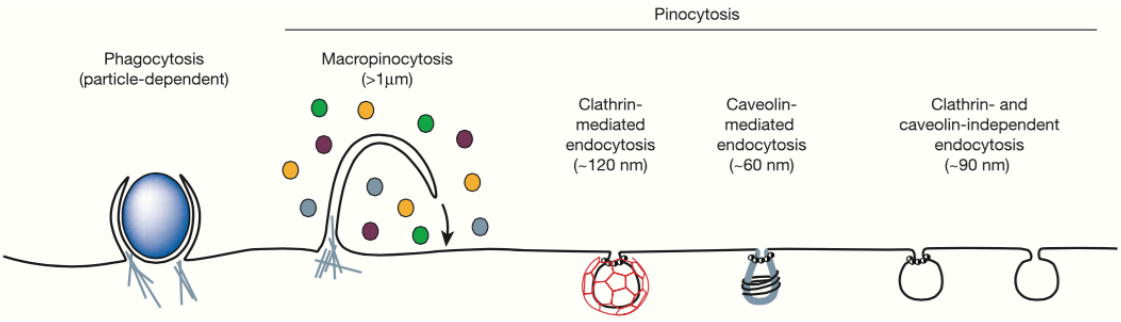

Figure 1.23. Endocytic pathways in mammalian cells.

Mechanisms used by mammalian cells to internalise extracellular molecules. The type of vesicle formation depends on the nature of the cargo. Adapted from (Conner 2011).

1.12.1. Clathrin-mediated endocytosis.

The major pathway of endocytosis in eukaryotic cells is clathrin-mediated endocytosis. The protein components of this process are conserved between mammals and yeast, and their spatial and temporal organization have been extensively studied (Conner & Schmid 2003) (Kaksonen et al. 2003) (Kaksonen et al. 2005). However much of the control mechanisms of this pathway remain unknown. For example the mechanism by which cargos are captured into lipid

rafts at sites of endocytosis, and how the localisation of these patches are determined.

Clathrin-mediated endocytosis comprises of a basic pathway starting with assembly of the clathrin coat and cargo at a site on the plasma membrane (Figure 1.24). Membrane binding proteins, scaffold and adaptor proteins are recruited to the endocytic patch, where actin assembles to drive invagination of the forming vesicle (Kaksonen et al. 2003). Many different proteins play roles in sculpting the lipid bilayer for eventual scission of the vesicle from the membrane. Once detached from the membrane, the vesicle is rapidly internalised by actin polymerization and the endocytic coat immediately disassembles.

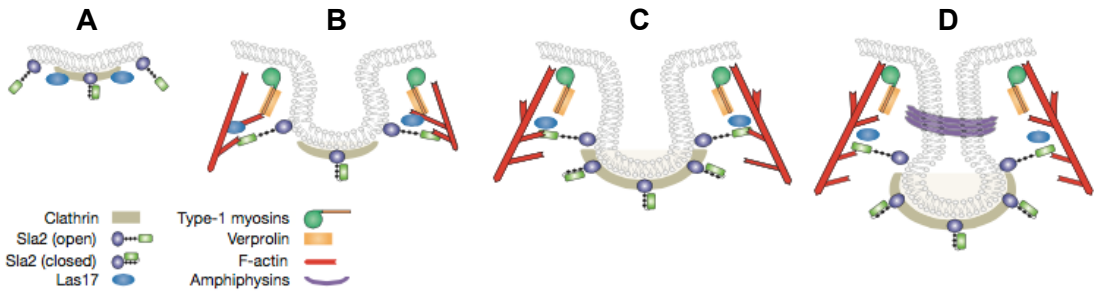

Figure 1.24. Formation of clathrin mediated endocytic vesicles.

(A) Early coat proteins, including clathrin, localise to the membrane and begin to form a coated pit. (B) NPFs, Class I myosin and WASP proteins arrive and recruit Arp2/3. (C) A branched network of actin forms around the vesicle. This actin network is cross-linked to the membrane by Sla2/Hip1R/Talin proteins, and facilitates elongation of the vesicle tubule. (D) Amphiphysin proteins, such as dynamin are involved in pinching off the vesicle from the membrane. Adapted from (Beottner 2011)

There are some key differences between clathrin-mediated endocytosis in yeast and mammalian cells. Most strikingly being that actin appears essential in yeast

endocytosis (Munn 2001), but not in mammalian cells (Engqvist-Goldstein & Drubin 2003). The role of actin is thought to be required to generate force for vesicle internalisation (Merrifield et al. 2002) – The high turgor pressure of a yeast cell requires more force to deform than in a metazoan cell (Basu et al. 2014; Aghamohammadzadeh & Ayscough 2009).

1.12.2. Endocytic patch formation.

Little is known about the precise mechanisms for locating and initiating the formation of endocytic patch sites. However the requirement for phosphatidylinositol-4,5-biphosphate (PIP_2) in recruiting subsequent proteins involved in patch formation, implies that lipid phosphorylation by inositiol kinases functions during these early stages (Takeda & Chang 2005; Sun et al. 2007).

There is a defined pathway of endocytic complex formation (Figure 1.25), beginning with the first early coat protein to arrive at the membrane, clathrin, which polymerises to form a polygonal curved lattice structure, shown by EM (Cheng et al. 2007). This clathrin coated pit induces the curvature in the membrane that develops into the forming vesicle.

The timings of subsequent protein recruitment to endocytic patches have been characterised in budding yeast and these relative timings are shown in Figure 1.25 (Kaksonen et al. 2005). Once the clathrin coat has formed, further adaptor proteins arrive including Sla1, End3, Pan1, Las17 all thought to be activators of the Arp2/3 complex. Also recruited is Sla2, the mammalian Hip1R homologue (Engqvist-Goldstein et al. 1999).

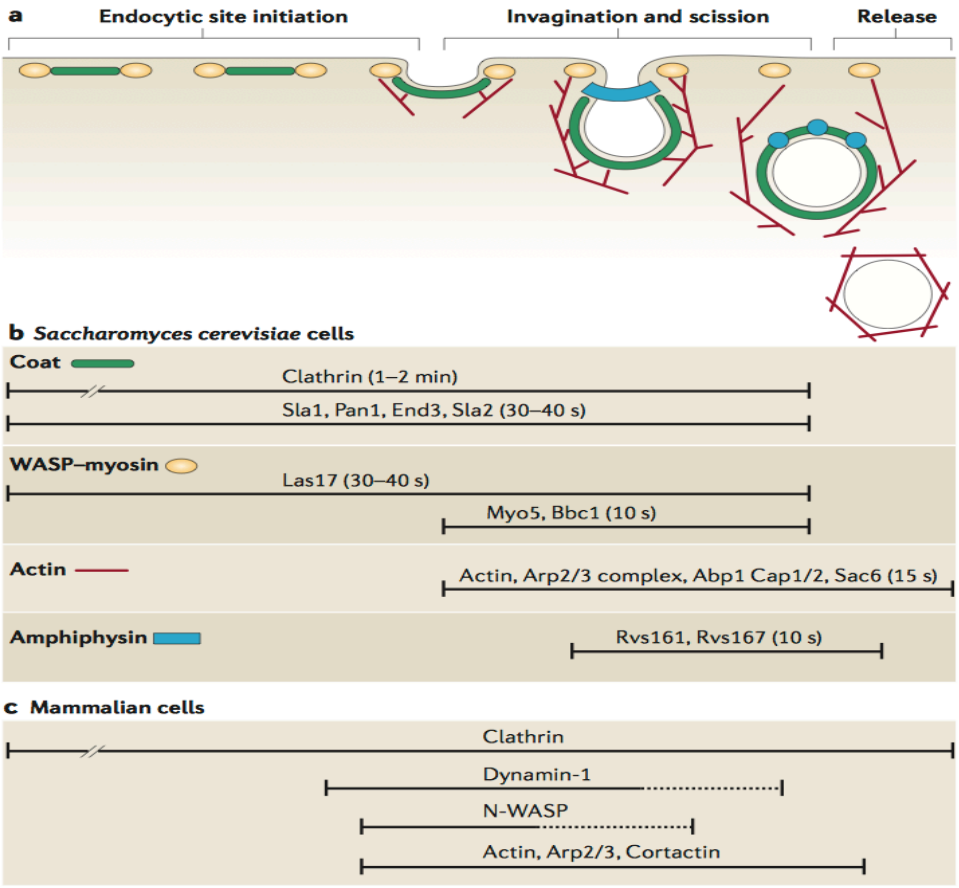

Figure 1.25. Formation of clathrin mediated endocytic vesicles.

Timings of sequential assembly of protein components of the endocytic patch. Timings determined in *S. cerevisiae* and approximated in mammalian cells in relation to vesicle internalisation. From (Kaksonen 2006)

Sla2 is conserved in yeasts and is homologous to human Hip1R (Seki et al. 1998) and contains a talin-like C-terminal region (McCann & Craig 1997). Sla2 has three key domains that are crucial for its ability to link the coated membrane pit to the polymerizing actin network. Sla2 is recruited to the endocytic site through binding of its ANTH domain to PIP_2 in the membrane. The central coiled coil region interacts directly with clathrin light chain further stabilizing its interaction at the growing patch. This leaves the C-terminal THATCH domain free to interact directly with actin filaments as they form around the vesicle. It is thought that this interaction may be involved in translating the force of actin polymerization into invagination of the membrane. Cells deficient of Sla2/Hip1R are unable to internalise the endocytic vesicle (Kaksonen et al. 2003; Engqvist-Goldstein & Drubin 2003).

1.12.3. Internalisation of endocytic vesicles.

Many proteins of the early coat contain membrane binding domains that interact or insert into the lipid bilayer, destabilizing the membrane, allowing curvature of the invagination and membrane fission as the vesicle pinches off (Conner & Schmid 2003). In yeast cells polymerization of a branched actin network is essential for extension of the coated pit into an invagination ready for scission. This burst of actin polymerization is tightly regulated through NPF activation of the Arp2/3 complex. The recruitment and activation of these NPF's are in turn closely regulated.

Fission yeast have two independent but co-operative pathways of activating Arp2/3. The first nucleating factor to arrive at the endocytic patch is Wsp1 bringing with it verprolin, an enhancer of the second NPF, Myo1. Deletion of either *wsp1* or *myo1* results in delayed patch internalisation, however deletion of both genes is lethal (Sirotkin et al. 2005). Both Wsp1 and Myo1 contain an acidic C-terminal domain which activates the Arp2/3 complex to nucleate the formation of branched actin filaments around the forming vesicle (Sirotkin et al. 2005). Wsp1 and verprolin are seen to internalise with the vesicle, while Myo1 remains at the membrane before disappearing. This is consistent with reports of a possible role for Myo1 in vesicle scission (Jonsdottir & Li 2004)

It is the force of this actin polymerization which is though to contribute to the extension of membrane tubules (Kaksonen et al. 2006). This burst of actin polymerization stops when scission occurs and the vesicle is internalised. While actin is not essential for endocytosis in mammalian cells (Yarar et al. 2002), in yeast, both depolymerisation of actin by Latrunculin A and stabilization by jasplakinolide completely block endocytosis (Ayscough et al. 1997; Ayscough 2000).

The final stage of vesicle scission is thought to require the yeast dynamin homologue, Vps1. Vps1 forms a ring at the neck of the endocytic tubule, where it binds and bundles actin filaments. This reorganization of actin is thought to facilitate vesicle scission (Palmer et al. 2015). The internalising vesicle moves into

the cell in a rapid, centripetal movement (Lee et al. 2000). The F-actin network is rapidly disassembled by actin severing molecules such as cofilin. The protein coat surrounding the vesicle is also disassembled and recycled, with Ark and Prk family kinases playing a role in releasing these protein complexes.

1.13. Myosins.

Myosins are a group of highly conserved actin-based motor proteins. All eukaryotic organisms with an actin cytoskeleton, have at least one myosin, however most encode a significant number, each with defined functions. There are at least 15 known myosin classes (Figure 1.26.A), with different cell types expressing a subset of these proteins. Myosin proteins are required for a large number of diverse cellular functions, including muscle contraction, cytokinesis, endocytosis, and cell motility.

All myosins share the same basic domain structure (Figure 1.26.B). The conserved motor domain of myosin proteins contain an actin binding site, and nucleotide binding pocket specialised for ATP hydrolysis (Rayment 1996). The myosin neck region is formed of varying lengths of helical IQ domains, which bind myosin light chains. The structure of the tail region depends on the myosin class, and defines the specific function of the protein.

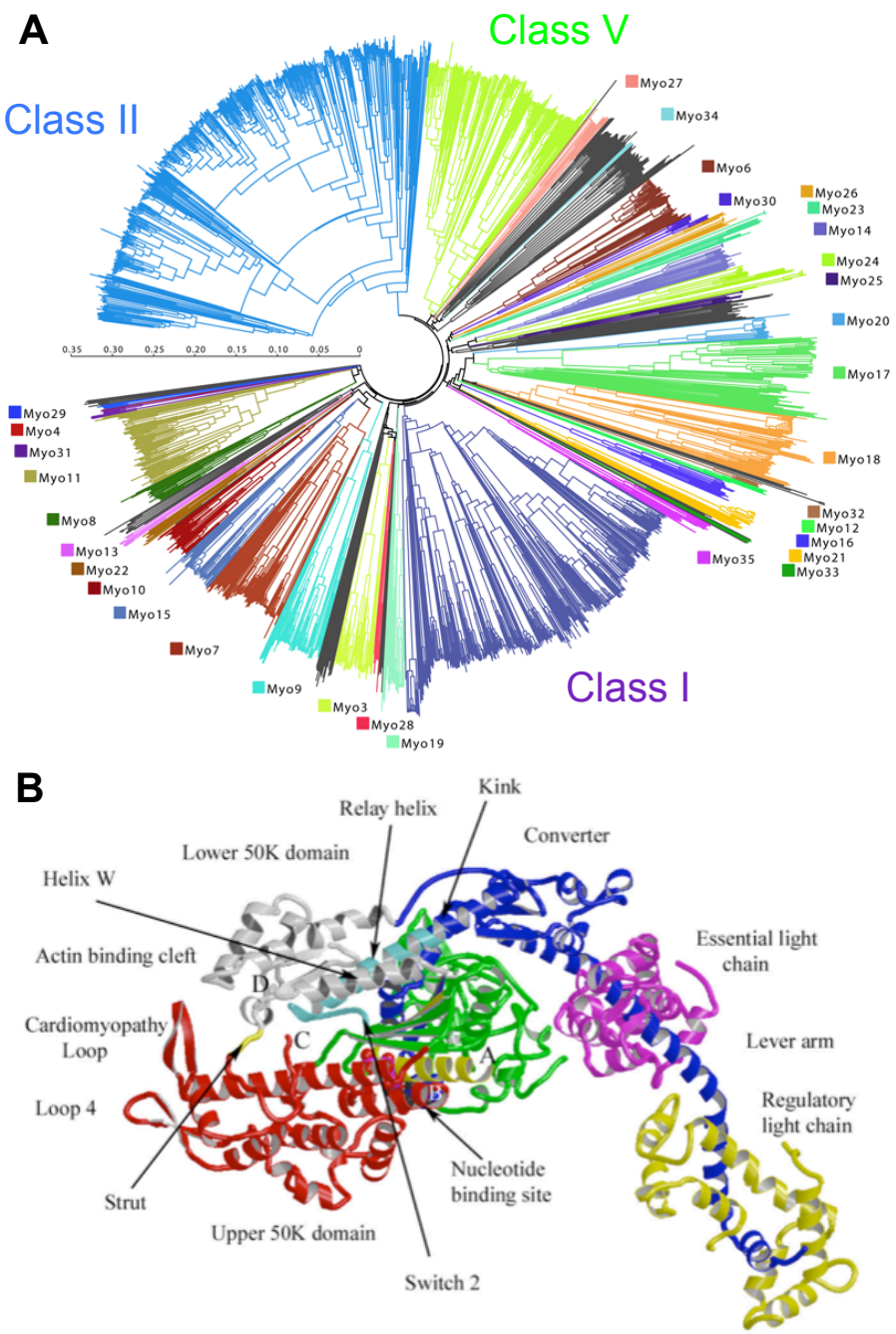

Figure 1.26. Myosin classification and typical structure.

(A) Phylogenetic tree constructed from 1984 myosin motor domain sequences. Myosin II, I and V form the largest classes. Adapted from (Odronitz 2007). (B) A ribbon diagram of the basic domains of myosin motor proteins, with two light chains bound to the neck region. From (Geeves 2005).

Myosins are classified into two broad classes, conventional filament forming myosins (Class II), and unconventional myosins. Unconventional myosins contain diverse tail domain structures, which determine their localisation and function (Sellers 2000; Hartman & Spudich 2012). Humans express 15 Class II myosins, and 25 unconventional myosins (HUGO gene Nomenclature Committee 2016). Figure 1.26.A shows a phylogenetic tree formed from an alignment of myosin motor domain sequences. This shows that amongst the multiple classes of myosins, Class II, I and V are the most abundant.

1.13.1. Class II.

Class II myosins are characterised by a long coiled-coil tail that allows dimerization. In muscle cells, homodimers of Class II myosins form part of the heavy chain filaments required for muscle contraction. Class II myosins are also found in non-muscle cells, where they are responsible for providing the contractile force during cytokinesis (La Cruz & Ostap 2004).

1.13.2. Class V.

Class V myosins also have a coiled-coil region of the tail, which allows dimerization. The C-terminal domain of Class V myosins is a cargo binding domain which allows the transport of organelles, vesicles, mRNA, and proteins along actin cables (Trybus 2008). Myosin V dimers are able to take multiple steps towards the barbed end of actin filaments without dissociating. This is achieved by the high duty ratio of the motor domain with Myosin V-ADP having a high affinity for actin. This allows one head to dissociate, take a step and reattach to actin before the other head detaches. The long neck regions of myosin V means that the two heads are able to span the 36 nm between helical repeats of actin (Walker et al. 2000). This allows linear movement along actin filaments which has been observed using electron microscopy and optical trap experiments (Mehta et al. 1999).

1.13.3. Class I.

The third major class of myosins are class I myosins. These are monomeric, membrane-associated motor proteins, which play essential roles in endocytosis, cell motility and cytoskeleton organization (Kim & Flavell 2008). As discussed in previous sections, Class I myosin proteins act as a cross-linker between the membrane and actin cytoskeleton, where they are involved in regulating tension and activating the Arp2/3 complex (McConnell & Tyska 2010).

Vertebrates have 8 class I myosin genes, Myo1b-e are expressed in most cell types, while Myo1a, f and g are expressed in only in specific tissue types (Berg et al. 2001). The diversity of the tail region of class I myosins results in diverse cellular functions including, regulation of membrane tension (Nambiar et al. 2009), endocytosis and release of vesicles from the membrane (Krendel et al. 2007; McConnell et al. 2009), and coupling of ion channels to the actin cytoskeleton (Stauffer et al. 2005).

Class I myosins have a set of unique biochemical properties which are specific for its function. The motor domain has a slow ATP turnover rate, slow actin motility and a low duty ratio (McConnell & Tyska 2010). The duty ratio of some class I myosins has been shown to be dependent on its mechanical load, making it a well adapted mechano-sensor (Laakso et al. 2008).

1.14. Fission yeast myosins.

In contrast to mammalian cells, unicellular organisms such as yeasts, are likely to express the minimum number of myosins required to maintain function (East & Mulvihill 2011). *S. pombe* expresses five myosins from 3 classes: Myo1 (class I), Myo2 and Myp2 (class II), Myo51 and Myo52 (class V), (Figure1.27) which are discussed in more detail below.

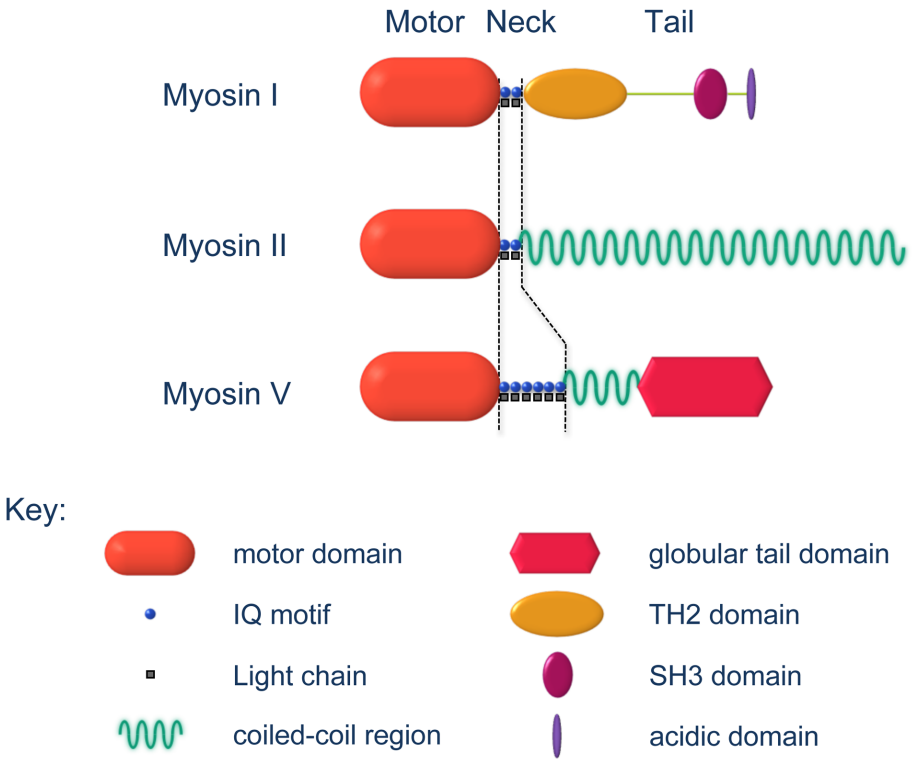

Figure 1.27. *S. pombe* myosin domain structure.

The domain structure of the three classes of myosin expressed in *S. pombe*. The motor domain allows myosin proteins to associate with actin in an ATP-ase dependent manner. The neck region is formed of IQ domains that allow binding of light chains, which induce a rigid lever arm structure and prevent auto-inhibition by folding of the protein. The tail domains of myosins are more variable and determine their specific function. From (East 2011).

1.14.1. Class II myosins, Myo2 and Myp2.

Myo2 and Myp2 are conventional class II motor proteins that are involved in actin ring constriction during cytokinesis. Myo2 is the only essential fission yeast myosin, whereas Myp2 plays a role in maintaining cell division under stress conditions (Mulvihill & Hyams 2003). Myo2 and Myp2 localise to the actin ring at distinct times during CAR formation (Wu et al. 2003) and are involved in assisting CAR constriction (Lord et al. 2005).

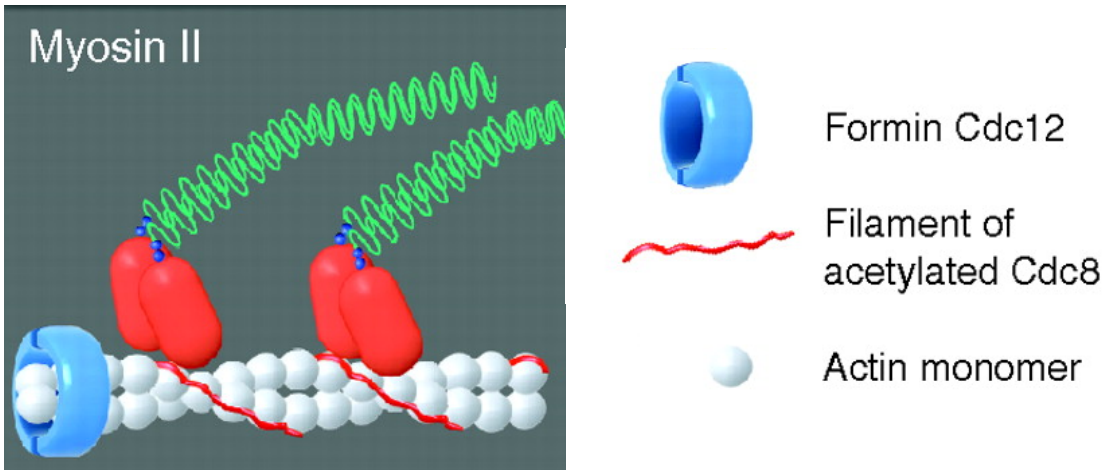

Figure 1.28. *S. pombe* class II myosins.

The coiled-coil tail region of Myo2 facilitates formation of a dimer, which associates with Cdc12 nucleated actin filaments at the CAR and is essential for CAR constriction. Adapted from (East 2011)

The long coiled-coil region of Myo2 allows the formation of stable homodimers (Figure 1.28) (Bezanilla & Pollard 2000) which are incorporated into the CAR independently of actin (Mulvihill, Barretto, et al. 2001). Myo2 localises to cortical nodes with Mid1 during early mitosis (Wong et al. 2002), and is involved in formation of the CAR through the SCPR mechanism (Figure 1.21). Myp2 however is not thought to form a dimer, and arrives at the CAR during the later stages of cytokinesis (Bezanilla & Pollard 2000). Both Myo2 and Myp2 are able to associate with a regulatory light chain (Rlc1) and an essential light chain (Cdc4) (Naqvi et al. 2000; D'souza et al. 2001).

The localisation and function of class II myosins at the CAR is in part regulated by composition of the actin filament. Myo2 and Myp2 associate predominantly with formin Cdc12 nucleated actin filaments at the CAR (Motegi et al. 2000; Pelham & Chang 2001) which are decorated with acetylated tropomyosin Cdc8 (Skoumpla et al. 2007; Stark et al. 2010).

1.14.2. Class V myosins, Myo51 and Myo52.

As with class II myosins, Myo51 and Myo52 are characterised by a motor domain and a coiled-coil region that permits dimerization (Figure 1.29). The long neck region of these proteins contains six IQ domains for calmodulin light chain binding. The cargo binding ability of myosin V is provided through a globular C-terminal tail domain.

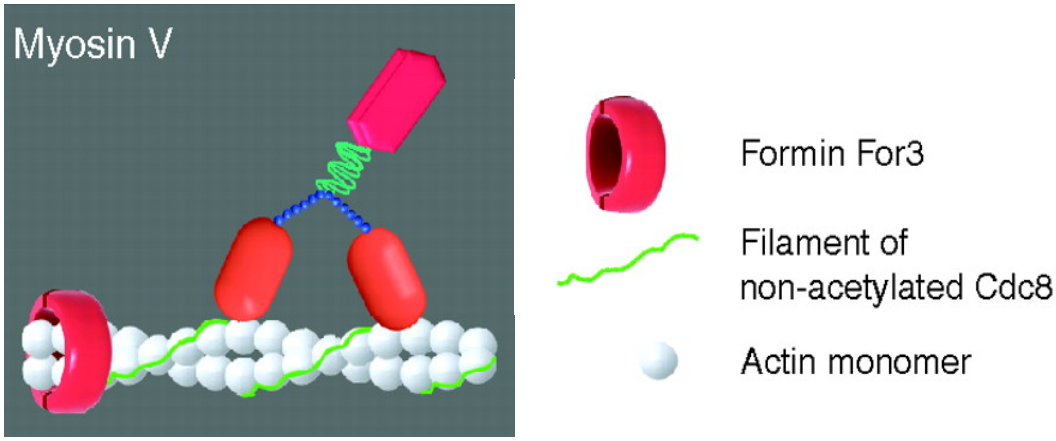

Figure 1.29. *S. pombe* class V myosins.

Class V myosins contain a coiled-coil region, allowing dimer formation, but in contrast to Class II myosins, have a long light chain binging neck region and a globular cargo binding domain. Adapted from (East 2011).

Myo51 localises to the CAR during cytokinesis, where its localisation is dependent on a functional actin network (Win et al. 2001). The role of Myo51 during the mitotic lifecycle is largely unknown but it shows no discernable movement. However during the meiotic lifecycle, Myo51 is involved in promoting cell fusion at the tips of mating cells, and directing spore formation (Doyle et al. 2009).

Myo52 is a more typical Class V myosin, which moves processively along actin cables (Win et al. 2001). Myo52 accumulates at sites of cell growth where it is has a role in delivery of proteins required for cell wall synthesis and septum deposition (Win et al. 2001; Mulvihill et al. 2006). Myo52 has a wide range of functions in the cell including regulation of vacuole distribution (Mulvihill, Pollard, et al. 2001; Martín-García & Mulvihill 2009) and transport of SNARE proteins (Edamatsu & Toyoshima 2003). Despite being in actin-based motor, Myo52 has been shown to play a role in the regulation of microtubule dynamics. Myo52 functions through the ubiquitin receptor Dph1, to target Tip1 degradation (Martín-García & Mulvihill 2009). Removal of Tip1 causes the catastrophe of growing microtubules, and potentially acts as a sensor of the cell boundary.

The velocity of Myo52 movement on actin filaments is thought to be dependent on the nature of the bound cargo. Some populations of Myo52 have been calculated to move at ~0.55 μm/s (Grallert et al. 2007), while others have been measured at ~2 μm/s (Clayton et al. 2010).

Both Myo51 and Myo52 bind calmodulin light chains, while Cdc4 essential light chain has also been shown to bind Myo51, possibly regulating its discrete localisation (D'souza et al. 2001). However the IQ domains of the Myo52 neck region appear redundant in protein localisation and dynamics (Grallert et al. 2007). Deletions of *myo51* show no morphological defects, however *myo52*Δ cells show slow growth rates, loss of polarity and cytokinetic defects (Win et al. 2001).

1.14.3. Class I myosin, Myo1.

Myo1 is a monomeric motor protein that is involved in actin polymerization and membrane remodeling (Figure 1.30). The N-terminal motor domain of Myo1 has characteristic ATPase activity, while the neck region contains two IQ domains involved in calmodulin dependent regulation (Toya et al. 2001; Sammons et al. 2011). The functional domains in the C-terminal region determine the unique function of Myo1. The TH1 domain is essential for association of Myo1 with sterol-rich plasma membrane domains (Takeda & Chang 2005). The acidic C-terminal domain activates the Arp2/3 complex, leading to nucleation of new actin filaments. Myo1 has a 20-fold weaker affinity to the Arp2/3 complex when compared to Wsp1, resulting in a weaker activation of actin nucleation (Sirotkin et al. 2005).

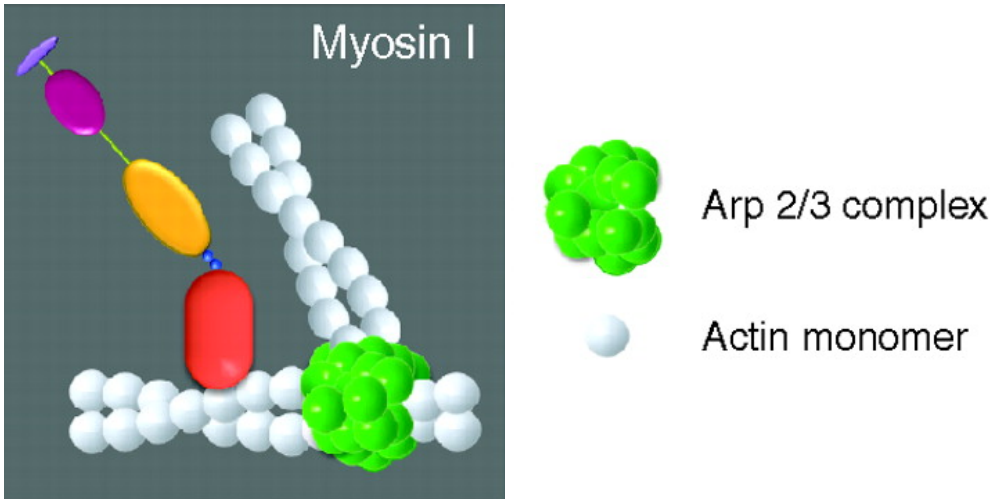

Figure 1.30. *S. pombe* class I myosin.

Myo1 is a monomeric myosin which associates with the membrane through its TH1 domain. The actin binding ability of the motor domain allows cross-linking of the actin cytoskeleton with the membrane. The acidic C-terminal tail region can activate the Arp2/3 actin nucleator. Adapted from (East 2011).

Myo1 localises to regions of polarized cell growth during interphase and to the division site during cytokinesis. These observations closely resemble that of actin patches previously described, supporting their interaction and associated function during growth. Myo1 foci are non-motile, and appear transiently at the cell membrane with an average lifetime of around 14 s (Attanapola et al. 2009). Most of these foci (93 %) have been shown to reside in sterol-rich membrane domains (Takeda & Chang 2005). Myo1 could potentially regulate the clustering of these lipid rafts, leading to changes in membrane composition seen in endocytosis. The tail domain is sufficient for its localisation to the cortical actin patches and in activating the Arp2/3 complex. However it is the functional motor activity that is essential for efficient endocytosis, a process regulated by phosphorylation of Ser361 site. (Attanapola et al. 2009).

The functional redundancy between Myo1 and Wsp1, means that a *myo1*Δ is not lethal. However, deletion of the *myo1* gene results in a reduction in growth rate and a loss of cell polarity.

1.15. Myosin regulation.

The major mechanisms identified for the regulation of myosins, are binding of light chains to the myosin neck region, and phosphorylation events at specific residues of myosin heavy and light chains.

1.15.1. Conventional myosin light chains

Myosin light chains are required for the structural integrity of myosin and for regulation of the motor activity (Heissler & Sellers 2014). Light chains associate non-covalently with the a-helical IQ motifs in the myosin neck region (Bähler & Rhoads 2002). The consensus sequence of the IQ motifs (IQXXXRGXXXR), (Cheney & Mooseker 1992) has an overall basic charge, and usually hydrophobic residues at positions, 1,8,and 14, (Vetter & Leclerc 2003).

Conventional Class II myosins, have two IQ motifs, which exclusively bind an essential light chain (ELC) at IQ1, and a regulatory light chain at IQ2 (Rayment et

al. 1993). Binding of light chains stabilises the myosin neck region as a rigid lever arm, amplifying movements of the motor domain into a power-stroke, propelling myosin along the actin filament (Uyeda et al. 1996; Ruff et al. 2001).

Binding of myosin light chains is tightly regulated by complex signalling pathways. (Sabry et al. 1997; Toepfer et al. 2013). The motor activity of many vertebrate smooth, and non-muscle myosin II's, is controlled by a combination of RLC phosphorylation events and calcium regulation of the ELC (Trybus 1991; Heissler & Sellers 2014). This regulated binding of light chains results in an extended conformation of the myosin which readily assembles into filaments.

1.15.2. *S. pombe* Rlc1 and Cdc4.

S. pombe express two conventional myosin light chains, Rlc1 – a regulatory light chain and Cdc4 – an essential light chain. Both have been shown to bind to the IQ domains of class II myosins (Motegi et al. 2000)

It is thought Cdc4 is required to maintain the correct state of Myo2 for its assembly into the CAR. The mechanism of Cdc4 regulation is unclear, although it is thought to be unable to bind Ca^{2+} (Slupsky 2000). Rlc1 has been shown to bind to the two IQ motifs of the neck region in both Class II myosins, Myo2 and Myp2. Rlc1 is required for the function of Myo2 in cytokinesis, but not for its localisation to the CAR. Phosphorylation of Rlc1 increases Myo2 motility *in vitro*, and increases the efficiency of cytokinesis *in vivo* (Sladewski et al. 2009).

As with vertebrate essential light chains, Cdc4 is thought to bind to the first IQ motif of Myo2, while Rlc1 binds to IQ2. Binding of Rlc1 extends the Myo2 protein from its inhibitory folded conformation (Naqvi et al. 2000). Binding of Cdc4 may play a more complex role during actin ring assembly and disassembly, through interactions with other proteins including Rng2. Cdc4 has also been shown to bind the IQ domain of Myo51, this may lead to its controlled localisation to the CAR (D'souza et al. 2001).

1.15.3. Calmodulin.

Calmodulin (CaM) is a calcium binding protein that is expressed in all eukaryotic cells. It is a small (~16.5 kDa) protein consisting of 4 EF-hand motifs, each with the ability to bind a Ca^{2+} ion (Moser et al. 1995). On binding of calcium, CaM undergoes a large conformational change, exposing two hydrophobic regions, these are involved in binding to target proteins (James et al. 1995).

CaM proteins have multiple functions in cells, one of which is as a myosin light chain. CaM acts as a signal transducer, sensing changes in Ca^{2+} ion gradients within the cell, caused by external signals. In response it is able to bind to a large array of target proteins, influencing gene expression, protein synthesis, muscle contraction and secretion among many other cellular functions (Figure 1.31) (O'Day 2003). Target proteins can bind calmodulin in a Ca^{2+} -dependent, Ca^{2+} -independent, or Ca^{2+} -inhibited manner.

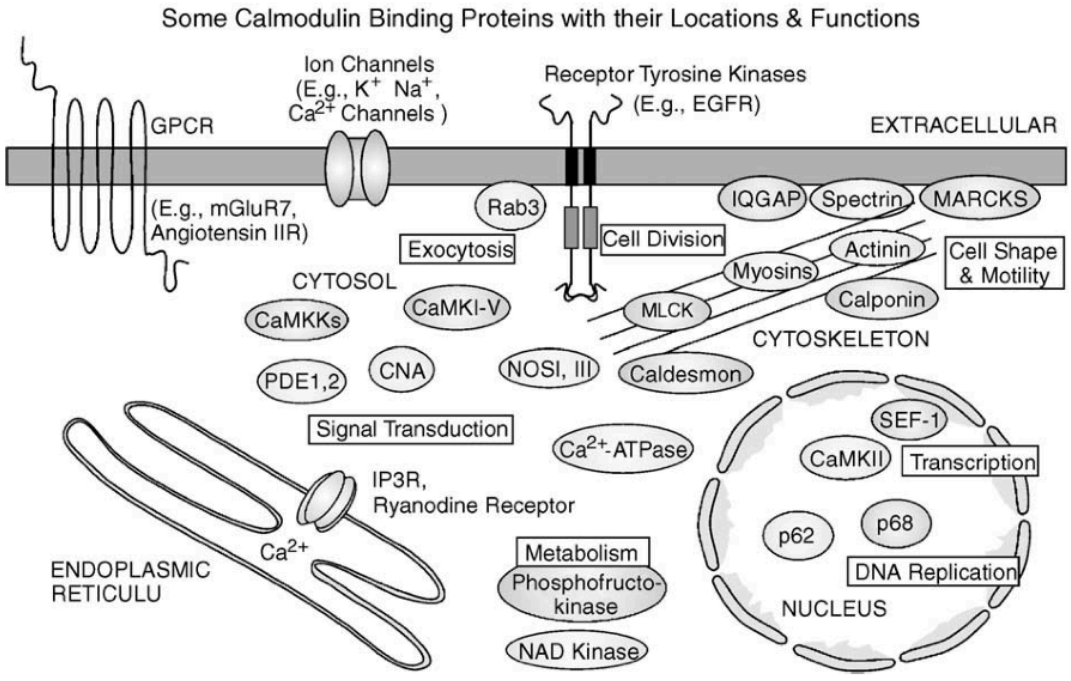

Figure 1.31. Targets of calmodulin binding in metazoan cells.

Some target proteins which are regulated by the binding of calmodulin. This indicates the ubiquitous nature of calmodulin regulation in the cell. From (O'day 2003)

Unconventional myosins predominantly bind CaM light chains, although many cases of ELC and RLC binding have also been identified (Table 1.2). The affinity of CaM binding to myosin heavy chains is altered in the presence calcium, in turn, regulating the activity of the myosin motor (Gillespie 2004; Adamek et al. 2008).

Table 1.2. Identified light chains of unconventional myosins.

Heavy chain	Organism*	ELC	RLC	CaM	Other	Reference
Myosin-1A	*Gg*			X		11,12
Myosin-1B	*Rn*			X		13,15
Myosin-1C	*Hs*	X		X		140,215
	Mm			X	CaBP1, CIB1	34,199
Myosin-2#	*All*	X	X			
Myosin-3	*Dm, Lp*			X		18–20
Myosin-5	*Dm*	X		X		172
Myosin-5A	*Gg*	X		X	Syntaxin-1A	16,200
	Mm	X				17
	Sc	X		X		36
Myosin-6	*Dm*	X		X	Androcam	170,187,188
	Ss	X		X		21,27
Myosin-7A	*Bt, Mm*			X		22,23
	Dm	X		X		170,216
Myosin-9B	*Hs*			X		24
Myosin-10	*Bt*			X		189,190
	Hs			X	CLP	191,192
Myosin-14$	*Tg*	X	X			169
Myosin-15	*Mm*	X	X			168
Myosin-18A	*Mm*	X	X			171
	Hs	X				140
	Ca		X			25
Myosin-19	*Hs*			X		173
	Mm		X			174
Myosin-21	*Ld*			X		167

From (Heissler 2014)

In contrast to other light chains, CaM binds to the IQ motif with both lobes, and more strongly in the absence of calcium (Terrak et al. 2005). The C-terminal of apo-CaM has been shown by crystal structure data to form a semi-open conformation which binds the beginning of the consensus sequence - IQxxxR. The conventional closed N-terminus interacts only weakly with the second GxxxR sequence (Heissler & Sellers 2014). The addition of a micromolar concentration of Ca^{2+} has been shown by cryo-EM to cause a conformational change in CaM which potentially disrupts the folded conformation (Trybus et al. 2007). Further increases

in the calcium concentration cause CaM binding lobes to adopt a fully open conformation and dissociate for the IQ domain.

Calcium bound calmodulin, associated with vertebrate class I myosins, Myo1a, Myo1b, and Myo1c, activates ATPase activity, but inhibits motility (Barylko et al. 1992; Collins et al. 1990; Williams & Coluccio 1994; Wolenski et al. 1993; Zhu et al. 1996). By contrast in other vertebrate class I myosins, Myo1d and Myo1e, the ATPase activity is decreased in the presence of calcium (Köhler et al. 2005; Stöffler & M. Bähler 1998).

1.15.4. *S. pombe* Cam1.

S. pombe express two calmodulin-like proteins, Cam1 and Cam2. These two proteins are 40 % identical to each other in protein sequence, and share ~35 % sequence homology with the myosin II light chains Rlc1 and Cdc4. Cam1 is more abundant throughout the cell than Cam2, with a reported 25600 molecules per proliferating cell, compared to 15800 molecules of Cam2 (Marguerat & Bähler 2012) supporting evidence of the many cellular functions of Cam1.

Cam1 is an essential protein that has a high sequence similarity to vertebrate calmodulin (Takeda & Yamamoto 1987). It has been shown that Cam1 is required for correct chromosome segregation and spore formation (Moser et al. 1997; Itadani et al. 2010). Evidence also suggests that Cam1 is likely to be a conventional calcium dependent light chain for the Class I myosin, Myo1, and Class V myosin, Myo52.

Although it has been shown that Cam1 interacts with myosin IQ domains, the mechanism of regulation, and effect on myosin activity is not known. Deletion of the Myo1 IQ domains does not have a detrimental effect on growth of cells over a range of temperatures (Toya et al. 2001). Similarly, deletion of all six IQ domains of Myo52 protein, does not effect the localisation or motility of Myo52. (Grallert et al. 2007).

Canonical EF-hand domains like those found in Cam1 (Figure 1.32), are calcium binding loops formed of 12 amino acids. The carboxylate groups of residues 1, 3, 5 and 12 are responsible for the binding of calcium ions (Zhou et al. 2006; Denessiouk et al. 2014). A sequence alignment of Cam1 and the second *S. pombe* calmodulin, Cam2 (Figure 1.32) shows Cam2 has only 3 of the 4 EF-hand domains present in Cam1. The highlighted calcium binding consensus sequences are not completely conserved, suggesting that Cam2 does not have the same ability as Cam1 to bind Ca^{2+} ions.

Figure 1.32. EF-hand domains of *S. pombe* calmodulin-like proteins.

An amino acid sequence alignment of Cam1 and Cam2 proteins. Boxes highlight the locations of Cam1 EF-hand domains and equivalent sequence of Cam2. Also shown is the calcium binding consensus sequence of a canonical EF-hand domain (Zhou 2006).

1.15.5. *S. pombe* Cam2.

Cam2 has been shown to function during meiosis, when transcription of the *cam2*$^{+}$ gene is increased five-fold (Mata et al. 2002). Cam2 localises as a single focus at the projection tip of conjugating *S. pombe* cells, and co-localises with Myo1 and actin at the forespore membrane. Cam2 is essential for sporulation at elevated

temperatures, with *cam2*Δ cells unable to correctly form the forespore membrane at 34ºC (Itadani et al. 2006).

During the mitotic growth cycle Cam2 has been shown to co-localise with Myo1, and is important for efficient function of Myo1 both *in vitro* and *in vivo* (Sammons et al. 2011). Cam2 was also shown to compete with Cdc4 for the binding of Pik1 – a type-IIIβ PI-4-kinase. Pik1 does not localise specifically to endocytic patches but is found throughout the cell and concentrated at the Golgi apparatus (Park et al. 2009).

1.16. Regulation of myosins by phosphorylation.

Phosphorylation sites on myosin heavy and light chains have been identified and shown to regulate the activity and function of myosin proteins in many different organisms (Redowicz 2001). Most Class II myosins are regulated by phosphorylation of their light chains by specific kinases such as myosin light chain kinase, PKC and Rho-dependent kinase (Toepfer et al. 2013; Trybus 1991). In fission yeast, phosphorylation of Rlc1 increases Myo2 motility *in vitro* and increases the efficiency of cytokinesis *in vivo* (Sladewski et al. 2009). Myosin II heavy chains can also be phosphorylated by kinases such as PKC or casein kinase, often in the tail region (Kelley et al. 1991). For example phosphorylation of threonine residues in the tail region of *Dictyostelium* conventional Class II myosin, regulates the localisation of myosin into thick filaments during cytokinesis (Sabry et al. 1997).

Multiple phosphorylation sites have been identified in Class I proteins, mainly in the head domain. Three *Acanthamoeba* myosin I proteins have a phosphorylated serine residue in the head domain which increases actin-activated ATPase rates and motility (Brzeska & Korn 1996). A TEDS rule (Bement & Mooseker 1995) phosphorylation site has been identified in yeast class I myosins (Grosshans et al. 2006; Attanapola et al. 2009) and mammalian class VI myosins (Roberts et al. 2004). In fission yeast, studies have shown that phosphorylation of this serine-361 residue in the myosin I motor domain, is dependent on two Ste20 kinases, Nak1

and Pak1. Phosphorylation is essential for Myo1 localisation to actin patches and activation of motor activity required for endocytosis.

In addition to phosphorylation sites in the head and tail regions, phosphorylation of residues in the neck region are potential mechanisms of regulation for light chain binding. Acidic residues in the IQ domains of MyoV have been implicated in the binding of calmodulin, (Houdusse et al. 2006) while phosphorylation of a serine residue in the IQ domain of neuromodulin also regulates calmodulin binding (Chapman et al. 1991).

Mammalian class I myosin, Myo1c has been shown to play a role in GLUT4 trafficking in adipocytes (Bose et al. 2002). A CaMKII dependent phosphorylation site has been identified at the start of the neck region of Myo1c. This serine-701 residue of Myo1c is phosphorylated in response to insulin stimulation and increases Myo1c ATPase activity. Insulin induced phosphorylation of Myo1c inhibits the interaction with calmodulin light chain but increases binding to 14-3-3 protein (Yip et al. 2008). It is therefore possible that introduction of a negative charge at the start of the Myo1c neck region impairs calmodulin binding directly or that enhanced interaction with 14-3-3 protein leads to steric hindrance of calmodulin binding.

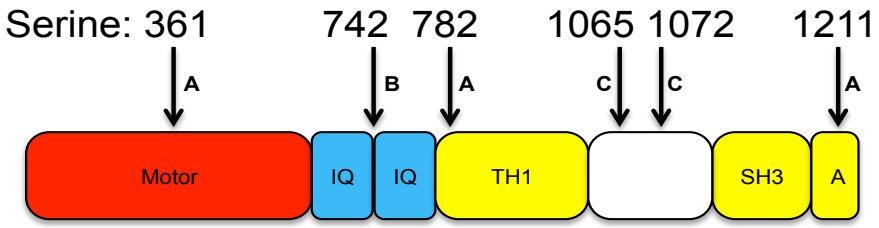

Figure 1.33. Phosphorylated serine residues identified on Myo1.

Location of phosphorylated serine residues identified in the *S. pombe* Myo1 protein through multiple phosphorylation screens. Residues labelled (A) were identified by Wilson-Grady (2007) Petersen and Hagan personal communications. (B) by Wilson-Grady and (C) by Carpy (2014).

There are many phosphorylated residues on myosin proteins of all classes, for which a function remains unknown. Identification of these residues in fission yeast has been made through phosphorylation screens, both of consensus kinase motifs in protein sequences, but also *in vivo* phosphorylation analysis (Wilson-Grady et al. 2008; Carpy et al. 2014), (Petersen personal communication, Hagan personal communication). Some of the phosphorylated serine residues identified in *S. pombe* Myo1 protein are shown in Figure 1.33.

1.17. Protein acetylation.

In eukayotic cells, post-translational modifications are made to regulate the function of the majority of proteins. One of these modifications, is addition of an acetyl group at the N-terminus of the protein. N-terminal acetylation is catalyzed by N-terminal acetyltransferases (NATs) which recognize specific amino acid sequence at the N-terminal of the protein (Starheim et al. 2012). The NAT complexes, NAT A-E are conserved between yeasts and humans. Each complex is formed of two subunits, a catalytic and regulatory (auxiliary). Figure 1.34 shows the specificity of each of the NAT complexes in yeast and humans.

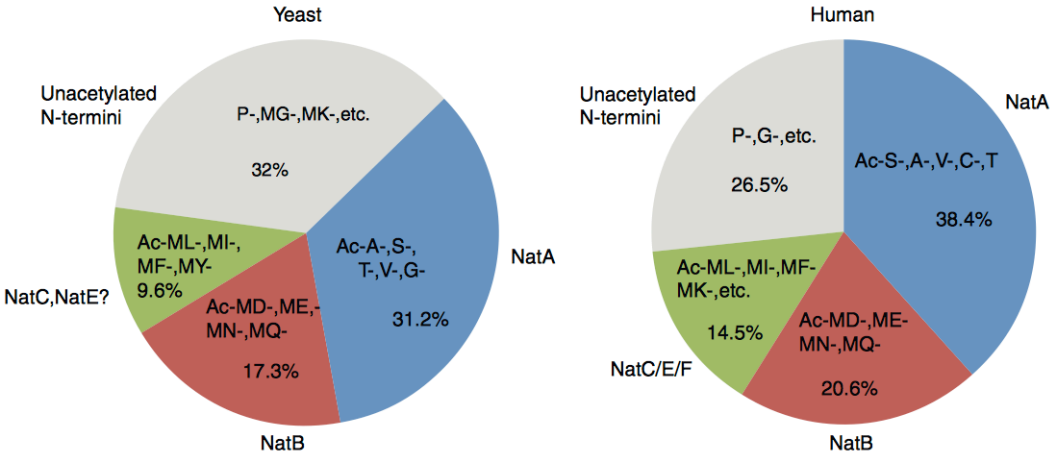

Figure 1.34. N-terminal sequences for Nat complex acetylation.

The predicted proportions of proteins in yeast and humans acetylated by each NAT complex. From the first two amino acid residues of the protein sequence, it is possible to predict the specificity of acetylation by NAT complexes From (Starheim 2012).

N-terminal acetylation has been shown to mediate protein complex formation (Scott et al. 2011), protein degradation (Hwang et al. 2010) and endoplasmic reticulum translocation (Forte et al. 2011). Acetylation of tropomyosin has been shown to effect its interaction with actin (Coulton et al. 2006; Monteiro et al. 1994) and stabilise end-to-end protein interactions (Holmes & Lehman 2008). In fission yeast, acetylation of Cdc8 influences the cellular localisation of the protein. Acetylated Cdc8 is enriched at the CAR, while unacetylated Cdc8 is incorporated into interphase actin filaments (Coulton et al. 2010).

1.18. Microscopy.

Following the development of simple compound microscopes in the early 17th century, Robert Hooke published the first microscopic observations in 'Micrographia' in 1665. Soon after, Antoni van Leeuwenhoek's improvement of lenses made it possible to observe samples at a considerably higher magnification. Van Leeuwenhoek made the first descriptions of bacteria that he termed 'animalcules' along with red blood cells and the fertilization process, dispelling the 'spontaneous generation' theories of the time. These discoveries paved the way for later scientists to develop the Cell Theory. By 1855 Matthias Schliden, Theodor Schwann and others had proposed that the cell was the basic unit of life, with all organisms composed of one or more cells, and all cells arising only from a pre-existing cell.

Since the first description of green fluorescent protein (GFP) by Osamu Shimomura in 1961, the development of methods to introduce fluorescence proteins into the genome of a cell (Bähler, Wu, et al. 1998; Janke et al. 2004) has led to many new live-cell imaging techniques.

1.18.1. Live-cell imaging.

Imaging of fluorescently labelled proteins in a living cell can give information about the cellular localisation and dynamics, and how these change in response to the environment or genetic alterations. By simultaneously imaging two differently labelled proteins within the same cell, it is possible to investigate the interaction and co-localisation of these proteins at different stages of the cell cycle. The size,

shape and genetic tractability of fission yeast make them amenable to virtually all imaging techniques. These include, Fluorescent Recovery after Photobleaching – FRAP (Hachet et al. 2011), Fluorescence Resonance Energy Tranfsfer – FRET (Flory et al. 2004), Bimolecular Fluorescence Complementation – BiFC (Ioannoni et al. 2010), and super-resolution microscopy (Bell et al. 2014).

When labelling proteins with fluorescent molecules, care must be taken to consider the potential impact on protein function (Hagan et al. 2016). N-terminal and C-terminal tagging of the same protein can result in altered protein characteristics, dependent on the functional domains and structure of the protein. The addition of extra molecular weight to either termini of a protein can also impact its function, this is particularly the case with cytoskeletal proteins (Snaith et al. 2010). There are many fluorescent actin reporters, both protein and peptide versions, but all have limitations. Each marker displays different patterns of localisation, likely to be due to altered interactions with actin nucleators and differential filament turnover rates (Belin et al. 2014).

1.18.2. Widefield

Widefield describes a standard epi-fluorescence microscope where the whole sample is illuminated, and is one of the most widely used live-cell imaging methods. Figure 1.35 shows the light path for a basic widefield imaging system. Excitation light of a specific wavelength reflects from the surface of the dichromatic mirror (dichroic) and illuminates the sample. Due to Stokes' shift phenomenon, the emitted light from a fluorophore in the sample has a longer wavelength. This longer wavelength emission light passes through the dichroic and is separated from any residual excitation light before being detected by the camera.

As the depth of an *S. pombe* cell is only 4 μm, the background signal generated from widefield imaging is minimal. However for larger metazoan samples it is important to reduce the background fluorescence.

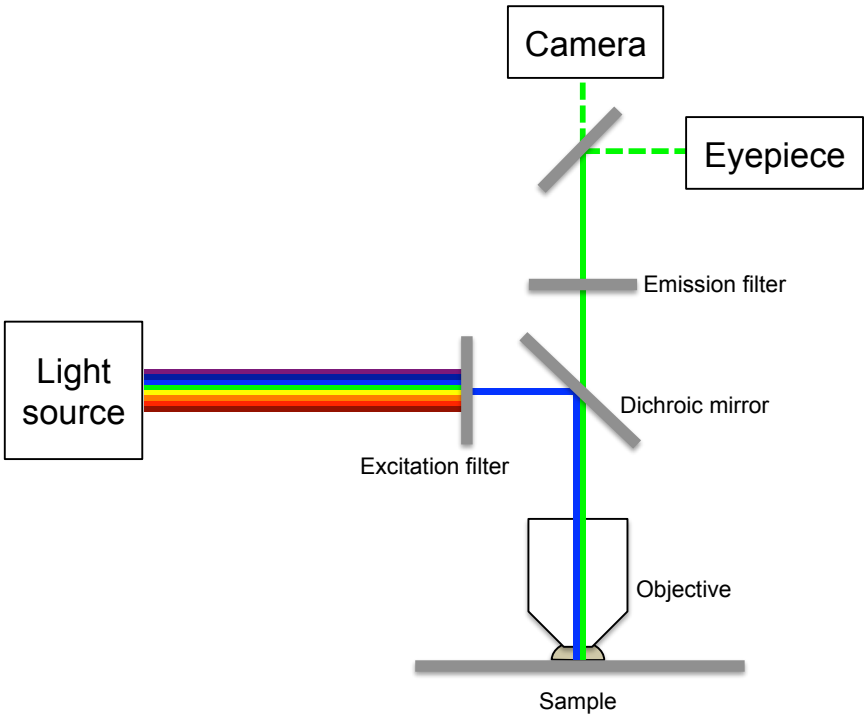

Figure 1.35. Basic light-path of a widefield imaging system.

Sample illumination is provided from a lamp or LED light source and passes through a filter to generate an excitation beam at specific wavelengths. This light is reflected from the dichroic mirror and illuminates the sample through the objective lens. Longer wavelength light emitted from fluorophores in the sample is collected by the objective lens, light passes through the dichroic and is detected by a camera.

1.18.3. Confocal

In contrast to widefield confocal systems only illuminate a thin section of the sample, reducing the amount of background fluorescence from out of focus light (Minsky, M. 1988). There are two methods of confocal microscopy, point scanning (laser scanning) and parallel scanning (eg. spinning disk). Confocal laser scanning microscopy involves illuminating a single point on the sample by a laser. Signal is detected at each point to create the entire image. This method is relatively slow, combined with the intensity of the illumination, makes it unsuitable for dynamic imaging of proteins in yeast cells (Kawamura, S. 2002).

Spinning disk confocal microscopy utilises a multiplex image system to simultaneously illuminate the sample and detect signal at multiple positions on the sample. This is achieved by spinning an array of pinholes on a disc with aligned microlenses on a collector disc (Figure 1.36). The pattern of pinholes allows illumination of the field of view, while eliminating out-of-focus light (A. Nakano 2002).

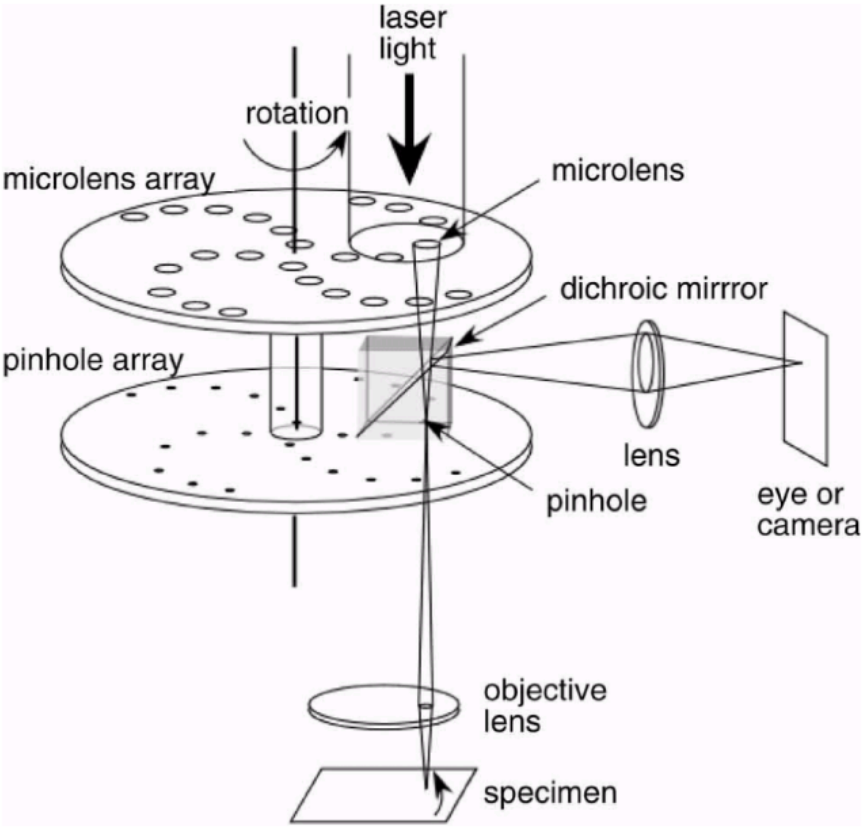

Figure 1.36. Spinning disk confocal microscopy.

A schematic diagram of spinning disk confocal microscopy. The sample is illuminated by light which passes through a coaxial spinning disk in which aligned microlenses guides light through an array of pinholes. Images can be directly visualised at a fast rate of up to 1000 frames per second. Adapted from (Nakano 2002).

1.18.4. TIRF

For imaging of fluorescent molecules at the surface of the cell, total internal reflection fluorescence (TIRF) microscopy provides an ideal method for illuminating a thin section of sample. The principle of TIRF microscopy is based on Snell's Law, which indicates that as light passes from a dense medium into a less dense medium, beyond a critical angle, TIR will take place. In the case of light passing from a coverslip into the cytoplasm of a cell, this critical angle is reached at ~65º. At this angle, energy penetrates into the sample as an 'evanescent wave' of illumination with identical frequency to the incident light, and excites fluorophores in the ~100 nm closest to the cover slip.

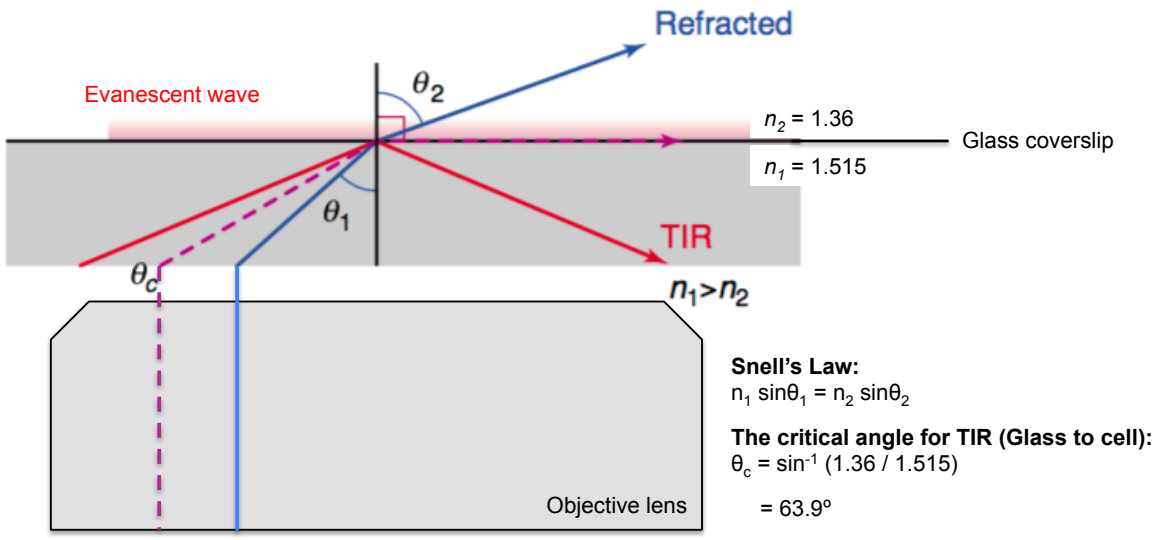

Figure 1.37. TIRF microscopy.
Illuminating the sample from the outer portion of the objective lens allows a critical angle of incidence light to be achieved. The resulting evanescent wave illuminates only the first ~ 100 nm of the sample, reducing background fluorescence. Adapted from (Toomre 2001).

A common method of TIRF sample illumination is by using a high numerical aperture (NA) objective lens (Axelrod 2001; Mashanov et al. 2003). Off-axis illumination at the edge of the objective back focal plane, results in incident light reaching the sample at an angle greater than the critical angle for TIR. TIRF

microscopy allows a thin section at the cell surface to be imaged using a standard widefield microscope, ideal for imaging processes at the cell membrane such as endocytosis (Toomre & Manstein 2001). TIRF reduces the background fluorescence from structures deeper in the cell, and also allows the possibility of detecting single molecules.

1.18.5. Super-resolution

Due to the physical properties of light diffraction as it passes through the aperture in the objective lens, there is a limit of resolution of objects separated by less than half the wavelength of the illumination light. To overcome this, instrument-based approaches have been taken, such as STORM (Bates et al. 2007), Structured illumination microscopy (SIM) (Neil et al. 1997) and Stimulated emission depletion (STED) (Hell & Wichmann 1994). These techniques can produce a resolution up to 10 times greater than standard fluorescent microscopy techniques.

Stochastic optical reconstruction microscopy (STORM) images molecules labelled with photo-switchable dyes, such as AlexaFluor and ATTO. Under appropriate conditions, a low power activation laser is sufficient to induce emission switching of the dye resulting in sequential ‘blinking’ which can be used to precisely locate single molecules in the sample (Bates et al. 2008). Multiple wavelength dyes can be used to image different molecules simultaneously.

These techniques greatly improve the resolution of fixed sample images, however super-resolution of live cell samples is more complex, due to the high intensities of light required for these methods (Cox 2015).

1.18.6. Deconvolution

Deconvolution is an algorithm-based image processing technique for removing the out-of-focus fluorescence from stacks of images (Van der Voort, H.). 3D-deconvolution uses the dimensions of the image acquisition and point spread function, to reassign scattered light to its original point source (Wallace et al. 2001).

1.19. Aims of this project.

The aims of this project were to explore mechanisms of regulation of the *S. pombe* actomyosin cytoskeleton. This study investigates the function of signalling dependent phosphorylation events on two *S. pombe* actin binding proteins, the actin capping protein, Acp1, and the class I myosin, Myo1. This study also aims to elucidate the contribution, if any, of signalling pathways and calmodulins in regulating the Myo1-driven endocytic process. The interactions of these proteins were investigated using *in vivo* cell biology techniques including fluorescence microscopy along with *in vitro* biochemical methods.

Chapter 2: Materials and methods.

2.1. Cell culture

2.1.1. *E. coli* cultures

All *E. coli* cell cultures were grown in Luria-Bertani (LB) medium at 37°C unless stated. Plasmid selection was achieved by addition of appropriate antibiotics from filter sterilised 1000x stocks, to give the following final concentrations.

Ampicillin
50 µg/ml
Chloramphenicol
25 µg/ml
Kanamycin
50 µg/ml

2.1.2. *S. pombe* cultures

All *S. pombe* strains listed in Table 2.6. were cultured under standard conditions as described by Moreno et al. (1991).

Cells were grown in Yeast Extract plus Supplements (YES) media for transformation and other general growth cultures.

For imaging and applications sensitive to signalling pathways, cells were grown for at least 48 hours in (EMMG): Edinburgh Minimal Media (FORMEDIUM EMM broth W/O nitrogen) supplemented with a Glutamate nitrogen source at 3.38 g/l. Where possible prototroph strains were used, requiring no additional amino acid supplements. For auxotrophic strains, appropriate amino acids were added to supplement the culture at a final concentration of 0.23 g/l. EMM2 was used for experiments replicating stress conditions, where the glutamate nitrogen source was replaced with ammonium chloride at 5 g/l.

2.1.3. Protein expression in *E. coli*

BL21 DE3 E. coli cells were used for all bacterial protein expression. Competent *E. coli* cells were transformed with plasmid DNA using a 90 second heat shock step at 42 °C. A single colony was used to set up a 5 ml overnight starter culture. 1 ml of this culture was used to inoculate 500 ml of LB medium, with appropriate antibiotic selection. Unless stated otherwise, cells were grown at 37 °C, 220 rpm shaking, to a density of between OD_{600} - 0.4 and 0.6. Isopropyl β-D-1-thiogalactopyranoside (IPTG) was then added to a final concentration of 0.1 mg/ml to induce protein expression under the T7 promoter. Cells were induced for 2 hours before being harvested by centrifugation at 3000 RCF for 20 minutes. Cell pellets were either frozen for storage at -20 °C or resuspended in appropriate buffer for protein purification.

Expression of acetylated proteins were achieved by co-expression with proteins of the NatA complex (described in section 3.4). When expressing multiple proteins under the control of the T7 promoter, cells were grown at 25 °C, induced with a lower final concentration of IPTG – 25 µg/ml, and left to induce overnight.

2.1.4. Production of calcium competent cells

$CaCl_2$-glycerol:

0.1 M $CaCl_2$, 10% w/v glycerol. (Filter Sterilised)

A 5 ml overnight starter culture from a single colony was used at 1:100 dilutions to inoculate 50 ml of fresh LB medium. Cells were grown at 37 °C until an OD_{600} density of 0.6 was reached. The culture was cooled on ice for 10 minutes, before cells were harvested at 1500 RCF for 10 minutes at 4 °C. Cells were resuspended in 10 ml of chilled $CaCl_2$-glycerol and incubated on ice for 15 minutes resulting in chemically competent bacterial cells. Cells were collected by centrifugation at 1500 RCF for 10 minutes at 4 °C. The pellet was gently resuspended in 1 ml of $CaCl_2$-glycerol and 40 µl aliquots frozen in liquid nitrogen for storage at -80 °C.

To prepare *E. coli DH10β* and *BL21 DE3* competent cells, the LB growth media contained no antibiotic selection. For expression of the acetylated proteins

described, the *E. coli BL21 DE3* cells used for transformations already contained the pDuet-NatA plasmid. Cell cultures grown to prepare these competent cells therefore contained chloramphenicol antibiotic to retain the plasmid. The same method was used to make *BL21 DE3* competent cells for Cam1 co-expression with Myo1 constructs. For these competent cells, Cam1 was expressed from a chloramphenicol marked pDuet-Cam1 plasmid.

2.1.5. Synchronous culture.

A mid-log culture of *cdc10-v50* cells were shifted from 25 °C to 36 °C and grown for 4.5 hours. Cells were checked under the light microscope to confirm arrested growth. The culture was quickly cooled to 25 °C on ice, with the temperature monitored by a thermometer. Once the culture reached 25 °C, it was returned to the 25 °C incubator. Samples were taken every 20 minutes from when the culture was released, with a 20 ml sample harvested for TCA extracts and 900 µl of cells added to 100 µl of formaldehyde and fixed for 10 minutes. Fixed cells were stained with Calcofluor to visualise septa formation.

2.1.6. *S. pombe* growth curves.

S. pombe OD_{600} growth curves were measured using a Spectrostar Nano (BMG Labtech) plate reader. 1 ml of culture was grown in a 24 well CellStar plate (Greiner Bio-One) from a starting density of OD_{600}=0.1, at 25ºC, with shaking at 200 rpm Measurements were taken every 15 minutes.

2.2. Protein purification

Expression vectors described in section 2.8.1 were used for recombinant expression of proteins as described in section 2.1.3. Proteins were purified using the protocols detailed below, and checked my mass spectrometry.

2.2.1. Cam1

Resuspension Buffer:

50 mM Tris, 2 mM EDTA, 1 mM DTT, 0.1 mM PMSF, pH 7.5.

Wash Buffer:

50 mM Tris, 1 mM DTT, 1 mM NaN_3, 5 mM $CaCl_2$, pH 8.0.

Elution Buffer:

50 mM Tris, 1 mM DTT, 1 mM NaN_3, 5 mM EGTA, pH 8.0.

Harvested cells were resuspended in 20 ml of 'Resuspension' buffer. Cells were lysed by 6 cycles of sonication; 30 second pulse, resting on ice for 60 second intervals. Lysates were centrifuged at 48,500 RCF for 30 minutes at 4 °C. Ammonium sulphate was added to the supernatant at 35 % saturation, and mixed for 30 minutes at 4 °C. (Calculated using EnCor Biotechnology Ammonium sulphate calculator, http://www.encorbio.com/protocols/AM-SO4.htm). Precipitated proteins were removed by centrifugation at 48,500 RCF, for 30 minutes at 4 °C. A 10 ml phenyl sepharose (CL-4B) column was equilibrated with 'Wash' buffer. The supernatant from the 35% Ammonium sulphate cut was loaded to the column, and washed with 4 volumes of 'Wash' buffer. Protein was eluted with 'Elution' buffer and collected in 1 ml fractions.

2.2.2. Cam2

Cell lysates were made using the same method and buffers as for Cam1. Ammonium sulphate was added to the supernatant at 25 % saturation, and mixed for 30 minutes at 4 °C. Precipitated proteins were removed by centrifugation at 48,500 RCF, for 30 minutes at 4 °C. This step was repeated at 35 % ammonium sulphate to precipitate further contaminating proteins. The supernatant was pH cut to 4.3, and centrifuged at 48,500 RCF for 30 minutes at 4 °C. The resulting pellet was resuspended in 5 ml of 'Resuspension' buffer using a homogeniser and adjusted to pH 7.5. The sample was heated to 80 °C for 5 minutes and denatured proteins removed by centrifugation at 16,000 RCF for 5 minutes.

2.2.3. FRET proteins

Binding Buffer:

20 mM Na_2PO_4, 500 mM NaCl, 20 mM β-mercaptoethanol, 10 mM imidazole, 1 mM PMSF, 1 % Triton X-100, pH 7.8

Wash Buffer:

20 mM Na_2PO_4, 500 mM NaCl, 20 mM β-mercaptoethanol, 10 mM imidazole, pH 6.0

Elution Buffer:

20 mM Na_2PO_4, 500 mM NaCl, 20 mM β-mercaptoethanol, 150 mM imidazole, pH 6.0

Expression of FRET proteins was carried out at 25 °C. Harvested cells were resuspended in 20 ml of 'Binding' buffer. Cells were lysed by incubation with 1 mg/ml lysozyme for 30 minutes at 4 °C. A further 30 minute incubation followed after addition of $MgCl_2$ to a final concentration of 10 mM, and DNase and RNase to 10 µg/ml. The lysate was centrifuged at 18,000 RCF for 30 minutes at 4 °C. The supernatant was loaded to an equilibrated 5 ml Sigma NiNTA column. The column was washed first with 5 volumes of 'Binding' buffer and then with 5 volumes of 'Wash' buffer. 1 ml fractions were eluted from the column with 'Elution' buffer.

2.2.4. Buffer exchange

Assay Buffer:

20 mM MOPS, 140 mM KCl, pH 7.0

Purified proteins were exchanged into 'Assay' buffer for all further experiments unless otherwise stated. Millipore Amicon Ultra-15 centrifugal filter devices (3000 MWCO) were used at 1500 RCF, 4 °C to concentrate proteins and exchange buffer. Where concentration was not needed, protein was dialysed using Thermo Scientific SnakeSkin dialysis tubing (7000 MWCO) overnight at 4 °C in 100x volume of buffer.

2.3. Biochemical Techniques

2.3.1. SDS PAGE

SDS-PAGE gels were either precast Invitrogen NuPage 4-20 % gradient gels or handcast 7.5 % polyacrylamide gels. Precast gels were run at 150 V for 50 minutes in 1x NuPage MOPS running buffer. 7.5 % polyacrylamide gels were made using the recipe in Table 2.1. and cast using Bio Rad Mini Protean III apparatus. These gels were run at 120 V for 90 minutes, in TRIS Running Buffer described below.

Table 2.1. Polyacrylamide gel recipes.

Resolving Gel			Stacking Gel	
	7.5 %	**18.5 %**		
dH_20	3.35 ml	-	**dH_20**	5.75 ml
1.5 M TRIS pH 8.8	3.75 ml	3.75 ml	**0.5 M TRIS pH 6.8**	2.5 ml
10 % w/v SDS	100 µl	100 µl	**10 % SDS**	50 µl
30 % Acrylamide	2.4 ml	6.4 ml	**30 % Acrylamide**	1.7 ml
10 % w/v APS	100 µl	100 µl	**10 % w/v APS**	50 µl
TEMED	20 µl	20 µl	**TEMED**	20 µl

TRIS Running Buffer:

25 mM Tris, 192 mM Glycine, 3.5 mM SDS, pH 8.3.

6 % PhosTag gel:

40µl of Phos-tag™(NARD Institute Wako chemicals, (Kinoshita et al. 2009) and 40 µl of 1 M $MnCl_2$ added to a 6 % acrylamide solution before APS and TEMED.

Firstly resolving gel was poured between two clean glass plates and isopropanol added to create a level gel interface. Once the gel had set, the isopropanol was removed and thoroughly washed with water. The stacking gel was then poured, and the comb inserted before being allowed to set. In order to separate proteins of smaller molecular weights, 18.5 % polyacrylamide gels were made using the same method, but run at a slower speed of 100 V.

5x SDS loading buffer was added to all protein samples, and heated to 90 °C for 10 minutes before being loaded to the wells. The protein standard run on all gels was Thermo Scientific PageRuler Unstained Protein Ladder (26614). Gels were stained with 0.1 % coomassie brilliant blue for at least 1 hour, and then fully destained.

2.3.2. Western blotting

Transfer Buffer:

25 mM Tris, 192 mM Glycine, 20% Methanol, pH 8.3.

Detection Buffer:

0.1 M NaCl, 0.1 M TRIS, pH 9.6, 5mM $MgCl_2$

All gels for western blotting were run with Bio Rad Kaleidoscope pre-stained Protein Ladder (161-0324) as the protein standard. Two methods of transfer were used for western blotting.

Primarily, a Bio Rad Trans-Blot® semi-dry electro blotter was used to transfer proteins onto methanol activated PVDF membrane. Transfer was achieved by applying 10 V for 30 minutes. For blots probed with a phospho-specific primary antibody, Bio Rad Mini Trans-Blot® apparatus was used to transfer proteins onto a nitrocellulose membrane in chilled transfer buffer without methanol. Proteins were transferred by applying a constant current of 300 mA for 90 minutes, with the apparatus set up on ice, at 4 °C.

Once transferred, a ponceau stain was used to confirm total protein transfer and equal loading, followed by a 1 hour block with 3 % milk powder dissolved in 1x PBS. The blot was incubated with primary antibody in 3 % milk at room temperature for 1 hour or 4 °C overnight at the concentrations stated in Table 2.2. Blots were washed 3 times with 1x PBS before alkaline phosphatase linked secondary antibodies (Sigma-Aldrich) raised against the primary antibody were incubated for 1 hour at RT in 3 % Milk. The blot was then washed twice with PBS and incubated for 5 minutes in ‘Detection’ buffer. After removing the ‘Detection’ buffer, 1-2 ml of Sigma BCIP/NBT Purple liquid substrate (B6404) was added and

incubated until bands developed (between 5 minutes and 3 hours). The reaction was stopped by washing the membrane with dH_2O.

Table 2.2. Antibody working conditions for western blotting.

Antibody	Source	Working Concentration	Conditions	Raised in
Myo1	This lab	1:1000	3 % Milk, PBS, RT, 1 hr	Rabbit
Myo1-S742P*	This study	1:500	3 % Milk, TBS, 4 °C, overnight.	Rabbit
Cam1	This study	1:1000	3 % Milk, PBS, RT, 1 hr	Rabbit
Cam2	This lab	1:250	3 % Milk, PBS, 4 °C, overnight.	Rat
GFP	Generous gift of Bill Gullick	1:500	3 % Milk, PBS, RT, 1 hr	Mouse
His6	Roche (11922416001)	1:500	3 % Milk, PBS, 4 °C, overnight.	Mouse
Anti-mouse IgG Alkaline Phosphatase	Sigma (A1293)	1:10,000	3 % Milk, PBS, RT, 1 hr	Goat
Anti-rabbit IgG Alkaline Phosphatase	Sigma (A9919)	1:10,000	3 % Milk, PBS, RT, 1 hr	Goat
Anti-rat IgG Alkaline Phosphatase	Sigma (6066)	1:10,000	3 % Milk, PBS, RT, 1 hr	Rabbit

2.3.3. Bradford Assay

Table 2.3. Bradford assay BSA standard curve dilutions.

BSA Standard concentration (mg/ml)	Volume of 10 mg/ml stock BSA (µl)	Volume of 1 mg/ml BSA (µl)	Volume of buffer (µl)
0.0	0	0	50
0.2	-	10	40
0.4	-	20	30
0.6	-	30	20
0.8	-	40	10
1.0	20	-	180
1.2	6	-	44

All protein concentrations were calculated using a Bradford assay. Each assay was run with a range of BSA concentrations (summarised in Table 2.3.) to make a standard curve. The equation of the linear line of regression was used to calculate the concentration of purified proteins.

1 ml of Sigma Bradford Assay Reagent (B6916) was added to 33 µl of protein sample in a cuvette, mixed and incubated at RT for 5 minutes before measuring absorbance at 595 nm.

2.3.4. Fluorimetry

Fluorimetry experiments were carried out using a Perkin Elmer Luminescence Spectrometer LS 50B. The slit width was set to 2.5 nm and measurement speed 200 nm/min. An excitation wavelength of 325 nm was used for experiments measuring the fluorescence of IAANS labelled Cam1. Emission was measured from 350 to 600 nm, and an emission maximum was calculated from the average fluorescence intensity between 437 to 443 nm. An excitation wavelength of 435 nm was used for experiments using CyPet - YPet FRET pairs with and emission measured from 450 to 600 nm. The CyPet fluorescence maximum was calculated from an average of fluorescence intensity between 475 and 479 nm, and YPet, between 528 and 532 nm. During titrations, addition of sample was made while constant magnetic stirring.

2.3.5. Stopped flow

All measurements were carried out using a Hi-Tech SF-61DX2 stopped-flow machine (TgK Scientific, Bradford-on-Avon, UK) with a 50 µl reaction volume. IAANS fluorescence was excited at 325 nm, and Quin-2 fluorescence at 333 nm, with emission detected after passing through a GG455 nm cut off filter. The stated concentrations of reactants are those after mixing in the stopped-flow observation cell. Stopped-flow data were analyzed using the Kinetic Studio software provided by TgK Scientific. Origin (Microcal) software was used to plot and analyse graphs from titration data to determine the dissociation constant of binding reactions (K_d).

2.3.6. Equations:

The following quadratic equation was used for calculating the affinity of protein ligand binding interactions:

$$y = F_0 - (F_0 - F_i) * ((A + x + K_d) - ((A + x + K_d) ^ 2 - 4 * x * A) ^ 0.5) / (2 * A)$$

Where x is [ligand] and y is % change in FRET, parameters are F_0, F_i, A and K_d

The following Hill equation was used to fit a sigmoidal line of best fit for pCa curves and to calculate pCa_{50} values:

$$y = [start] + ([end] – [start]) (x^n / (k^n + x^n)$$

Where x is pCa and y is change in fluorescence.

A Scatchard plot was used to determine whether saturating binding experiments were formed of a single phase, or were bi-phasic:

$$(\theta / [L]) = (1 / K_d) – (\theta / K_d)$$

θ was plotted against (θ / [L])

Where θ is fractional saturation calculated from % fluorescence change, and [L] Is total ligand (CaM) concentration.

2.3.7. Circular dichroism:

Measurements were made in 1 mm quartz cuvettes using a Jasco 715 spectropolarimeter. Proteins were diluted in CD buffer (10 mM Potassium phosphate, 500 mM NaCl, 5 mM $MgCl_2$ pH 7.0) to a concentration of 0.4 mg/ml. Thermal unfolding data were obtained by monitoring the CD signal at 222 nm with a heating rate of 1 deg/min.

2.3.8. IAANS labelling of Cam1-T7C

Resuspension Buffer:

50 mM Tris, 2 mM EDTA, 1 mM DTT, 0.1 mM PMSF, pH 7.5.

Urea Buffer:

6 M urea, 90 mM KCl, 1 mM EGTA, 50 mM TRIS, pH 7.5.

10-90 Buffer:

10 mM MOPS, 90 mM KCl, pH7.0.

Cam1-T7C mutant protein was expressed in *E. coli*, purified as described for Cam1, and dialysed into 'Resuspension' buffer. This modified Cam1 protein has the threonine at residue 7 replaced with a cysteine which can be covalently linked to an IAANS fluorescent label. Protein concentration was measured using a Bradford assay and diluted to 50 µM. DTT was added to a concentration of 5 mM and mixed at RT for 2 hours. The reduced Cam1-T7C was dialysed overnight in 2 L of 'Urea' buffer. Life Technologies 2-(4'-(Iodoacetamido)anilino)Naphthalene-6-Sulfonic Acid, Sodium salt (I-7) (IAANS) was dissolved at 6 mg/ml in DMF. A fivefold excess of IAANS was gradually added to the Cam1-T7C while mixing. After incubating at 4 °C for 10 hours, protected from light, the reaction was stopped by addition of 2 mM DTT. The sample was dialysed overnight in 2 L of 'Urea' buffer. The labelled Cam1 was then dialysed in '10-90' buffer, 2x 2 L for 4 hours, 1x 4 L for 4 hours followed by overnight in 5 L of 'Assay' buffer.

2.3.9. Generation of pCa buffers

Table 2.4. pCa buffer calculation.

pCa (2mM)	9.8	8.0	7.0	6.6	6.2	6.0	5.6	5.2	4.6
100 mM EGTA (µl)	1999.3	1955.7	1630.5	1274.3	822.6	611.4	296.4	124.5	9.5
100 mM Ca-EGTA (µl)	0.7	44.3	369.5	725.7	1177.4	1388.6	1703.6	1875.5	1990.5

Volumes of 100 mM EGTA and 100 mM Ca-EGTA combined to make stock buffers for use at 2 mM final concentration, to give the indicated pCa conditions. Volumes calculated using WEBMAXCLITE software.

2.4. Molecular Biology Techniques

2.4.1. *E. coli* transformation

40 µl aliquots of calcium competent *E. coli DH10β* cells were thawed on ice. 1 µl of plasmid DNA was added to the cells, mixed gently and incubated on ice for 30 minutes. Cells were heat shocked for 90 seconds at 42 °C and put on ice for 2 minutes. 100 µl of LB was added to the cells and allowed to recover for 1 hour at 37 °C before being plated onto an LB plate containing the appropriate antibiotic selection.

2.4.2. *S. pombe* transformation

S. pombe cells were grown in YES for 48 hours to a density of 3 x 10^6 cells/ml, and harvested by centrifugation at 1500 RCF, 25 °C. The pellet was washed in 0.1 M lithium acetate and resuspended to 2 x 10^8 cells/ml. Cells were incubated at 25 °C for 1 hour with gentle mixing every 20 minutes. DNA to be transformed was combined with 100 µl 70 % PEG-4000. 100 µl of cells were mixed well with the DNA before being incubated at 25 °C for a further 1 hour. Cells were heat shocked for 10 minutes at 42 °C. Cells were spun at 1500 RCF for 1 minute and resuspended in 1 ml of YES for a 1 hour recovery at 25 °C. Cells were washed into 100 µl of EMMG before being spread onto the appropriate selection plate.

2.4.3. Plasmid DNA preparation

Plasmid DNA from *E. coli DH10β* cells was extracted using a QIAprep spin Miniprep Kit (Qiagen - 27106), following the manufacturers instructions.

2.4.4. *S. pombe* genomic DNA preparation

Genomic DNA from *S. pombe* cells was extracted using the method described by Lõoke et al (2011). 3 x 10^7 cells were resuspended in 100 µl of 200 mM LiOAc, 1 % SDS and heated to 75 °C for 5 minutes. 300 µl of 100 % ethanol was added and vortexed. The pellet was collected by centrifugation at 16,000 RCF for 3 minutes and washed with 70 % ethanol. The dried pellet was resuspended in 50 µl

of water and centrifuged 16,000 RCF for 30 seconds. 1-2 µl of the genomic DNA was used for PCR reactions.

2.4.5. Agarose gel electrophoresis

0.5x TAE:

20 mM Tris, 0.5 mM EDTA, 10 mM Acetic acid

5x Loading Buffer:

0.5 mg/ml Bromophenol Blue, 30 % glycerol

1 % w/v agarose was dissolved in 0.5x TAE by heating in a microwave. After pouring into casting trays with appropriate size well comb, ethidium bromide was added to a final concentration of 0.5 µg/ml, and the gels allowed to set. Before loading samples to the gel, 5x loading buffer was added to the sample. Gels were run at 50 V for 50 minutes, and imaged using a UV transilluminator.

2.4.6. General cloning techniques

Typical restriction digest mixture:

10x Buffer – 10 µl (buffer type determined by enzyme activity)
Plasmid DNA – 10 µl
Restriction enzyme – 2 µl
dH_2O – to a final volume of 100 µl

The desired DNA fragment was cut out from an agarose gel and purified using QIAquick Gel Extraction kit (Qiagen - 28704). The manufacturers instructions were followed, but the final elution volume was reduced to 20 µl.

Typical ligation mixture:

10x ligation Buffer – 2 µl
DNA fragments – 0.1 µg per fragment
T4 DNA ligase – 1 µl
dH_2O – to a final volume of 20 µl

DNA concentration was determined by comparison to the Hyperladder 1 kb standard (Bioline – BIO-33026). When loading 5 µl of this ladder, the 1 kb band is equivalent to 0.1 µg of DNA.

2.4.7. Generating genomic GFP fusions.

S. pombe proteins were C-terminally tagged at the genomic locus using the method described by Bahler et al. (1998). pFA6a-kanMX6-GFP plasmid was used as the template for tagging proteins with a GFP fluorescent label and kanMX6 resistance marker. Gene specific oligonucleotides were designed to allow integration of the tag at the correct genomic locus. PCR conditions were as follows:

Denaturation – 30 seconds at 92 °C;
Annealing – 1 minute at 45 °C;
Elongation – 5 minutes at 68 °C;
Final extension – 10 minutes at 68 °C.

The PCR product was purified using phenol chloroform extraction, and used to transform a wild type *S. pombe* strain (1929).

2.4.8. TCA whole cell extracts

Stop Buffer:

150 mM NaCl, 10 mM EDTA, 1mM sodium azide pH 8.0.

Sample Buffer:

80 mM TRIS, 5 mM EDTA, 5mM DTT pH 7.5.

1 x 10^7 *S. pombe* cells were harvested by centrifugation at 1500 RCF for 5 minutes. The pellet was resuspended in 1 ml Stop Buffer and transferred to a microfuge tube with O-ring seal screw cap. The pellet was collected by centrifugation at 16,000 RCF for 1 minute and was frozen in liquid nitrogen for storage at -80 °C if required. 200 µl of 20 % TCA and 0.5 ml of glass beads were added to the pellet. Cells were lysed by 40 seconds in a FastPrep® Instrument (Bio101) at full power, and returned to ice to cool. A hole was punched in the bottom of the tube, 400 µl of 5 % TCA added to the lysate and collected in a microfuge tube, removing the glass beads. Lysate was centrifuged at 16,000 RCF for 3 minutes, and the supernatant discarded. The pellet was resuspended in 50 µl of 1x SDS loading buffer and 30 µl of 1 M Tris pH 8.8. The sample was heated to 80 °C for 5 minutes before loading to an SDS-PAGE gel.

For extracts to be subsequently used for a western blot probed with phosphospecific anti-Myo1 antibodies (anti-Myo1-S742-P*), the pellet collected after cell lysis was washed twice with 0.1 % TCA and resuspended in 50 µl of Sample Buffer. The sample was then heated to 90 °C for 1 minute, before addition of SDS loading buffer and incubation at 70 °C for 3 minutes.

2.5. Yeast Genetic Techniques

2.5.1. Crossing two strains.

Two strains of opposite mating type were mixed in a region of an MSA plate, as described by Egel et al. (1994). After two to three days incubation at 25 °C, the cells were checked under the light microscope for the presence of acsi. If the two genes of interest were marked with different selection markers, the cross mixture was suspended in 1 ml of water and 3 µl of β-Glucuronidase (Sigma – G7017) was added. After an incubation at 37 °C, the light microscope was used to check for complete digestion of the cells wall, before spores were plated out onto appropriate selection plates.

2.5.2. Tetrad dissection

This method was used for strains where the two genes were marked with the same selection marker to ensure unambiguous determination of strains containing both genes of interest. Cells were crossed and forced into meiosis using the method described above. Once confirmed that asci has formed, a small amount of the cross was streaked onto one side of a YES plate. A Singer Instruments MSM-400 dissection microscope was used to separate the four spores of each tetrad. The plate was incubated at 25 °C for 2-3 days to allow spores to germinate. Colonies were then replica plated onto appropriate selection medium to identify 2:2 ratio of growth indicating non-parental segregation and confidence the strain contains both genes of interest.

2.6. Microscopy

2.6.1. Mounting cells

Cover slips were coated by addition of 10 µl of 1 mg/ml lectin (Sigma – L2380) to the surface and allowed to dry. 20 µl of mid log cell culture was added to the dried lectin and allowed to settle for 5 minutes (Figure 2.1). Excess cells were removed by gentle washing with a few drops of media. A small chamber was created using strips of double sided sticky tape on the slide, with the coverslip placed on top. The chamber created was then flooded with media, allowing cells to be imaged for up to 30 minutes.

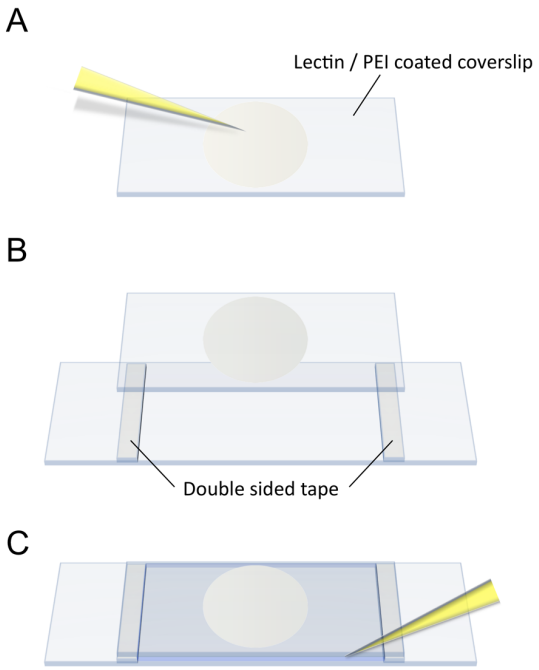

Figure 2.1. Mounting cells for imaging using lectin.

Diagram showing steps for mounting cells onto a coverslip using lectin. Figure by D. Mulvihill.

For longer term and temperature controlled experiments cells were mounted in a Bioptechs FCS2 chamber Bioptechs, Butler, PA) also using lectin. This allowed the sample, environmental chamber and objective lens to be maintained at a stable temperature.

2.6.2. Sample visualization

Unless stated, widefield images were acquired using an Olympus IX71 microscope with a PlanApo 100x OTIRFM-SP 1.45 NA or a UApoN 100x TIRF 1.49 NA lens mounted on a PIFOC z-axis focus drive (Physik Intrumente, Karlsruhe, Germany). The sample was illuminated using LED light sources (Cairn Research Ltd, Faversham, UK) with appropriate filters (Chroma, Bellows Falls, VT). Detection was either by a QuantEM (Photometrics) EMCCD camera or a Zyla 4.2 (Andor) CMOS camera. An Optosplit device (Cairn Research Ltd.) was used to allow simultaneous acquisition of signals from two fluorophores that emitted light at different wavelengths. The system was controlled with Metamorph software (Molecular Devices). 3D-maximum projections were calculated from 31 z-plane images, each 0.2 µm apart. Images were analysed using Metamorph and Autoquant X software (see section 1.18.6 for further details of deconvolution)

2.6.3. TIRF

TIRF microscopy images were taken using a custom built, Nikon microscope based TIRF system in collaboration with Justin Molloy (Medical Research Council). Images were acquired and analysed using GMimPro software (Mashanov and Molloy 2007).

2.6.4. Immunofluorescence

30 % Paraformaldehyde:

3g of paraformaldehyde powder dissolved in 10 ml PEM by heating to 60 °C and pH adjusting with 5 M NaOH until almost all of the formaldehyde was in solution. The solution was clarifies by centrifugation at 2000 rpm.

PEM:

100 mM PIPES, 1 mM EGTA, 1 mM MgSO4, pH 6.9.

PEMS:

PEM + 1.2 M Sorbitol.

PEMBAL:

PEM + 1 % BSA (essentially globulin free)

Mid-log cells were fixed for IF by addition of paraformaldehyde to a final concentration of 3%, and incubation for 30 minutes at room temperature with agitation. Cells were washed 3 times in PEM before the cell walls were digested with Zymolase-20T (ICN Biomedicals) at a final concentration of 1.25 mg/ml, for 30 minutes at 37 °C. The cell pellet was washed once in PEMS + 1% triton X-100, and immediately washed twice in PEM. Cells were resuspended in 100 µl of primary antibody diluted in PEMBAL, at the concentration stated in Table 2.4. After an overnight incubation the cells were washed 3 times in PEMBAL and resuspended in secondary antibody. Cells were again incubated overnight at room temperature on a rotating mixer, protected from light. Secondary antibody was removed and the cells washed in PEM before being resuspended in PBS. 5 µl of cells were mounted to a coverslip with DAPI mounting media.

Table 2.5. Antibody working concentrations for immunofluorescence.

Antibody	Source	Working Concentration	Raised in
Cdc8	This lab	1:1000	Rabbit
Myo1	This lab	1:500	Rabbit
Cam1	This study	1:1000	Rabbit
Anti-rabbit IgG FITC	Sigma (F0382)	1:100	Goat
Anti-rabbit IgG TRITC	Sigma (T6778)	1:100	Goat
Anti-rabbit AlexaFluor-647	ThermoFisher (A21245)	1:1,000	Goat

2.6.5. STORM Super-resolution

Imaging media:

1 % β-mercaptoethanol
1% GLOX
1 % COT

STORM Super-resolution images were taken using an iLas based system in collaboration with Steve Tovey (Department of Pharmacology, Cambridge). Cells were fixed for immunofluorescence as described in section 2.6.4. The primary antibody used in these experiments was anti-Myo1 at a concentration of 1:500. An AlexaFluor-647 secondary antibody was used at 1:000, and cells were stored in PBS before imaging. Cells were mounted to a cover slip fixed to the base of a petri dish, with lectin as described in section 2.7.1. A metal disk was sealed to the base of the petri dish with grease to create a chamber, to which 500 µl of Imaging media carefully was added.

2.6.6. Calcofluor staining

9 µl of fixed cells were mixed on a slide with 1 µl of 10 mg/ml Calcofluor. Cells were imaged using an automated 300W Xenon light source (Sutter, Novato, CA) with appropriate filters (Chroma, Bellows Falls, VT).

2.7. Image Analysis:

2.7.1. Foci detection and localisation.

Maximum projections of 31 z-plane images were deconvolved in AutoQuant X3 software using 3D blind deconvolution. Cell regions were isolated individually from the image using the freehand crop tool, allowing the ‘Statistics’ function to provide the following information for each cell.

Cell size: The region of interest area gives a 2D indication of cell size.
Whole cell fluorescence: Sum of fluorescence intensity of all pixels in region.
Maximum Intensity: Highest fluorescence intensity value in region.

The ‘Counting and Tracking’ function was then used to extract more specific information about the fluorescent protein of interest within the cell. For each fluorescently labelled protein an intensity threshold was set – regions of the image above this were detected as ‘foci’. As the imaging conditions for each protein were consistent, the same threshold was used throughout the analysis. Figure 2.2.D. summarises the intensity thresholds used for each molecule analysed.

Figure 2.2.A-C. shows an example of foci detection from a typical deconvolved image. The ‘Counting and Tracking’ function provided the following information about detected foci:

Number of foci per cell: Number of discrete foci above the set threshold.
Foci volume: Volume contained within the detected foci.
Foci intensity: Sum of fluorescence intensity of all pixels within detected foci.
Foci localisation: The X, Y and Z coordinates of the foci within the cell region.

From the X and Y-coordinates of the foci it is possible to define the localisation of each foci within the cell. Each cell was divided into 5 regions by length – the two cell ends, cell equator and two regions between, as shown in Figure 2.3. The number of foci located in each region of the cell, and information about distribution of fluorescence allowed analysis of potential loss of polarized protein distribution in mutant strains.

2.7.2. Statistical analysis.

Statistically significant differences in the values calculated from image analysis of mutant strains were calculated using an unpaired Student *t*-test (GraphPad online software).

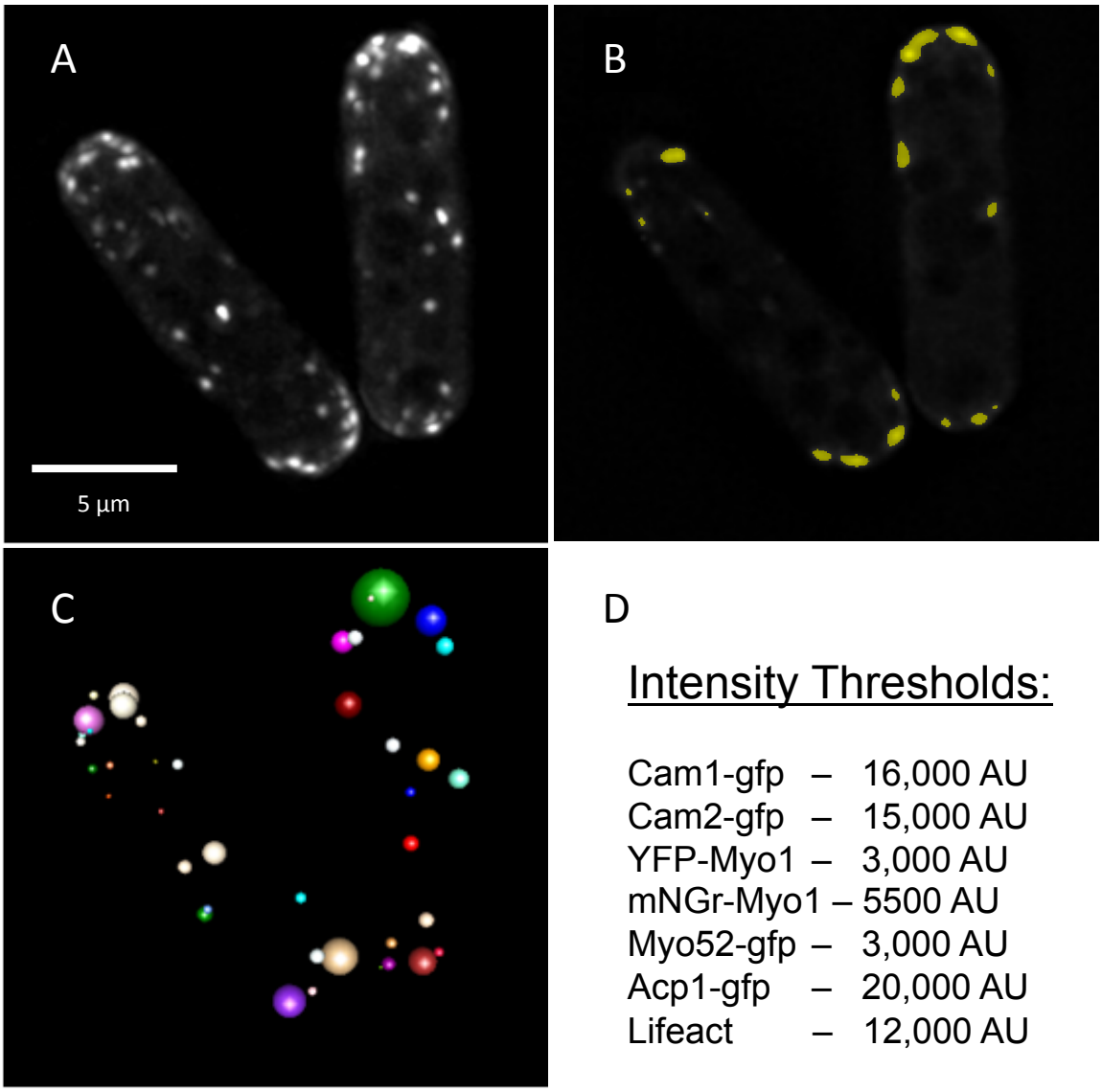

Figure 2.2. AutoQuantX3 deconvolution and analysis.

(A) shows a typical deconvolved maximum projection of 31 z-plane images of *cam1-gfp* cells. A single plane of this image is shown in (B) after applying the threshold intensity tool, while (C) shows a 3D view of the size and positions of the detected foci. The threshold intensities used for each fluorescently labelled protein imaged are summarised in (D).

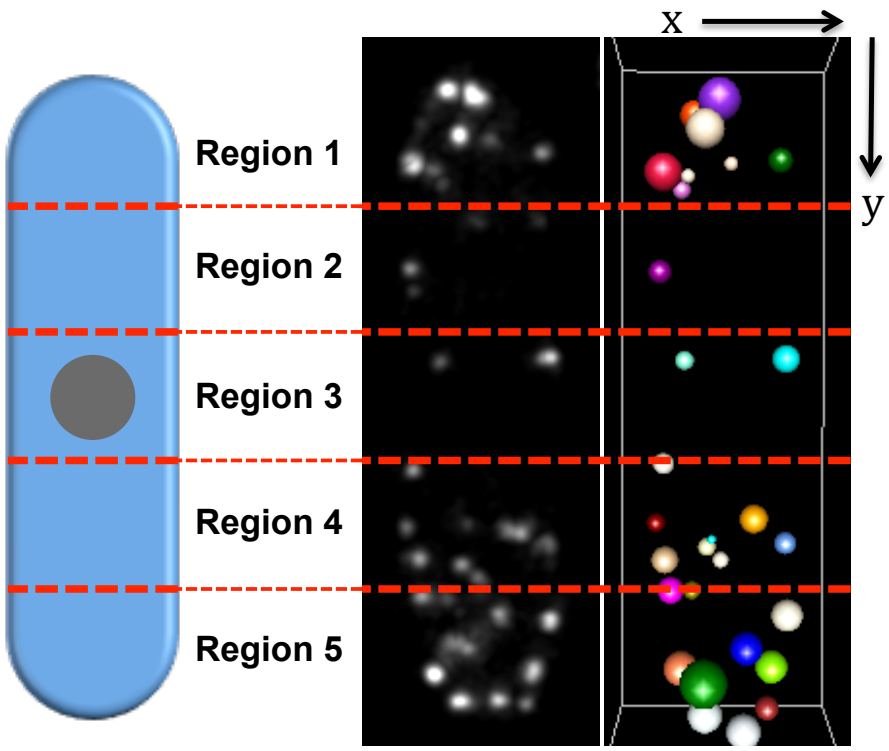

Figure 2.3. Determining cellular localisation of foci.

A schematic diagram showing 5 cell regions, determined for each cell based on cell length. Using the x and y coordinates given for each foci, it was possible to allocate foci to a specific cell region. Here, an example image of a *cam2-gfp* cell with detected foci divided into these defined regions.

2.7.3. Kymographs.

Unless stated, kymographs were generated in Metamorph, from maximum projections of 13 z-plane timelapse images. Dynamics of proteins within the whole cell were observed using a longitudinal axis for the kymograph (Figure 2.4.A). To visualise cytokinetic actomyosin ring constriction the kymograph axis was perpendicular, across the equator of the cell (Fig 2.4.B). To visualise the internalisation of individual foci at the membrane, a kymograph was made at a small region of the membrane (Fig 2.4.C). These kymographs were made from either maximum projections, as above, or single z-plane images in the case of highly dynamic proteins. Comparison of the length of time that proteins persisted as foci at the membrane was determined from kymographs made from timelapse images with identical exposure time and number of planes.

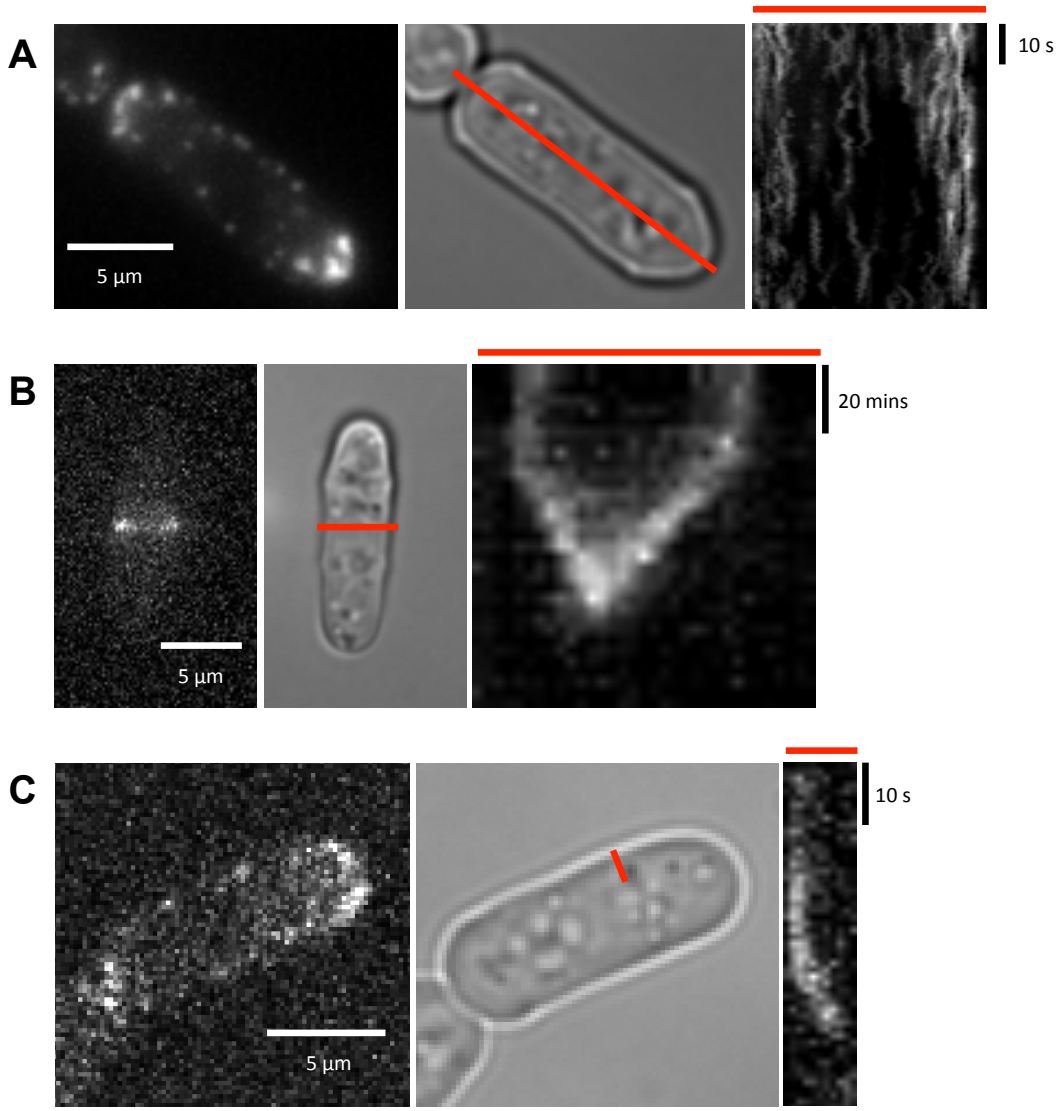

Figure 2.4. Generation of kymographs in Metamorph.

The red line in (A) shows the axis used to make a kymograph from the whole cell. (B) shows the axis used to observe ring constriction, while (C) shows the small region used to characterise internalisation of individual foci.

2.7.4. Analysis of NETO

Metamorph software was used to analyse timelapse images made from maximum projections of 31 z-slices taken every 3 minutes. A 25 pixel (4 µm) diameter circular region was created and the 'Average Intensity' measurement of this region used for all analysis of NETO in various strains. Measurements of fluorescence intensity at each end of the cell were taken for cells where it was possible to

identify the ‘old’ and ‘new’ end – cells having just completed cytokinesis. The average intensity of the same circular region was used to correct for background fluorescence adjacent to each cell (Figure 2.5). The background corrected fluorescence values at each end were used to determine a ratio of ‘new’ cell end fluorescence / ‘old’ cell end fluorescence. The length of each cell was also measured, allowing the changing ratio of fluorescence to be plotted against cell length.

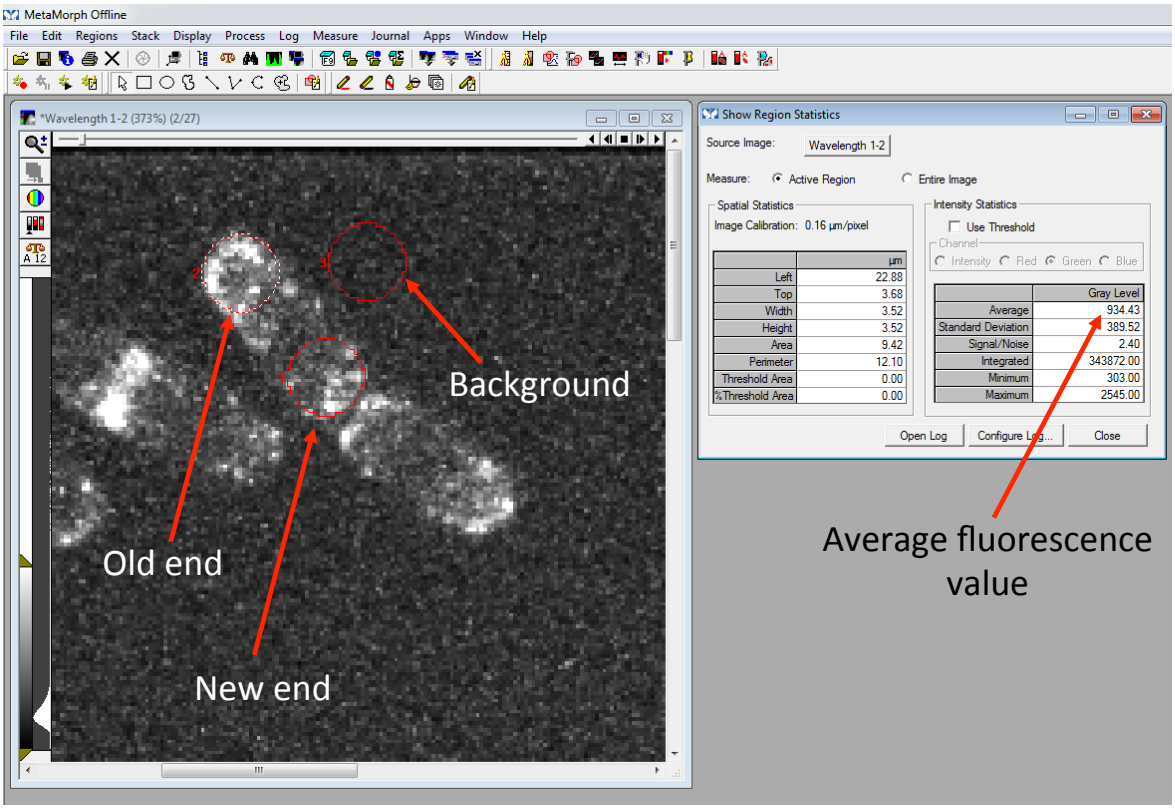

Figure 2.5. Analysis of NETO in Metamorph.

The circular regions are equivalent to 25 pixels or 4µm in diameter. The average fluorescence value of these active regions was measured in the ‘Region Statistics’ tool. Background correction was measured adjacent to the cell.

2.8. Plasmid constructs:

2.8.1. Bacterial expression vectors:

All plasmids used for expression of recombinant protein in *E. coli* were pJC20 based high copy number vectors (Clos & Brandau 1994) allowing expression under the control of T7 RNA polymerase. All constructs were confirmed by sequencing.

pJC20 cam1 – v320
cam1 gene cloned as a NdeI-BamHI fragment for expression of full length Cam1.
pJC20 cam2 – v521
cam2 gene cloned as a NdeI-BamHI fragment for expression of full length Cam2.
pJC20 cam1-T7C – v607
A plasmid designed for the expression of T7C modified Cam1 protein, allowing IAANS labelling of the Cam1 N-terminal. The *cam1* gene was amplified from the v320 template by PCR. The forward primer - O489 (5' – GGAATTCCATATGACTACCCGTAACCTTTGTGATGAGCAGATTGC – 3'), retains the NdeI site but introduces a cysteine codon TGT in place of the wild type ACA (Threonine). The reverse primer – O490 (5' – GGAAGATCTCTACTTGGAAGAAATGACACG – 3'), introduces a BglII restriction site in place of BamHI. This PCR fragment was compatible for ligation into a NdeI-BamHI cut pJC20 vector, and correct clones identified by removal of BamHI/ BglII sites.
pJC20 CyPet-cam1-YPet – v638
A plasmid designed to express Cam1 protein between a FRET pair. Cam1 was fused to an N-terminal CyPet and C-terminal YPet molecule. *cam1* was amplified from v320 as a SalI-XhoI fragment using O508 (5' – ACGCGTCGACGGAGGAGGAATGACTACCCGTAACCTTAC – 3') and O509 (5' – GAAGATCTCTCGAGTCCTCCTCCCTTGGAAATGACACG – 3') primers. This introduced 3 glycine codons both 5' and 3' as linkers allowing flexibility between the fluorophores. The SalI-XhoI fragment was then cloned between CyPet and YPet sequences, replacing the myo1IQ1 SalI-XhoI fragment of v541. All FRET constructs contain an N-terminal his-tag for purification.

pJC20 CyPet-myo1IQ1-YPet – v541

A bacterial expression vector coding for the 15 amino acids of myosin I IQ1, fused to an N-terminal CyPet and C-terminal YPet molecule.

pJC20 CyPet-myo1IQ2-YPet – v550

A bacterial expression vector coding for the 23 amino acids of myosin I IQ2, fused to an N-terminal CyPet and C-terminal YPet molecule.

pJC20 CYPet-myo1IQ1-2-YPet – v543

A bacterial expression vector coding for the 38 amino acids of myosin I IQ1 and IQ2, fused to an N-terminal CyPet and C-terminal YPet molecule.

pJC20 CYPet-myo1IQ12-S742D-YPet – v545

A bacterial expression vector coding for the 38 amino acids of myosin I IQ1 and IQ2, fused to an N-terminal CyPet and C-terminal YPet molecule. The serine codon representing amino acid S742 in the full length Myo1 protein has been mutated to a sequence encoding for a phosphomimic aspartic acid.

pJC20 myo1IQ12-SAH – v574

A bacterial expression vector coding for a fusion of the two myo1 IQ domains and a stable alpha helix (SAH) domain as an NdeI-BamHI fragment, with a N-terminal his-tag.

pGEX-4T-3 GST-myo1IQ12-SAH

pGEX-4T-3 based vector for bacterial expression of myo1IQ12-SAH fusion with a GST molecule. Myo1IQ12-SAH cloned as an NdeI-BamHI fragment from v574.

pNatA – v657

A lab stock of a pDUET based vector containing both *S. pombe* NatA acetylation complexes, Naa10 and Naa15 under control of the T7 promoter. Used for co-expression and *in vivo* acetylation of proteins.

pFA6a-kanMX6-GFP – v22

A lab stock of a plasmid coding for a GFP fluorophore and kanMX6 resistance marker, used as a template for C-terminal tagging of proteins at the genomic locus (J. Bähler, Wu, et al. 1998).

2.8.2. Yeast cloning vectors:

pTOPO myo1:URA4 – M13

A lab stock containing the sequence of full length *S. pombe myo1* marked with the *URA4* gene. ~250 Bp of upstream sequence and the downstream *ubm1* gene are also included.

pTOPO myo1-S742A:URA4 – v688

A plasmid containing a S742A modified *myo1* sequence, which was subsequently integrated at the genomic locus of *S. pombe myo1*, replacing the wild-type sequence. A 450 Bp region containing the S742 codon was removed from the *myo1* gene in M13 with a SnaB1-Hpa1 digest. A region of synthetic DNA containing the S742A mutation was used as a template for PCR amplification with the following primers. O526 (5' – GTACGATTAAACCCAATCAG – 3') and O527 (5' – AACTTTGTTCCTATTCCAC – 3'). The resulting blunt ended fragment was ligated into the digested M13 pTOPO vector. An NdeI-NcoI fragment was used for the integrating yeast transformation.

pTOPO mCherry-myo1:URA4 – v710

A plasmid designed to produce a KpnI-NheI fragment used to integrate an N-terminal mCherry tag at the *myo1* genomic locus. The N-terminal 730 bp of the *myo1* gene was removed from M13 by a KpnI-NdeI digest. DNA was synthesized containing the upstream promoter of *myo1*, mCherry coding sequence, and the first 730 bp of *myo1* as KpnI-NdeI fragment (v707). This region was cloned into the digested M13 vector.

pTOPO mCherry-myo1-S742A:URA4 – v711

A plasmid designed to produce a KpnI-NheI fragment used to integrate an N-terminal mCherry tag and S742A mutation at the *myo1* genomic locus. The same synthesized DNA as for v710 was used to insert the mCherry sequence as a KpnI-NdeI fragment into the v688 vector, creating a mCherry tagged S742A myo1 sequence.

pTOPO myo1-S742D:URA4 – v739

A plasmid containing a S742D modified *myo1* sequence which was subsequently integrated at the genomic locus of *S. pombe myo1*, replacing the wild-type sequence. A 450 Bp region including the S742 codon of the *myo1* gene was removed from M13 with a BsiW1-Hpa1 digest. A GeneArt pMK-RQ plasmid (v736)

containing the S742D mutation as a BsiW1-Hpa1 fragment was used to replace the S742D region in the pTOPO plasmid. The introduction of the mutation was checked by removal of a BglII restriction site.

pTOPO mNeongreen-myo1:URA4 – v741

mNeongreen removed from a GeneArt synthesized pMK-RQ-mNeongreen (v724) plasmid as a KpnI-AflII fragment, and used to insert in a KpnI-AflII digested pTOPO myo1:URA4 plasmid. Correct clones identified by introduction of an additional NdeI restriction site in the mNeongreen sequence. A KpnI-NheI fragment used for transformations to introduce the mNeongreen sequence at the myo1 genomic locus.

pTOPO mNeongreen-myo1-S742A:URA4 – v785

A plasmid designed to produce a KpnI-NheI fragment used to integrate an N-terminal mNeongreen tag and S742A mutation at the *myo1* genomic locus. The same synthesized DNA as for v741 was used to insert the mNeongreen sequence as a Kpn I-Afl II fragment into the v688 vector, creating a mNeongreen tagged S742A myo1 sequence.

pTOPO mNeongreen-myo1-S742D:URA4 – v788

A plasmid designed to produce a KpnI-NheI fragment used to integrate an N-terminal mNeongreen tag and S742D mutation at the *myo1* genomic locus. The same synthesized DNA as for v741 was used to insert the mNeongreen sequence as a KpnI-AflII fragment into the v739 vector, creating a mNeongreen tagged S742D myo1 sequence.

2.9. *S. pombe* strain list.

Table 2.6. *S. pombe* strains used in this study.

Lab Stock	Strain name	Genotype
201	*myo1:leu2*	*myo1:leu2 ura4.d18 leu1-32*
416	*cdc10-v50*	*cdc10-v50 leu1-32 ura4.d18*
1601	*cdc25-22 myo52-mCherry*	*cdc25-22 myo52-mCherry:hphMX6*
1658	*gef1Δ*	*gef1::URA4 ura4.d18*
1767	*cam1-gfp cam2-mCherry*	*cam1-gfp:MX6 cam2-mCherry:hphMX6*
1875	*ura4.d18*	*ura4.d18*
1927	*myo2-mCherry ste20-3gfp*	*myo2-mCherry:hphMX6 ste20-3gfp:kanMX6 prototroph*
1929	wild type	Prototroph
2056	*ste20Δ*	*ste20::kanMX6 prototroph*
2102	*myo2-mCherry ste20-3gfp myp2Δ*	*myo2-mCherry:hphMX6 ste20-3gfp:kanMX6 myp2::URA4 ura4.d18*
2122	*myo2-mCherry ste20-gfp acp1Δ*	*myo2-mCherry:hphMX6 ste20-3gfp:kanMX6 acp1::URA4 ura4.d18*
2129	*cam1-gfp*	*cam1-gfp:kanMX6 prototroph*
2146	*acp1-gfp myo2-mCherry*	*acp1-gfp:kanMX6 myo2-mCherry:hphMX6 prototroph*
2150	*leu1-32*	*leu1-32*
2153	*cam2-gfp*	*cam2-gfp:kanMX6*
2157	*cam1-gfp myo52-tdTomato*	*cam1-gfp:kanMX6 myo52-tdTomato:hphMX6 prototroph*
2172	*cam2-gfp myo52-tdTomato*	*cam2-gfp:kanMX6 myo52-tdTomato:hphMX6 prototroph*
2208	*gad8Δ*	*gad8::kanMX6 prototroph*
2209	*YFP-myo1*	*YFP-myo1:kanMX6 prototroph*
2216	*acp1-gfp lifeact-mCherry*	*acp1-gfp:kanMX6 lifeact-mCherry:leu2 leu1-32*
2221	*cam1-mCherry cam2-gfp*	*cam1-mCherry:hphMX6 cam2-gfp:kanMX6 prototroph*
2251	*cam1-gfp ste20Δ*	*cam1-gfp:kanMX6 ste20::kanMX6 prototroph*
2252	*cam2-gfp ste20Δ*	*cam2-gfp:kanMX6 ste20::kanMX6 prototroph*
2259	*acp1-AA-HA*	*acp1-AA-HA:kanMX6 prototroph*
2267	*cam1-gfp cam2Δ*	*cam1-gfp:kanMX6 cam2::URA4 ura4.d18*
2270	*myo2-mCherry YFP-myp2 acp1Δ*	*myo2-mCherry:hphMX6 YFP-myp2:kanMX6 acp1::URA4 ura4.d18*
2272	*YFP-myo1 ste20Δ*	*YFP-myo1:kanMX6 ste20::kanMX6 prototroph*
2274	*acp1-AA-gfp lifeact-mCherry*	*acp1-AA-gfp:kanMX6 lifeact-mCherry:leu2 leu1-32*
2304	*lifeact-mCherry ste20Δ*	*lifeact-mCherry:leu2 ste20::kanMX6 leu1-32*
2323	*myo1Δ*	*myo1::kanMX6 prototroph*
2324	*acp1-AA-HA myo2-mCherry YFP-myp2*	*acp1-AA-HA:kanMX6 myo2-mCherry:hphMX6 YFP-myp2:kanMX6 ura4.d18*
2343	*acp1-gfp myo2-mCherry myp2Δ*	*acp1-gfp:kanMX6 myo2-mCherry:hphMX6 myp2::URA4 ura4.d18*
2346	*cam1-gfp myo1Δ*	*cam1-gfp:kanMX6 myo1::kanMX6 prototroph*
2354	*cam1-gfp myo52Δ*	*cam1-gfp:kanMX6 myo52::URA4 ura4.d18*
2355	*YFP-myo1 cam2Δ*	*YFP-myo1:kanMX6 cam2::URA4 ura4.d18*
2357	*myo52-gfp cam2Δ*	*myo52-gfp:kanMX6 cam2::URA4 ura4.d18*

2360	*YFP-myo1 sid4-tdTomato*	*YFP-myo1:kanMX6 sid4-tdTomato:hphMX6 prototroph*
2365	*cam2-gfp myo52Δ*	*cam2-gfp:kanMX6 myo52::URA4 ura4.d18*
2371	*cam2-gfp sla2Δ*	*cam2-gfp:kanMX6 sla2::kanMX6*
2405	*YFP-myo1 sla2-mCherry*	*YFP-myo1:kanMX6 sla2-mCherry:kanMX6 prototroph*
2407	*myo2-mCherry cut12-gfp*	*myo2-mCherry:hphMX6 cut12-gfp:URA4 ura4.d18*
2408	*myo2-mCherry YFP-myp2*	*myo2-mCherry:hphMX6 YFP-myp2:kanMX6 prototroph*
2409	*myo2-mCherry sid4-tdTomato ste20-3gfp*	*myo2-mCherry:hphMX6 sid4-tdTomato:hphMX6 ste20-3gfp:kanMX6 prototroph*
2414	*cut12-gfp myo2-mCherry ste20Δ*	*myo2-mCherry:hphMX6 cut12-gfp:URA4 ste20::kanMX6 ura4.d18*
2415	*myo2-mCherry YFP-myp2 ste20Δ*	*myo2-mCherry:hphMX6 YFP-myp2:kanMX6 ste20::kanMX6 prototroph*
2437	*myo1-S742A*	*myo1-S742A:URA4 ura4.d18*
2438	*cam1-gfp myo1-S742A*	*cam1-gfp:kanMX6 myo1-S742A:URA4 ura4.d18*
2458	*cam1-gfp mCherry-myo1-S742A*	*cam1-gfp:kanMX6 mCherry-myo1-S742A:URA4 ura4.d18*
2459	*cam2-gfp mCherry-myo1-S742A*	*cam2-gfp:kanMX6 mCherry-myo1-S742A:URA4 ura4.d18*
2521	*mCherry-myo1-S742A*	*mCherry-myo1-S742A:URA4 ura4.d18*
2523	*mCherry-myo1*	*mCherry-myo1:URA4 ura4.d18*
2525	*cam1-gfp mCherry-myo1*	*cam1-gfp:kanMX6 mCherry-myo1:URA4 ura4.d18*
2527	*cam2-gfp myo1Δ*	*cam2-gfp:kanMX6 myo1::kanMX6 prototroph*
2534	*acp1-gfp cam2Δ*	*acp1-gfp:kanMX6 cam2::URA4 ura4.d18*
2540	*acp1-gfp myo1Δ*	*acp1-gfp:kanMX6 myo1::kanMX6*
2546	*acp1-gfp mCherry-myo1*	*acp1-gfp:kanMX6 mCherry-myo1:URA4 ura4.d18*
2547	*cam2-gfp mCherry-myo1*	*cam2-gfp:kanMX6 mCherry-myo1:URA4 ura4.d18*
2556	*lifeact mNeongreen-myo1*	*lifeact:leu2 mNeongreen-myo1:URA4 ura4.d18*
2560	*myo1-S742D*	*myo1-S742D:URA4 ura4.d18*
2561	*cam1-gfp myo1-S742D*	*cam1-gfp:kanMX6 myo1-S742D:URA4 ura4.d18*
2563	*acp1-gfp myo1-S742A*	*acp1-gfp:kanMX6 myo1-S742A:URA4 ura4.d18*
2565	*acp1-gfp myo1-S742D*	*acp1-gfp:kanMX6 myo1-S742D:URA4 ura4.d18*
2569	*lifeact myo1-S742A*	*red-lifeact:leu2 myo1-S742A:URA4 ura4.d18*
2571	*lifeact myo1-S742D*	*red-lifeact:leu2 myo1-S742D:URA4 ura4.d18*
2573	*lifeact myo1Δ*	*red-lifeact:leu2 myo1::kanMX6 leu1-32*
2574	*sla2-mCherry myo1-S742A*	*sla2-mCherry:kanMX6 myo1-S742A:URA4 ura4.d18*
2576	*cam1-gfp naa15Δ*	*cam1-gfp:kanMX6 naa15::kanMX6*
2607	*acp1-AA-HA mNeongreen-myo1*	*acp1-AA-HA:kanMX6 mNeongreen-myo1:URA4 ura4.d18*
2613	*cam2-gfp myo1-S742A*	*cam2-gfp:kanMX6 myo1-S742A:URA4 ura4.d18*
2614	*mNeongreen-myo1*	*mNeongreen-myo1:URA4 ura4.d18*
2625	*sla2-mCherry cam2-gfp*	*sla2-mCherry:kanMX6 cam2-gfp:kanMX6 prototroph*
2633	*mNeonGreen-myo1 sid4-tdTomato*	*mNeongreen-myo1:URA4 sid4-tdTomato:hphMX6 ura4.d18*
2634	*mNeongreen-myo1-S742A*	*mNeongreen-myo1-S742A:URA4 ura4.d18*
2635	*mNeongreen-myo1-S742D*	*mNeongreen-myo1-S742D:URA4 ura4.d18 leu1-32*
2674	*cam2Δ*	*cam2::URA4 ura4.d18*
2675	*sla2-mCherry cam1-gfp*	*sla2-mCherry:kanMX6 cam1-gfp:kanMX6 prototroph*

Chapter 3: Calmodulin association with IQ motifs of Myo1 and Myo52.

Introduction:

Calmodulin (CaM) is a small, ubiquitous calcium binding protein with multiple signalling functions in cells. One of these roles is as a myosin light chain, where it binds to the neck region of myosin heavy chains, stabilizing the lever arm and facilitating the power stroke (Houdusse 1996; Uyeda et al. 1996). Additionally, the ATPase activity of vertebrate Myo1c is modulated by calmodulin binding to the first IQ domain (Adamek et al. 2008). Vertebrate CaM has been identified as the light chain for numerous classes of myosin heavy chain, as reviewed by Heissler & Sellers, (2014). The *S. pombe* calmodulin, Cam1 is an essential protein that has a high sequence similarity to vertebrate CaM (Takeda & Yamamoto 1987), with studies showing that in *S. pombe* Cam1 is required for correct chromosome segregation and spore formation (Moser et al. 1997; Itadani et al. 2010).

Studies have shown that Cam1 is also likely to be a conventional calcium dependent light chain for the Class I myosin, Myo1, and Class V myosin, Myo52. Co-immunoprecipitation experiments by Toya et al. (2001) showed that Cam1 interaction with Myo1 only occurs in the absence of calcium, and is dependent on the IQ domains of the Myo1 neck region. Similarly, two-hybrid experiments by Grallert et al. (2007) identified that Cam1 binds to the neck region of Myo52. Although Cam1 has been shown to bind to myosin IQ domains, and therefore likely to play a role in stabilizing the neck region, the precise mechanism of how Cam1 associates with and regulates myosin activity is not known. Intriguingly deletion of the IQ domains from both Myo1 and Myo52 do not appear to impact the overall function of either protein in the maintenance of normal cell growth (Grallert et al. 2007; Toya et al. 2001).

This chapter describes *in vivo* observations of Cam1 co-localisation with myosin heavy chains to elucidate the role Cam1 may have during Myo1 dependent processes such as endocytosis. This is combined with an *in vitro* characterisation of Cam1 interactions with the IQ domains of Myo1, and provides evidence of a role for N-terminal acetylation in regulating Cam1 function.

3.1. Cam1 shares the same localisation as Myo1 and Myo52 in *S. pombe*.

To explore possible interactions between the fission yeast calmodulin, Cam1 and two myosin heavy chains, Myo1 and Myo52, strains were generated with the chromosomal copy of these genes fused with cDNA encoding fluorescent proteins. Fluorescently labelled fusion proteins were therefore expressed under their endogenous promoter, at their genomic locus on the chromosome. Figure 3.1 shows typical images of these strains in which a single protein is fluorescently labelled. When comparing the cellular localisations of Cam1-GFP with that of the fluorescently labelled myosin heavy chains, there are distinct similarities.

YFP-Myo1 foci are observed at sites of cell growth – the tips of interphase cells and the equator of dividing cells – consistent with its role in endocytosis. Myo52-GFP also localises as foci which concentrate at sites of cell growth. Cam1 is seen to localise to the spindle pole body where it is known to be an essential component (Moser et al. 1997). In addition to this, Cam1-GFP also localises to discrete foci at regions of cell growth. These similarities in distribution of Cam1 with Myo1 and Myo52 are consistent with evidence of Cam1 being a light chain of Myo1 and Myo52.

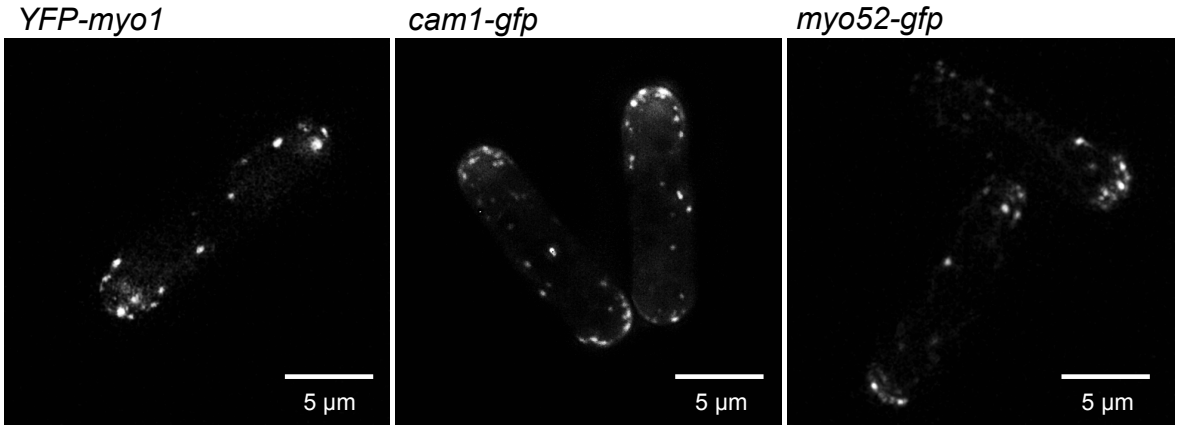

Figure 3.1. Fluorescently labelled Myo1, Cam1 and Myo52 in *S. pombe*. Maximum projections of 31 z-plane images showing the cellular localisation of myosin heavy chains, Myo1 and Myo52, and the fission yeast calmodulin, Cam1.

The localisation of Cam1 was observed in strains expressing Cam1 as a fusion protein with multiple fluorescent molecules. Figure 3.2 shows maximum projection images of *cam1-gfp, cam1-LanFP*, and *cam1-mCherry* strains. Distinct foci of Cam1 are visible in *cam1-gfp* and *cam1-LanFP* strains, consistent with the reported roles of Cam1 at endocytic patches and the SPB. In contrast, the distribution of Cam1-mCherry fluorescence is more cytoplasmic with the only distinct foci at the SPB. Cytoplasmic localisation of Cam1-mCherry is inconsistent with the expected role of Cam1 as a myosin light chain suggesting C-terminal labelling of Cam1 protein with mCherry is not suitable. This indicates that tagging Cam1 with different fluorophores, all at the C-terminus of the protein, results in an alteration of Cam1 distribution in the cell. Care must therefore be taken when choosing fluorescent labels to visualise proteins *in vivo*. For consistency, all analysis of Cam1 localisation and dynamics were determined from Cam1-GFP fluorescence.

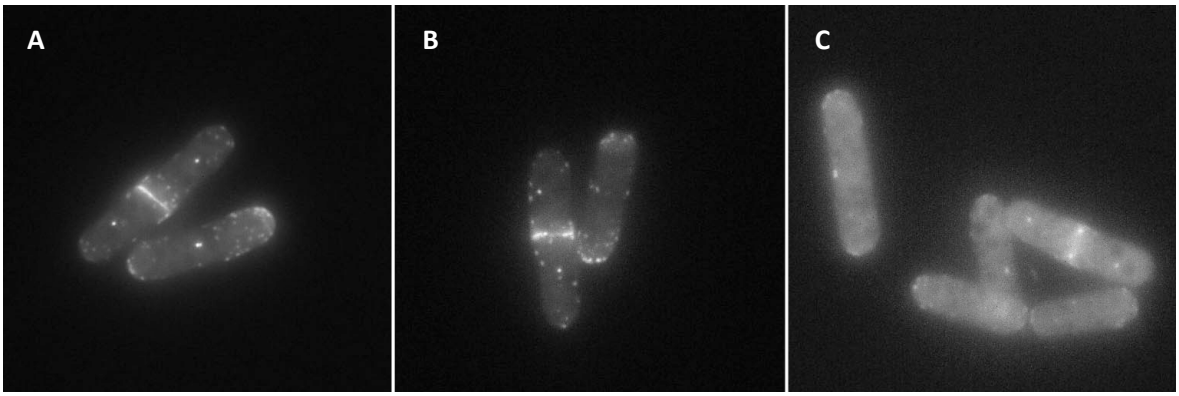

Figure 3.2. Localisation of Cam1 labelled with GFP, LanFP and mCherry. Maximum projections of 31 z-plane images showing the cellular localisation of Cam1-GFP (A), Cam1-LanFP (B) and Cam1-mCherry (C).

3.2. Cam1 shares the same dynamics as Myo1 and Myo52 in *S. pombe*.

Having observed similarities in the localisation of Cam1 with Myo1 and Myo52, next the dynamics of these proteins were compared. In order to image Myo1 over a prolonged period of time, an *mNeongreen-myo1* strain was generated (as described in materials and methods Section 2.8.2.) The mNeongreen fluorophore (Shaner 2013) was significantly brighter and more stable than YFP (and GFP), allowing extended and detailed timelapse imaging that was not possible with a *YFP-myo1* strain. Figure 3.3 shows kymographs generated from timelapse images of the strains described, allowing comparison of the dynamics of Cam1, Myo1 and Myo52.

Foci of mNeongreen-Myo1 appear and disappear (Figure 3.3.A), with these events lasting on average 14 seconds (+/-0.24 s), and exhibit no lateral movement (see Movie 1 – Appendix 2). These observations are consistent with previously reported lifetimes of Myo1 at endocytic patches (Berro et al. 2010; Attanapola 2009). The kymograph from a *myo52-gfp* cell (Figure 3.3.B) shows an example of the rapid lateral dynamics which are characteristic of Class V myosins moving along actin cables.

When comparing the dynamics of Cam1, there are again similarities with both Myo1 and Myo52. The kymographs in Figure 3.3.C (and Movie 2 – Appendix 2) show the majority of Cam1 foci are stationary, and appear for on average 10.4 seconds (+/-0.14 s) before disappearing, just shorter than the Myo1 events observed. However, also highlighted are foci of Cam1-GFP with dynamic lateral movements, similar to those seen for Myo52-GFP. Many more Myo1-like dynamics are seen in *cam1-gfp* cells compared to Myo52-like movements. This is likely to be because there are over 10 fold more molecules of Myo1 in a cell than Myo52 (Carpy et al. 2014; Marguerat & Bähler 2012). The average speed of these movements in a *cam1-gfp* strain is 0.58 (+/-0.07) μm/s, comparable with the 0.62 (+/- 0.09) μm/s observed in *myo52-gfp* strains and published speed of Myo52 (0.55 μm/s) (Grallert et al. 2007). These data are again consistent with Cam1 being an associated light chain of both Myo1 and Myo52 motor proteins.

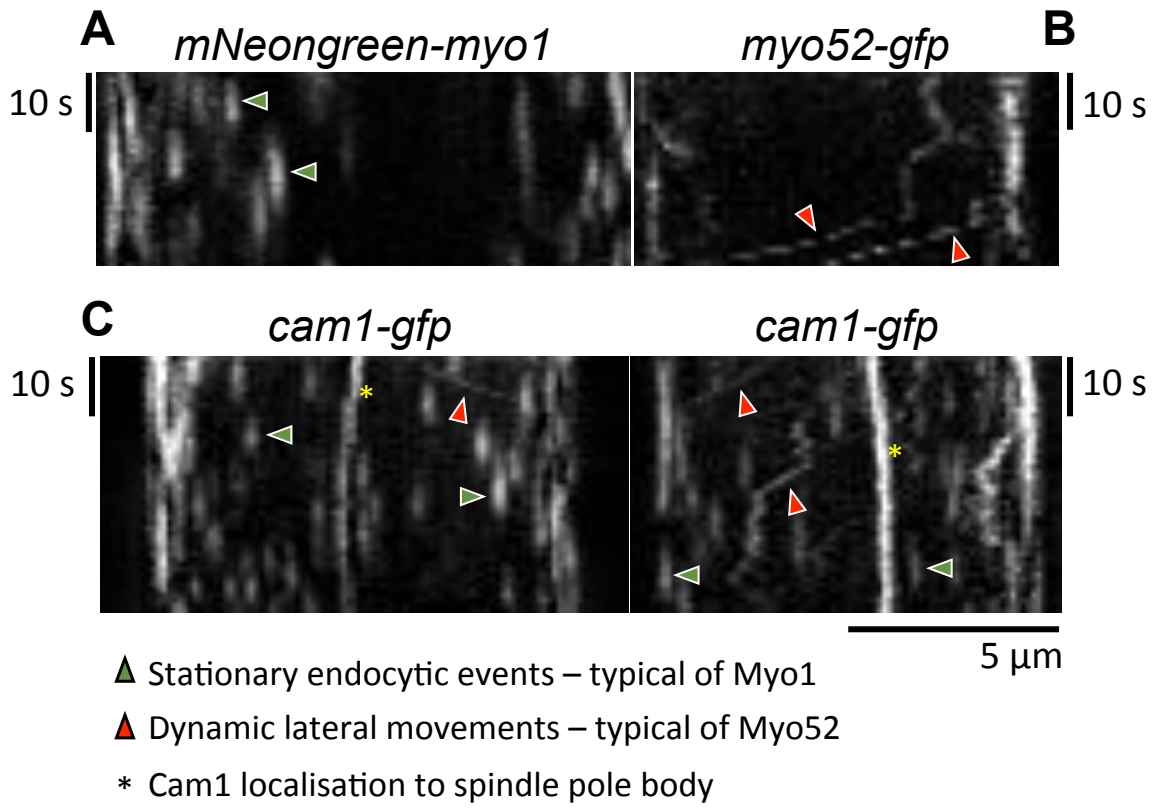

Figure 3.3. Dynamics of fluorescently labelled Myo1, Cam1 and Myo52. Typical kymographs generated from maximum projections of 13 z-plane images, of (A) *mNeongreen-myo1*, (B) *myo52-gfp*, or (C) *cam1-gfp* cells. Green arrows indicate Myo1-like endocytic events, and red arrows indicate Myo52-like movements. * Highlights persistent fluorescence of Cam1-GFP at the SPB.

3.3. Cam1 dynamically co-localises with Myo52 in *S. pombe* cells.

Having observed similar dynamics for Cam1 and both Myo1 and Myo52, strains were generated to allow these proteins to be imaged simultaneously in order to establish co-localisation. Firstly a *myo52-tdTomato cam1-gfp* strain was imaged, expressing both Myo52 and Cam1 proteins labelled at the C-terminus. Due to the rapid dynamic nature of Myosin V movements within the cell, simultaneous imaging of the two wavelengths using an Optosplit device (Cairn Reasearch Ltd.) was required to determine their co-localisation. Figure 3.4 shows a micrograph composed of overlaid images from the green and red channels, captured

simultaneously using an Optosplit. Each frame is a maximum projection of 13 z-slice images taken at 0.67 s intervals. Arrows highlight molecules of Cam1 moving together with Myo52. This dynamic co-localisation of foci suggests that these molecules are interacting with one another within the cell. These data do not rule out that Cam1 travels as a cargo bound to the Myo52 tail, but combined with previous data showing Cam1 binds the IQ domains of Myo52 (Grallert et al. 2007), it is likely that Cam1 is associated with the neck region of Myo52 as it moves along actin cables in the cell.

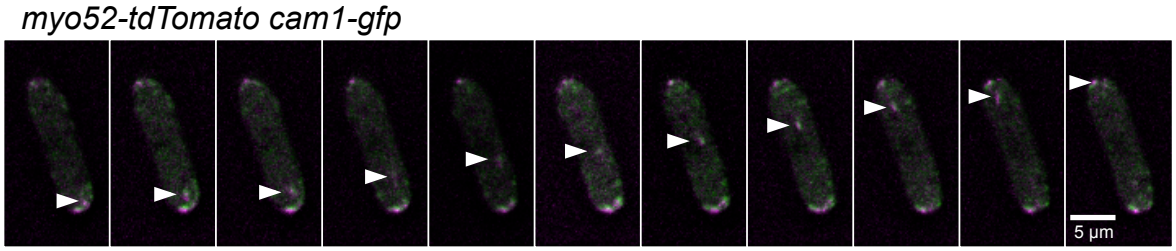

Figure 3.4. Co-localisation of Cam1 with Myo52.

Maximum projection of 13 z-plane images of a *myo52-tdTomato cam1-gfp* cell, taken at 0.67 s intervals. GFP and Tomato images were captured simultaneously using an Optosplit and overlaid using Metamorph software. The arrow highlights co-localisation of Cam1-GFP and Myo52-tdTomato molecules.

3.4. Myo1 and Cam1 cannot be labelled simultaneously.

Next strains were generated to visualise co-localisation of Cam1 with Myo1. However as discussed further in Section 4.9, when double tagging some combinations of proteins within the cell, one or both lose functionality. This was the case with Myo1 and Cam1 when using multiple combinations of fluorescent labels. It was therefore not possible to determine Cam1 co-localisation with Myo1 in the same way as for Myo52 (Figure 3.4). Two of the combinations of fluorescently labelled Cam1 and Myo1, were *cam1-gfp mCherry-myo1* and *CFP-myo1 cam1-*

mCherry (Figure 3.5.A&C). As shown (Figure 3.2) Cam1-mCherry protein alone does not appear fully functional, and the same cytoplasmic Cam1 localisation was also seen in *CFP-myo1 cam1-mCherry* cells. Cam1-GFP fluorescence in *cam1-gfp mCherry-myo1* cells is also highly cytoplasmic, with very few individual foci visible. This is in contrast to the defined localisation seen in a *cam1-gfp* single tagged strain, (Figure 3.5.B) This apparent partial loss of Cam1 functionality in cells where Myo1 is also tagged, results in an overall reduction in growth rates (Figure 3.5.D).

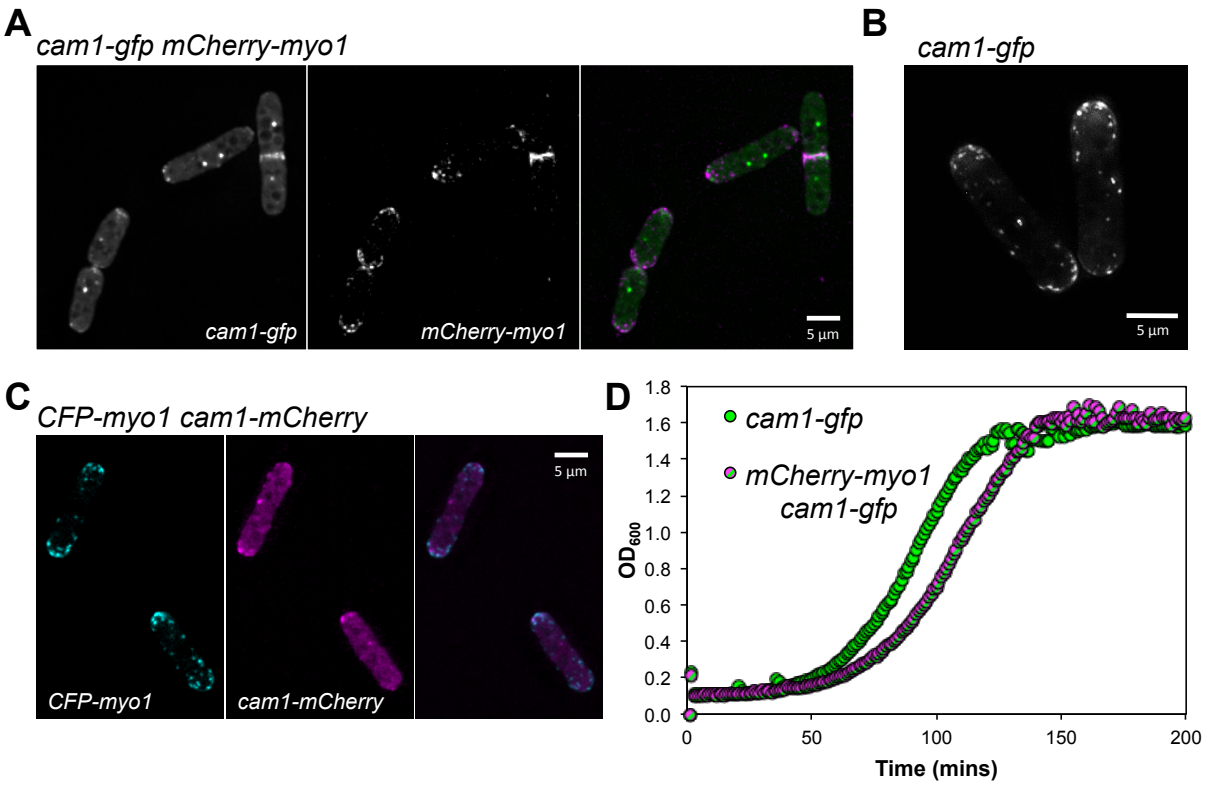

Figure 3.5. Simultaneous labelling of Cam1 and Myo1.

Maximum projections of 31 z-plane images of (A) *mCherry-myo1 cam1-gfp* cells and (C) *CFP-myo1 cam1-mCherry* cells, with (B) showing a comparison image of single tagged *cam1-gfp* cells. (D) shows a growth curve of OD_{600} measurements for cultures of *cam1-gfp* and *mCherry-myo1 cam1-gfp* cells.

3.5. Myo1 and Cam1 recruit to cortical patches but are not internalised.

Being unable to directly visualise co-localisation of Myo1 and Cam1, the localisation of both proteins to endocytic patches was observed. *cam1-gfp sla2-mCherry* and *mNeongreen-myo1 lifeact-mCherry* strains were generated to image Cam1 and Myo1 co-localisation with known endocytic patch markers. Sla2 is an early endocytic patch marker, arriving at the membrane ~30 s before patch internalisation (Berro et al 2010). While actin (imaged using the Lifeact-mCherry marker (Riedl et al. 2008; Huang et al. 2012)) arrives later, ~9 seconds before patch internalisation (Berro et al 2010). In budding yeast, both proteins have been shown to associate with the endocytic vesicle as it is internalised (Kaksonen et al. 2003).

Figure 3.6.A shows a maximum projection image and kymographs generated from timelapse imaging of *mNeongreen-myo1 lifeact-mCherry* cells using an Optosplit device. Arrows indicate instances of mNeongreen-Myo1 co-localisation with cortical actin patches marked by Lifeact-mCherry. Kymographs generated for individual endocytic patches show in more detail Myo1 co-localisation with actin. Actin is seen to internalise from the membrane (top of kymograph) into the cell, consistent with its association with the endocytic vesicles (Gachet 2005). In contrast, Myo1 remains at the membrane before disappearing. The timing of Myo1 and actin recruitment to the endocytic patch appears similar, consistent with previously reported patch timings (Berro et al 2010).

Cam1 co-localisation with the early endocytic coat protein Sla2 was also determined. Figure 3.6.B shows a maximum projection and kymographs of *cam1-gfp sla2-mCherry* cells. Sla2-mCherry fluorescence was not bright enough for visualization using an Optosplit device, instead single z-plane images of each wavelength were captured sequentially. Co-localisation of these proteins can be seen, particularly at the cell tips, where Sla2-mCherry is brightest. In the expanded views of individual patches, Sla2 can be seen to move away from the cell membrane, while Cam1 is not internalised.

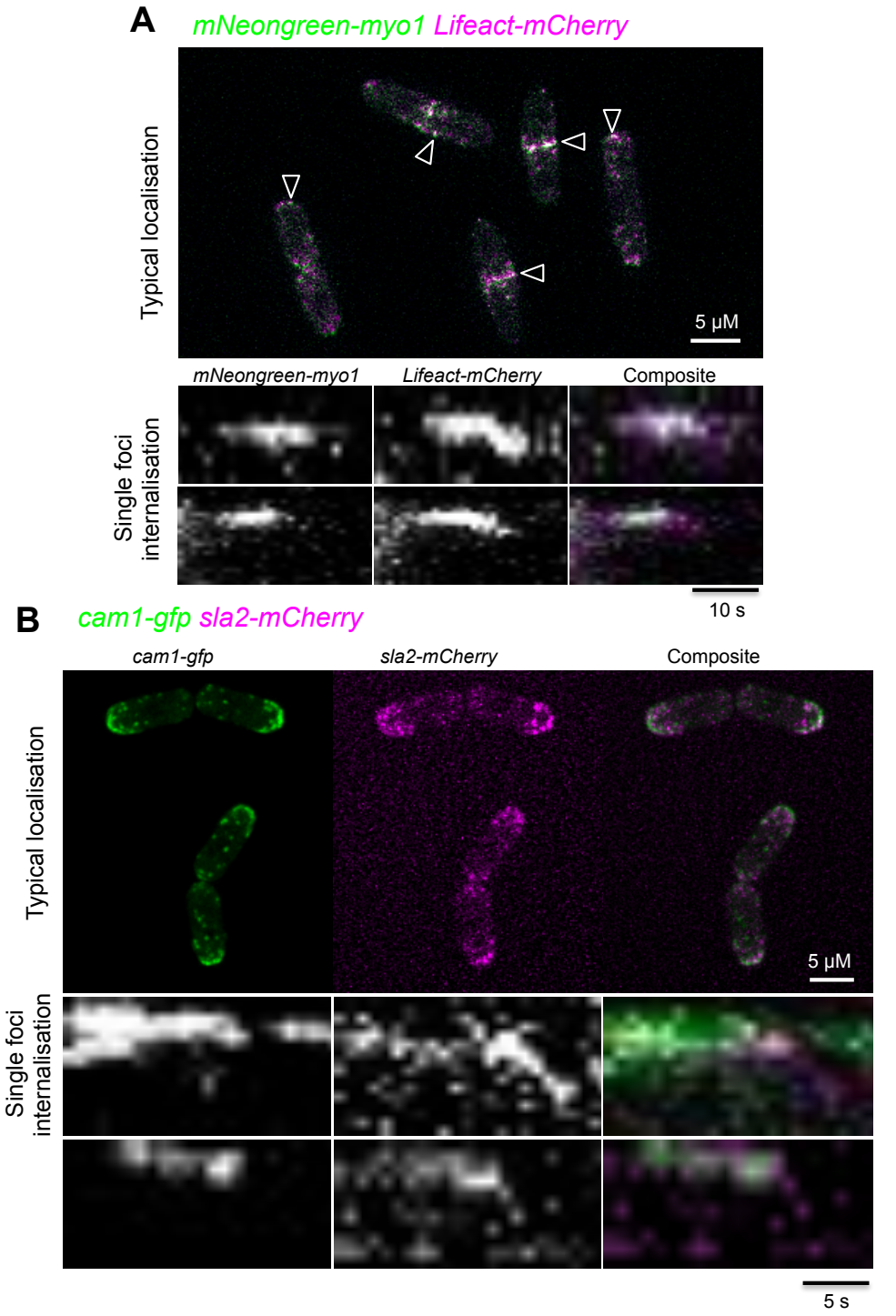

Figure 3.6. Association of Cam1 and Myo1 with endocytic patches.
(A) Overlaid GFP and mCherry signal from single z-plane images of *mNeongreen-myo1 Lifeact* cells captured using an Optosplit, and kymographs generated from timelapse images, showing individual foci at the membrane. (B) Maximum projection of 31 z-plane images of *cam1-gfp sla2-mCherry* cells and kymographs generated from single z-plane timelapse images taken alternately of GFP and mCherry wavelengths.

Together these data indicate that Myo1 and Cam1 associate with endocytic patches, where they remain at the membrane upon vesicle internalisation. However, from these strains it was not possible to correlate exact timings of Myo1 and Cam1 recruitment to patches.

3.6. Cam1 localisation and dynamics are dependent on Myo1 and Myo52.

Having shown that Myo1 and Cam1 associate with endocytic patches, it was next determined if the recruitment of Cam1 was dependent on Myo1. In order to do this, Cam1-GFP dynamics were observed in a *myo1*Δ strain. In the absence of Myo1, Cam1 no longer recruits to endocytic patches (Figure 3.7). A large proportion of the Cam1-GFP fluorescence is cytoplasmic with very few of the defined foci at the membrane that are seen in *myo1*$^{+}$ strains. Cam1 still localises strongly to the spindle pole body independently of Myo1. The only other discrete localisation of Cam1 in a *myo1*Δ strain is at the CAR and cell tips, reflecting its distribution via Myo52. Looking at the dynamics of Cam1 in a *myo1*Δ also reflects these observations – with all endocytic-associated events abolished, leaving only rapid directional movements visible, suggesting Cam1 remains associated with Myo52 (see Movie 3 – Appendix 2).

Cam1-GFP fluorescence was also imaged in a *myo52*Δ background. The maximum projection image of *cam1-gfp myo52*Δ cells (Figure 3.7) shows Cam1 localisation at endocytic patches, suggesting Cam1 association with Myo1 is not affected. Figure 3.7 also shows a typical kymograph of a mitotic *cam1-gfp myo52*Δ cell, no dynamic lateral movements are observed, confirming that these are dependent on Myo52. Cam1 endocytic events are less well defined in *myo52*Δ cells, particularly at the cell equator, possibly due to the role Myo52 plays in transporting new material for septum formation (Mulvihill et al. 2006; Wang et al. 2016).

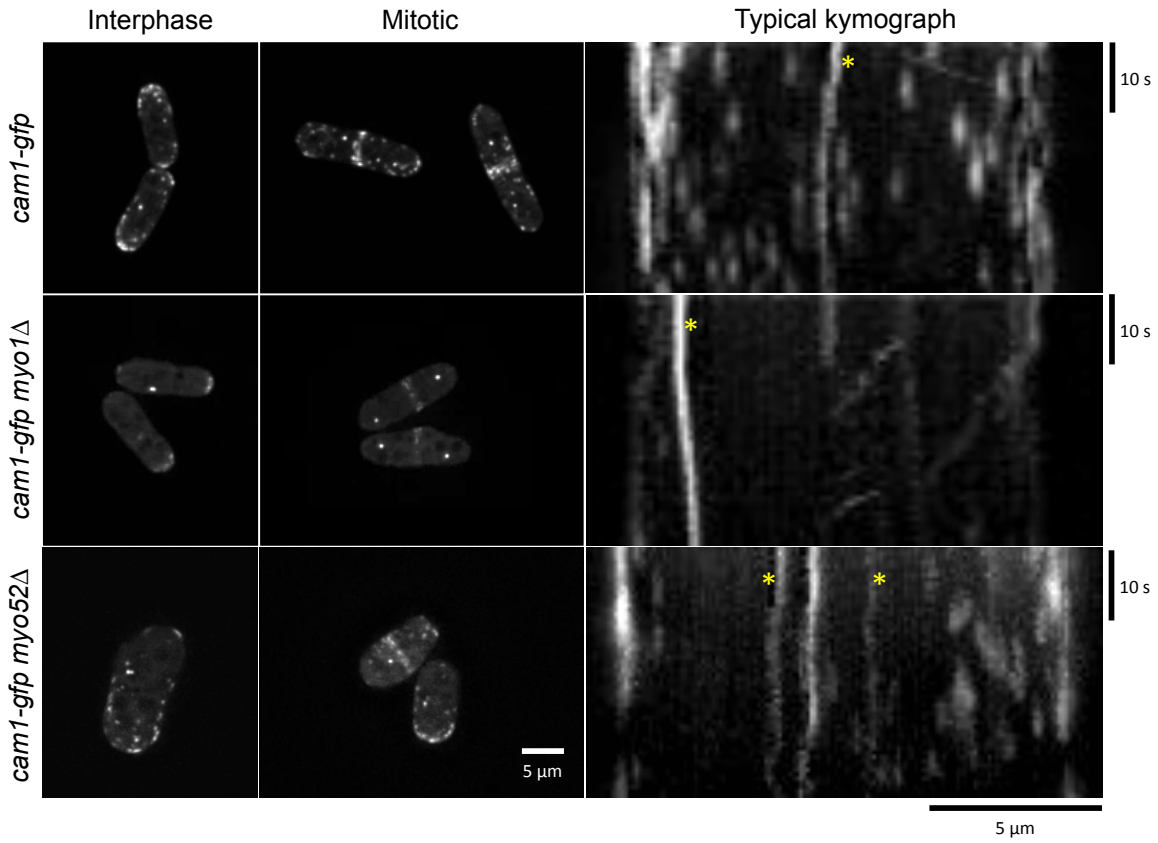

Figure 3.7. Cam1 dependence on Myo1 and Myo52.

Maximum projections of 31 z-plane images of Cam1-GFP fluorescence in a wild-type genetic background (top panel), *myo1*Δ (middle panel) and *myo52*Δ (bottom panel). Kymographs of the same strains are generated from maximum projections of 13 z-plane images. * Represents SPB signal.

3.7. Calmodulin and myosin based proteins for *in vitro* analysis.

These *in vivo* observations suggesting Cam1 associates with both Myo52 and Myo1, are consistent with Cam1 acting as a conventional myosin light chain. It would therefore be predicted that the interaction between Cam1 and both Myo1 and Myo52 is via the IQ domains of the myosin neck region. In order to investigate this association more specifically, an *in vitro* approach was taken to determine the binding interactions of Cam1 with the IQ domains of Myo1 and Myo52. Figure 3.8 shows the purified proteins used in this study. Generation of the plasmid constructs and methods of purification are detailed in Section 2.8.1.

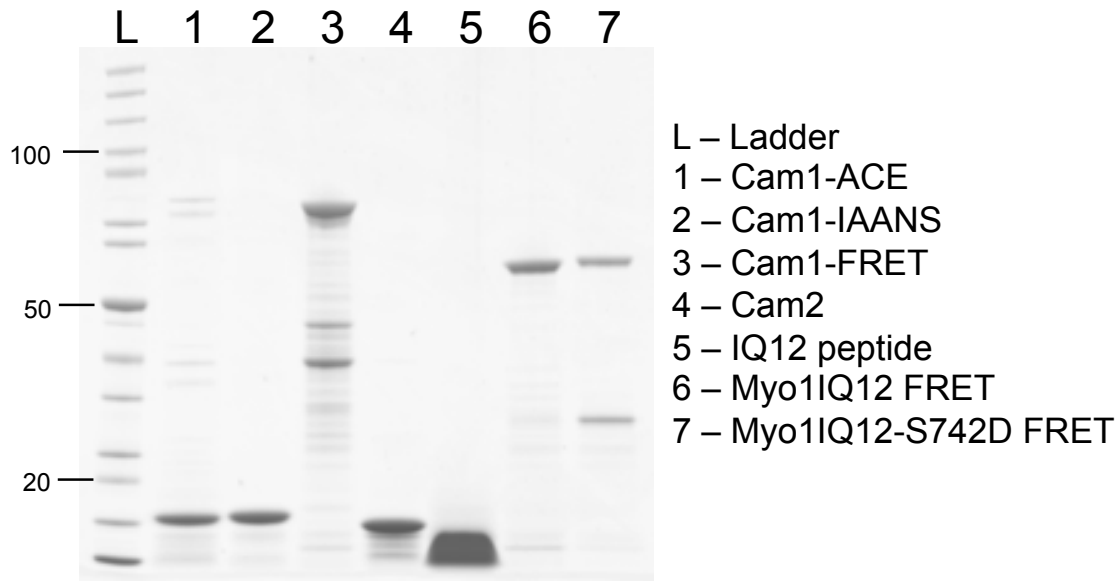

Figure 3.8. Purified proteins used in this study.

A coomassie stained 4-20% SDS-PAGE gel of proteins expressed and purified during this study. All lanes loaded with 5 µg of protein, as determined by Bradford assay.

Recombinant *S. pombe* Cam1 protein is acetylated at its N-terminus, and is referred to here as Cam1-ACE. Fluorescent variants of Cam1 protein include a Cam1-T7C mutant, with an IAANS fluorescent label covalently linked to a cysteine introduced in place of the threonine-7 residue. Changes in IAANS fluorescence indicate changes in the hydrophobicity of the environment around the label at the N-terminus of Cam1. Figure 3.9.C shows the design of a bacterial expression construct where the *cam1* gene was cloned between DNA encoding Cypet and Ypet fluorophores. The resulting FRET pair fusion with Cam1 protein forming the linker region, was used for analysis of Cam1 binding to other proteins.

Figure 3.9.C also shows the DNA sequence encoding the two IQ motifs of Myo1 and the first two of Myo52, which was cloned between the same pair of fluorophores. The fusion proteins expressed, Myo1IQ12, and Myo52IQ12, were used in the FRET experiments described in Section 3.8 and Figure 3.9.B. The Myo1 IQ12 peptide (Figure 3.8 and Figure 4.7) was kindly synthesized by Jody

Mason (University of Bath), and is formed of 38 amino acid residues including the two Myo1 IQ domains.

Also shown in Figures 3.8 and 3.9.C are two phosphomimic FRET proteins, Myo1IQ12-S742D and Myo52IQ12-S798D. Residues S742 of Myo1 and S798 of Myo52 are both within the neck region of the myosins and have been identified as residues which are phosphorylated (Wilson-Grady et al. 2008; Carpy et al. 2014)(Petersen personal communication). In these phosphomimic proteins the serine residue has been replaced with an aspartic acid. The effect this amino acid change in the Myo1 IQ domains has on calmodulin binding is described in more detail in Chapter 5.

3.8. FRET experiments show the IQ regions of Myo1 and Myo52 have different helical flexibility.

Figure 3.9.B explains the experimental design of using a FRET pair fused by a linker region of IQ domains to investigate the binding of calmodulin. When the IQ domains are in an unbound, collapsed conformation, the FRET pair are in close proximity. Excitation of the donor Cypet fluorophore results in emission of photons at 475 nm which are quenched by the adjacent Ypet molecule (Overlay of spectra shown in Figure 3.9.A). This transfer of energy excites the Ypet molecule resulting in an observed emission peak at 530 nm. When calmodulin binds to the IQ domains, they are thought to take on a more rigid, extended form. Extension of the linker region forces the fluorophores apart, resulting in reduced FRET as the transfer of energy is highly sensitive to the distance between the fluorophores (Shimozono & Miyawaki 2008). A larger distance between the fluorophores, results in less Cypet emission absorbed by the Ypet fluorophore, resulting in a decrease in the 530 nm peak and increase in the observed Cypet emission at 475 nm.

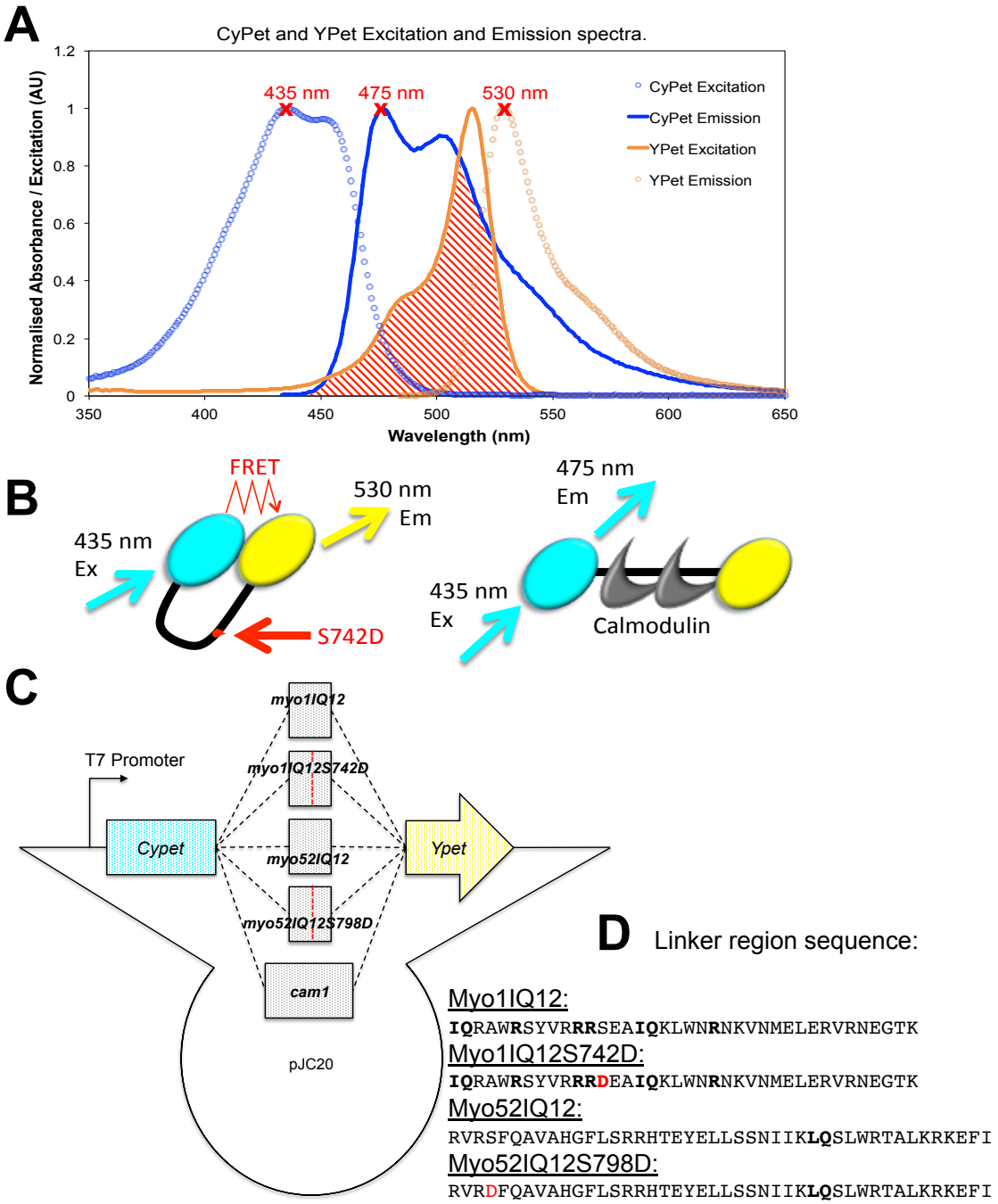

Figure 3.9. Design of FRET experiments and constructs.

(A) normalised absorbance and emission spectra of Cypet and Ypet fluorophores. The region highlighted in red shows the overlap of Cypet emission and Ypet absorbance – allowing transfer of energy when molecules are in close proximity. (B) A schematic diagram showing the expected changes in FRET which occur on binding of CaM to the IQ linker region. (C) The design of bacterial expression vectors for FRET proteins, the sequence of the IQ linker regions are detailed in (D)

Once purified using the method described in Section 2.2.3, FRET proteins were excited at 435 nm under the fluorimetry conditions described in Section 2.3.4, and the emission spectra recorded. The emission spectra alone provided information about the stability and flexibility of the IQ regions themselves. Figure 3.10. shows the overlaid emission spectra of equivalent concentrations (determined by Bradford assay) of Myo1IQ12 and Myo52IQ12 FRET proteins.

The spectra of the Myo1IQ12 FRET proteins show a large Ypet emission peak at 530 nm and a very low Cypet emission peak. This suggests that the two IQ domains of Myo1 are flexible enough to allow a tightly folded or completely collapsed conformation where the Cypet and Ypet molecules are very close together to allow FRET to occur efficiently. The un-modified Myo52IQ12 FRET protein did not fluoresce at the expected Cypet or Ypet wavelengths, suggesting the protein was not correctly folded (Figure 3.10). However, the phosphomimic Myo52IQ12-S798D FRET protein showed an expected emission peak at 530 nm, although much smaller than that seen with the Myo1 IQ domains. Comparing the ratios of Cypet:Ypet - 2:3 for Myo52IQ12-S798D and 2:9 for both Myo1 FRET proteins, confirms that despite differences in overall fluorescence levels, there is less FRET occurring when Cypet and Ypet are linked by the Myo52 IQ domains. These results suggest that, when compared to the IQ domains of Myo1, the first two α-helical IQ domains of Myo52 form a more rigid structure which inhibits the two fluorophores of the FRET pair coming into close proximity of one another. A more rigid and extended neck region could facilitate the function of Myo52 as a transport myosin, as some studies suggest a longer, stable neck region facilitates class V myosin movement along actin filaments. (Schott et al. 2002; Purcell et al 2002).

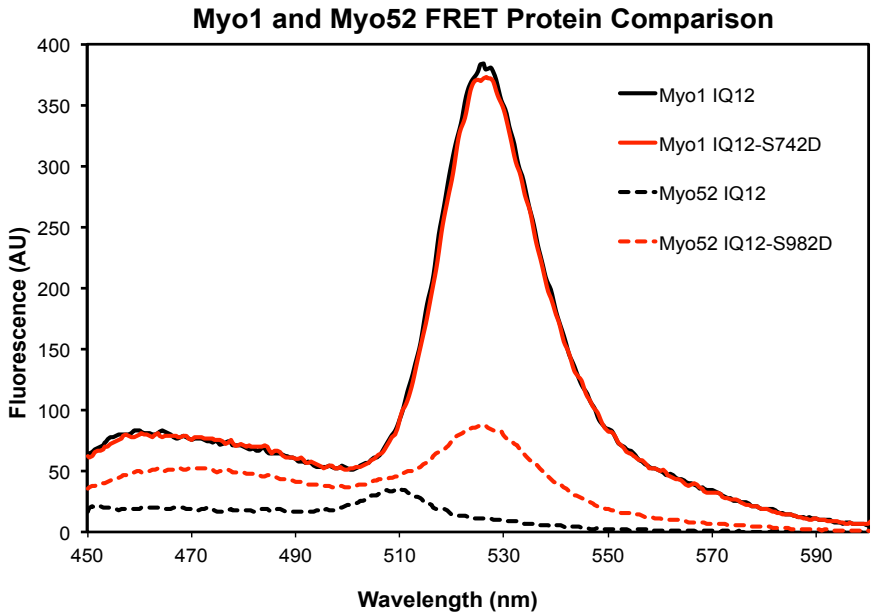

Figure 3.10. Emission spectra of Myo1IQ12 and Myo52IQ12 FRET proteins.

Emission spectra of Myo1IQ12 FRET protein (solid lines) and Myo52IQ12 FRET protein (dashed lines) following excitation at 435 nm. The red lines show spectra of the phosphomimic protein variants.

Due to bacteria lacking the ability to add post-translational modifications, the 'un-modified' FRET proteins are essentially a phosphorylation-null version of the IQ domains, while the aspartic acid, 'D' substitutions form a constitutively charged version, mimicking phosphorylation. It is possible that introduction of charged residues can destabilise interactions in the secondary or tertiary structure allowing more flexibility in the linker region (Roque et al. 2008). Phosphorylation events in the IQ domains therefore have potential to regulate myosin function, either by direct structural changes or through the modulation of calmodulin light chain binding (Yip et al. 2008).

Changing the charge of residue 742 in the Myo1 IQ linker regions does not change the emission spectra of these FRET proteins. This suggests that phosphorylation may not have a significant effect on the conformation of the IQ domains, with both forms being flexible enough to allow FRET. Effects of Myo1-S742 phosphorylation on calmodulin binding and the role it plays *in vivo* is discussed in Chapter 5.

3.9. It was not possible to determine Cam1 binding to Myo52 IQ12 domains.

The low levels of FRET signal from the phosphomimic Myo52IQS798D FRET protein suggest that the IQ domains of Myo52 have a relatively rigid nature. However, titrations of Cam1 were made in the presence and absence of calcium to test whether binding of calmodulin resulted in detectable changes in FRET signal. Figure 3.11 shows the emission spectra before and after addition of 10 fold excess concentration of Cam1, in the presence of EGTA. No change in FRET was observed, either in the absence or presence of calcium. It is not possible to determine whether this is due to Cam1 not binding to the first two IQ domains of Myo52 or that binding of Cam1 does not change the conformation of the relatively rigid helical structure, sufficiently to allow changes in FRET to be observed.

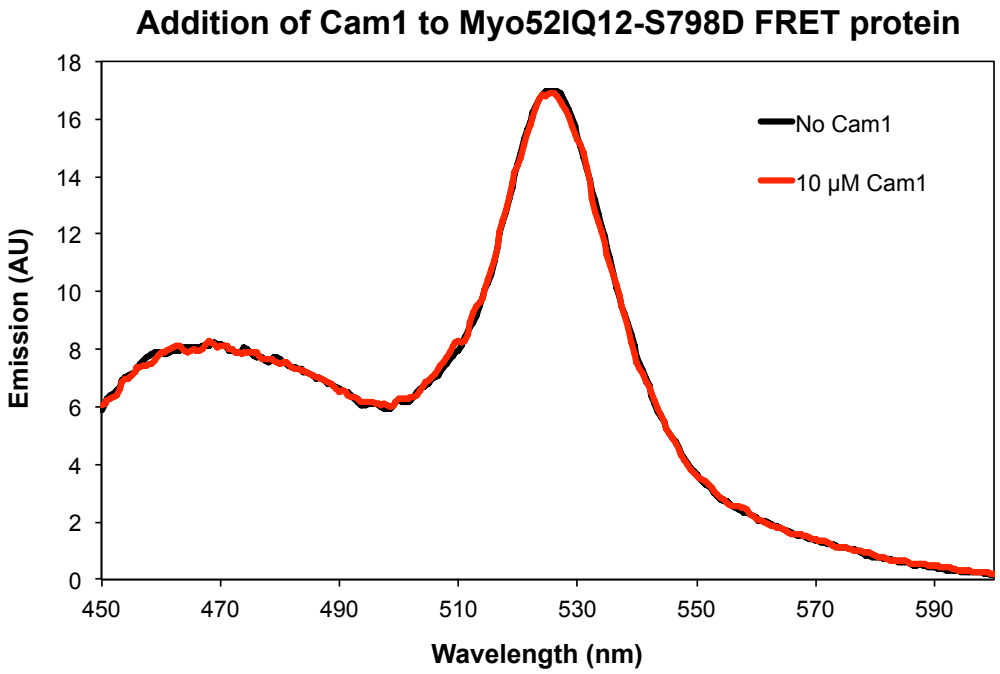

Figure 3.11. Addition of Cam1 to the Myo52IQ12-S798D FRET protein.

Black line shows the emission spectrum of 1 µM Myo52IQ12-S798D FRET protein in the presence of 4 mM EGTA after excitation at 435 nm, before addition of excess (10 µM) Cam1 protein (red line).

3.10. Cam1 has a strong affinity for the IQ domains of Myo1 in the absence of calcium.

A clear FRET signal indicates the relatively flexible nature of the Myo1 IQ domains, making it was possible to assess the binding of Cam1. To validate the assay with the published observations of calcium dependent binding of Cam1 (Toya et al. 2001), Cam1 was added to the Myo1IQ12 FRET protein in the presence and absence of calcium – 50 μM $CaCl_2$ providing an excess of Ca^{2+} ions and 4 mM EGTA used to sequester Ca^{2+} ions from the reaction solution. Figure 3.12 shows the recorded emission spectra after addition of excess Cam1 to Myo1IQ12 FRET protein in the presence and absence of calcium.

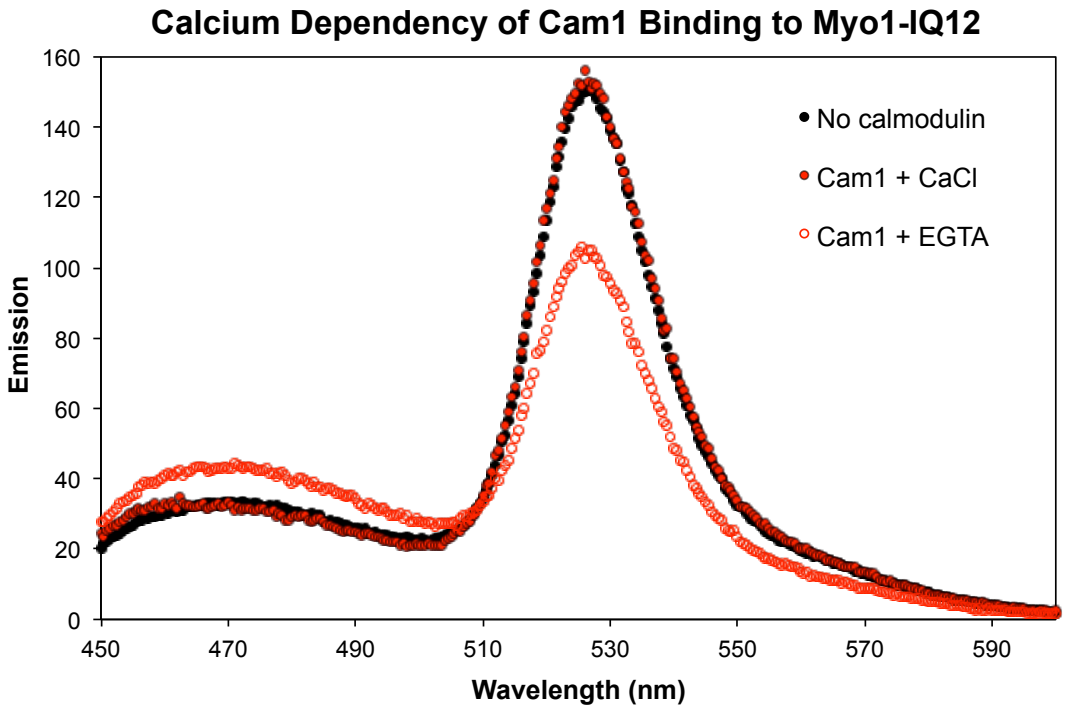

Figure 3.12. Addition of Cam1 to the Myo1IQ12 FRET protein.

Black circles show the emission spectrum of Myo1IQ12 FRET protein alone in the presence of 4 mM EGTA after excitation at 435 nm (identical spectrum recorded in calcium conditions). Empty red circles show an altered FRET spectrum after addition of excess Cam1 protein in the presence of EGTA, compared to no change seen when Cam1 is added in the presence of calcium (filled red circles).

No change in FRET signal is observed in the presence of calcium (Figure 3.12 filled red circles), indicating Cam1 does not bind under these conditions. However, an increase in signal at 477 nm and a reduction in the 530 nm peak are recorded in the absence of calcium (Figure 3.12 empty circles). This reduction in FRET, shows that Cam1 binds to the Myo1 IQ domains in the presence of EGTA. These data firstly confirm that the FRET assay is suitable for measuring the binding of calmodulin to IQ domains, and also confirms previous reports that Cam1 only binds to Myo1 in the absence of calcium, and this interaction occurs through the IQ domains (Toya et al. 2001).

Adding increasing amounts of Cam1 to the Myo1IQ12 FRET protein further reduces the FRET signal (Figure 3.13.A). A titration of Cam1 into a solution of 0.5 μM Myo1IQ12 FRET protein was used to determine the affinity of Cam1 binding in the absence of calcium. The graph in Figure 3.13.C shows the decrease in maximum Ypet fluorescence and reciprocal increase in Cypet fluorescence as Cam1 binds. The change in levels of FRET can also be presented as a change in the Ypet/Cypet fluorescence ratio (Figure 3.13.D).

All measurements can be fitted with a best fit line described by the quadratic equation in section 2.3.4 to give an affinity of Cam1 binding. However the K_d value obtained from each set of measurements (Cypet and Ypet maxima or FRET ratio) varies. Therefore, throughout this thesis all calculations of affinity from FRET experiments are made from percentage changes in Cypet fluorescence, as this measurement gives the most direct and sensitive read out of changes in FRET.

Figure 3.13.B shows these changes in Cypet fluorescence as Cam1 is added to the Myo1IQ12 FRET protein. Using Origin to plot the percentage changes in fluorescence and fit a quadratic equation (section 2.3.6), the calculated K_d of Cam1 binding to the two Myo1 IQ domains is 0.80 μM. For titrations of Cam1, initial addition of very small amounts of Cam1 protein to a solution of Myo1 IQ12 FRET resulted in unexpectedly large changes of fluorescence (Figure 3.13). It is possible that this change in fluorescence does not completely reflect Cam1 binding, but an additional event such as separation of FRET protein dimers. All

quadratic equations fitted for titration data therefore exclude the first data point (discussed further in Section 7.1.2).

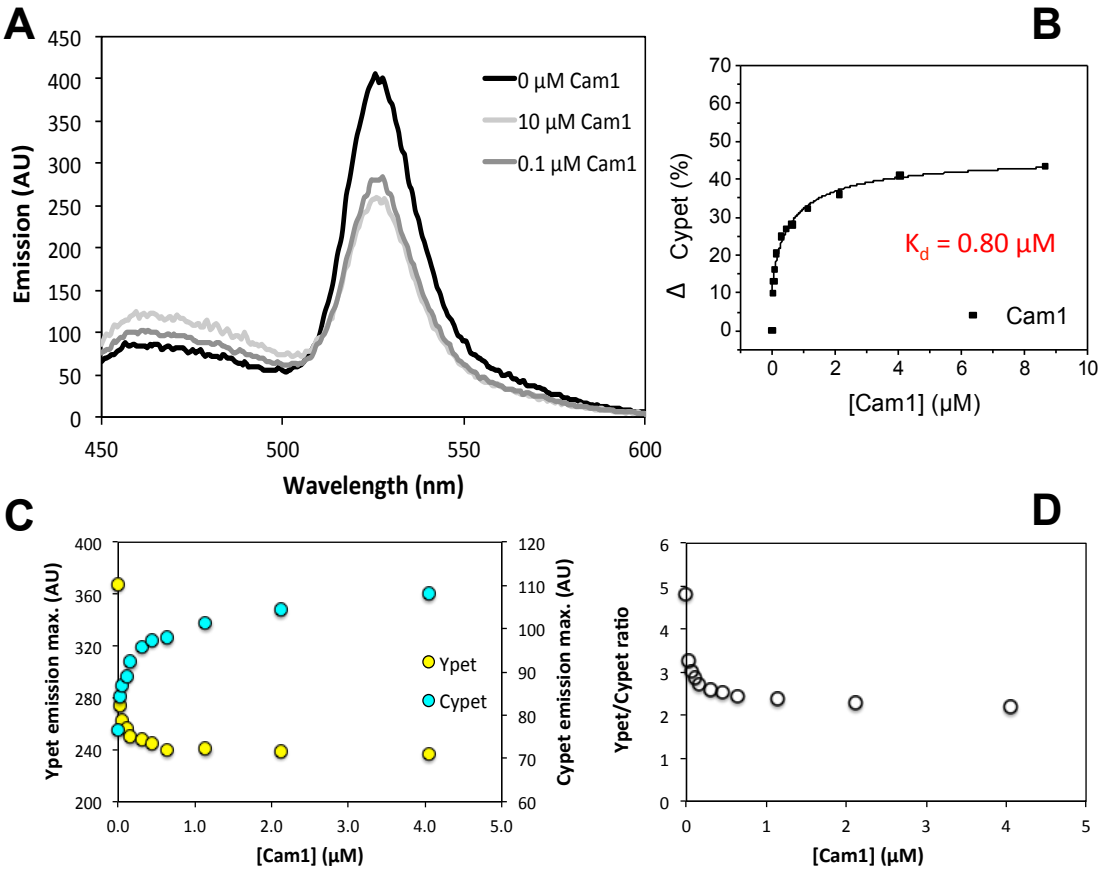

Figure 3.13. Titrations of Cam1 with the Myo1IQ12 FRET protein.

(A) Example spectra from a titration of Cam1, showing the start of the titration – 0.5 µM Myo1IQ12 FRET protein with no Cam1 present, (black line), an intermediate 0.1 µM concentration of Cam1 (dark grey line) and the final concentration of Cam1 at 10 µM (light grey line). (B) shows the % change in Cypet fluorescence maxima as additional Cam1 is added. Using Origin software to fit a quadratic equation excluding the first titration point, the K_d value was calculated. (C) shows the Cypet and Ypet emission maxima at each concentration of the titration, with the Ypet/Cypet ratio plotted in (D).

3.11. N-terminal acetylation affects the stability and calcium sensitivity of Cam1 *in vitro*.

Unless stated the recombinant Cam1 protein used in all experiments described carried a post-translational N-terminal (Nt) acetylation modification, identical to that found in the endogenous *S. pombe* protein. Nt acetylation has been shown to be essential for the function of various proteins (Starheim et al. 2012). During regular bacterial protein expression, Nt acetyl groups cannot be added as cells lack the proteins required for this post-translational modification. Within the lab, a method has been developed to acetylate proteins within the bacterial cell, by expressing the *S. pombe* NAT complexes in addition to the target protein. NatB co-expression - (Johnson et al. 2010) and NatA - unpublished.

Figure 3.14.A shows the N-terminal protein sequence of *S. pombe* Cam1 with human and *Drosophila* homologues. As discussed in section 1.17 (Figure 1.34) it is predicted that an acetyl group is added to the N-terminus of Cam1 by the NatA acetylation machinery within the cell. To explore the impact of N-terminal acetylation on the function of Cam1, the structure and binding characteristics of acetylated and unacetylated Cam1 were compared *in vitro*. Unacetylated Cam1 was produced from standard *E. coli BL21DE3.* Acetylated Cam1 was recombinantly expressed in *E. coli BL21* cells co-expressing the both NatA subunits – Naa10 and Naa15. (Section 2.1.4).

Figure 3.14.B shows the co-induction of Cam1 along with the NatA regulatory subunit Naa15 and the catalytic subunit Naa10. Addition of the acetyl group to the Cam1 protein was confirmed by mass spectrometry. The trace in Figure 3.14.C shows the mass spectrometry peak of unacetylated Cam1 at 16774.5 Da. This corresponds to the predicted molecular weight of Cam1 following cleavage of the first methionine residue. The peak in Figure 3.14.D shows a peak of purified Cam1-ACE. The molecular weight of 16816.5 Da corresponds to Cam1 protein without the first methionine, with an additional 42 Da of an acetyl group. The absence of an unacetylated Cam1 peak, confirms a 100 % purification yield of fully Nt-acetylated Cam1 protein.

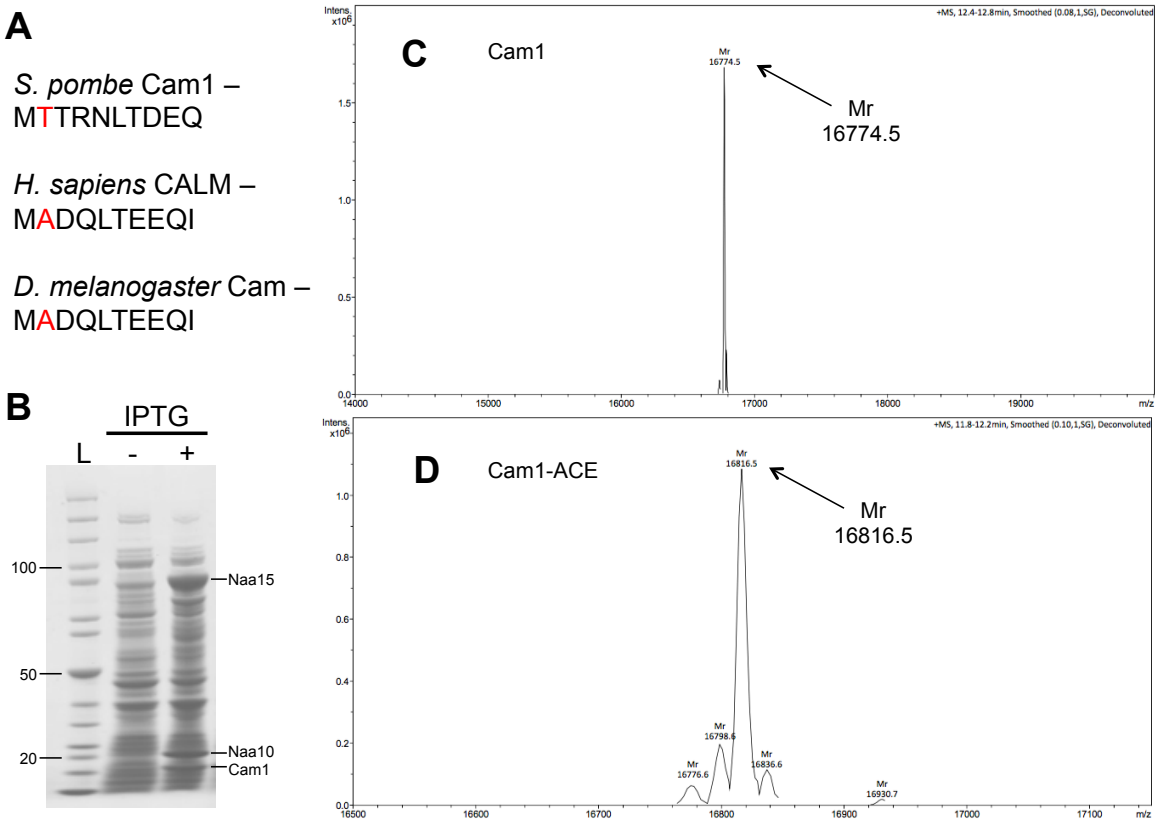

Figure 3.14. Expression of acetylated Cam1.

(A) The N-terminal amino acid sequence of *S. pombe*, *H. sapiens* and *D. melanogaster* calmodulins. The second amino acid residue predicts that all are acetylated via the NatA complex. (B) Pre and post induction samples of Cam1 co-expressed with the NatA complexes Naa10 and Naa15. Molecular weight markers indicate protein size in kDa. The resulting purified protein was confirmed by mass spectrometry, the trace in (D) shows the yield of acetylated Cam1 compared to unacetylated (C).

Firstly the protein structure of the two forms of Cam1 were compared using circular dichroism (CD). The far UV CD spectrum for each Cam1 protein was collected to determine if acetylation of the N-terminus influences the overall protein structure. Figure 3.15.A shows the overlaid CD spectra of equivalent amounts of acetylated and unacetylated Cam1 (by Bradford assay) in the absence of calcium (4 mM EGTA). The spectra of both unacetylated Cam1 (red line) and Cam1-ACE

(black line) shows negative peaks at 208 nm and 222 nm. The 222/208 nm ratio from both CD spectra is <1, indicating that both proteins are formed primarily of α-helicies, (rather than a continuous coiled coil structure). (Lau et al. 1984; Greenfield 2006) This is consistent with published structures of vertebrate calmodulin proteins (Houdusse et al. 2006). However, Nt-acetylation causes a significant shift in the CD spectra of Cam1, with deeper negative peaks, particularly at 208 nm. This change in the 222/208 nm ratio suggests that acetylation of the N-terminus of Cam1 alters the alters the overall structure of Cam1 (Kelly et al. 2005), possibly by stabilizing the N-terminal α-helix region, as seen in other examples of Nt-acetylation (Bartels et al. 2014).

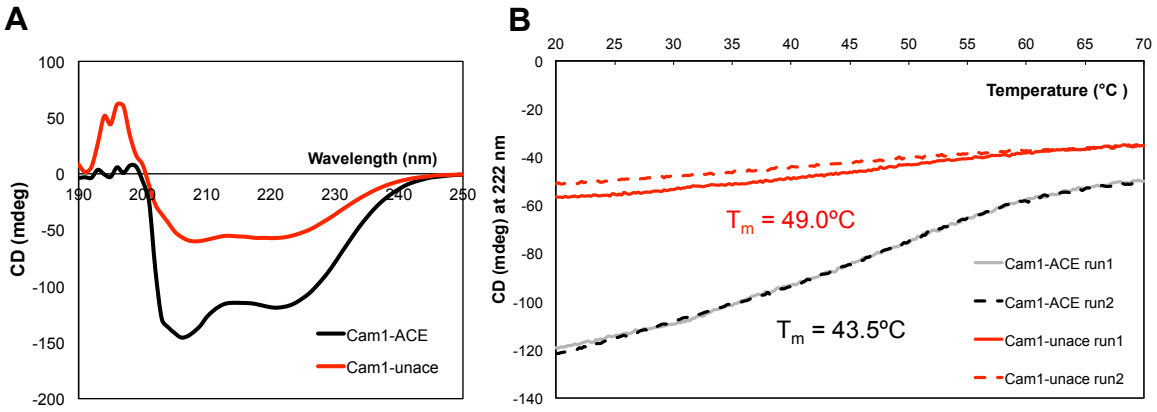

Figure 3.15. CD spectra of acetylated and unacetylated Cam1.

(A) CD spectra of equivalent concentrations of Cam1 (red line) and Cam1-ACE (black line). (B) Melting curves for Cam1 and Cam1-ACE following CD signal at 222 nm as the temperature was increased from 20 °C and 70 °C at a rate of 1 °C/min. Solid lines show the first melt, before the sample was cooled to 20 °C and repeated (dashed lines). Midpoint melting temperatures (T_m) are shown for Cam1 and Cam1-ACE.

Having determined that the overall structure of the protein is altered by N-terminal acetylation, next the stability of the protein was investigated. Two melting curves of Cam1 were made between 20 °C and 70 °C following the 222 nm α-helical

negative peak. Between measurements the temperature of the sample was reduced to 20 °C to allow the protein to refold.

Calmodulin is a thermodynamically stable protein (Masino et al. 2000), and the melting curves (Figure 3.15.B) indicate that neither form of Cam1 is completely unfolded at 70 ºC. The mid point melting temperatures were calculated for Cam1 unfolding between 20 ºC and 70 ºC. For unacetylated Cam1 protein, the mid point melting temperature is 49.0 ºC, compared to a lower temperature of 43.5 ºC for acetylated Cam1-ACE (Figure 3.15.B). This indicates that Nt-acetylation confers a significant difference in the sensitivity of Cam1 to changes in temperature.

Figure 3.15.B shows that the two melting curves of acetylated Cam1 were almost identical (grey line and black dashed line), showing that all acetylated Cam1 refolds completely and maintains its stability. By contrast, not all unacetylated Cam1 is refolded at the start of the second melting curve (red dashed line), shown by a significant reduction in the amount of structured α-helix. These data suggest that although unfolding of acetylated Cam1 is more sensitive to lower temperatures, is it resistant to irreversible unfolding at higher temperature. N-terminal acetylation is therefore important for the structure and stability of Cam1.

Next, modified Cam1-T7C protein was expressed in an acetylated and unacetylated form, purified, and labelled with IAANS (as described in Section 2.3.6). It is possible that any changes in the structure or binding properties caused by acetylation of Cam1, could by detected as changes in this environmentally sensitive fluorescent molecule at the N-terminus of the protein. A pCa curve was plotted from the IAANS fluorescence of both acetylated and unacetylated versions of the protein, across a range of calcium conditions (Figure 3.16.A). From the sigmoidal line of best fit (Hill equation section 2.3.6), the pCa_{50} value of Cam1-IAANS fluorescence for each protein can be determined. For acetylated Cam1-IAANS protein, the calculated pCa_{50} value of 6.54 is significantly higher than for the unacetylated form – 6.03. This change in pCa_{50} value determined from Cam1-IAANS fluorescence, indicates that the change in Cam1 conformation induced by binding of calcium, occurs at lower calcium concentrations when Cam1 is

acetylated. This may indicate that N-terminal acetylation affects the sensitivity of Cam1 calcium binding.

Next, it was determined if the change in calcium sensitivity caused by N-terminal acetylation, resulted in any changes in the calcium-dependent interaction with Myo1. Un-labelled Cam1 and Cam1-ACE proteins were added to the Myo1IQ12 FRET protein (at half saturating concentrations – determined from K_d values in Figure 3.17. Cam1 – K_d = 2.5 μM, Cam1-ACE – K_d = 0.80 μM) over the same range of pCa values. Figure 3.16.B shows the change in Ypet fluorescence induced by binding of Cam1 to the Myo1 IQ domains in each calcium condition. (Ypet fluorescence was used as changes in Cypet fluorescence were too small in these experiments). However, N-terminal acetylation of Cam1 does not change the calculated pCa_{50} value for binding to Myo1 IQ domains, pCa_{50} 5.87 for Cam1-ACE, and pCa_{50} 5.76 for unacetylated Cam1. These data indicate that, although N-terminal acetylation changes Cam1 sensitivity to calcium, this does not impact on the interaction of Cam1 with Myo1 IQ domains.

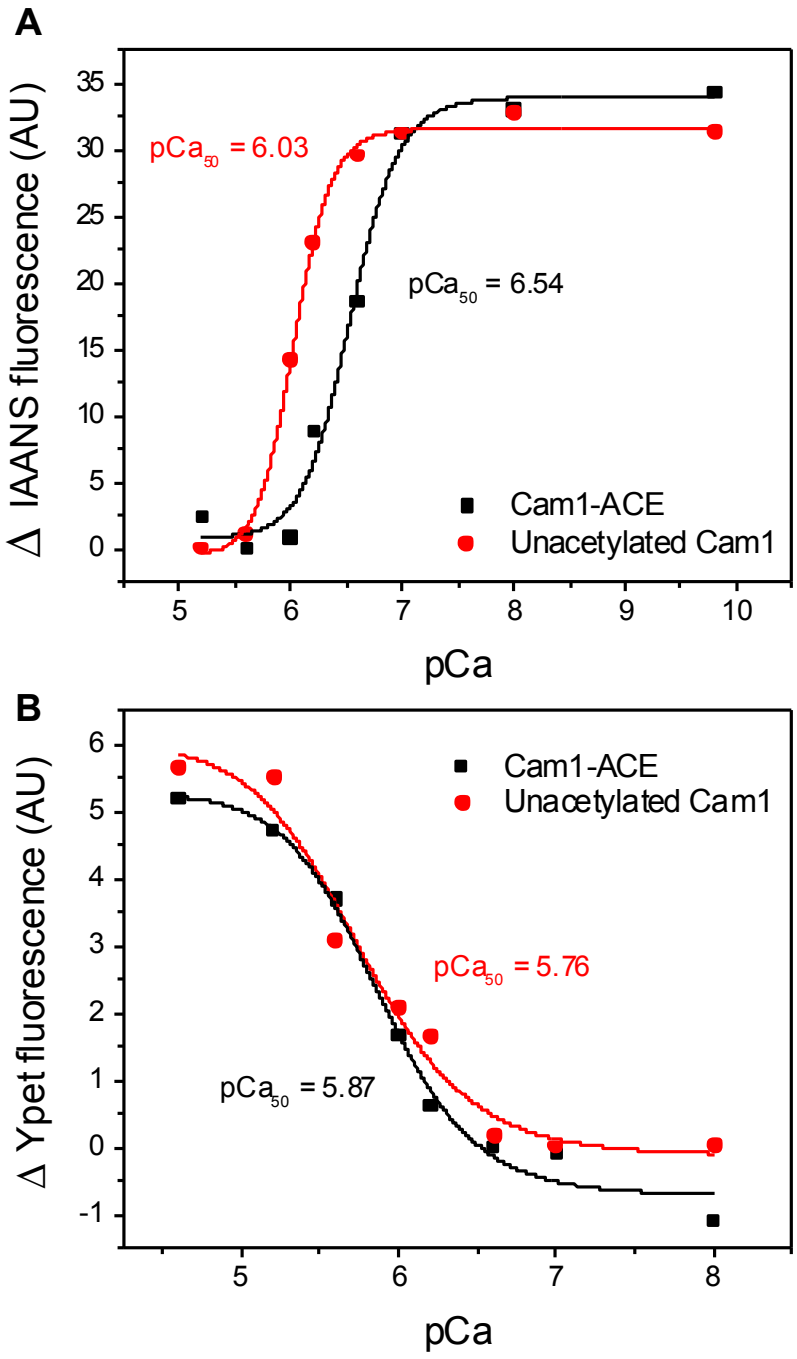

Figure 3.16. Effect of Nt-acetylation of Cam1 calcium sensitivity.

(A) pCa curves showing changes in IAANS fluorescence of Cam1-IAANS and Cam1-ACE-IAANS proteins. (B) Changes in Ypet fluorescence of 0.25 μM Myo1IQ12 FRET protein on binding of 1.25 μM Cam1 or 0.4 μM Cam1-ACE (half saturating concentrations) across a range of pCa conditions. 2 mM Ca-EGTA buffers used to give indicated pCa values. pCa_{50} values calculated from Origin fitting analysis - Hill equation.

3.12. N-terminal acetylation affects the affinity of Cam1 binding to Myo1 *in vitro*.

Cam1 has multiple roles in the cell and acetylation may not be required for each of these functions. To determine whether acetylation effects Cam1 binding to Myo1, the Myo1IQ12 FRET assay (described above), was used to compare the binding of acetylated and unacetylated Cam1. Both Cam1 and Cam1-ACE proteins were titrated into a solution of 0.5 μM Myo1-IQ12 FRET protein in the absence of calcium. Unacetylated Cam1 has more than 3 fold weaker affinity for the IQ domains of Myo1, with a K_d of 2.56 μM compared to 0.80 μM of acetylated Cam1 (Figure 3.17).

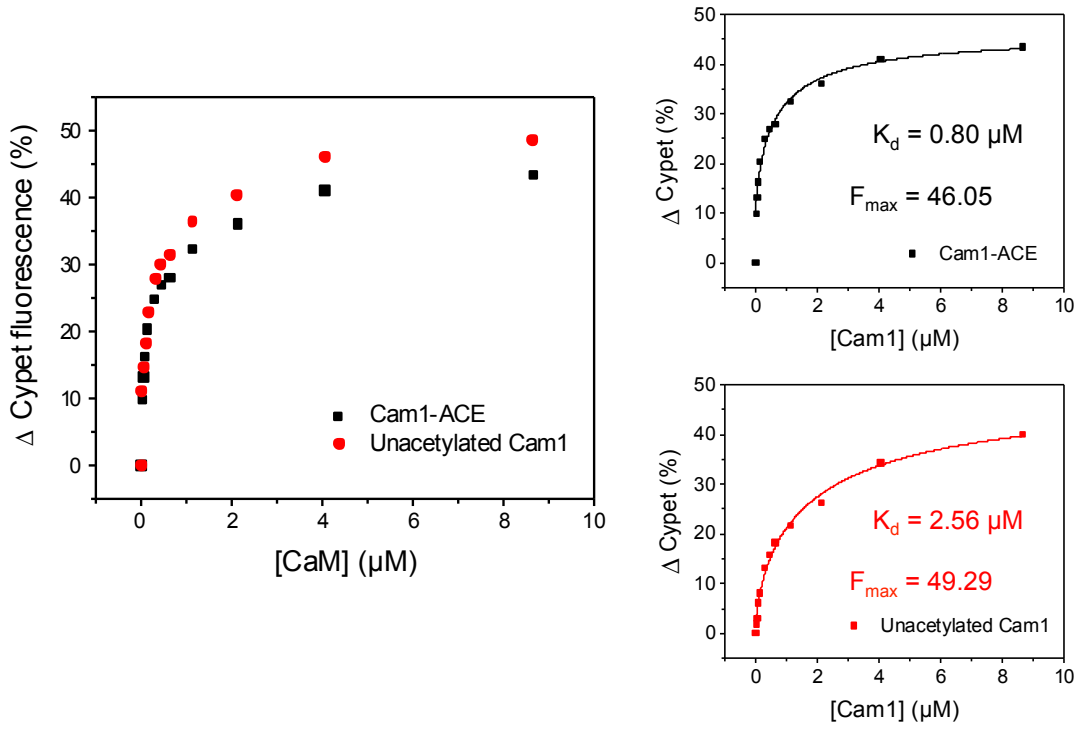

Figure 3.17. Binding of Cam1 and Cam1-ACE to Myo1IQ12 FRET protein. Graphs showing percentage changes in Cypet fluorescence throughout a titration of either Cam1 of Cam1-ACE into a 0.5 μM solution of Myo1IQ12 FRET protein. Individual graphs show each set of data fitted with a quadratic equation, giving the K_d value. Cam1-ACE titration data seen in (Figure 3.13).

3.13. N-terminal acetylation affects Cam1 localisation and dynamics *in vivo*.

To determine whether the reduced affinity between Cam1 and the IQ domains of Myo1 *in vitro* resulted in noticeable defects in the cell, *cam1-gfp* was crossed with a *naa15*Δ strain. A *naa15*Δ strain renders the NatA complex non-functional, meaning a subset of proteins including Cam1 lack their native post-translational modification.

Cam1-GFP fluorescence in a *naa15*Δ background was simultaneously compared using *cam1-gfp naa15*Δ cells in a mix with *naa15*$^{+}$ *cam1-gfp myo52-tdTomato* cells indicated with arrows in Figure 3.18.A. Total levels of Cam1 expression were unchanged in *naa15*Δ strain (Figure 3.18.F), indicating that despite changes in the Cam1 structure and stability *in vitro*, this does not appear to reduce the protein abundance within the cell under the growth conditions used. Cam1 protein still localises to endocytic patches in the absence of acetylation, from the biochemistry data, this would be expected as the unacetylated Cam1 still binds to Myo1 IQ domains despite having a weaker affinity than the acetylated form.

However looking closely at the size and distribution of Cam1 foci, there are subtle differences. Automatic foci detection using image analysis software indicates there are a greater number of smaller volume Cam1 foci in *naa15*Δ cells (Figure 3.18.D-E). When looking at the distribution of Cam1 within the cell, it appears that in a *naa15*Δ background, Cam1 does not have the strong polarized distribution seen in wild-type cells. Cam1 foci localise closely at the cell tips forming a horseshoe shaped cap, this clear localisation is not as strong in *cam1-gfp naa15*Δ cells. Due to the resolution of the image, many Cam1 foci at the tips of *naa15*$^{+}$ cells cannot be distinguished as individual foci by the analysis software. This results in larger volumes being detected which may account for 2-3 Cam1 foci in close in proximity. Figure 3.18.G shows the calculated average volume of foci in five regions of the cell. Regions 1 and 5 – the cell tips – in *naa15*$^{+}$ cells contain a significant number of larger volume foci. In *naa15*Δ cells these larger volumes are not detected at the cell ends indicating that the foci do not closely coalesce and are therefore detected as smaller individual foci.

Next the dynamics of Cam1-GFP were compared in *naa15*$^{+}$ and *naa15*Δ backgrounds. Timelapse images of *cam1-gfp naa15*$^{+}$ and *cam1-gfp naa15*Δ cells were used to generate kymographs at the cell surface to facilitate analysis of individual endocytic foci (Figure 3.18.C). As these kymographs do not include movements at the cell tips, the greater number of events counted in a *naa15*Δ strain reflects the less polarised localisation described above. Of the events measured, the duration of Cam1 association to endocytic patches was significantly longer in a *naa15*Δ background (13.2 +/-0.5 seconds) than in *naa15*$^{+}$ cells (9.9 +/-0.4 seconds)(Figure 3.18.B).

Whether this difference in localisation of Cam1 is due directly to the change in affinity for the IQ domains of Myo1, or whether the observed changes in Cam1 are due to changes in the localisation of Myo1 itself is unclear as Myo1 is also unacetylated in a *naa15*Δ strain.

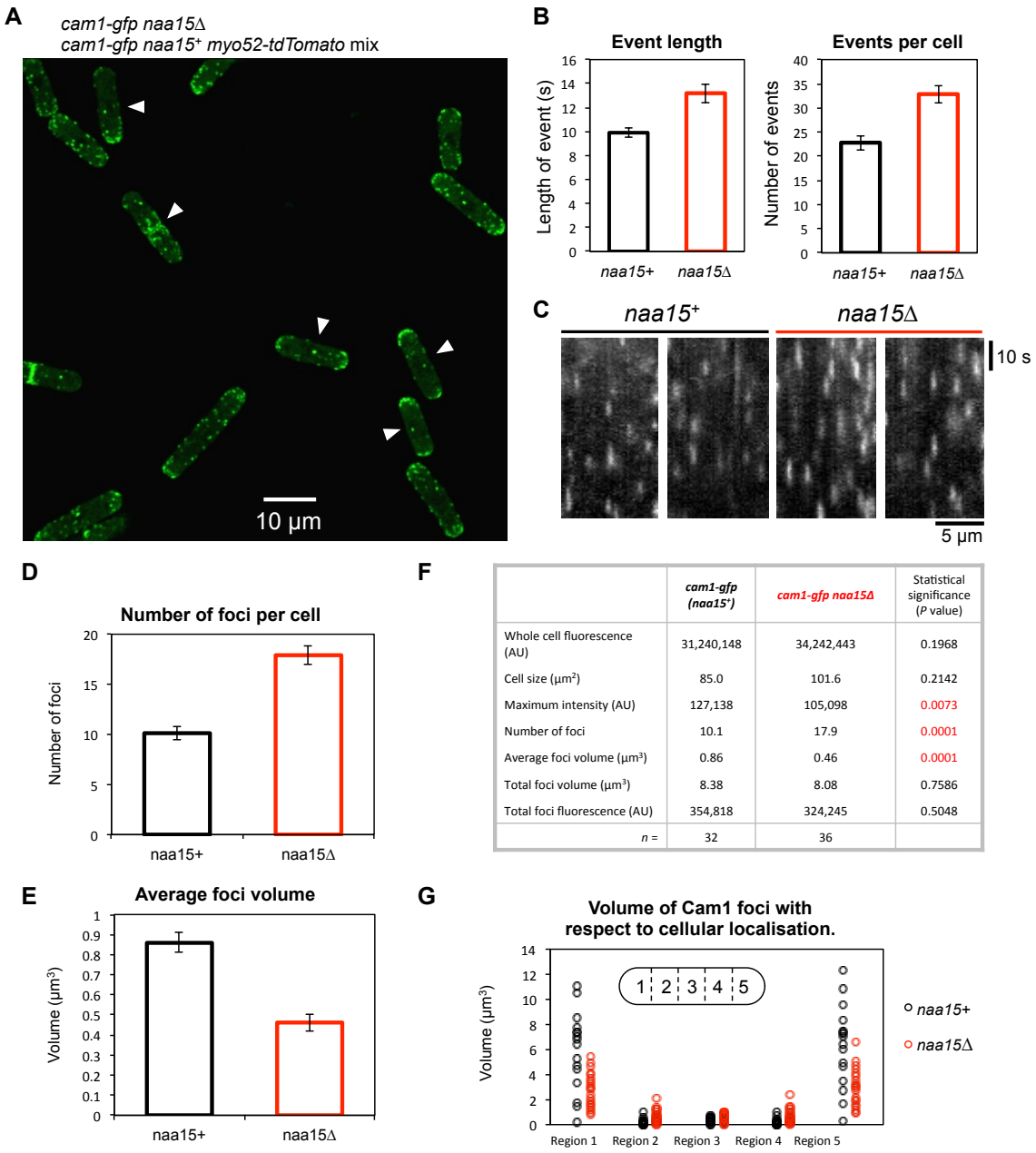

	cam1-gfp (naa15+)	*cam1-gfp naa15Δ*	Statistical significance (*P* value)
Whole cell fluorescence (AU)	31,240,148	34,242,443	0.1968
Cell size (µm²)	85.0	101.6	0.2142
Maximum intensity (AU)	127,138	105,098	0.0073
Number of foci	10.1	17.9	0.0001
Average foci volume (µm³)	0.86	0.46	0.0001
Total foci volume (µm³)	8.38	8.08	0.7586
Total foci fluorescence (AU)	354,818	324,245	0.5048
n =	32	36	

Figure 3.18. Analysis of Cam1-GFP fluorescence in *naa15*Δ cells.

(A) Maximum projection of 31 z-plane images of *cam1-gfp myo52-tdTomato* cells (indicated with arrows) and *cam1-gfp naa15*Δ cells. (B) Quantification of Cam1-GFP foci from 200 kymographs. Total events per cell were calculated over 60 s duration of the timelapse. (C) Typical kymographs generated at the cell surface, from single z-plane images of *cam1-gfp* and *cam1-gfp naa15*Δ cells. (D-F) Quantification of Cam1-GFP foci in *naa15*$^{+}$ and *naa15*Δ cells. (G) shows the total volume of Cam1-GFP foci detected, relative to the position within the cell (Region 1 & 5 – cell tips, Region 3 – cell equator) *n* = 30.

Summary:

Statement	Evidence
Cam1 associates with Myo52 *in vivo*.	Cam1-GFP co-localises with Myo52-mCherry and has the same dynamics as Myo52-GFP.
Cam1 associates with Myo1 *in vivo*.	Cam1-GFP has the same localisation and dynamics as mNeongreen-Myo1.
Cam1 binds to the IQ domains of Myo1 *in vitro*.	Cam1 protein binds Myo1IQ12-FRET protein.
Cam1 and Myo1 recruit to endocytic patches but are not internalised.	Myo1 and Cam1 co-localise with known endocytic patch markers, but remain at the membrane as the vesicle is internalised.
Cam1 recruitment to endocytic patches is dependent on Myo1.	No endocytic Cam1-GFP foci observed in *cam1-gfp myo1*Δ cells.
Cam1 only binds to the Myo1 IQ domains in the absence of calcium.	Cam1 only binds to Myo1IQ12 FRET protein in the presence of EGTA.
Nt-acetylation affects the structure of Cam1.	Altered CD spectra of Cam1-ACE and unacetylated Cam1 proteins.
Acetylated Cam1 is more thermo-sensitive.	Lower T_m of Cam1-ACE protein compared to unacetylated Cam1.
Nt-acetylation stabilises Cam1 protein.	Not all unacetylated Cam1 is able to re-fold after heating to 70ºC.
Nt-acetylation affects the calcium sensitivity of Cam1.	Lowered pCa_{50} value of unacetylated Cam1-IAANS protein.
Nt-acetylation does not affect the calcium dependency of Cam1 binding to Myo1.	No difference in Cam1 or Cam1-ACE binding to Myo1IQ12 FRET across a range of pCa's.
Nt-acetylation increases the affinity of Cam1 for Myo1 IQ domains.	Higher affinity of Cam1-ACE binding to the Myo1IQ12 FRET protein. (K_d = 0.80 µM compared to K_d = 2.56 µM for Cam1).
Unacetylated Cam1 does not accumulate at the cell tips	Larger volumes of detected Cam1-GFP foci not observed in *naa15*Δ cells.
In the absence of Nt-acetylation, Cam1 persists for longer at endocytic patches.	Longer lifetime of Cam1-GFP foci in *naa15*Δ (13.2 s) than in *naa15*$^+$ cells (9.9 s).

Data presented in this chapter provides evidence both *in vitro* and *in vivo*, that the *S. pombe* calmodulin light chain, Cam1 associates with the Class I myosin, Myo1, and class V myosin, Myo52. The Cam1 interaction with Myo1 occurs in a calcium dependent manner, via the IQ motifs of the neck region. The structure, stability and calcium sensitivity of Cam1 is influenced by acetylation at the N-terminus, which also affects its ability to bind Myo1. Both Myo1 and Cam1 localise to endocytic patches for similar lengths of time, where they remain at the membrane upon vesicle internalisation. This suggests that Cam1 functions to regulate Myo1 during the endocytic process.

Chapter 4: Effect of the second *S. pombe* calmodulin-like protein, Cam2, on *S. pombe* myosins.

Introduction:

Cam2 was first suggested to be a calmodulin-like protein and a potential myosin light chain due to its sequence similarity with the Myo2 light chain Cdc4 and localisation as patches at sites of cell growth (Lord & Pollard 2004). A protein sequence alignment between Cam1 and Cam2 in (Figure 1.32) shows that only 3 of the EF-hand domains are present in Cam2, with the calcium binding consensus sequence (Zhou et al. 2006) not completely conserved in all domains. There is no published evidence that Cam2 is able to bind calcium ions.

Transcription of the *cam2* gene is enhanced during meiosis (Mata et al. 2002), where Cam2 localisation to the forespore membrane is dependent on Myo1. Cam2 is required for sporulation at elevated temperatures (Itadani et al. 2006). However the role of the Cam2 protein during the mitotic growth cycle in fission yeast is not described. The most extensive study of Cam2 function to date (Sammons et al. 2011) reports that Cam2 is required for efficient Myo1 localisation to endocytic patches and Myo1-driven actin filament motility *in vitro*. In addition to this, Cam2 was shown to compete with Cdc4 for the binding of Pik1 – a type-IIIβ PI-4 kinase.

This ability of Cam2 to bind proteins other than Myo1 suggests Cam2 may have multiple functions in the cell (Sammons et al. 2011). Type-IIIβ PI-4 kinases are known to play a role in the early formation of endocytic patches. Pik1 specifically has been shown to regulate secretion at the Golgi (Walch-Solimena & Novick 1999) and facilitate septation (Park et al. 2009). The ability of Cam2 to bind Pik1, and potentially other proteins besides Myo1, may indicate Cam2 function in coordinating the cytoskeleton at sites of endocytosis.

4.1. Cam2 associates with the IQ motifs of Myo1 independently of calcium but with a weaker affinity than Cam1.

Unlike Cam1, *S. pombe* Cam2, is not the substrate for any of the Nat complexes, and so does not exist in an acetylated form within yeast cells. Recombinant Cam2 protein was therefore expressed in regular *E. coli BL21* cells, and purified as described in materials and methods (Section 2.2.2). Purified protein was analysed by mass spectrometry and can be seen on the SDS-PAGE gel in Figure 3.8. To determine if Cam2 binds directly to the Myo1 IQ domains in the same manner as Cam1, the Myo1IQ12 FRET assay was used, as described previously. Although Cam2 has been shown to co-localise with Myo1 *in vivo*, and disruption of the Myo1IQ2 domain eliminates this Cam2-Myo1 association (Sammons et al. 2011) direct interactions of these molecules have not been studied.

Titrations of Cam2 with the Myo1IQ12 FRET protein were made using the same method used to examine Cam1 binding. Figure 4.1.A shows the emission spectra after addition of excess Cam2 to the Myo1IQ12 FRET protein in both the presence and absence of calcium. In contrast to Cam1 (red lines), which only binds in the absence of calcium, Cam2 (blue lines) causes a reduction in FRET signal under both calcium and EGTA conditions. Titrations of Cam2 show that the affinity of Cam2 binding to Myo1 is the same in the presence and absence of calcium. These data confirm that Cam2 binds directly to the Myo1 IQ domains, but in contrast to Cam1, this binding is in a calcium independent manner.

This result is perhaps unsurprising as Cam2 has only a 49% sequence identity to Cam1, with essential calcium binding residues of the EF-hands absent (Figure 1.32). Stopped flow experiments were carried out to determine the calcium binding ability of Cam1 and Cam2 using Quin-2. Quin-2 is a dye with a strong calcium affinity, with calcium binding resulting in an increase in the emission peak at 495 nm (Tatsumi et al. 1997). When calcium-bound CaM is rapidly mixed with Quin-2, the rate of calcium dissociation from CaM can be determined by the increase in Quin-2 fluorescence. Figure 4.1.B. shows normalised calcium dissociation curves when a solution of 4 μM Cam1 (black line) or Cam2 (red line) plus 50 μM $CaCl_2$ is rapidly mixed with 150 μM Quin-2. These data show that Cam1 has the ability to

bind calcium ions, which subsequently dissociate when mixed with Quin-2. However Cam2 shows no observed calcium off rate, suggesting Cam2 does not have the ability to bind calcium *in vitro*. By calibrating the amplitudes of Quin-2 fluorescence using known concentrations of calcium, the equivalent of 9.2 μM $CaCl_2$ was dissociated from 2 μM Cam1 consistent with calcium ions being released from all four Cam1 EF-hand motifs.

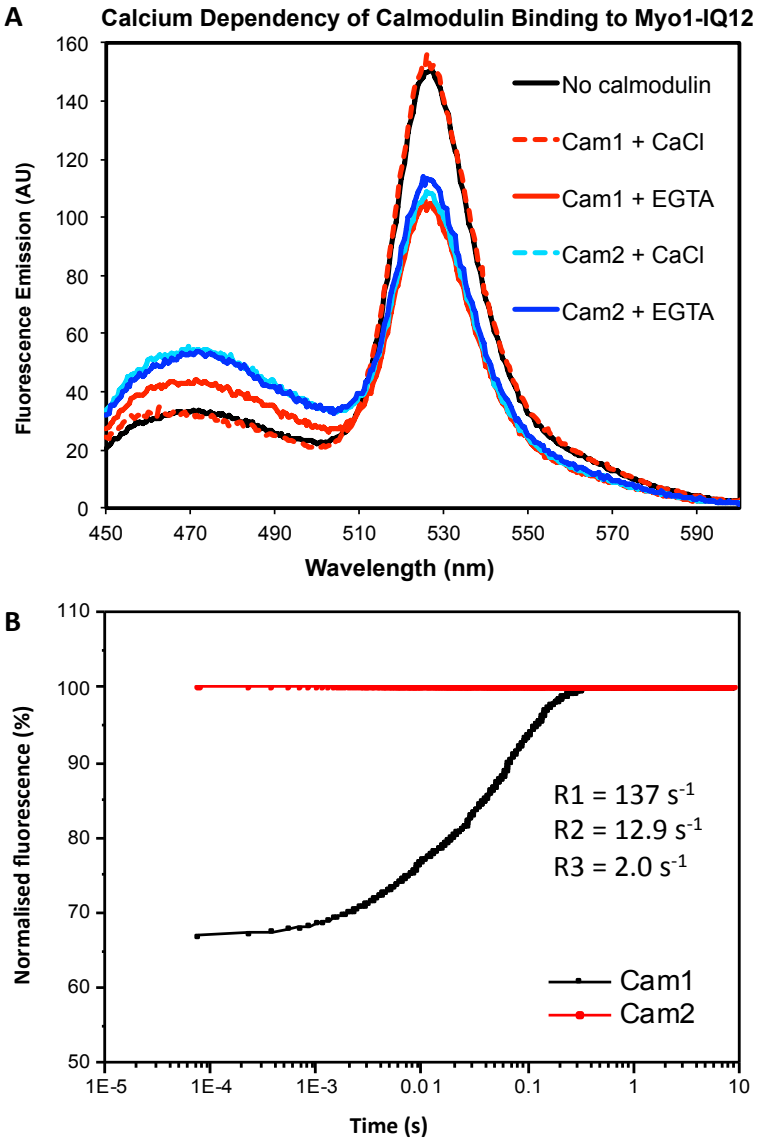

Figure 4.1.Calcium binding of Cam1 and Cam2 and effect on its interaction with Myo1 IQ domains.

(A) Cam1 (red) and Cam2 (blue) binding to the Myo1IQ12 FRET protein in the presence (dashed) and absence (solid) of calcium. (B) Quin-2 calcium dissociation experiments from Cam1 (black line) and Cam2 (red line).

Having determined that Cam2 binding to Myo1 IQ domains is calcium insensitive, all subsequent experiments were carried out using 4 mM EGTA buffer conditions, to allow direct comparison with Cam1 binding. Titrations of Cam2 were made into a solution of 0.5 μM Myo1IQ12. A comparison was made of the binding affinities of Cam1 and Cam2 for the Myo1 IQ domains (Figure 4.2). The calculated affinity for Cam2 is more than 1.5-fold weaker than that of Cam1, with a K_d value of 1.16 μM, compared to 0.80 μM for Cam1 binding to the Myo1IQ12 FRET protein.

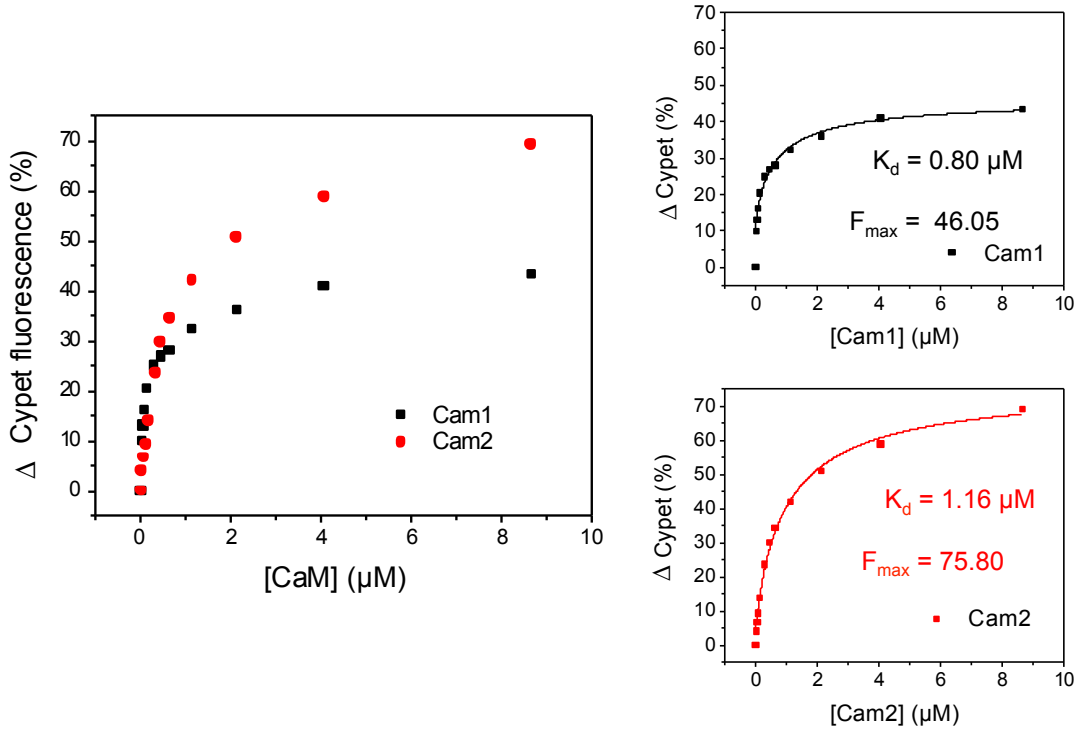

Figure 4.2. Titrations of Cam1 and Cam2 with Myo1IQ12 FRET protein.

Binding curves showing the percentage change in Cypet fluorescence as additional Cam1 or Cam2 is added. Each set of data was analysed using Origin software to fit a quadratic equation, individual graphs show the calculated K_d and F_{max} values. Averaged Cam1 titration data previously shown (Figure 3.13).

When Cam2 binds to the Myo1 IQ domains in the linker region of the FRET protein, it results in an expected reduction in Ypet fluorescence and a corresponding increase in Cypet fluorescence. However there is a greater overall

change in the Cypet fluorescence value as a result of binding Cam2 when compared to Cam1, (signal at 475 nm in Figure 4.1.A and Figure 4.2). This larger change in Cypet fluorescence level when binding Cam2 is despite equivalent Ypet fluorescence values in both spectra. This difference in the FRET ratios may indicate that Cam2 is binding to a different region of the IQ domains or resulting in the IQ domains taking on a different conformation when either Cam1 or Cam2 is bound.

4.2. Cam1 has a stronger affinity than Cam2 for the single IQ1 domain.

Each IQ domain has the ability to bind a calmodulin light chain, therefore one hypothesis is that Cam1 and Cam2 bind exclusively or at least preferentially to the different IQ domains of Myo1. Sammons et al (2011) showed that Cam2 co-localised with Myo1 in a *myo1-IQ1* mutant strain but not in a *myo1-IQ2* mutant strain, suggesting that the second IQ domain is the binding site for Cam2. To examine this *in vitro*, and explore whether IQ1 was the preferred binding site for Cam1, FRET proteins containing either an IQ1 or IQ2 linker region alone were used. Both linker regions produce a functional FRET protein, each with a similar emission spectrum. An overlay of the spectra from equivalent concentrations of Myo1IQ1 and Myo1IQ2 FRET proteins (Figure 4.3.A) indicates the two IQ domains have a similar conformational flexibility. Cam1 and Cam2 titrations were made with these proteins to determine the affinity of each calmodulin for both of the single IQ domains.

Figure 4.3. shows the result of titrations of Cam1 and Cam2 into a 0.5 μM solution of Myo1IQ1 (B) and Myo1IQ2 (C) FRET proteins. For the first IQ domain, IQ1, binding of Cam1 and Cam2 resulted in changes in FRET signal. Figure 4.3.D. shows that Cam1 again has a higher affinity than Cam2, but both bound more tightly to IQ1 than the longer IQ12 region. The K_d of Cam1 binding to IQ1 was 0.06 μM, over 13-fold tighter binding than to the IQ12 region (K_d = 0.8 μM). For Cam2, there was a 3-fold increase in affinity, from a K_d of 1.16 μM for the IQ12 region, compared to 0.39 μM for IQ1 alone.

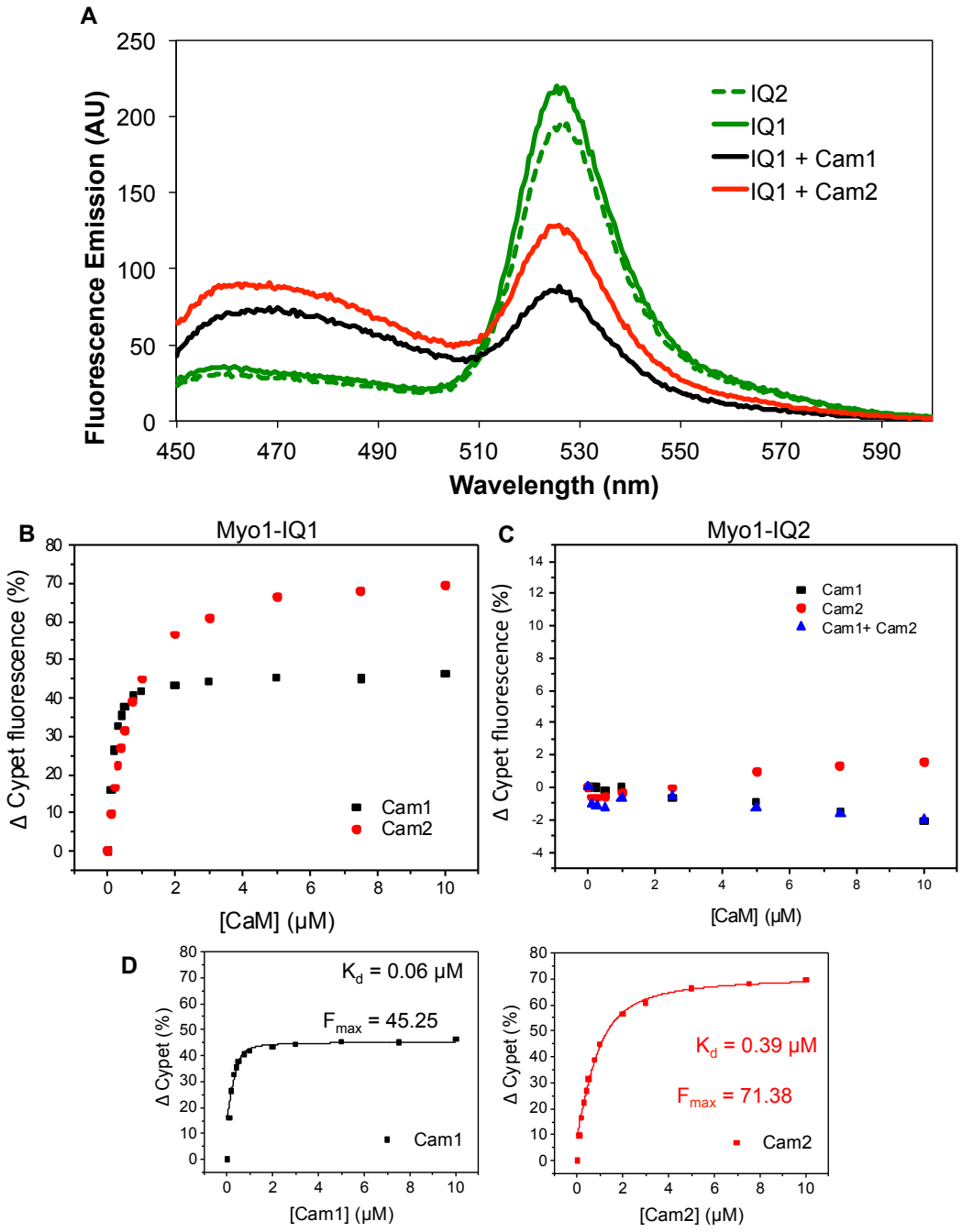

Figure 4.3. CaM binding to single Myo1 IQ FRET proteins.

(A) An overlay of the emission spectra of 0.5 μM Myo1IQ1 (green) and Myo1IQ2 (green dashed) FRET proteins. Also shown are the spectra of Myo1IQ1 FRET protein after addition of 10μM Cam1 (black) and Cam2 (red). Titrations of Cam1 (black) and Cam2 (red) with the Myo1IQ1 protein (B) and Myo1IQ2 (C). Individual Cam1 and Cam2 binding curves for the Myo1IQ1 FRET protein are shown in (D) with the calculated K_d and F_{max} values.

However for the second IQ domain, IQ2, no change of FRET signal was detected after the addition of either Cam1 or Cam2, or a mixture of both proteins (Figure 4.3.C). This indicates several possibilities; Cam1 and Cam2 may not bind to the IQ2 region, the IQ2 sequence used in the linker region may not contain the complete region of protein necessary for calmodulin binding or to take on its native conformation. Alternatively, in order for a calmodulin to bind to the second IQ domain, it requires the binding of a calmodulin to the IQ1 to facilitate the second binding event.

4.3. Cam1 binding to the Myo1 IQ domains is bi-phasic.

Using a Scatchard plot (Section 2.3.6) to linearise the data from saturated FRET binding experiments it was possible to determine if the binding events are a single phase, or bi-phasic. For each set of data, the saturation was calculated as a fraction of the F_{max} value (determined by Origin quadratic equation fitting). These fractional saturation (θ) values were plotted as a function of (θ / [ligand]), where [ligand] was total [CaM]. A straight line plot indicates a single binding phase.

Scatchard plots were made from data of Cam1 and Cam2 binding to the two IQ domains of the Myo1IQ12 FRET protein (Figure 4.2), and to the single Myo1IQ1 FRET protein (Figure 4.3). These plots (Figure 4.4) show that binding of both Cam1 and Cam2 to the Myo1IQ1 FRET protein is a single phase (Figure 4.4.C-D), as expected for a single CaM binding site. Cam2 binding to the Myo1IQ12 protein also appears to fit a single phase (Figure 4.4.B), possibly indicating that Cam2 is only able to bind one of the Myo1 IQ domains. However, the Scatchard plot of Cam1 binding to the Myo1IQ12 FRET protein is not a single phase binding event (Figure 4.4.A). A bi-phasic binding event would be consistent with Cam1 binding to both Myo1 IQ domains.

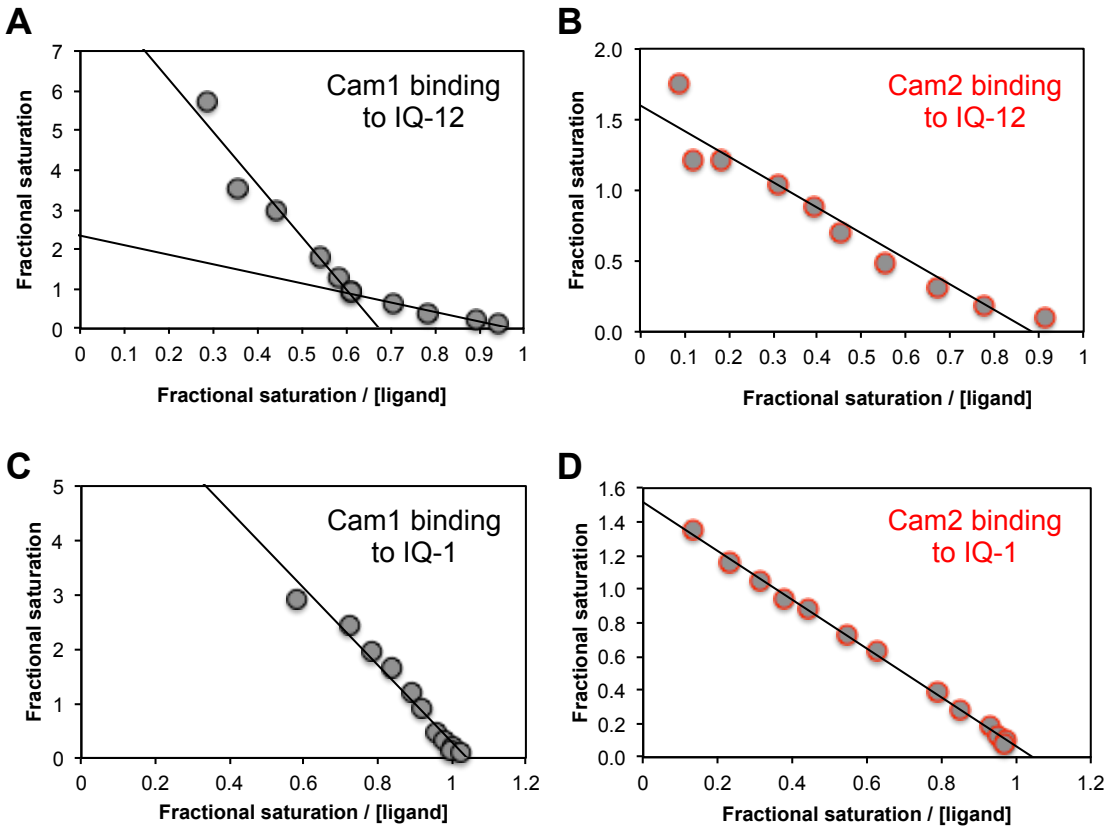

Figure 4.4. Scatchard plots of CaM binding to Myo1 IQ FRET proteins.

Scatchard plots of Cam1 (A) and Cam2 (B) binding to the Myo1IQ12 FRET protein, and Cam1 (C) and Cam2 (D) binding to the single IQ1 domain in the Myo1IQ1 FRET protein.

4.4. Cam1 enhances the binding of Cam2 to Myo1IQ12 FRET protein, while Cam2 inhibits Cam1 binding.

In order to investigate any potential co-ordination of calmodulin binding to the IQ domains, the Myo1IQ12 FRET protein was used to observe the effect that each calmodulin has on binding of the other. These experiments were limited due to only being able to pre-load small amounts of one calmodulin to prevent all potential for FRET being abolished before titrations of the second calmodulin could be observed. Therefore to investigate how Cam1 affects the binding of Cam2, a half saturating concentration of Cam1 (1 μM) was pre-loaded to 0.5 μM Myo1IQ12 FRET protein before titrations of Cam2 were made.

The presence of 1 μM Cam1 increases the affinity of Cam2 binding to the Myo1IQ12 FRET protein (Figure 4.5). A K_d value of 0.33 μM was observed for Cam2 binding in the presence of Cam1, compared to 1.16 μM for binding of Cam2 alone. This 3.5-fold tighter affinity of Cam2 binding, indicates that Cam1 enhances the binding of Cam2 to the Myo1 IQ domains.

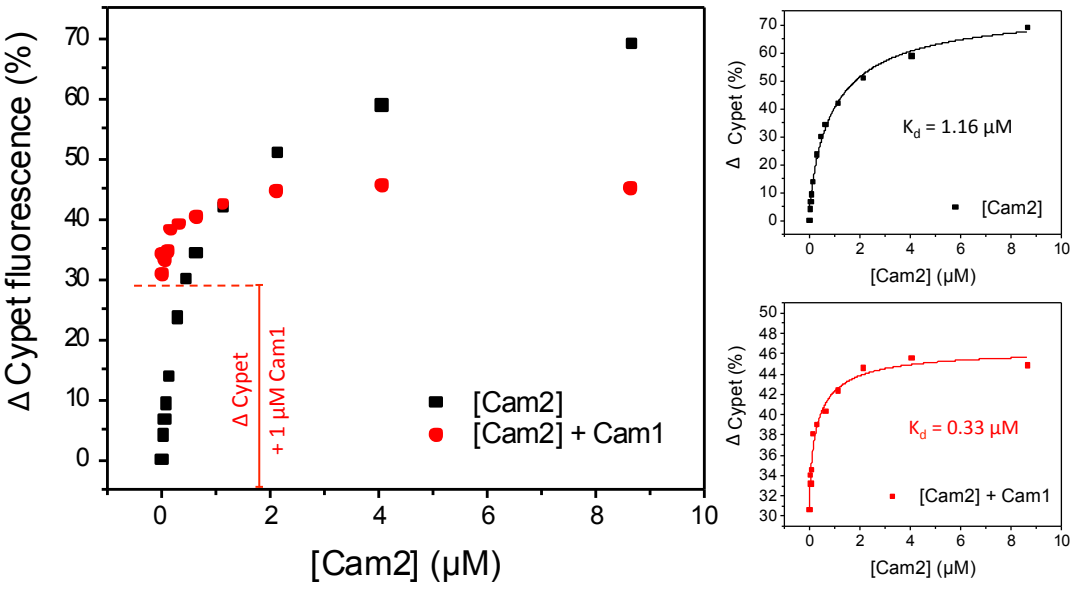

Figure 4.5. Effect of Cam1 on Cam2 binding to Myo1IQ12 FRET protein.

Black symbols show the change in Cypet fluorescence as Cam2 it titrated into a 0.5 μM solution of the Myo1IQ12 FRET protein. Red symbols show the change in Cypet fluorescence on addition of increasing amounts of Cam2 after 1 μM of Cam1 is initially bound to the Myo1IQ12 FRET protein. Individual binding curves are shown with the calculated K_d values.

To investigate the reverse relationship, and determine whether Cam2 affects the binding of Cam1, 0.5 μM Myo1IQ12 FRET protein was pre-loaded with 0.2 μM Cam2, before titrations of Cam1 were made into this mixture. Due to the larger fluorescence changes induced by the binding of Cam2 compared to Cam1, it was not possible to pre-load the Myo1 IQ domains with an excess of Cam2 protein. However, addition of a half saturating concentration of Cam2 (0.2 μM) appears to

have the opposite effect on the binding of Cam1. The affinity of Cam1 alone binding to Myo1IQ12 is 0.80 μM, however in the presence of 0.2 μM Cam2, the affinity is 2.5 fold weaker, with a K_d of 1.98 μM (Figure 4.6). The increased K_d value of Cam1 binding to the Myo1 IQ domains in the presence of Cam2, indicates that Cam2 negatively effects the binding of Cam1.

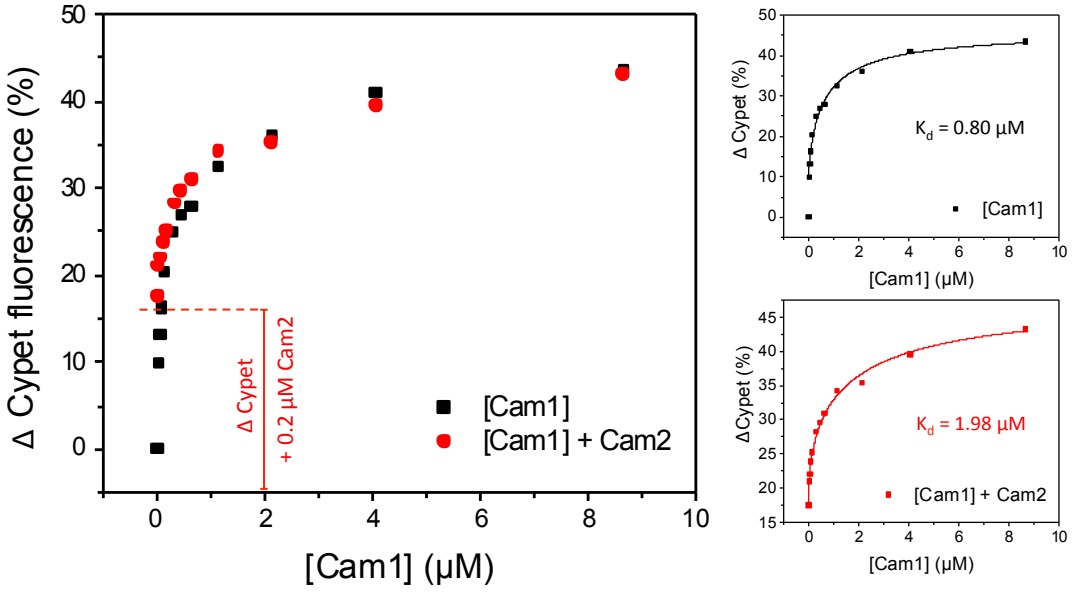

Figure 4.6. Effect of Cam2 on Cam1 binding to Myo1IQ12 FRET protein. Black symbols show the change in Cypet fluorescence as Cam1 it titrated into a 0.5 μM solution of the Myo1IQ12 FRET protein. Red symbols show the change in Cypet fluorescence on addition of increasing amounts of Cam1 after 0.2 μM of Cam2 is initially bound to the Myo1IQ12 FRET protein. Individual binding curves are shown with the calculated K_d values.

4.5. Cam2 binds preferentially to a Cam1 Myo1 IQ complex.

In order to better study the possible cooperative binding of Cam1 and Cam2 to the Myo1 IQ domains, an IAANS labelled Cam1 protein was used to observe its binding to Myo1IQ domains in the presence and absence of Cam2. The initial approach was to recombinantly express the Myo1 IQ domains as a fusion with a stable alpha helix (SAH) domain to improve folding. However this was not

successful, with very low levels of expression and apparent toxicity to the bacterial cells, resulting in very low cell densities. Subsequently, expression of a longer region of the Myo1 protein, including IQ domains and the TH1 domain was successfully co-expressed with Cam1. Figure 4.7 shows induction of Myo1-IQ12-TH1 protein when co-expressed with Cam1 protein. However a suitable purification method had not yet been optomised to allow this protein to be used in these binding assays.

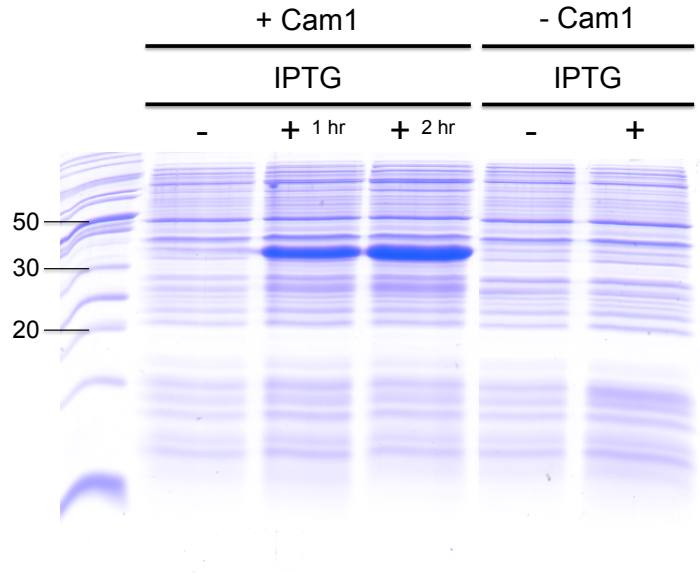

Figure 4.7. Co-expression of Myo1 constructs with Cam1.

SDS-PAGE gel of whole bacterial lysates from *BL21 E. coli* cells transformed with an expression vector containing DNA encoding Myo1IQ12-TH1 protein. The first lanes show samples before and after induction of expression with IPTG, in cells co-expressing Cam1. The lanes on the right are from cells without Cam1 co-expression. Bands of expressed Myo1IQ12-TH1 protein can be seen at 32 kDa.

As an alternative to recombinant expression of a Myo1 IQ construct, a peptide was synthesized of the 38 amino acid residues forming the complete IQ domain region of Myo1 (Figure 4.8). The circular dichroism spectra of the synthesized peptide shows a characteristic alpha helical negative peak at 208 nm. However there is not a clear negative 222 nm peak, indicating that the IQ peptide has alpha helical structure but is likely to be partially unstructured (Kelly et al. 2005). From CD measurements alone it is not possible to determine which residues of the peptide

are structured and which are not. Whilst being aware that the conformation of the peptide may not be in its native state, experiments were carried out to determine its ability to bind calmodulin. It is possible that in order to adopt a fully folded conformation, the IQ peptide requires binding of a calmodulin light chain.

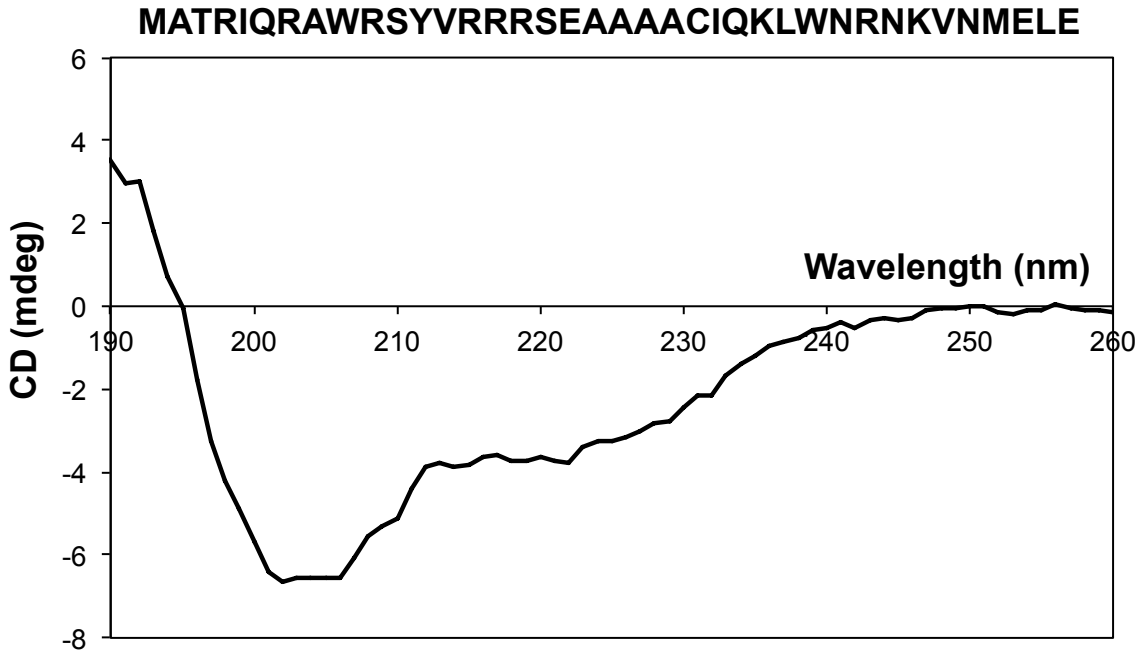

Figure 4.8. CD spectrum of synthesized Myo1-IQ12 peptide.

The CD spectrum of synthesized Myo1-IQ12 peptide, showing a negative peak at 208 nm. The sequence of the 38 amino acid residues is shown at the top of the graph.

The Myo1 IQ peptide was used for fluorimetry experiments with IAANS labelled Cam1 in the presence and absence of Cam2. Fluorescence of the IAANS molecule is dependent on its reaction with thiol groups located in hydrophobic sites. Therefore IAANS fluorescence is very sensitive to changes in the local environment caused by ligand binding or changes in protein conformation. (Hazard et al. 1998; Bhattacharyya & Horowitz 2000). This measurement of conformational change in Cam1 upon binding of Myo1 IQ domains provides a different measurement of protein interaction to that from FRET experiments, therefore K_d values were not comparable to those obtained from FRET data.

Two experiments were used to determine the effect Cam2 has on the binding of Cam1-IAANS to the Myo1 IQ peptide (Figure 4.9). The starting solution for the titrations in Figure 4.9.A was 1 μM Cam1-IAANS. Black symbols show the changes in IAANS fluorescence on addition of increasing amounts of a Myo1-IQ peptide titration solution. The red symbols indicate the changes in IAANS fluorescence on addition of an equimolar titration solution of Myo1-IQ peptide together with Cam2. Figure 4.9.A shows firstly that addition of increasing amounts of Myo1 IQ peptide bound to Cam1-IAANS, results in an increase in IAANS fluorescence (black symbols). Binding reaches saturation at around 10 μM IQ peptide, with 3 μM IQ peptide being required to reach ½ saturation.

When the titration solution contains both Myo1 IQ peptide and Cam2 protein, (red symbols), there is also an increase in Cam1-IAANS fluorescence indicating that the Myo1 IQ peptide does bind to Cam1 in the presence of Cam2. However there is a significant shift in the binding curve in the presence of Cam2, >5 μM IQ peptide is required to reach ½ saturation, compared to 3 μM in the absence of Cam2. The concentration of the IQ peptide limited the maximum concentration of the titration to 11 μM, at which complete saturation was not reached. However, this is well above the cellular concentrations of both Myo1 and Cam2.

This apparent lag phase in IQ peptide binding to Cam1 in the presence of Cam2 indicates that Cam2 inhibits Cam1 binding to the Myo1 IQ domains. This is consistent with the observations from the FRET binding assays, where the presence of Cam2 inhibits Cam1 binding (Figure 4.6). Changes in Cam1-IAANS fluorescence were not directly due to Cam2, which alone does not alter Cam1-IAANS fluorescence (Figure 4.9.B black symbols).

It is possible that the negative effect of Cam2 on Cam1 binding to the Myo1 IQ domains is due to competition for binding. To determine if this is the case, Cam2 protein was titrated into a starting solution of 0.5 μM Cam1-IAANS bound to a 10-fold excess of Myo1 IQ peptide. The resulting titration curve (red symbols in Figure 4.9.B) shows that on addition of Cam2, the Cam1-IAANS fluorescence falls, likely to indicate dissociation of Cam1-IAANS from the Myo1 IQ peptide. After addition of

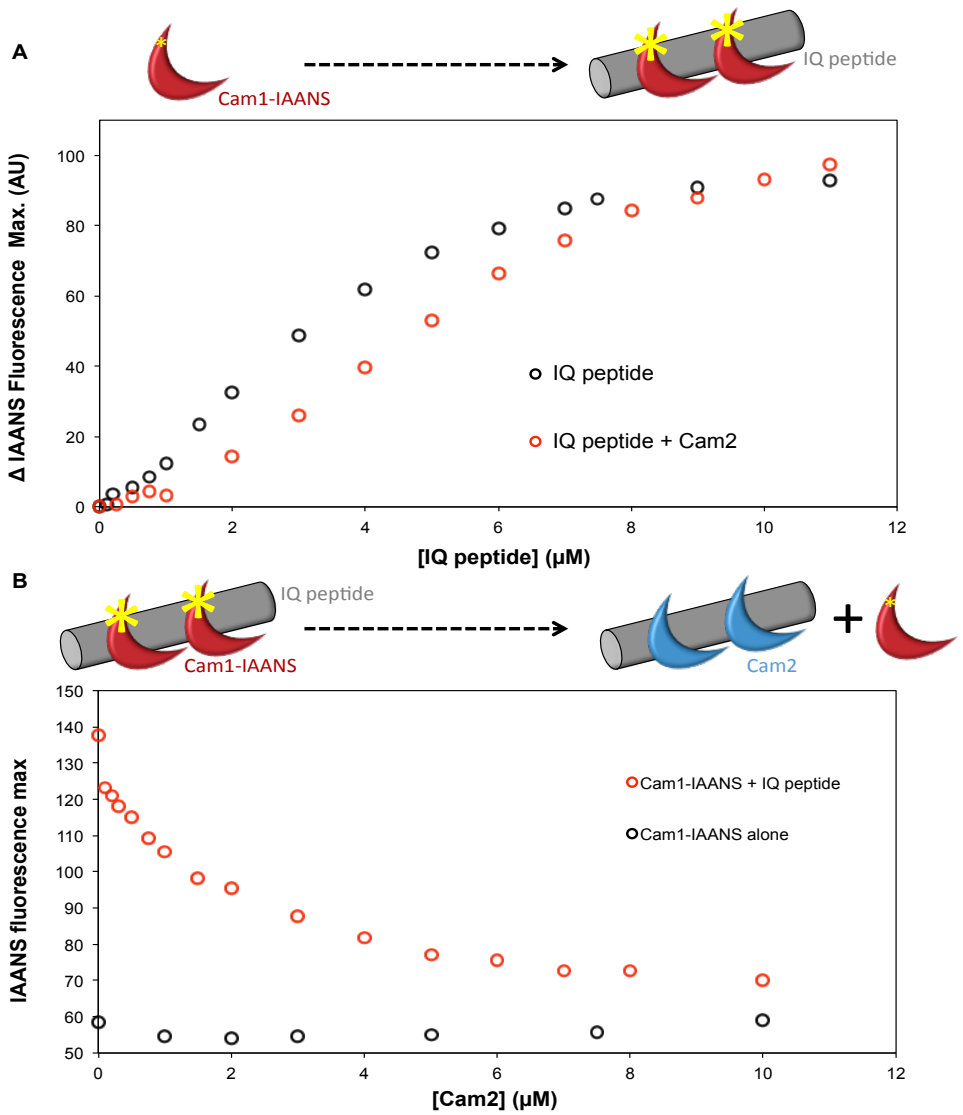

Figure 4.9. Effect of Cam2 on the binding of Myo1-IQ peptide to Cam1-IAANS.

(A) Change in IAANS fluorescence during a titration of either Myo1 IQ peptide (black circles) or a Myo1 IQ peptide + Cam2 mix (red circles) into a solution of 1 μM Cam1-IAANS. The schematic diagram indicates that as IQ peptide is added to Cam1-IAANS, the IAANS fluorescence increases. (B) Red circles show changes in IAANS fluorescence of a 0.5 μM Cam1-IAANS + 5 μM Myo1-IQ peptide solution on addition of Cam2. Black circles represent fluorescence of 0.5 μM Cam1-IAANS alone during addition of Cam2. The schematic diagram indicates the Cam1-IAANS – Myo1 IQ peptide complex at the start of the titration is dissociated as Cam2 is added, resulting in a reduced Cam1-IAANS fluorescence.

around 6 μM Cam2, there is no further reduction in the IAANS fluorescence. The concentration of Cam2 required to reach ½ saturation of this reaction is 1 μM.

The schematic diagram in Figure 4.9.B shows one possibility for the binding events that are occurring in this reaction. With Cam2 competing with the Cam1-IAANS for binding to the Myo1 IQ domains, resulting in Cam2 bound to the IQ peptide leaving free Cam1-IAANS at the end of the reaction. However, from the Myo1-IQ12 FRET binding data (Figure 4.3) Cam2 was shown to have a lower affinity for the Myo1 IQ domains compared to Cam1, making it unlikely that it could out-compete the pre-bound Cam1. In this reaction, there is a large amount of free IQ peptide available for Cam2 to bind on addition to the solution. Assuming that Cam2 has a lower affinity for the IQ peptide, as shown for the same IQ domains in the FRET protein, it would be predicted that Cam2 would first bind the freely available IQ peptide before displacing Cam1. If this were the case, there would be a long lag phase with no change in IAANS fluorescence as the un-labelled IQ peptide and Cam2 associate in the solution.

Consistent with Cam1 being shown to enhance the binding of Cam2 (Figure 4.5), these data suggest that Cam2 may bind preferentially to a Myo1-IQ12-Cam1 complex. In Figure 4.9.B, at saturation of Cam2 binding, Cam1-IAANS fluorescence is reduced to levels similar to those of an equivalent Cam1-IAANS solution containing no IQ peptide (black symbols). This is likely to indicate that binding of Cam2 results in displacement of Cam1 from the Myo1 IQ domain, leaving Cam1-IAANS free in solution. This does not eliminate the possibility that Cam1 remains bound in a Myo1IQ-Cam1-Cam2 ternary complex, also resulting in a decrease in IAANS fluorescence.

Following these observations that suggest Cam2 binds preferentially with a Myo1IQ-Cam1 complex, it was next explored whether this is due to a direct interaction with Cam1. Sections 4.5 and 4.6 summarise the experiments used to determine if Cam2 binds directly to Cam1.

4.6. Cam2 does not directly affect Cam1 conformation.

To address whether Cam1 and Cam2 interact directly with one another to influence binding to the IQ domains, several methods were used. Firstly, no change in Cam1-IAANS fluorescence was observed on addition of Cam2 to a 20-fold excess (black symbols in Figure 4.9.B). This excess concentration is higher than would be observed under cellular conditions, considering the 10 fold lower abundance of Cam2 in the cell. This data suggests there is no direct interaction between the two proteins, as binding of Cam2 to any region of Cam1 would be likely to result in conformational changes that would affect IAANS fluorescence, as seen for binding of the IQ peptide.

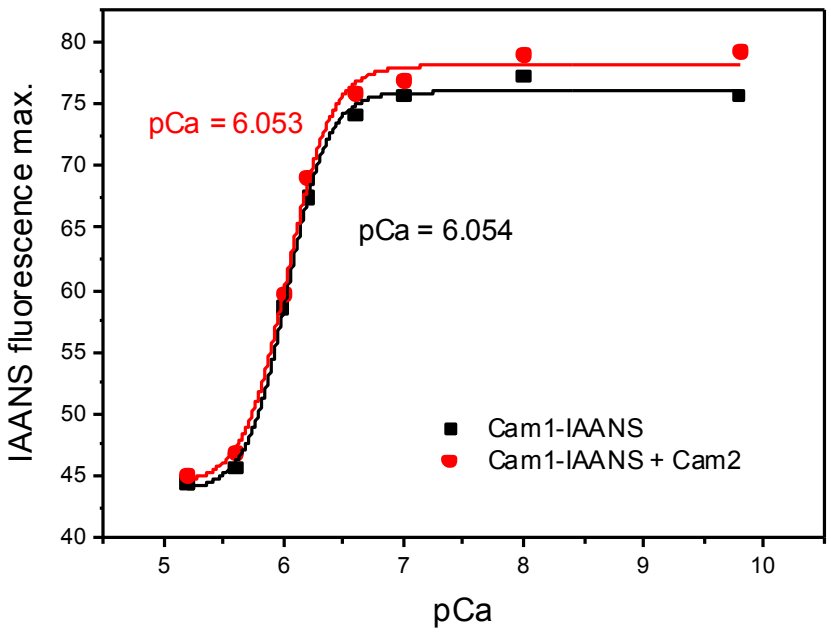

Figure 4.10. Cam1-IAANS pCa curve in the presence and absence of Cam2.

Maximum IAANS fluorescence values (440 nm) of 0.5 µM Cam1-IAANS at a range of pCa values. Black symbols show values of Cam1-IAANS, red symbols show values of Cam1-IAANS with 5 µM Cam2 protein. 2 mM Ca-EGTA buffers were used to give indicated pCa values. pCa_{50} values calculated from Origin fitting analysis - Hill equation.

To assess whether Cam2 has an impact in Cam1 calcium binding, a pCa curve was generated from Cam1-IAANS fluorescence, in the presence and absence of excess Cam2. There is no change in the pCa_{50} value of Cam1-IAANS fluorescence following addition of Cam2 (Figure 4.10). This highlights that addition of Cam2 under a wide range of calcium conditions does not induce a conformational change in Cam1-IAANS, and does not affect the calcium binding properties of Cam1.

4.7. Cam1 and Cam2 do not form a complex *in vitro*.

Gel filtration was used to confirm there was no direct interaction between Cam1 and Cam2. A total of 2 mg of purified Cam1 or Cam2 protein was loaded to a Superdex 75 (GE Healthcare Life Sciences) gel filtration column in Assay buffer (section 2.2.4) containing either EGTA or calcium. Assay buffer was flowed through the column at a rate of 1 ml/min and fractions collected. Figure 4.11.A shows overlaid OD_{280} spectra of the eluted fractions of Cam1 and Cam2, when loaded to the column individually. Due to the similar molecular weights of Cam1 (16,906 Da) and Cam2 (16,218 Da), both proteins elute from the column at similar elution volumes of 62 ml and 64 ml respectively.

The molecular weights marked in Figure 4.11 are determined from the elution volumes of standard proteins run on the same column, under the same buffer conditions. If a stable complex were formed between Cam1 and Cam2, a peak would be expected at a smaller elution volume of around 55 ml – equivalent to a 33 kDa protein complex. Purified Cam1 and Cam2 protein were then mixed prior to loading the gel filtration column. Figure 4.11.B shows the OD_{280} spectrum of the elution fractions when Cam1 and Cam2 are loaded together under the same conditions used in Figure 4.11.A.

There was no peak observed at a smaller elution volume in the presence of EGTA, (Figure 4.11.B), or in the presence of 50 μM calcium. The peak at an elution volume of 63 ml coincides with the molecular weights of monomeric Cam1 and Cam2. The total OD_{280} value of this peak corresponds to the combined total of the Cam1 and Cam2 OD_{280} fluorescence (Figure 4.11.A). The SDS-PAGE gel shows

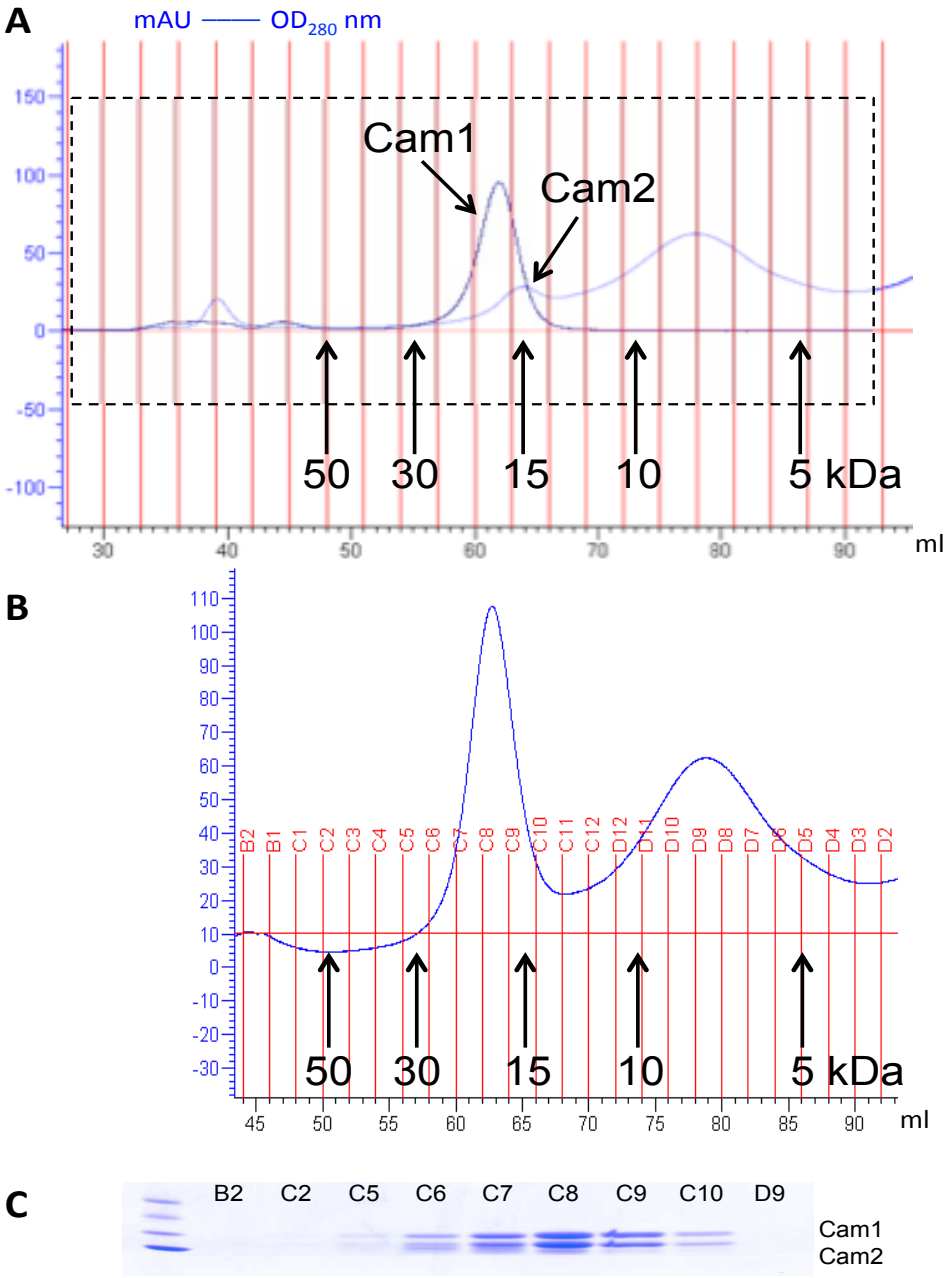

Figure 4.11. Gel filtration analysis of Cam1 and Cam2.

The overlaid OD_{280} spectra in (A) were recorded from the eluate of Cam1 and Cam2 loaded separately to a Superdex 75 gel filtration column, under identical 4 mM EGTA buffer conditions. Standard molecular weight markers were also eluted from the column under identical conditions to calibrate the elution volumes shown in all spectra. The presence of Cam1 and Cam2 in the indicated peaks was confirmed by SDS-PAGE. (B) shows the OD_{280} elution spectrum of a mix of Cam1 and Cam2. (C) shows coomassie stained SDS-PAGE samples from the corresponding fractions in (B).

samples from the eluted fractions indicated, and confirms this peak is a mixture of Cam1 and Cam2 (Figure 4.11.C). Data from these gel filtration experiments suggest that no stable complex is formed between Cam1 and Cam2 either in the presence or absence of calcium.

The Cam1 FRET protein described in Section 3.7. was used as a final method to confirm that there is no direct interaction between Cam1 and Cam2. Firstly the functionality of this FRET protein was determined by observing the FRET spectrum upon changes in calcium conditions and addition of a known binding partner – Myo1 IQ peptide. Despite relatively small changes in FRET, a pCa_{50} value of 6.10 was calculated from Cam1-FRET data comparable with pCa_{50} 6.05 obtained from IAANS labelled Cam1 data (Figure 4.10). Significant changes in the FRET spectra were observed on addition of Myo1 IQ peptide, with Cam2 again inhibiting the binding of Cam1 to the Myo1 IQ domains. All results consistent with data shown using other methods (Figures 4.5 and 4.8.A).

Having determined that Cam1 has sufficient conformational change to measure FRET signal, Cam2 was added to Cam1-FRET protein to determine any binding events. Figure 4.12 shows the emission spectra of 1 μM Cam1-FRET protein following addition of a 10-fold excess of Cam2, in 2 mM Ca-EGTA buffers providing a buffer of pCa 9.8 (A) and pCa 4.6 (B). There was no change in FRET on addition of Cam2 in either calcium condition. Together these data provide substantial evidence that there is no stable interaction between Cam1 and Cam2 *in vitro*.

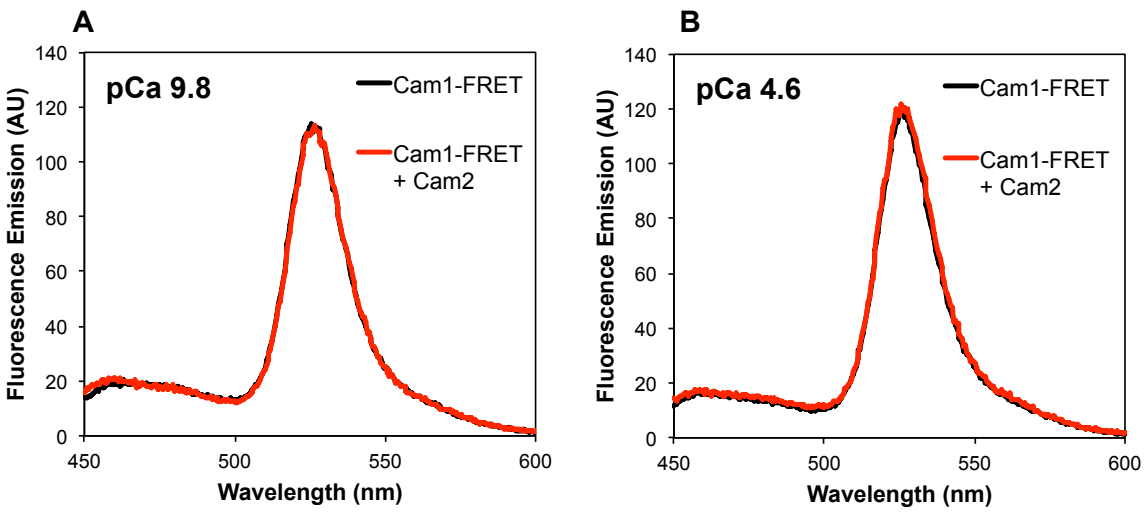

Figure 4.12. Cam1-FRET spectra after addition of Cam2.

Cam1-FRET emission spectra following excitation at 435 nm. Black lines show the spectrum of 1 μM Cam1-FRET alone, and red lines after the addition of 10 μM Cam2 protein. 2 mM Ca-EGTA buffers were used to provide low calcium conditions, pCa 9.8 (A) and a high calcium conditions, pCa 4.6 (B).

4.8. Cam2 localisation and dynamics *in vivo* are distinct from Cam1 and Myo1.

In order to determine the cellular localisation and dynamics of Cam2, a single tagged *cam2-gfp* strain was generated using GFP genomic PCR fusion described in materials and methods (2.4.7). Therefore Cam2 was expressed from its genomic locus with a C-terminal GFP fusion (Figure 4.13.A). As for all imaging experiments in this study, *cam2-gfp* cells were imaged after growth in EMMG at a mid-log density for 48 hours.

Comparison with Cam1-GFP and YFP-Myo1 fluorescence, (Figure 4.13.B and Figure 3.1), shows Cam2 has a distinct localisation. While both proteins generally localise to regions of cell growth – the growing cell tips and cell equator during division, there appear to be a greater number of distinct Cam2 foci when compared with Cam1. Although not analysed from a mix experiment and therefore not directly comparable, image analysis confirms this observation. There are on

average 13 discrete foci of Cam1 and Myo1 per cell, compared to 20 foci of Cam2. Cam2 foci do not have the strongly polarized localisation seen with Cam1 and Myo1, in which foci coalesce at sites of cell growth. However TIRF microscopy imaging of fluorescence at the cell surface (Figure 4.13.C-D), shows that Cam1 and Cam2 both associate closely with the cell membrane. However, at any one time there are more Cam1 foci associated with the membrane when compared to Cam2. This suggests that Cam2 association with the membrane is more transient than Cam1.

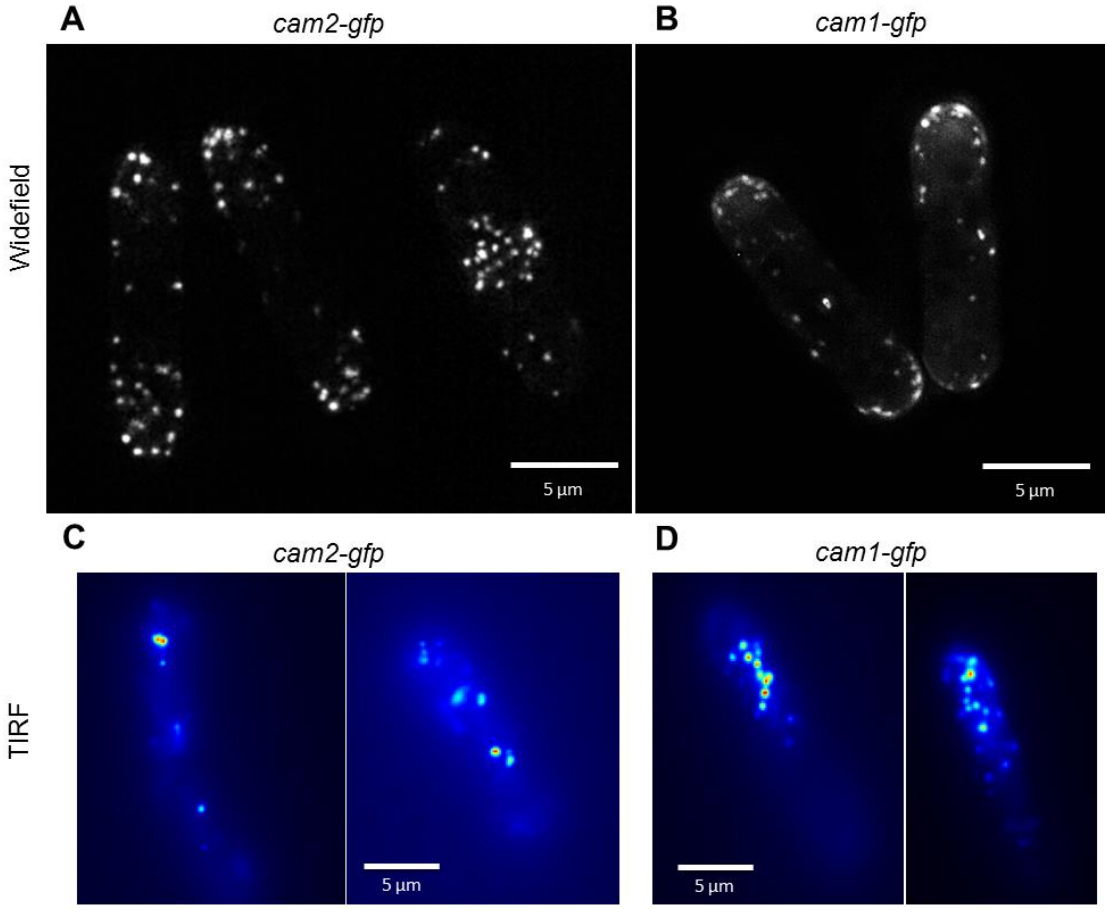

Figure 4.13. Cellular localisation of Cam2-GFP.

Maximum projections of 31 z-plane images of (A) *cam2-gfp* cells and (B) *cam1-gfp* cells for comparison. Images taken using TIRFM of (C) a *cam2-gfp* or (D) *cam1-gfp* cell.

Along with differences in the number and localisation of foci, the most striking difference between Cam1 and Cam2 is in their dynamics. While stationary foci of Cam1 and Myo1 appear and disappear at the membrane (Figure 3.2) Cam2 has different dynamics, showing significant lateral movements (see Movie 4 – Appendix 2). Kymographs generated from maximum projections of 13 z-plane images (Figure 4.14.A), illustrate these lateral oscillating movements. Myo1 and Cam1 are recruited to the forming endocytic vesicle but remain at the membrane after the vesicle is internalised (Figure 3.6), before dispersing. In contrast, Cam2 foci have a short stationary phase before making oscillating movements. These movements are similar to the lateral movements observed for actin (see movie 5 – Appendix 2) and actin associated proteins such as Acp1, (Figure 4.14.B). Lateral movements are likely to correspond to the internalisation of endocytic vesicles, and suggest that Cam2, unlike Myo1 and Cam1, is internalised into the cell rather than remaining associated with the membrane.

To confirm this observation, kymographs where generated of individual foci at the cell membrane (Materials and methods Figure 2.4.C). These kymographs of single foci (Figure 4.14.C) show the typical movement of each protein component perpendicular to the cell membrane. As discussed previously, foci of both Myo1 and Cam1 remain at the cell surface before disassembling. Sla2 and actin (Lifeact) proteins are known to be internalised (Sirotkin et al 2010), and kymographs confirm these movements away from the cell membrane. The kymograph of a typical single Cam2-GFP foci (Figure 4.14.C) show Cam2 is also internalised into the cytosol, with a similar oscillating motion seen for actin.

This data would suggest that Cam2 is in some way linked to the actin network during internalisation of endocytic vesicles, in contrast to Myo1 and the associated light chain, Cam1, which remain bound to the membrane. Despite the strong evidence from *in vitro* data showing Cam2 binding to Myo1 IQ domains, the observations of Cam2 dynamics raises the question of what interactions the two proteins make *in vivo* during the mitotic cell cycle. Does Cam2 only bind to Myo1 at defined localisations or times during endocytosis, and do they require each other for function as previous data suggests? (Sammons et al. 2011).

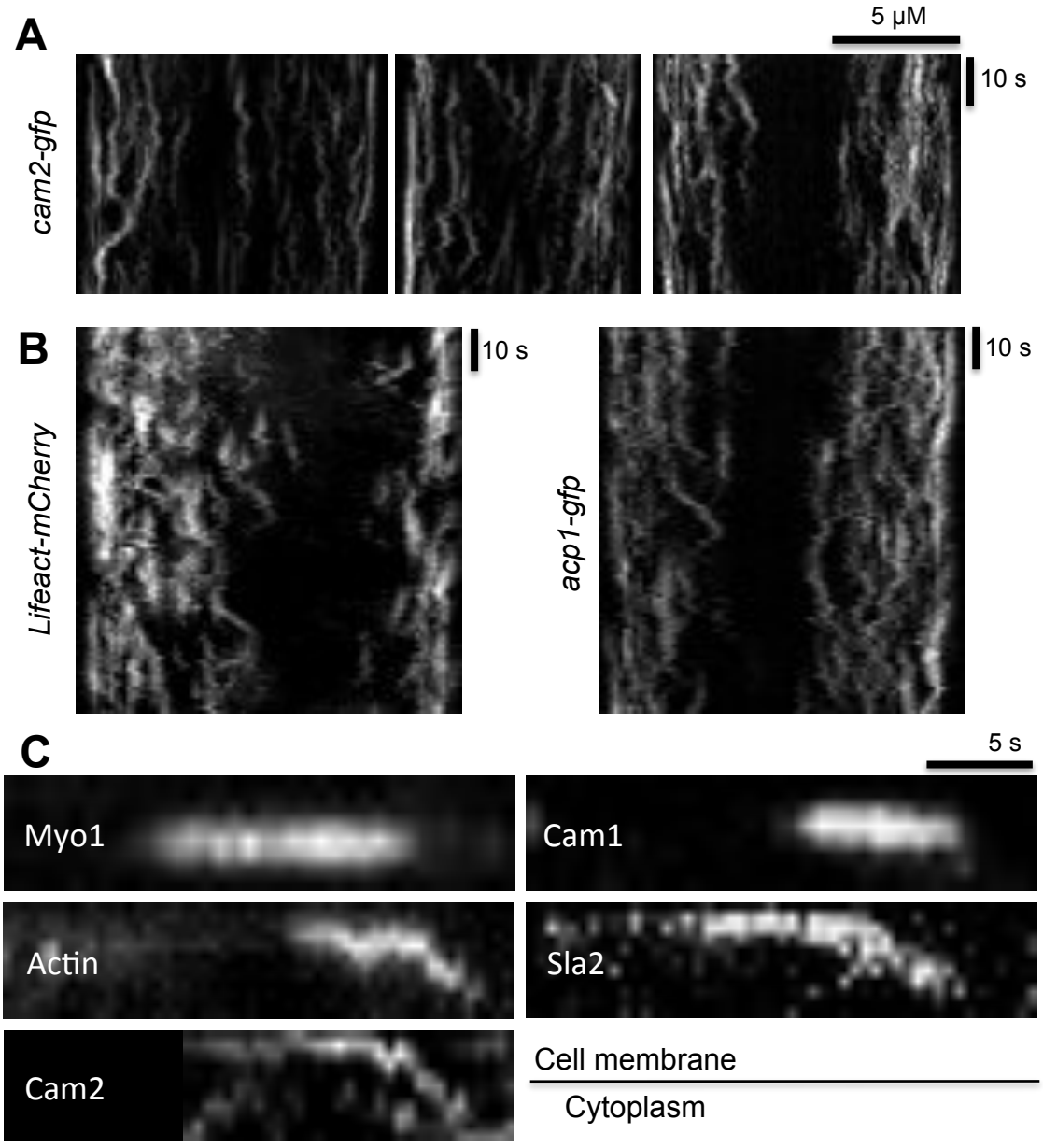

Figure 4.14. Dynamics and internalisation of Cam2.

(A) Kymographs generated from maximum projections of 13 z-plane images of *cam2-gfp* cells. (B) comparable kymographs generated from timelapse images of *Lifeact* and *acp1-gfp* cells. (C) shows kymographs of individual foci of the fluorescently labelled proteins indicated. The top of the kymograph is parallel to the cell surface, with time proceeding from left to right.

4.9. Double tagging Cam1, Cam2 and Myo1 combinations *in vivo* result in abnormal localisation.

To assess any interactions between Myo1 and Cam2 *in vivo*, strains were generated to simultaneously visualise these proteins within the cell. *mCherry-myo1 cam1-gfp* and *CFP-myo1 cam1-mCherry* strains (Figure 3.5) indicated it is not possible to label both Myo1 and Cam1 in the same cell whist maintaining a normal distribution of both proteins. Therefore, when making a double labelled strain, the localisation of each protein was carefully compared to a single labelled strain.

Maximum projection images of *mCherry-myo1 cam2-gfp* (Figure 4.15.A) show the cellular localisation of Cam2-GFP and mCherry-Myo1 proteins. When compared to single labelled strains (Figure 4.15.B), it would appear the overall localisation is unaffected by double tagging of these two proteins. Some Myo1 and Cam2 foci co-localise (indicated by arrows Figure 4.15.A) however a significant number of Cam2-GFP foci do not coincide with mCherry-Myo1 fluorescence. As these images were not captured simultaneously, instead by sequentially capturing GFP and mCherry images, this lack of co-localisation may be due to the dynamic nature of Cam2. This suggests that Cam2 only associates with Myo1 transiently. However, from this data alone it is not possible to confirm Cam2 interaction with Myo1.

Having established that no direct interaction of Cam1 and Cam2 takes place *in vitro*, strains were generated to try and assess the relationship of these proteins *in vivo*. A *cam1-gfp cam2-mCherry* strain was generated to determine relative cellular localisations and timings of protein recruitment to endocytic patches. However, when both of these proteins are tagged within the same cell the proteins no longer have the same localisation of that seen in single tagged strains (Figure 4.15.C). In these cells, Cam1-GFP is frequently seen to bind to microtubule structures including the mitotic spindle, not seen in a *cam1-gfp* strain and clearly a synthetic defect of tagging both Cam1 and Cam2. A *cam1-mCherry cam2-gfp* strain, shown in Figure 4.15.D. also results in incorrect localisation, with very few distinct Cam1 foci, and a large amount of cytoplasmic fluorescence.

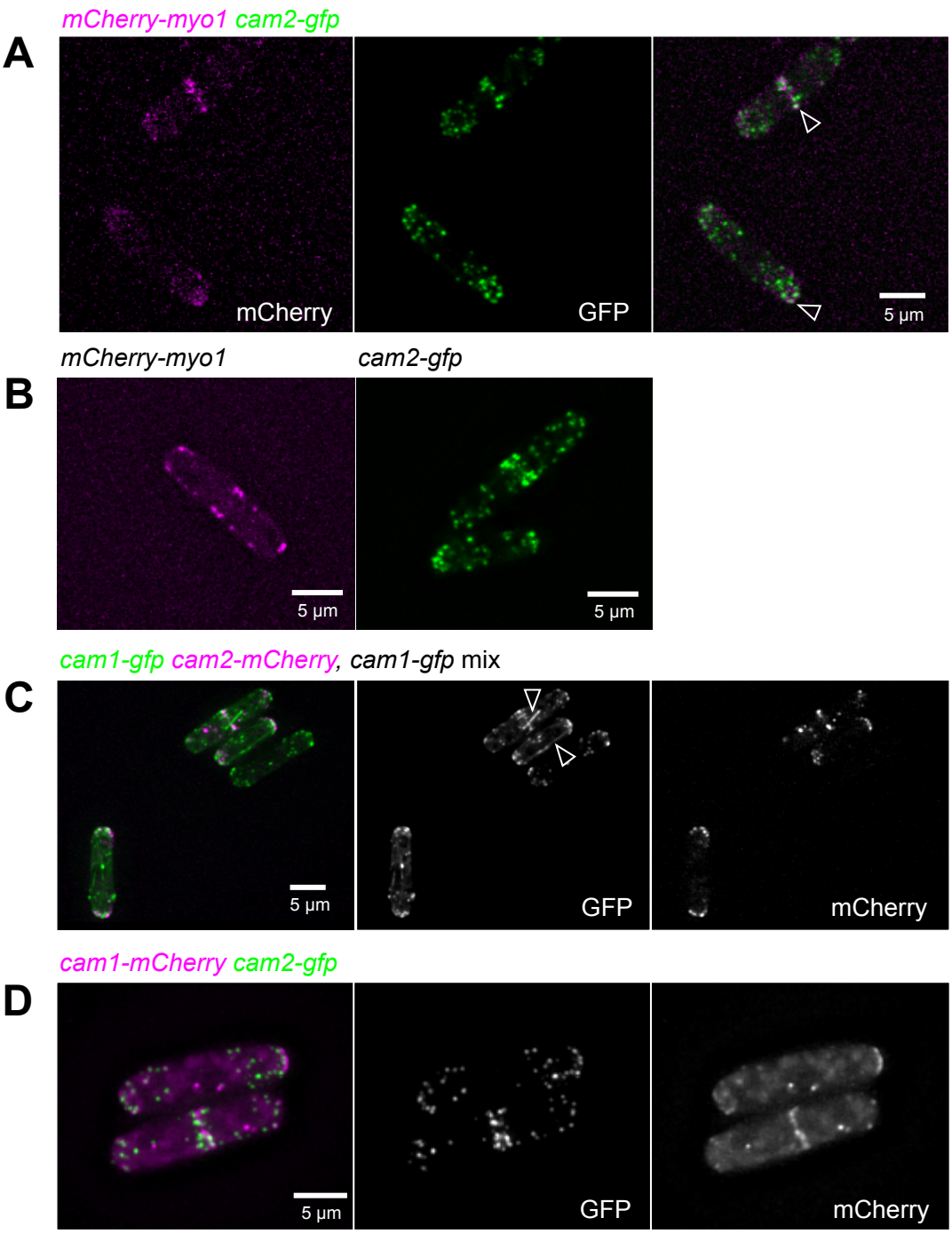

Figure 4.15. Simultaneous labelling of Cam2 with Myo1 and Cam1.

Maximum projections of 31 z-plane images of (A) *mCherry-myo1 cam2-gfp* cells and (B) single labelled cells for comparison. Arrows indicate mCherry-Myo1 and Cam2-GFP co-localisation. (C) shows a mixed image of double labelled *cam1-gfp cam2-mCherry* cells with a single labelled *cam1-gfp* strain. Arrows indicate Cam1-GFP localisation to microtubule structures. Images in (D) show *cam1-mCherry cam2-gfp* cells.

Throughout this study care was taken to avoid use of double tagged strains, and where possible other experiments were used to verify any conclusions made. For mix experiments where a second fluorescent label was required, a protein was tagged which was unlikely to affect the specific interaction being observed, for example Sid4, an essential component of the SPB.

4.10. Cam2 localises to endocytic patches during the early stages of internalisation.

The dynamics of Cam2 suggest that it is associated with endocytic vesicles as they are internalised. To confirm this, and determine the timings of Cam2 arrival at the endocytic site, a *cam2-gfp sla2-mCherry* strain was used. Imaging of Myo1 and Cam1 with known endocytic patch markers (Figure 3.6) showed that both Myo1 and Cam1 are early components of the endocytic patch and are not internalised. The same methods of imaging and analysis were used to determine Cam2 association with the Sla2-mCherry marker.

The arrows in Figure 4.16.A. indicate examples of Cam2-GFP co-localisation with Sla2-mCherry at endocytic patches. Sla2-mCherry signal was not intense enough to successfully image using an Optosplit device, therefore single z-plane images of 50 ms exposure were taken alternately in the mCherry and GFP channels. The resulting timelapse images in each channel were used to generate kymographs. Figure 4.16.B shows the internalisation of single foci in *sla2-mCherry cam2-gfp* cells. Cam2-GFP can be seen to arrive at the patch as Sla2 is internalised into the cell.

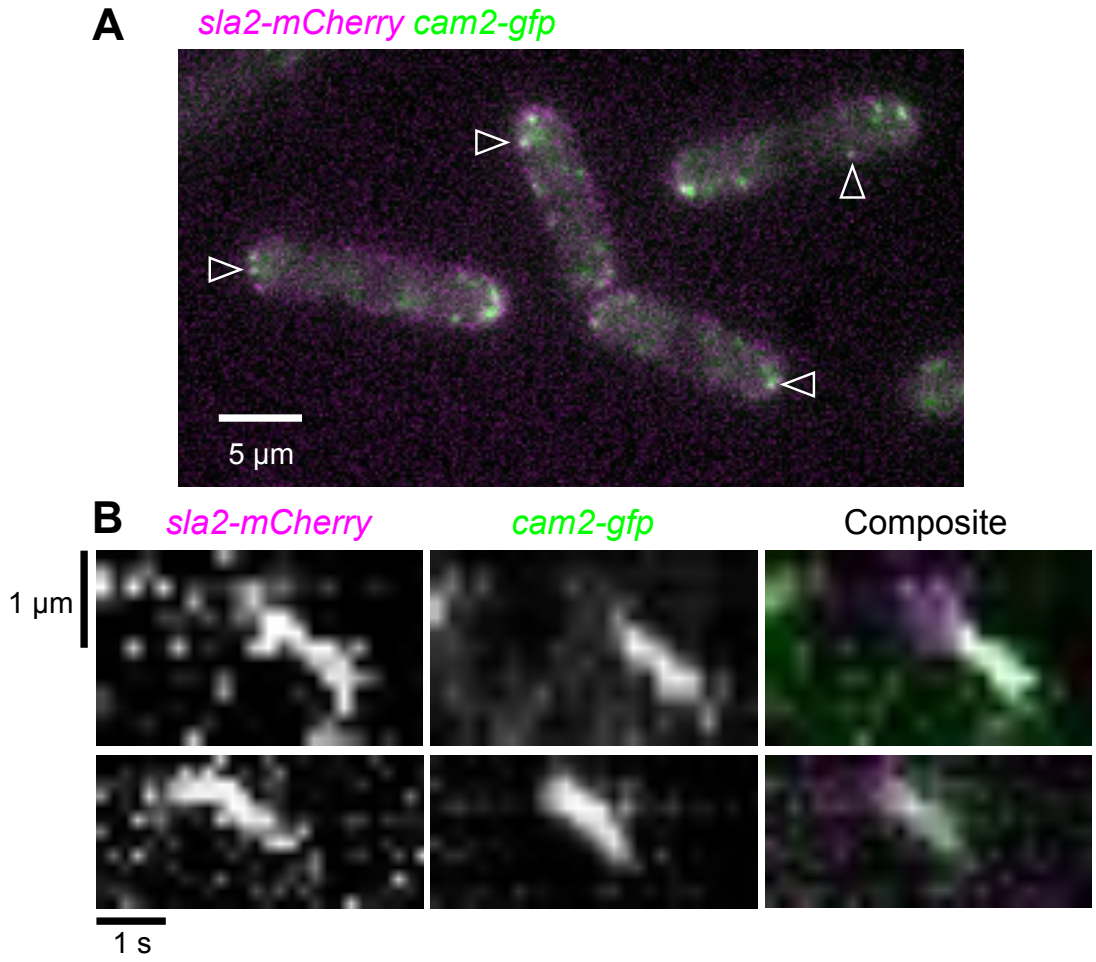

Figure 4.16. Cam2 recruitment to endocytic patches.

(A) Overlaid mCherry and GFP single z-plane images of *sla2-mCherry cam2-gfp* cells. Arrows highlight instances of Sla2-mCherry and Cam2-GFP co-localisation. (B) Kymographs generated from single z-plane timelapse images show internalisation of single foci.

4.11. Cam2 dynamics, but not recruitment, are dependent on Myo1.

The data presented so far in this chapter indicates possibilities of Cam2 association with Myo1, but also highlights significant differences when compared to Cam1 association with Myo1. *In vitro* binding data show both CaM light chains bind to the Myo1 IQ domains, combined with Myo1, Cam1 and Cam2 all co-localising with endocytic patches. However, Cam2 has distinct dynamics and

timing of recruitment to endocytic patches. Together these data suggest that Cam2 plays a very different role to Cam1 in regulating Myo1 function in the cell.

To elucidate the role of Cam2 in regulating Myo1, it was first determined what element of Cam2 localisation and dynamics are dependent on the function of Myo1. A *cam2-gfp myo1*Δ strain was generated to determine whether Myo1 was required for recruitment of Cam2 to the membrane. Examination of the cellular localisation of Cam2-GFP in the absence of Myo1, shows foci form throughout the cell, recruiting to the ends of the cell and the equator during division, as seen in *myo1*$^+$ cells (Figure 4.17). This indicates that Cam2 recruitment to foci at the cell membrane is independent of Myo1. Despite Cam1 and Cam2 both binding to Myo1 IQ domains *in vitro*, Cam2 localisation to the membrane in the absence of Myo1 is in contrast to Cam1 (Figure 3.6). Analysis of Cam2-GFP foci in *myo1*Δ cells (Figure 4.18) indicates Cam2-GFP fluorescence is incorporated into significantly more, larger foci than in *myo1*$^+$ cells.

Having determined that the cellular localisation of Cam2 was independent of Myo1, *cam2-gfp myo1*Δ and *cam2-gfp myo52*Δ strains were used to determine whether either of these myosin heavy chains were necessary for the distinct dynamics of Cam2. Rapid lateral movements in the cell are often the result of movement by the class V motor, Myo52 – as seen with Cam1. However the lateral movements of Cam2 are significantly shorter and not the single directional movements associated with Myo52 processive movement along actin filaments (Grallert et al. 2007). It is therefore not surprising that Cam2 lateral movements were not affected in a *myo52*Δ strain (Figure 4.17). By contrast, the distinctive lateral movements are abolished in *cam2-gfp myo1*Δ cells (Figure 4.17, Movie 6 – Appendix 2). While Cam2 foci form at the membrane in the absence of Myo1, these foci appear to persist on average 6 s longer, and lack the oscillating movements seen in *myo1*$^+$ cells. In *myo1*$^+$ cells, Cam2-GFP foci persist for 11 s (+/- 0.16 s) and have 1.2 μm (+/- 0.05 μm) lateral movement, while Cam2-GFP foci in *myo1*Δ cells persist for 17 s (+/- 0.50 s) and have negligible lateral movement. These data are consistent with the suggestion that class I myosins are involved in the pinching off of vesicles from the membrane during internalisation (Jonsdottir & Li 2004).

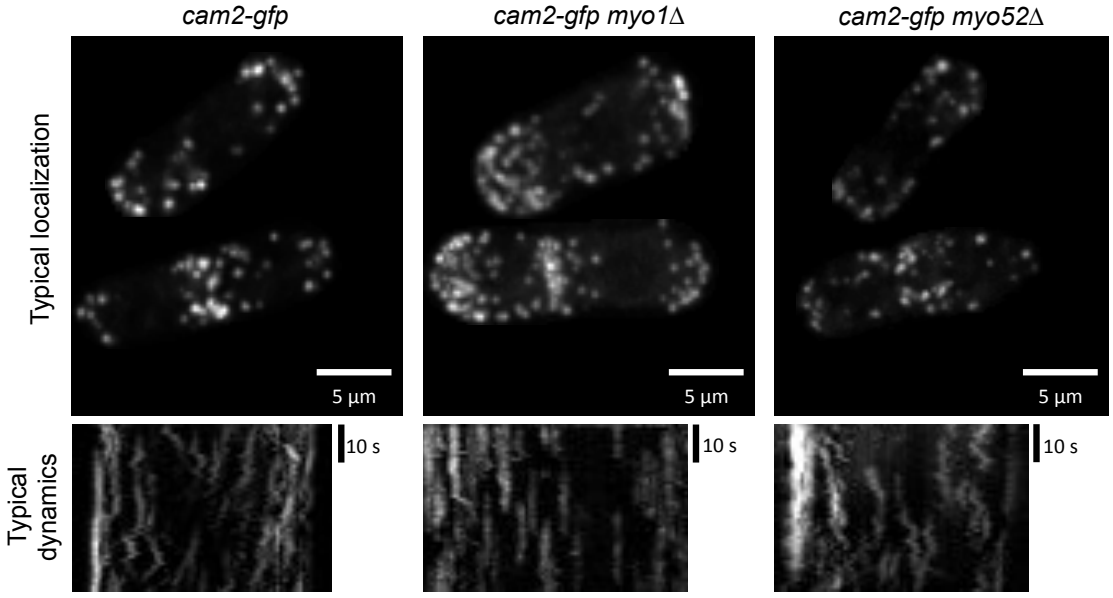

Figure 4.17. Cam2 localisation and dynamics in *myo1*Δ and *myo52*Δ cells.

Maximum projections of 31 z-plane images of Cam2-GFP in *myo1*$^{+}$, *myo1*Δ and *myo52*Δ backgrounds. Kymographs of these strains are generated from maximum projections of 13 z-plane images taken at 0.65 s intervals.

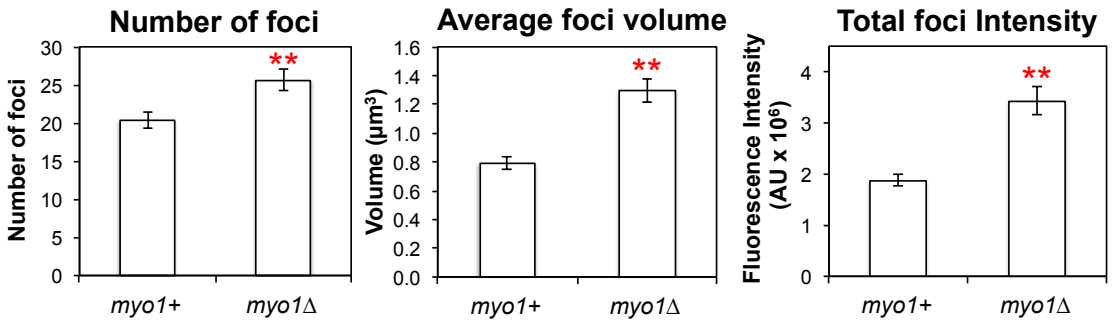

Figure 4.18. Analysis of Cam2 foci in *myo1*Δ cells.

Analysis of Cam2-GFP foci in *cam2-gfp myo52-tdTomato* cells (*myo1*$^{+}$) and *cam2-gfp myo1*Δ cells. Graphs show the average number of Cam2-GFP foci, average volume of each foci and total Cam2-GFP fluorescence incorporated into foci, in each cell. For each strain > 20 cells were analysed and error bars indicate standard error values. ‘ ** ’ denotes statistical significance of $p < 0.0001$.

To further explore this observation, and examine whether Myo1 is required for the internalisation of endocytic vesicles and not just Cam2, the dynamics of the actin marker Lifeact were observed in *myo1*Δ strains. Localisation of Lifeact fluorescence in *myo1*Δ cells was depolarised when compared to *myo1*$^{+}$ cells (Figure 4.19). Timelapse images of Lifeact in *myo1*Δ cells show, as for Cam2, oscillating movements are no longer seen, and the actin coated endocytic patches, persist at the membrane (Figure 4.19, Movie 7 – Appendix 2). As seen for Cam2, Lifeact patches remain assembled for on average 7.4 s longer in *myo1*Δ cells. In *myo1*$^{+}$ cells Lifeact foci persist for 11.5 s (+/- 0.2 s) with 1.4 µm (+/- 0.1 µm) lateral movement. In *myo1*Δ cells Lifeact foci persist for 18.9 s (+/- 0.7 s) with negligible lateral movement These data suggest that the oscillating motion of the internalising vesicle occurs as a result of a Myo1 dependent mechanism of internalisation.

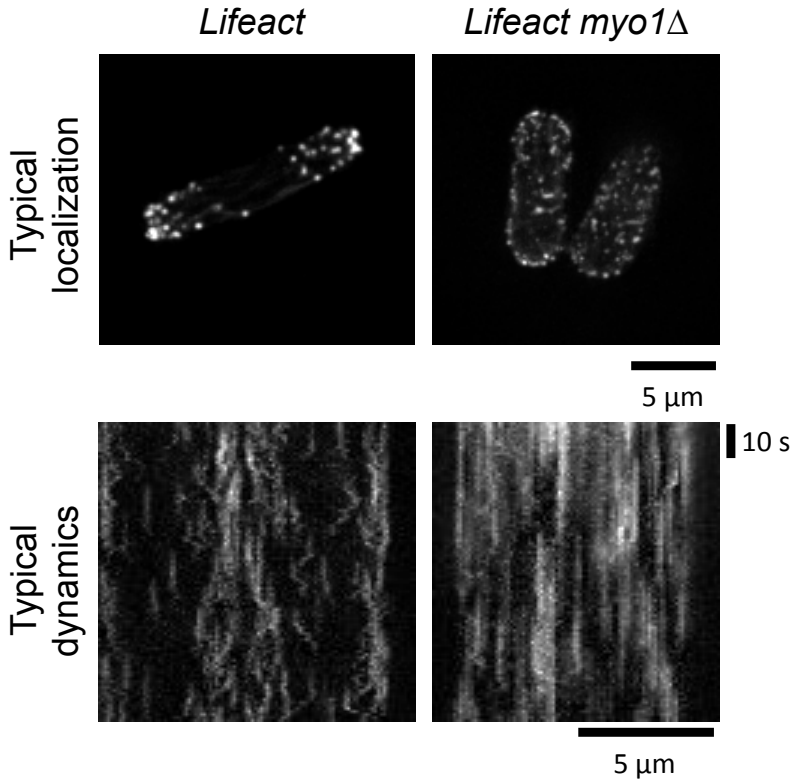

Figure 4.19. Lifeact localisation and dynamics in *myo1*Δ cells.

Maximum projections of 31 z-plane images showing typical Lifeact localisation in *myo1*$^{+}$ and *myo1*Δ cells. Lower panels show kymographs generated from maximum projections of 13 z-plane images of Lifeact in *myo1*$^{+}$ and *myo1*Δ cells.

Together these observations strongly indicate that during vegetative cell growth, Cam2 is recruited to endocytic patches by a protein other than Myo1, and is internalised with the actin-coated vesicle. Myo1 is essential for the internalisation of endocytic vesicles, and therefore the associated Cam2.

4.12. Cam2 enhances Cam1 recruitment to endocytic foci.

Having determined that Cam2 associates with endocytic patches, but Myo1 does not directly influence its recruitment, the role of Cam2 during endocytosis was explored. Unlike Cam1, Cam2 is not an essential protein in *S. pombe* cells. Deletion of the *cam2* gene results in cells with mild phenotypic effects including temperature sensitivity and mating defects (Itadani et al. 2006). To determine whether Cam2 affects Myo1, Cam1 and Myo52 localisation; *YFP-myo1, cam1-gfp* and *myo52-gfp* alleles were crossed into a *cam2*Δ strain in which the *cam2* gene was deleted with a *URA4* selection marker (Itadani et al. 2006).

Biochemistry data in Section 4.4. showed that Cam2 inhibited the binding of Cam1 to Myo1 *in vitro*. It would therefore be predicted that in a *cam2*Δ cell, Cam1 binding to Myo1 may be enhanced. To explore this hypothesis, levels of Cam1 fluorescence incorporated into foci and the lifetimes of Cam1 association to endocytic patches were determined in *cam1-gfp cam2*Δ cells.

Figure 4.20.A shows a typical mix image of *cam1-gfp myo52-tdTomato cam2*$^{+}$ (indicated by arrows) and *cam1-gfp cam2*Δ cells. On initial observation, it would appear that Cam1-GFP foci are less well defined in a *cam2*Δ cell, and that Cam1-GFP fluorescence localises as a ‘haze’ at the cell membrane (Movie 8 – Appendix 2). Analysis of these images (Figure 4.20.C) indicates that the number of Cam1-GFP foci in a *cam2*Δ cell is not significantly reduced, but that the average volume is 25% smaller, resulting in a reduced total amount of Cam1 protein incorporated into foci. Whole cell fluorescence is unchanged in a *cam1-gfp cam2*Δ strain, indicating that the absence of Cam2 does not affect the overall Cam1 expression levels or Cam1 stability. However the maximum intensity measurements of foci are

on average 50% brighter in *cam2*$^{+}$ cells. The data presented in Figure 4.20. suggests that Cam2 is required for the coalescence of Cam1 with endocytic foci.

The duration of Cam1-GFP appearance at the membrane was measured from kymographs generated from single z-plane timelapse images of Cam1-GFP in *cam2*$^{+}$ and *cam2*Δ cells (Figure 4.20.B-C). Analysis of the durations of these events show that Cam1-GFP foci persist at the membrane for 10.4 s (+/- 0.13 s) in *cam2*$^{+}$ cells and 13.3 s (+/- 0.15 s) in *cam2*Δ cells. This longer association of Cam1 at the membrane is possibly due to enhanced binding to Myo1 – consistent with *in vitro* data.

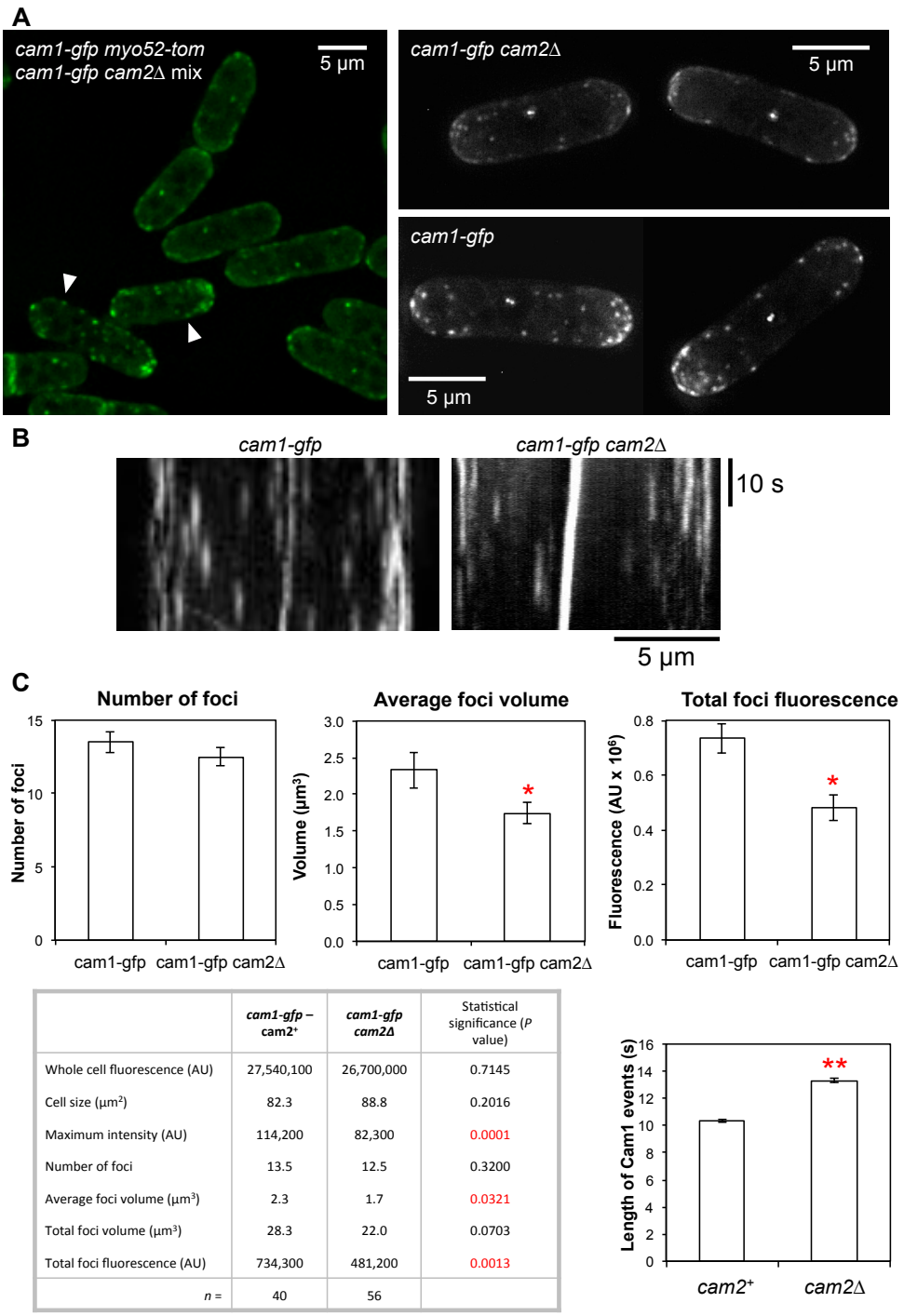

	cam1-gfp – cam2⁺	*cam1-gfp cam2Δ*	Statistical significance (*P* value)
Whole cell fluorescence (AU)	27,540,100	26,700,000	0.7145
Cell size (μm²)	82.3	88.8	0.2016
Maximum intensity (AU)	114,200	82,300	0.0001
Number of foci	13.5	12.5	0.3200
Average foci volume (μm³)	2.3	1.7	0.0321
Total foci volume (μm³)	28.3	22.0	0.0703
Total foci fluorescence (AU)	734,300	481,200	0.0013
n =	40	56	

Figure 4.20. Analysis of Cam1-GFP in *cam2*Δ cells.

(A) Maximum projections of 31 z-plane images showing Cam1-GFP localisation in *cam2*$^+$ and *cam2*Δ cells. In the mix image, arrows indicate *cam2*$^+$ cell (*cam1-gfp myo52-tdTomato*). (B) Kymographs generated from single z-plane timelapse images of *cam1-gfp* and *cam1-gfp cam2*Δ cells. (C) Summary of analysis of Cam1-GFP foci from mix images as shown in (A). ‘ * ’ denotes p <0.05, ‘ ** ‘ denotes p <0.0001.

4.13. Myo1 and Myo52 are significantly affected in *cam2*Δ cells.

Having seen a reduction in the amount of Cam1 incorporated into foci in *cam2*Δ cells, it was next explored whether the myosin heavy chains, Myo1 and Myo52 were also affected by *cam2*Δ, as Cam1 acts as a light chain for these myosin heavy chains. Figure 4.21.A shows a typical mix image of *YFP-myo1 sid4-tdTomato cam2*$^{+}$ cells with *YFP-myo1 cam2*Δ cells. Analysis of YFP-Myo1 foci in each of these strains is summarised in Figure 4.21.B-C.

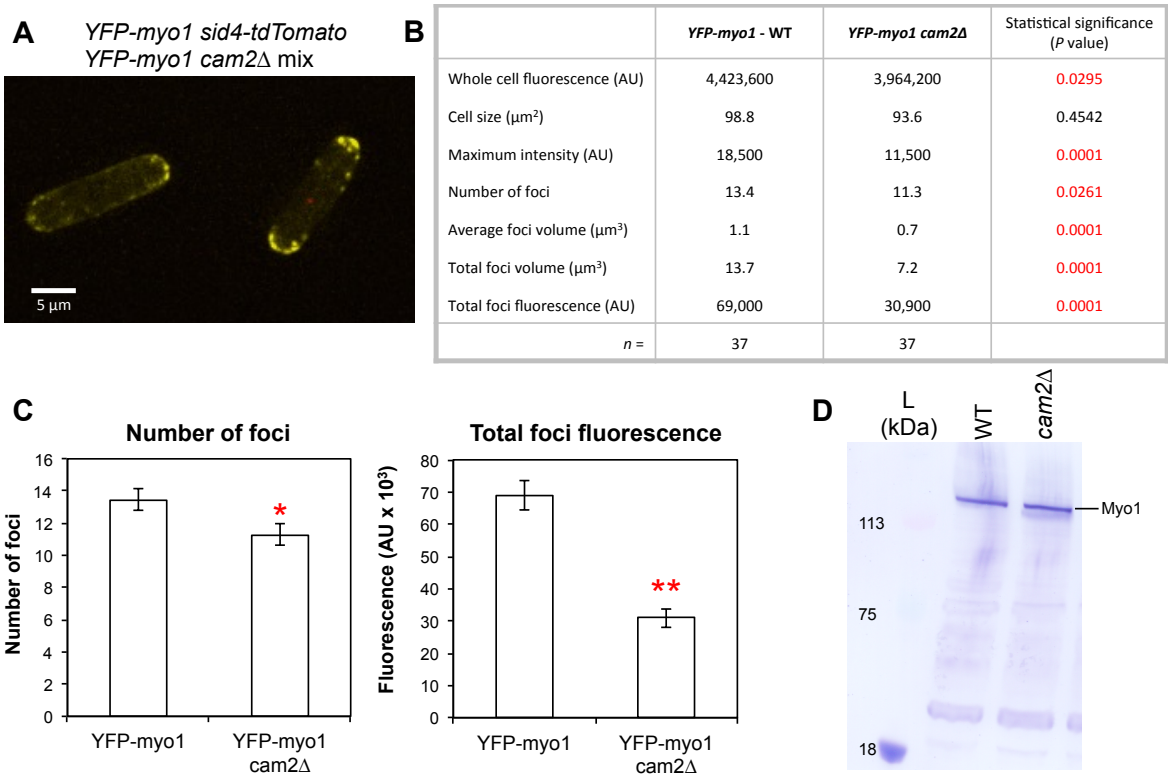

	YFP-myo1 - WT	*YFP-myo1 cam2Δ*	Statistical significance (*P* value)
Whole cell fluorescence (AU)	4,423,600	3,964,200	0.0295
Cell size (µm²)	98.8	93.6	0.4542
Maximum intensity (AU)	18,500	11,500	0.0001
Number of foci	13.4	11.3	0.0261
Average foci volume (µm³)	1.1	0.7	0.0001
Total foci volume (µm³)	13.7	7.2	0.0001
Total foci fluorescence (AU)	69,000	30,900	0.0001
n =	37	37	

Figure 4.21. Analysis of YFP-Myo1 fluorescence in *cam2*Δ cells.

(A) Maximum projection of 31 z-plane images showing YFP-Myo1 localisation in *cam2*$^{+}$ (*YFP-myo1 sid4-tdTomato*) and *cam2*Δ cells. (B-C) Analysis of YFP-Myo1 foci in > 35 cells. ' * ' denotes p <0.05, ' ** ' denotes *p* <0.0001. (D) anti-Myo1 western blot of wild type and *cam2*Δ cells, lower non-specific bands included to confirm equal loading.

Deletion of the *cam2* gene appears to have a more significant affect on Myo1 than Cam1. There are on average 2 fewer Myo1 foci per cell, but most significantly, the average size of each focus is reduced by a third. Fewer, smaller Myo1 foci in *cam2*Δ cells resulted in more than 50 % reduction in the total amount of YFP-Myo1 protein detected in discrete foci. There was also a statistically significant reduction in the overall levels of detectable YFP-Myo1 protein per cell. Such a significant reduction in Myo1 protein levels are not seen when extracts of wild type and *cam2*Δ cells are probed with anti-Myo1 antibodies (Figure 4.21.D). Although in the *cam2*Δ extract, some protein is detected directly under the Myo1 band, it is possible that this could be degraded Myo1 protein.

In the absence of Cam2, there were less dramatic changes in Myo52-GFP localisations. Analysis of Myo52-GFP foci in *cam2*$^+$ and *cam2*Δ cells indicates a significant change in the number and size of Myo52 foci (Figure 4.22). Overall Myo52-GFP fluorescence levels were not affected, but protein was distributed between fewer, larger foci.

A

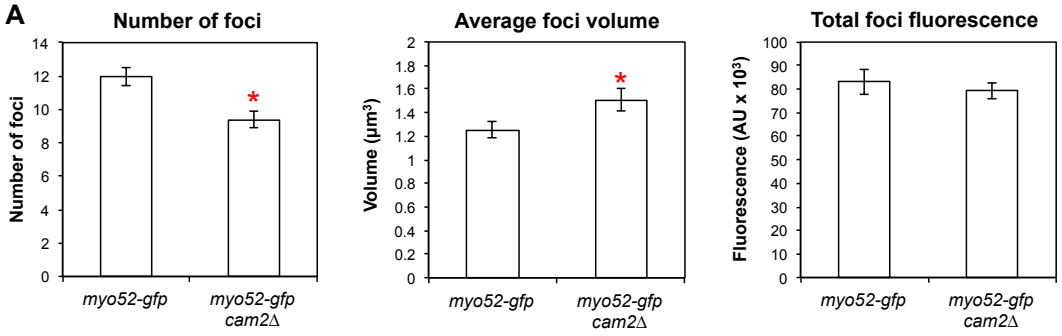

B

	myo52-gfp - WT	*myo52-gfp cam2Δ*	Statistical significance (*P* value)
Whole cell fluorescence (AU)	4,757,200	4,653,900	0.5785
Cell size (µm²)	82.0	86.1	0.5357
Maximum intensity (AU)	29,900	32,900	0.2007
Number of foci	12.0	9.4	0.0015
Average foci volume (µm³)	1.25	1.51	0.0492
Total foci volume (µm³)	14.5	12.8	0.0477
Total foci fluorescence (AU)	83,000	79,200	0.5085
n =	28	41	

Figure 4.22. Analysis of Myo52-GFP in *cam2*Δ cells.

(A-B) Analysis of Myo52-GFP foci from mix images of *cam2*$^+$ (*myo52-gfp sid4-tdTomato*) and *myo52-gfp cam2*Δ cells. ‘ * ’ denotes p <0.05.

4.14. TIRF imaging of *cam1-gfp cam2*Δ cells.

Widefield images of *cam1-gfp cam2*Δ (Figure 4.20.A) suggest that the Cam1 fluorescence appears to be localised as a diffuse cloud at the membrane. To investigate this observation further, TIRF microscopy was used to look specifically at Cam1 dynamics at the membrane. TIRF microscopy illuminates ~100 nm of the cell closest to the coverslip, eliminating fluorescent signal from outside the focal plane. Timelapse imaging of *cam1-gfp* cells using TIRFM (section 2.6.3) gave more detailed information about how Cam1 assembles and disassembles at endocytic patches. Figure 4.23.A shows a typical TIRFM image of Cam1-GFP fluorescence in a *cam2*$^+$ and *cam2*Δ background. GMimPro Software (Mashanov and Molloy 2007) was used to analyse the fluorescence intensities of individual patches over time, Figure 4.23.B shows typical fluorescence intensity traces obtained from a single foci in *cam2*$^+$ (black line) and *cam2*Δ (red line) strains. The average rate of accumulation and disassociation of Cam1 from the foci was calculated from the gradients of 100 fluorescence traces (Figure 4.23.C).

In the absence of Cam2, maximum Cam1 fluorescence is reduced more than 2-fold, consistent with a reduction in maximum fluorescence shown by analysis of widefield images (Figure 4.20.C). The rate at which Cam1 is recruited to foci is 4 times slower in the absence of Cam2, with disassembly of Cam1 also reduced by 3 fold. This resulted in an overall increase in duration of Cam1-GFP endocytic events in *cam2*Δ cells. This data is consistent with the longer persistence of Cam1-GFP foci observed by widefield imaging (Figure 4.20).

Consistent with observations from widefield images of *cam1-gfp cam2*Δ cells, TIRF data shows Cam1-GFP foci are less compact in a *cam2*Δ background. Figure 4.23.D shows equivalent images of typical Cam1-GFP foci from a *cam2*$^+$ and *cam2*Δ cell. In *cam2*$^+$ strains, Cam1-GFP fluorescence is largely contained within a 7x7 pixel region (1.1 μm^2), whereas in a *cam2*Δ strain, fluorescence is spread over a wider area. The average Cam1-GFP fluorescence intensity per pixel was calculated for each of the regions defined in Figure 4.23.D, for 50 individual foci. Figure 4.23.E shows that in *cam2*$^+$ cells, pixels at the centre of a focus (Region 1) have a higher intensity than those at the edge (Region 3). This is in

contrast to the Cam1-GFP intensities measured in *cam2*Δ strains where the average intensity per pixel is constant across all regions.

Quantitative analysis of Cam1-GFP foci fluorescence specifically at the cell surface supports the data from widefield image analysis, indicating that in the absence of Cam2, Cam1 is unable to form the same compact foci that are observed in the presence of Cam2.

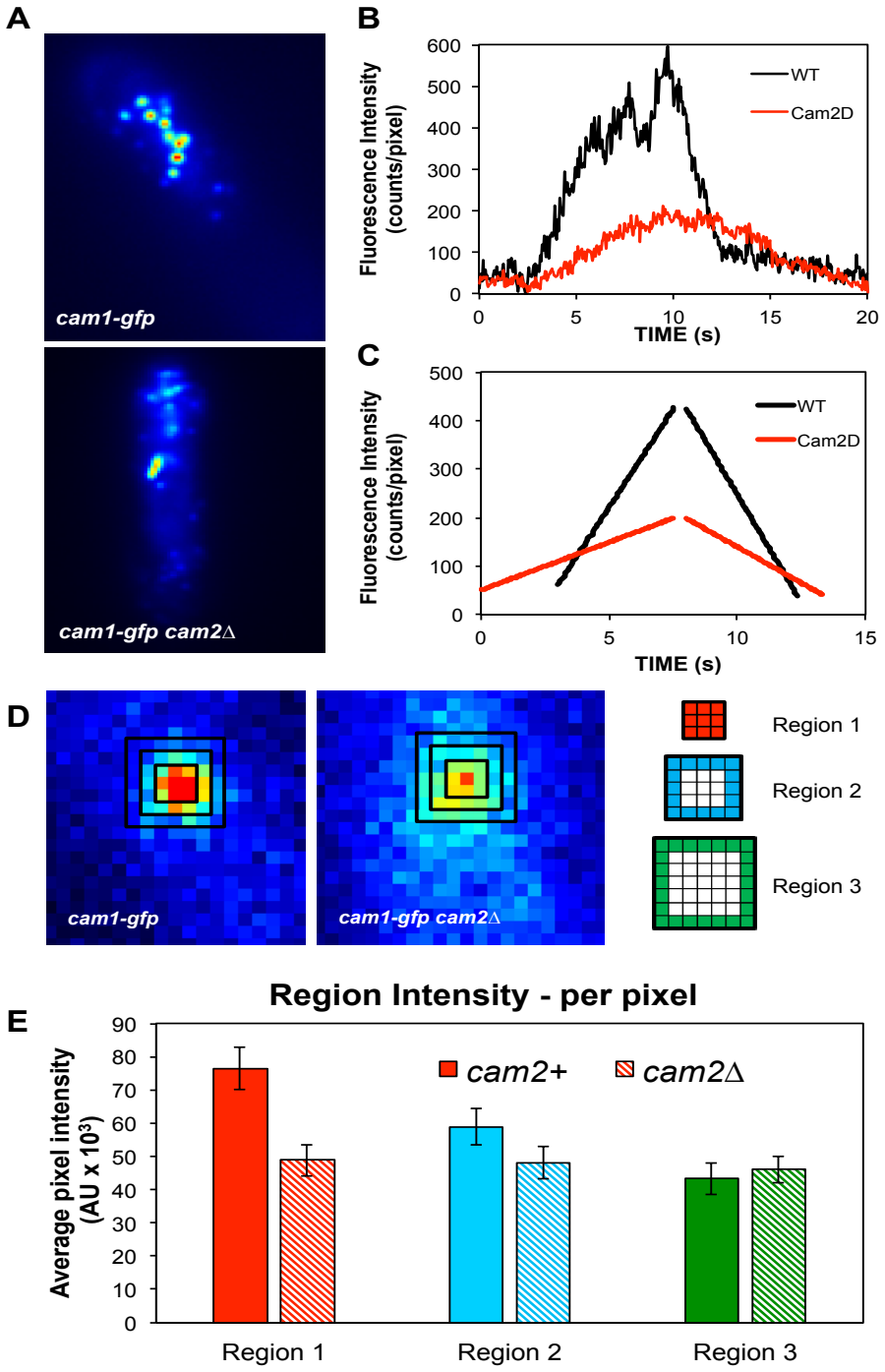

Figure 4.23. TIRF imaging of Cam1-GFP in *cam2*$^{+}$ and *cam2*Δ cells.

(A) Stacked TIRF timelapse images of *cam1-gfp* and *cam1-gfp cam2*Δ cells. (B) Fluorescence intensity traces over the lifetime of single Cam1-GFP foci in *cam2*$^{+}$ and *cam2*Δ cells with the average gradients of 50 traces plotted in (C). (D) Expanded view of single Cam1-GFP foci at maximum intensity, with indicated regions of 3x3, 5x5, 7x7 pixels. The intensity of these regions were calculated over the lifetime of 50 foci, the average intensity of pixels in the coloured regions correspond to the graph in (E).

Summary:

Statement	Evidence
Cam1 is able to bind calcium ions, Cam2 does not.	Quin-2 calcium dissociation rates and EF-hand sequence alignments.
Cam1 only binds to Myo1 IQ domains in the absence of calcium, Cam2 binds under either condition.	Cam1 and Cam2 binding to Myo1IQ12 FRET protein.
Cam1 binds to Myo1 IQ domains 1.5x more strongly than Cam2.	Cam1 – 0.80 μM, Cam2 – 1.16 μM affinities to Myo1IQ12 FRET protein.
Cam1 binds to the first Myo1 IQ1 domain 6.5x more strongly than Cam2.	Cam1 – 0.06 μM, Cam2 – 0.39 μM affinities to Myo1 IQ1 FRET protein.
Cam1 and Cam2 bind differently to Myo1 IQ domains – either to a different region of the helix or induce a different conformation of the IQ domains.	Different FRET spectra and Cypet:Ypet ratios on binding of equivalent amounts of Cam1 and Cam2.
Cam1 binds to both Myo1 IQ domains.	Scatchard plot indicates bi-phasic binding of Cam1 to the Myo1IQ12 FRET protein.
Cam2 inhibits Cam1 binding to Myo1 IQ domains.	Affinity of Cam1 binding to Myo1IQ12 FRET protein reduced from 0.80 μM to 1.98 μM.
Cam1 enhances Cam2 binding to Myo1 IQ domains.	Affinity of Cam2 binding to Myo1IQ12 FRET protein increased from 1.16 μM to 0.33 μM.
Cam2 binds preferentially to a Myo1-Cam1 complex.	Cam2 binds to Cam1-IAANS-Myo1IQ complex over free IQ peptide in solution.
Cam1 and Cam2 do not form a complex.	Cam1-IAANS, Cam1-FRET and gel filtration experiments.
Myo1 required for vesicle internalisation.	No lateral oscillating movement characteristic of vesicle internalisation in *cam2-gfp myo1*Δ or *Lifeact myo1*Δ cells.
Cam2 dynamics are very different to Myo1 and Cam1.	Kymographs from *cam2-gfp* cells compared to *mNeongreen-myo1* and *cam1-gfp* cells.
Cam2 does not need Myo1 to recruit to the membrane, unlike Cam1.	Cam2-GFP vs Cam1-GFP localisation in *myo1*Δ cells.
Myo1 and Cam1 recruit to endocytic patches ~ 10-15 s before internalisation.	Imaging of *mNeongreen-myo1 lifeact* and *cam1-gfp sla2-mCherry* single foci.
Cam2 arrives at the endocytic patch as the vesicle internalises	Imaging of *cam2-gfp sla2-mCherry* single foci.
Cam2 is required for Myo1/Cam1 to coalesce into compact foci.	Widefield and TIRF imaging of *YFP-myo1 cam2*Δ*, cam1-gfp cam2*Δ cells.
Cam2 transiently localises to endocytic patches.	Cam2 is highly dynamic and only seen to co-localise with endocytic patches as they internalise. TIRF images show few foci at the surface at any one time.

Summary:

Data presented in this chapter compares the function of the two *S. pombe* calmodulin-like light chains, Cam1 and Cam2. *In vitro* analysis shows that both CaMs are able to bind the IQ motifs of Myo1. In contrast to Cam1, Cam2 can bind to Myo1 in the presence of calcium, but in the absence of calcium, Cam2 affinity for Myo1 is weaker than Cam1. The cellular localisation and dynamics of Cam2 is different to that observed for Cam1 and Myo1, and its localisation to patches is independent of Myo1. Cam2 associates with endocytic patches, possibly facilitated by preferential binding to Cam1-bound Myo1, however this interaction appears transient. Again in contrast to Cam1, Cam2 is internalised with the endocytic vesicle rather than remaining at the membrane. Cam2 is not essential for the endocytic process, but functions to increase the rate of endocytosis. Analysis of *cam2*Δ strains, suggests that Cam2 does this by enhancing the density of Myo1/Cam1 at the endocytic patch.

Chapter 5: Effects of phosphorylation of Myo1 at serine-742.

Introduction:

Phosphorylation of myosin heavy chains is a known mechanism of regulating motor activity (Redowicz 2001). Multiple phosphorylation sites have been identified in Class I myosins, mainly in the head domain. For example TEDS rule phosphorylation sites in yeast myosin I proteins have been shown to regulate protein localisation (Grosshans et al. 2006; Attanapola et al. 2009). In addition to sites in the head domain, phosphorylation events in the neck region of myosins are predicted to affect the binding of light chains (Houdusse et al. 2006). This has been shown to be the case in mammalian Myo1c protein, which is phosphorylated by CaMKII at the start of the IQ domains in the neck region (Yip et al. 2008). This phosphorylation event in response to insulin inhibits binding of calmodulin light chains, but enhances the binding of a 14-3-3 protein.

There are currently no known functions of phosphorylation events in the neck or tail region of *S. pombe* Myo1. However multiple serine residues have been identified as potential sites of phosphorylation. Figure 1.33 highlights some of these residues which have been identified in phosphoproteome screens (Wilson-Grady 2007, Carpy 2014, Petersen and Hagan personal communications). Although only identified in the Wilson-Grady phosphoproteome screen, the serine-742 residue is located between the two IQ domains of Myo1. It is therefore possible that phosphorylation of this residue could have implications in the binding of calmodulin light chains to the neck region, therefore regulating the function of Myo1.

In order to investigate potential regulatory effects of phosphorylation at Myo1 serine-742, recombinantly expressed proteins containing phosphorylation-null and phosphomimic Myo1 serine-742 sequences were used for *in vitro* biochemical analysis. In addition, Myo1 serine-742 phosphorylation mutant strains were generated to analyse the effect of this phosphorylation event *in vivo*.

5.1. Cam2 binds more tightly to Myo1IQ12-S742D but Cam1 affinity is unchanged.

Having explored calmodulin binding to the IQ motifs of Myo1, it was next investigated whether phosphorylation at the Myo1 serine residue 742 (S742) has a role in regulating this interaction. The S742 residue is located between the two IQ motifs of Myo1, and is therefore included in the Myo1IQ12 FRET protein described in Figure 3.9. A phosphomimic version of this Myo1 FRET protein (Myo1IQ12-S742D) was generated by replacing the DNA sequence encoding for the serine with a sequence encoding an aspartic acid residue. The resulting amino acid sequence of the linker region is shown in Figure 3.9.D. The substitution of serine for a negatively charged amino acid, mimics the charged state of a constitutively phosphorylated protein. The Myo1IQ12 FRET protein used in previous experiments contains the native serine residue, but due to bacteria having no mechanism for post-translational addition of phosphate groups, this protein therefore simulates a constitutively un-phosphorylated state.

There are no significant differences in the spectra of these two FRET proteins (Figure 5.1, green and blue lines), indicating that a change in charge at residue 742 does not appear to change the overall α-helical stability or flexibility of the Myo1 IQ domains.

Both Cam1 and Cam2 are able to bind to the phosphomimic FRET protein (Figure 5.1, black and red lines), indicating that this phosphorylation event is not a simple ‘on-off’ switch for calmodulin binding to Myo1. As seen for the un-phosphorylated Myo1IQ12 FRET protein (Figure 4.1), addition of Cam2 results in a greater change in Cypet fluorescence despite equivalent Ypet fluorescence values. However, this difference in FRET ratio on binding of Cam1 and Cam2 is not as evident in the phosphomimic Myo1 IQ FRET protein (Figure 5.1, black and red lines).

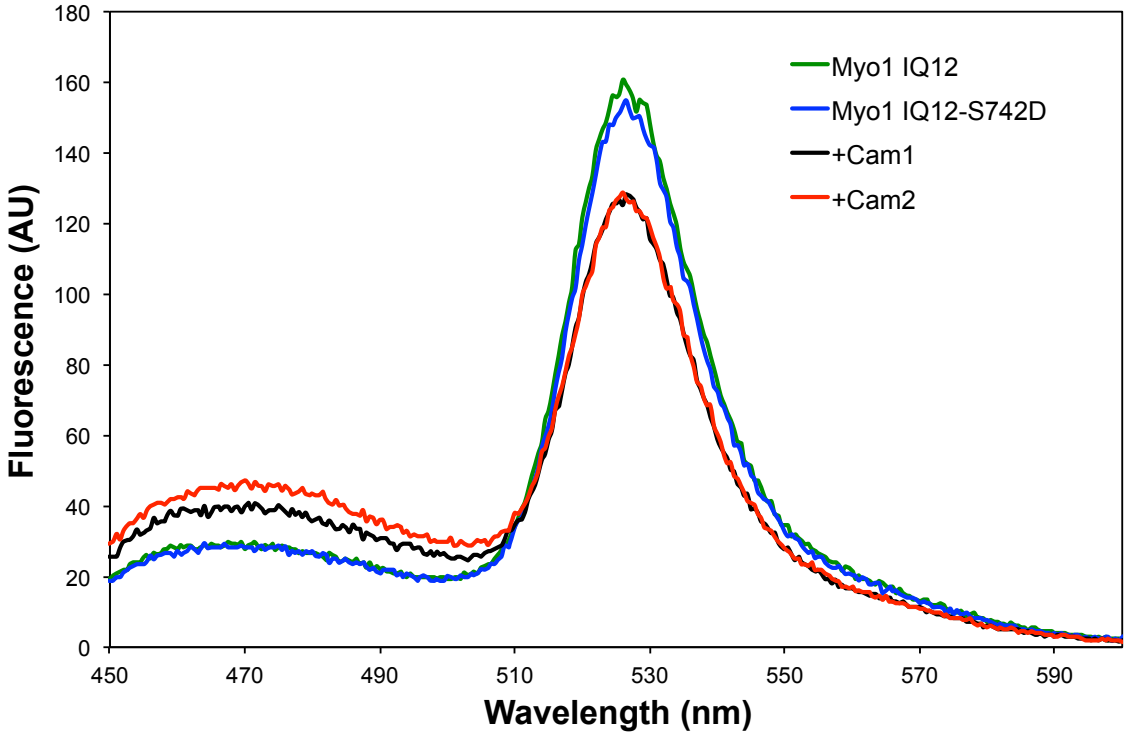

Figure 5.1. Emission spectra of Myo1IQ12 and Myo1IQ12-S742D FRET proteins.

Overlaid emission spectra of equivalent concentrations of 'un-phosphorylated' Myo1IQ12 (green line) and the phosphomimic Myo1IQ12-S742D (blue line) FRET protein, after excitation at 435 nm. A decrease in FRET signal is observed for the Myo1IQ12-S742D phosphomimic FRET protein on addition of excess Cam1 (black line) and Cam2 (red line).

Next, the affinity of calmodulin binding to the Myo1IQ12-S742D FRET protein was determined using the same FRET assay described previously and compared with data from the MyoIQ12 FRET protein. Figure 5.2. shows the binding curves of Cam1 to the phosphomimic Myo1IQ12-S742D protein (blue symbols), and the un-phosphorylated' Myo1IQ12 FRET protein (black symbols - WT). The calculated affinity of Cam1 binding to the Myo1IQ12-S742D, is not significantly different from that of the Myo1IQ12, with a K_d of 0.87 μM compared to 0.80 μM. As for the un-phosphorylated Myo1IQ12 FRET protein, binding of Cam1 was bi-phasic, suggesting both IQ domains are bound.

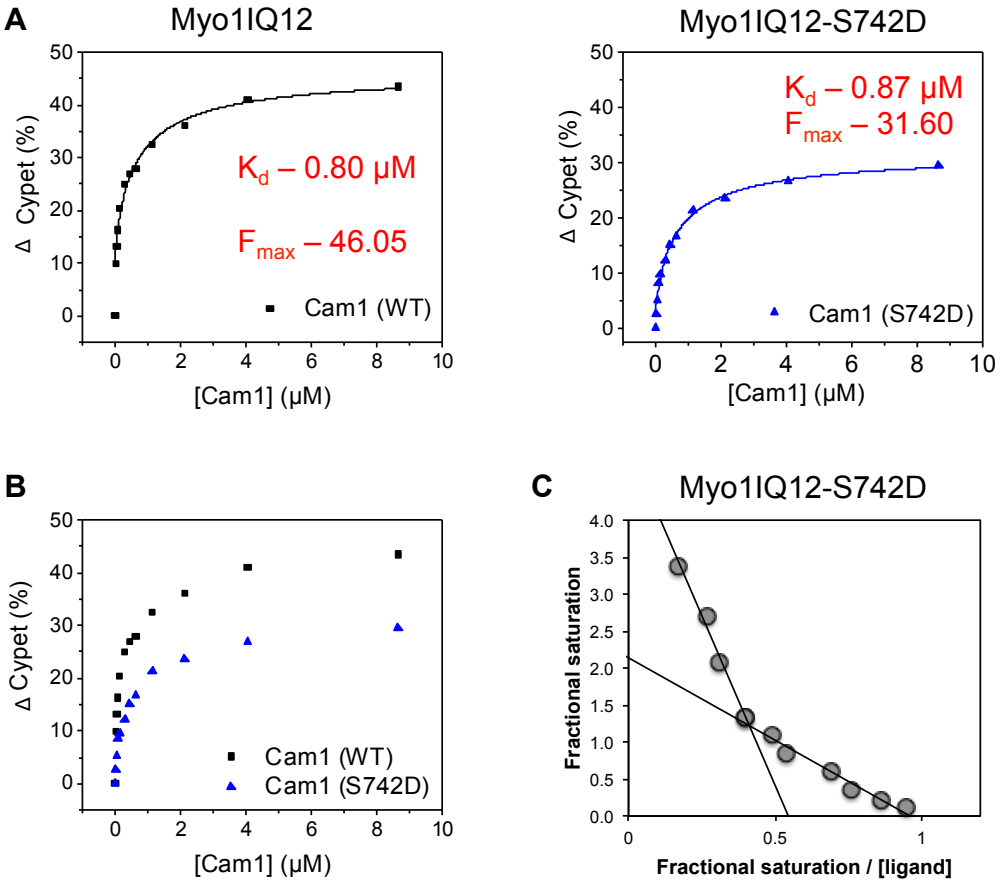

Figure 5.2. Cam1 binding to Myo1IQ12 and Myo1IQ12-S742D.

(A-B) Graphs show percentage change in Cypet fluorescence of Myo1IQ12 and Myo1IQ12-S742D FRET proteins on addition of increasing amounts of acetylated Cam1 protein. Individual graphs show the calculated K_d and F_{max} values for each curve. (C) Scatchard plot of Cam1 binding to the Myo1IQ12-S742D FRET protein fitted for two phases.

Next, the affinity of Cam2 binding to the to Myo1 FRET proteins was compared. The binding curves from titrations of Cam2 (Figure 5.3) with Myo1IQ12-S742D (blue symbols) and Myo1IQ12 (red symbols) indicate that Cam2 binds more tightly to the 'phosphorylated' Myo1 IQ domains. The affinity of Cam2 for the charged Myo1 IQ domains is increased over 4-fold, with a K_d of 0.28 μM compared to 1.16 μM for the 'un-phosphorylated' Myo1IQ12 protein.

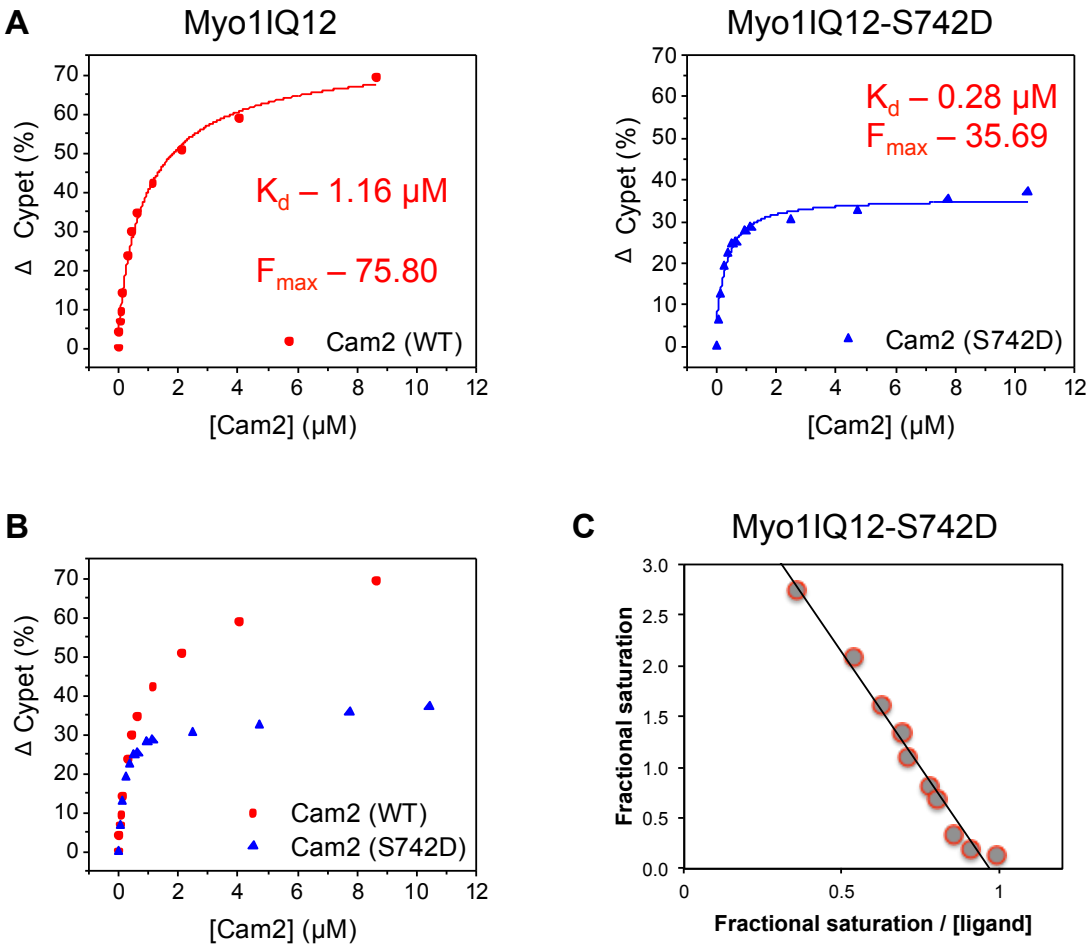

Figure 5.3. Cam2 binding to Myo1IQ12 and Myo1IQ12-S742D.

(A-B) Graphs show percentage change in Cypet fluorescence of Myo1IQ12 and Myo1IQ12-S742D FRET proteins on addition of increasing amounts of Cam2 protein. Individual graphs show the calculated K_d and F_{max} values for each curve. (C) Scatchard plot of Cam2 binding to the Myo1IQ12-S742D FRET protein fitted for a single phase.

These changes in affinity of Cam1 and Cam2 binding suggest that phosphorylation of the serine-742 residue between the Myo1 IQ1 and IQ2 motifs, results in Cam2 having a higher affinity for the IQ domains than Cam1. This would suggest that this phosphorylation event may provide a switch between Cam1 and Cam2 binding.

To further explore this potential switch in calmodulin binding, a synthetic peptide was made for the same 38 amino acid region described in Figure 4.8, with the equivalent S742 residue replaced with an aspartic acid. However, CD measurements showed this peptide was unstructured, suggesting that as an isolated helix, the change in charge destabilises the α-helical structure. This, combined with the smaller changes in FRET observed in the Myo1IQ12-S742D protein, meant it was not possible to carry out the equivalent experiments shown in Sections 4.4 and 4.5, to asses co-operativity of Cam1 and Cam2 binding.

5.2. Generation of *S. pombe* Myo1 IQ mutant strains.

Having determined *in vitro* that phosphorylation within the Myo1 IQ domains at serine-742 may influence which calmodulin light chain binds to the myosin, the effect of this phosphorylation event was explored *in vivo*. Strains were generated in which the sequence encoding serine-742 was replaced at the genomic locus of *myo1* with either an alanine codon (*myo1-S742A*) or an aspartic acid codon (*myo1-S742D*). The *myo1-S742A* strain prevents a phosphate group being added at residue 742, while the *myo1-S742D* strain mimics a constitutively phosphorylated state. This section describes the methods used to generate and confirm these mutant strains.

Firstly, molecular biology techniques were used to replace the serine-742 coding sequence for that of an alanine or glutamic acid. Figure 5.4 shows the plasmid map of the pTOPO based vector (M13 – lab stock) used for all cloning steps. This vector contains cDNA encoding the full length Myo1 protein and a *URA4* gene, for selection. Either side of this sequence are ~ 250 bp of flanking region, from upstream and downstream of the genomic *myo1* gene sequence. The locations of relevant restriction sites and the S742 codon are indicated. Figure 5.4 shows the cloning strategy used to replace the serine-742 sequence in the *pTOPO-myo1:URA4* vector, with the sequence encoding each mutation.

Introduction of both ‘A’ and ‘D’ mutations removes the Bgl II site present in M13 (Figure 5.4.C). Correct clones were identified by removal of this site and confirmed by sequencing. Fragments from the resulting plasmids – v688 (*pTOPO-myo1-S742A*) and v739 (*pTOPO-myo1-S742D*) were used for transformation of *S. pombe* cells and subsequent cloning steps.

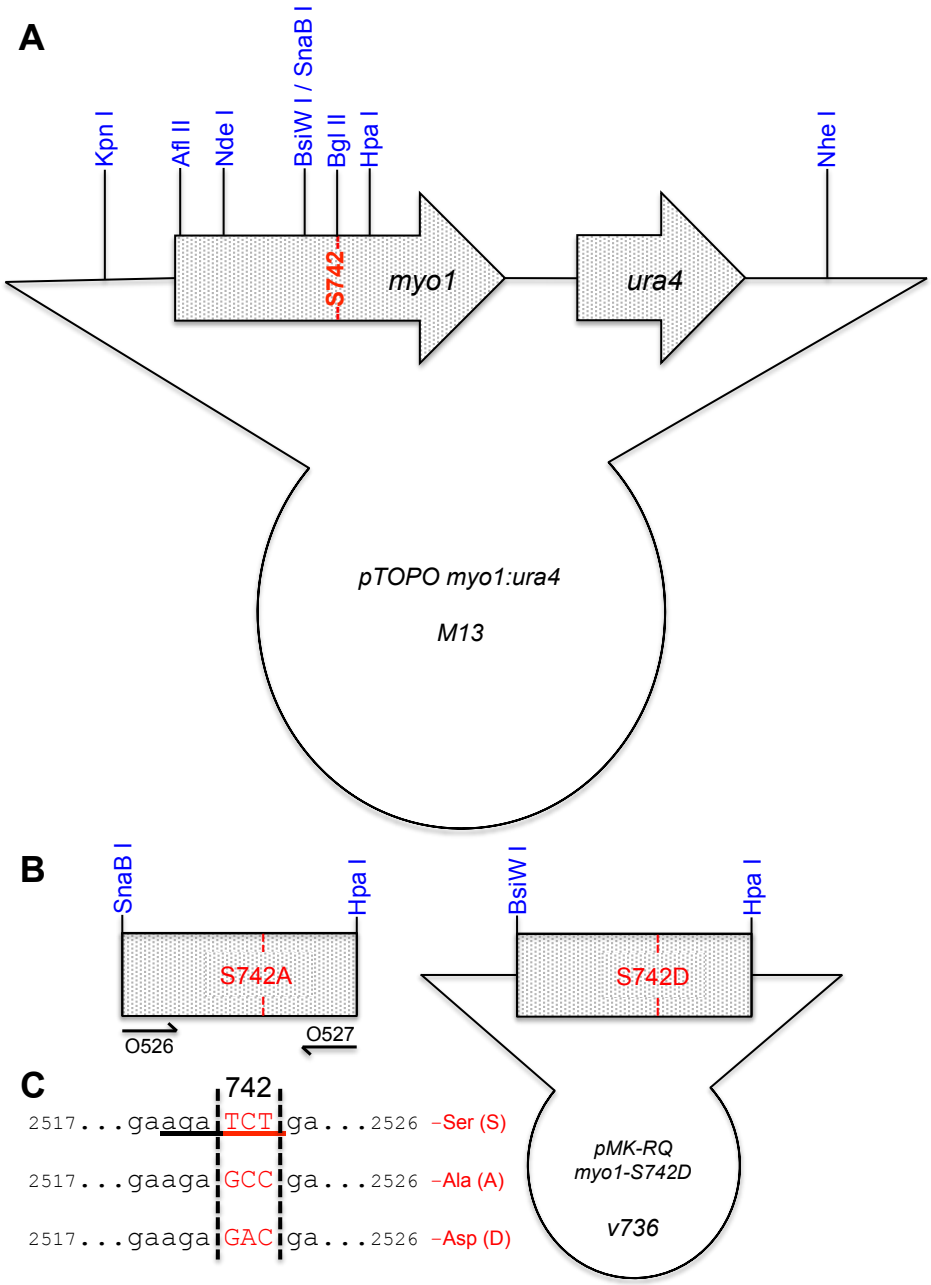

Figure 5.4. Cloning of *myo1-742* mutant sequences for yeast transformation.

(A) Plasmid map of the *pTOPO-myo1:URA4* vector used for cloning of *myo1-S742A* and *myo1-S742D* sequences. (B) Generation of fragments of DNA for replacement of part of the *myo1* gene of M13, between the indicated restriction enzyme sites. (C) shows details of the mutations introduced to encode an alanine or aspartic acid residue. The native serine codon forms part of a Bgl II restriction enzyme site (underlined). Substitution of this codon, in the case of both mutants, removes this Bgl II restriction site.

A KpnI-NheI fragment was removed from these vectors and used in a yeast transformation, as described in Section 2.4.2. The *S. pombe* strain used for this transformation, was *myo1:LEU2 ura4.d18* (201) in which a *LEU2* gene (budding yeast functional homologue of the *S. pombe leu1*$^{+}$ gene) had been introduced to mark the *myo1* gene at the genomic locus. Recombination between the flanking regions upstream of the *myo1* gene, and downstream of the amino acid selection marker, resulted in replacement of the *LEU2* gene with *URA4*, along with introduction of DNA encoding the appropriate *myo1-742* mutation.

Following amino acid selection of URA^{+} *LEU*$^{-}$ strains, genomic DNA was extracted and a region of the *myo1* gene amplified by PCR. All mutant strains were checked for removal of the Bgl II restriction site from the amplified PCR product. Figure 5.5 shows a typical example of the confirmation of a correct *myo1-S742A* clone. When compared with the same region amplified from the genomic DNA of a wild type strain, equivalent undigested PCR fragments are seen at 3.64 kbp. When the wild type PCR fragment is digested with Bgl II, two fragments are seen at 2.21 kbp and 1.43 kbp. The PCR product amplified from the *myo1-S742A* strain remains undigested, confirming replacement of the *myo1-742* codon.

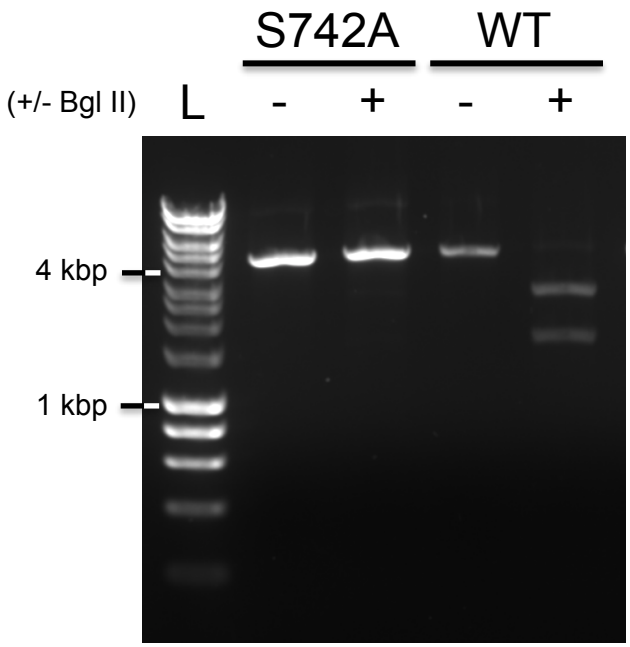

Figure 5.5. Restriction digests of *myo1* genomic DNA to confirm introduction of mutations.

Ethidium bromide stained agarose gel, showing the 3.64 kbp region of the *myo1* gene amplified by PCR from genomic DNA extracted from wild type (WT) or *myo1-S742A* (S742A) cells. Lanes headed ' - ' are DNA without the addition of BglII restriction enzyme, DNA in lanes headed ' + ' are following a 1 hr digest with BglII.

5.3. Characterisation of *S. pombe* Myo1 IQ mutant strains.

Having identified and confirmed correct *myo1-S742A* and *myo1-S742D* clones, the effect of these mutations *in vivo* were investigated. Neither mutation resulted in any significant visual phenotypic characteristics or temperature sensitivity. Next, the growth rates of *myo1-S742A* and *myo1-S742D* cells, were compared to wild type and *myo1*Δ cells. Figure 5.6 shows the average OD_{600} growth curves of 3 separate cultures of each strain, measured at 25 ºC, until stationary phase was reached. The growth rate of *myo1-S742A* (red line) is identical to that of wild type cells (black line). The *myo1-S742D* (blue line) cultures grew marginally faster than wild type, although this change was small when compared to the reduction in growth caused by complete deletion of the *myo1* gene (green line). This indicates

that any effect of phosphorylation at the Myo1-S742 residue is likely to result in subtle changes in Myo1 regulation during the mitotic cell cycle.

It is not known what kinase phosphorylates Myo1 at serine-742, or if this phosphorylation event is regulated at specific stages of the cell cycle or under certain growth conditions. The similarity of the *myo1-S742A* growth curve to wild type, may suggest that Myo1 is normally in an un-phosphorylated state under these standard growth conditions. Mimicking a phosphorylated state in *myo1-S742D* cells appears to slightly enhance the rate of growth, suggesting that this phosphorylation event may increase the efficiency of cell growth. This increase in growth indicates that in wild type cells, Myo1 may only be in a phosphorylated state briefly, or only be required under stress conditions.

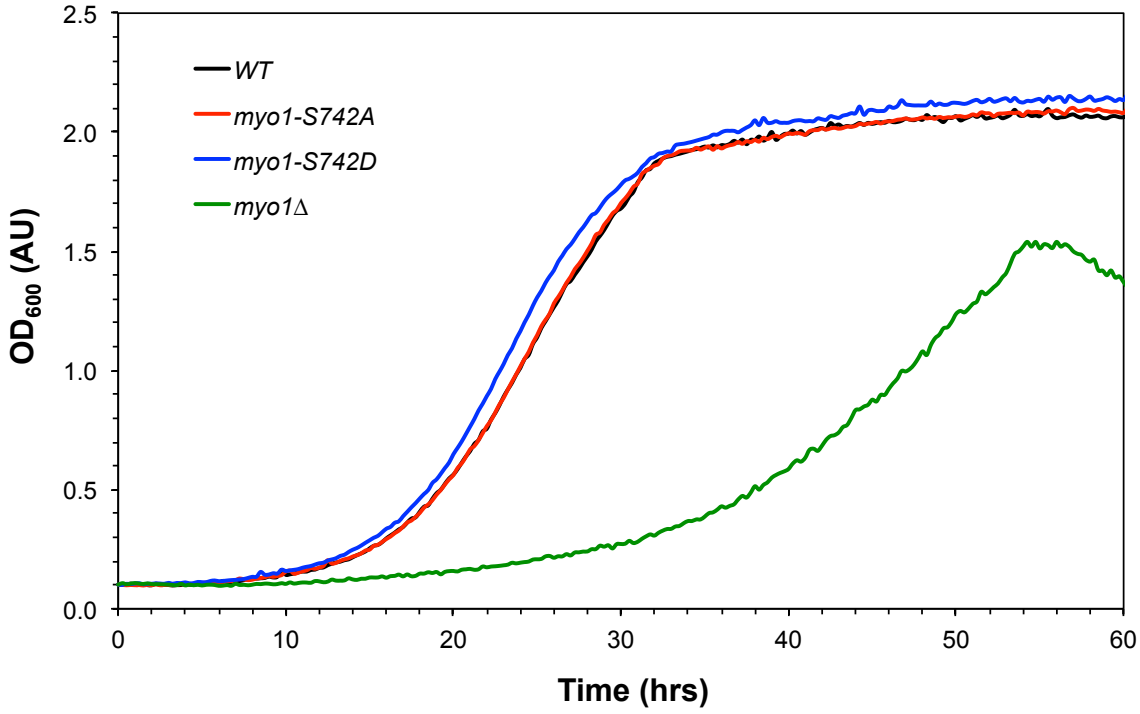

Figure 5.6. Growth curves of *S. pombe myo1* mutant strains.

OD_{600} growth curves of *myo1-S742A* (red) and *myo1-S742D* (blue) strains, with wild type (black) and *myo1*Δ (green) strains for comparison. All cultures were grown in 1 ml of EMMG media at 25 ºC.

Next the effect that these phosphorylation mutants have on the localisation of Myo1 was investigated. The effect of a *myo1-S742A* mutation was initially made by STORM super-resolution imaging (section 1.18.5), of *myo1-S742A* and wild type cells. Anti-Myo1 immunofluorescence samples were prepared as described in materials and methods (section 2.6.5) using an AlexaFluor-647 linked secondary antibody for imaging. AlexaFluor-647 is a photo-switchable fluorophore allowing resolution of single molecules using STORM imaging. Super-resolution images of Myo1 localisation in wild type and *myo1-S742A* cells were acquired using an iLas based STORM imaging system (Steve Tovey – University of Cambridge). These images suggest that there are subtle differences in Myo1 localisation in the absence of Myo1-S742 phosphorylation. In wild type cells there appears to be a greater number of more intense white foci. More intense foci are detected as a result of more AlexaFluor647 molecules emitting photons and are therefore proportional to the amount of Myo1 present.

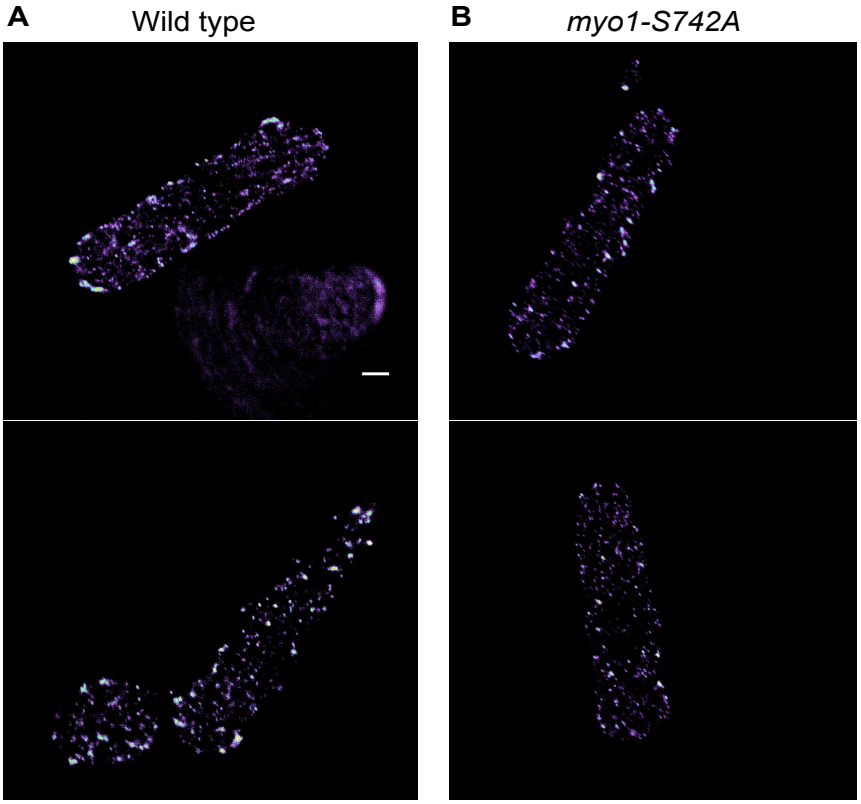

Figure 5.7. STORM images of wild type and *myo1-S742A* cells.

STORM super-resolution images of fixed Anti-Myo1 - AlexaFluor647 labelled immunofluorescence samples of wild type (A) and *myo1-S742A* (B) cells. Scale bar represents 1 μm.

5.4. Generation of fluorescently labelled *S. pombe* Myo1 IQ mutant strains.

Having observed subtle differences in Myo1 localisation in fixed *myo1-S742A* cells, using STORM super-resolution imaging, fluorescently labelled *S. pombe myo1-S742* mutant strains were generated. These strains allowed potential effects of this phosphorylation event on Myo1 dynamics to be investigated, and quantified, in live cells. The same *pTOPO-myo1:URA4* vector was used for generation of DNA for use in *S. pombe* transformations, to generate strains with the genomic copy of *myo1*, or *myo1* mutant, labelled with mCherry or mNeongreen at the N-terminus. Figure 5.8 shows the cloning strategy used for introduction of these fluorophores at the 5' end if the *myo1* gene, into the M13 vector containing the 'wild type' *myo1* sequence. The same strategy was used with the *myo1-S742A* and *myo1-S742D* sequences contained in the plasmids generated by cloning described in section 5.2. (Figure 5.4)

DNA was synthesized containing the upstream promoter region of *myo1*, the sequence encoding mCherry, and the first 730 bp of the *myo1* gene as a KpnI-NdeI fragment. Equivalent DNA was synthesized containing the mNeongreen sequence as a KpnI-Afl II fragment. These fragments were ligated into the appropriately digested M13, v688 and v739 vectors to produce DNA encoding fluorescently labelled Myo1 with a serine, alanine or aspartic acid at residue 742. All plasmid constructs were checked by sequencing, and a KpnI-NheI fragment was again used to transform *myo1:LEU2 ura4.d18* cells. Correct colonies were identified by amino acid selection, followed by screening for mCherry or mNeongreen fluorescence. Presence of *myo1-742A* and *myo1-742D* mutations were also confirmed with a Bgl II digest of genomic DNA, as shown in Figure 5.5.

For comparison of the localisation and dynamics of Myo1 in *myo1*$^{+}$ and *myo1-S742* mutants, mNeongreen strains were used due to the this fluorophore being brighter and more photo-stable than mCherry. An added advantage of mNeongreen over many other fluorescent proteins, is its monomeric and has a rapid protein folding time (Shaner et al. 2013).

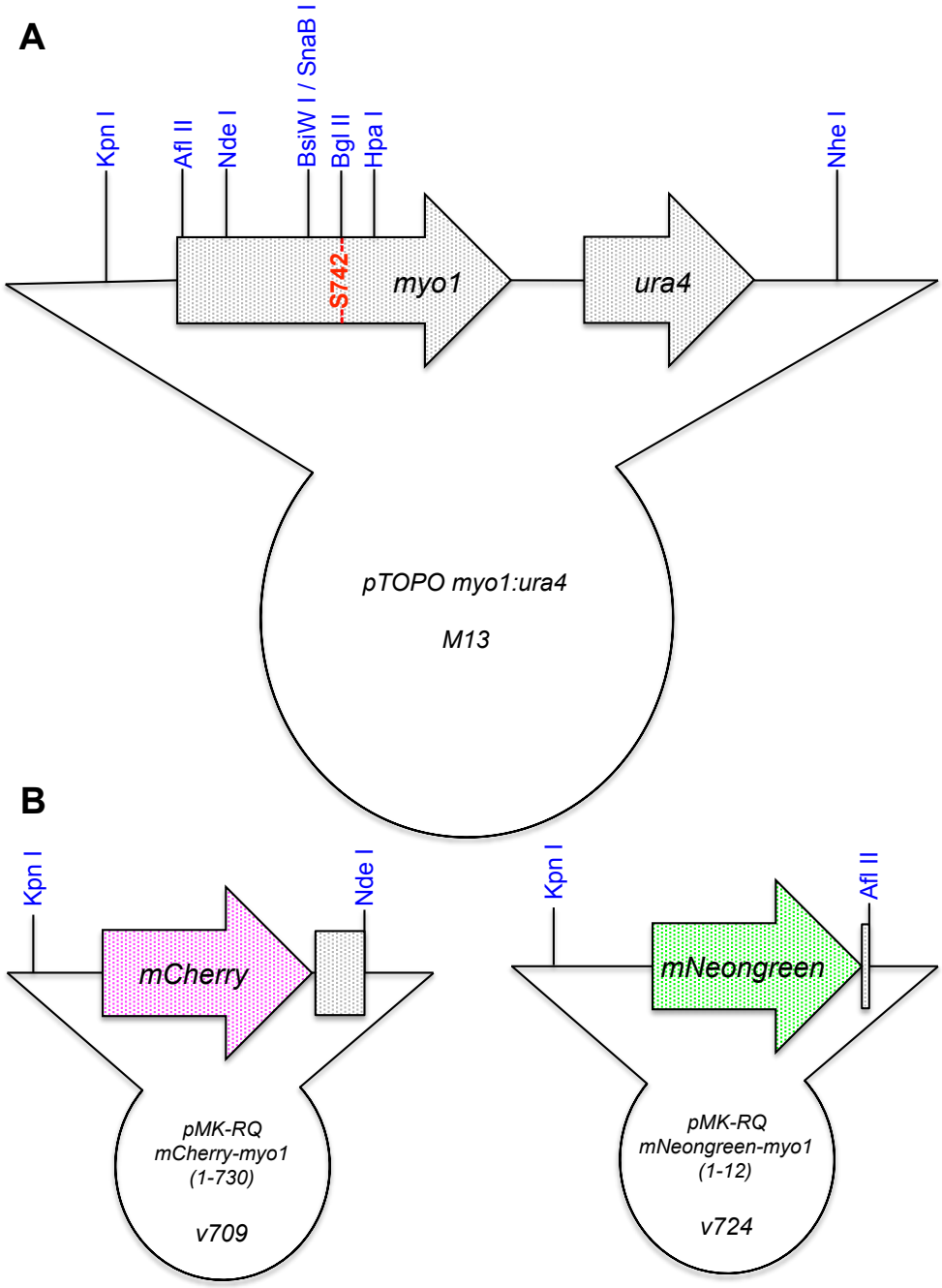

Figure 5.8. Cloning of fluorescently labelled *myo1-742* sequences for yeast transformation.

(A) Map of the *pTOPO-myo1:URA4* vector used for cloning of *mCherry-myo1 and mNeongreen-myo1* sequences. (B) Generation of fragments of DNA for replacement of the 5' end of the *myo1* gene of M13, between the indicated restriction enzyme sites.

5.5 Characterisation of the dynamics and localisation of Myo1 and Myo1-S742A.

For imaging, an *mNeongreen-myo1 sid4-tdTomato* strain was generated, the red labelled, SPB component allowed identification of these cells from *mNeongreen-myo1-S742A* cells in mix experiments. Figure 5.9.A shows a maximum projection image of *mNeongreen-myo1 sid4-tdTomato* and *mNeongreen-myo1-S742A* cells. Analysis of mNeongreen-Myo1 fluorescence and detection of foci in these cells (Figure 5.9B-C) is consistent with the observations made from STORM imaging. Although the average size of each focus is not significantly different, less mNeongreen-Myo1 fluorescence is detected. In addition, there are fewer detected foci per cell, indicating that in the absence of phosphorylation at Myo1-S742 less Myo1 is incorporated into endocytic patches.

A

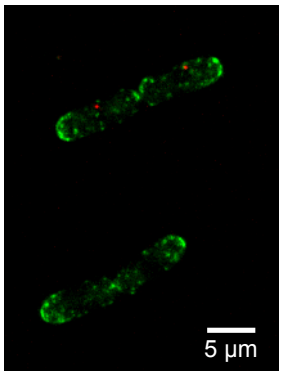

B

	mNeonGreen-myo1	*mNeonGreen-myo1-S742A*	Statistical significance (*P* value)
Whole cell fluorescence (AU)	9,453,813	8,092,682	0.8628
Cell size (µm²)	98.9	83.5	0.0863
Maximum intensity (AU)	33,477	30,798	0.1446
Number of foci	15.9	13.1	0.0203
Average foci volume (µm³)	0.98	0.96	0.8595
Total foci volume (µm³)	15.2	11.4	0.0020
Total foci fluorescence (AU)	139,712	105,768	0.0061
n =	32	30	

C

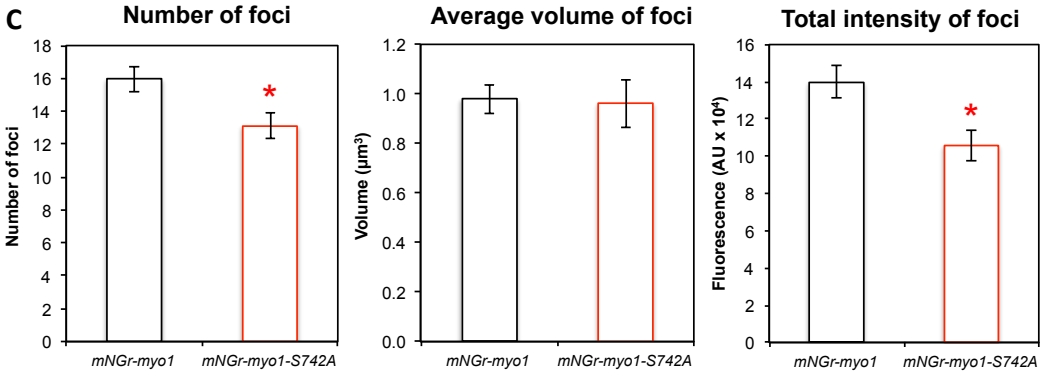

Figure 5.9. Analysis of mNeongreen-Myo1 and mNeongreen-Myo1-S742A foci.

(A) A typical maximum projection of 31 z-plane images of *mNeongreen-myo1 sid4-tdTomato* and *mNeongreen-myo1-S742A* cells. (B-C) Summary of mNeongreen-Myo1 fluorescence in these cells. Error bars indicate standard error values. ‘ * ‘ Denotes statistical significance of $p < 0.05$.

Next, the dynamics of Myo1 and Myo1-S742A proteins in these cells were analysed from kymographs generated from single z-plane timelapse images of *mNeongreen-myo1* and *mNeongreen-myo1-S742A* cells (Figure 5.10.A). Over 250 of these events were used to calculate the average duration of Myo1 dynamics at the membrane in each strain (Figure 5.10.B). In cells containing the native serine-742, mNeongreen-Myo1 forms foci at the membrane that persist, on average, for 13.9 seconds. This is consistent with previous data published, showing GFP-myo1 foci have a lifetime of ~15 seconds (Attanapola et al. 2009). In *mNeongreen-myo1-S742A* cells, the duration of these Myo1 events are significantly reduced, to on average, 10.9 seconds.

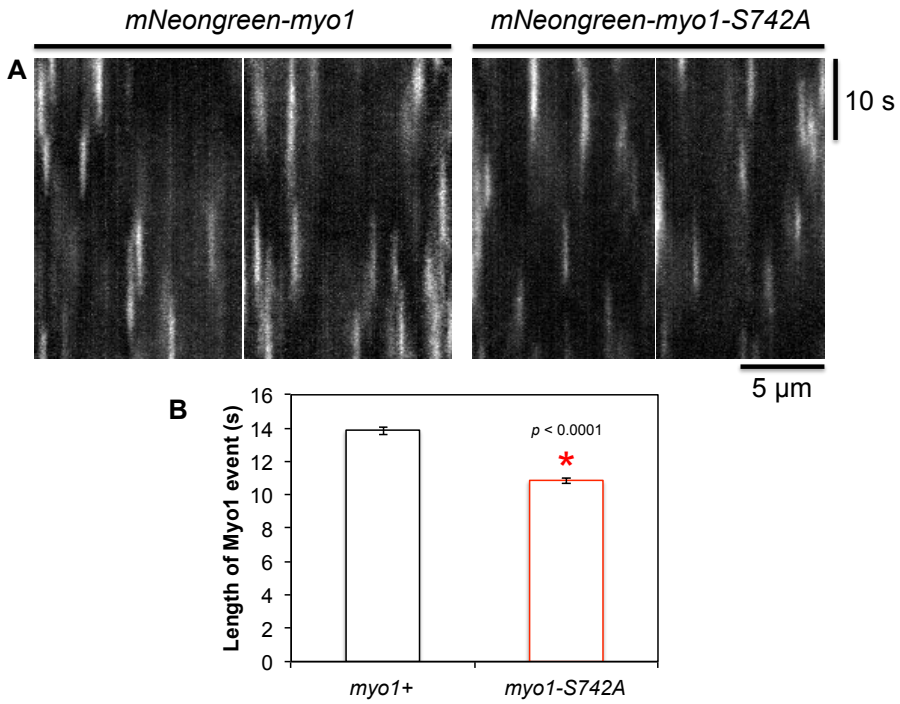

Figure 5.10. Analysis of mNeongreen-Myo1 and mNeongreen-Myo1-S742A dynamics.

(A) Typical kymographs generated from single z-plane timelapse images of *mNeongreen-myo1* and *mNeongreen-myo1-S742A* cells. The average measurements of the duration of >250 of these Myo1 events in each strain are shown in the histogram in (B). Error bars indicate standard error values.

5.6. Effect of *myo1-742* mutations on calmodulin binding *in vivo*.

The data presented in section 5.1. showed that Cam2 bound more tightly than Cam1 to the Myo1-S742D FRET protein. It was next investigated whether this change in affinity *in vitro*, results in noticeable changes in calmodulin localisation or dynamics in cells. Cam1-GFP fluorescence was analysed in *myo1*$^{+}$ and *myo1-S742A* genetic backgrounds (Figure 5.11).

A

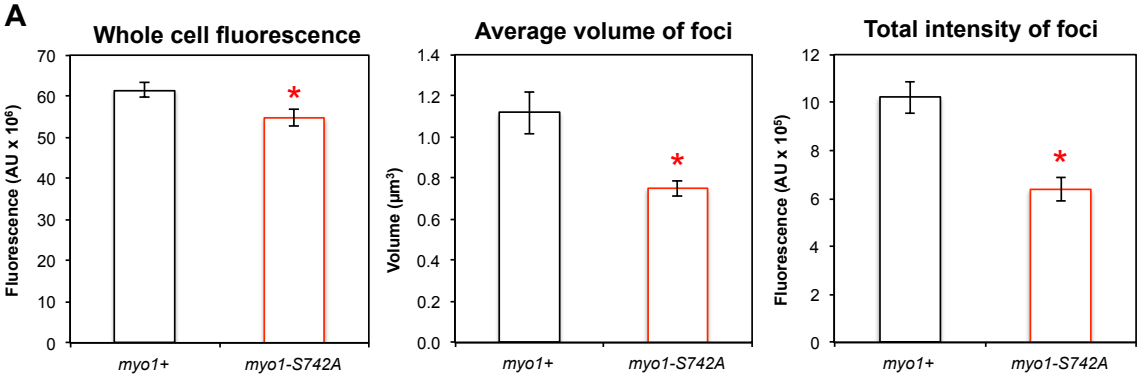

B

	cam1-gfp (myo1⁺)	*cam1-gfp myo1-S742A (myo1-S742A)*	Statistical significance (*P* value)
Whole cell fluorescence (AU)	61,530,900	54,744,700	0.0197
Cell size (µm²)	86.1	85.3	0.9271
Maximum intensity (AU)	251,700	207,550	0.0563
Number of foci	14.1	13.5	0.6960
Average foci volume (µm³)	1.12	0.75	0.0081
Total foci volume (µm³)	14.33	9.80	0.0004
Total foci fluorescence (AU)	1,020,350	638,090	0.0002
n =	25	15	

C

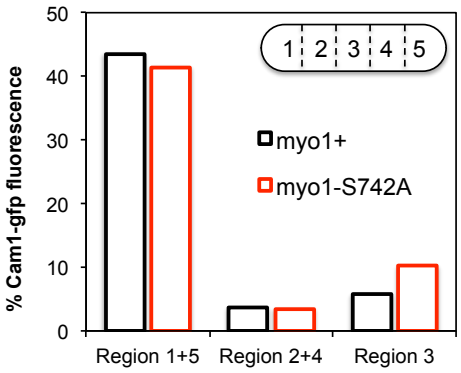

Figure 5.11. Analysis of Cam1-GFP foci in *myo1*$^{+}$ and *myo1-S742A* strains.

(A-B) Summary of analysis of Cam1-GFP foci from *cam1-gfp myo52-tdTomato* (*myo1*$^{+}$) and *cam1-gfp myo1-S742A* cells. Error bars indicate standard error values. (C) shows the % of Cam1-GFP fluorescence detected, relative to each region of the cell, for both strains. ' * ' Denotes statistical significance of $p < 0.05$.

There is a small although not statistically significant reduction in the number of Cam1 foci, which is consistent with the reduced number of Myo1 foci detected in *myo1-S742A* cells (Figure 5.9.B). On average these foci are smaller and contain less Cam1-GFP fluorescence (Figure 5.11.A). This is again consistent with the reduced levels of mNeongreen-Myo1-S742A detected in foci. The larger reduction in Cam1-GFP foci fluorescence in *myo1-S742A* cells (40%) when compared to Myo1 (25%) would suggest a cumulative effect of less Myo1 recruited to patches, and Cam1 binding more weakly to the Myo1 that is present.

There is also a small, but significant, reduction in the overall levels of Cam1-GFP fluorescence in *myo1-S742A* cells. There was no change in the polarized distribution of Cam1, with >80% of Cam1-GFP foci localising to the cell tips in both *myo1*$^{+}$ and *myo1-S742A* strains (Figure 5.11.C).

The dynamics of Cam1-GFP protein were also compared between *myo1*$^{+}$ and *myo1-S742A* cells from kymographs generated from single z-plane timelapse images (Figure 5.12.A). As with mNeongreen-Myo1-S742A, Cam1-GFP localises to cortical patches at the membrane in *myo1-S742A* cells, with the same stationary dynamics. Measurement of the duration of over 250 of these events, show a significant reduction in the length of time these foci persist at the membrane (Figure 5.12.B). In *myo1*$^{+}$ cells, the lifetime of Cam1-GFP foci is on average 10.4 seconds, however in *myo1-S742A* cells, this is reduced by 10%, to on average 9.4 seconds. This result is consistent with the shorter Myo1 events seen at the membrane, although the lifetime of Myo1 foci were reduced by over 20%.

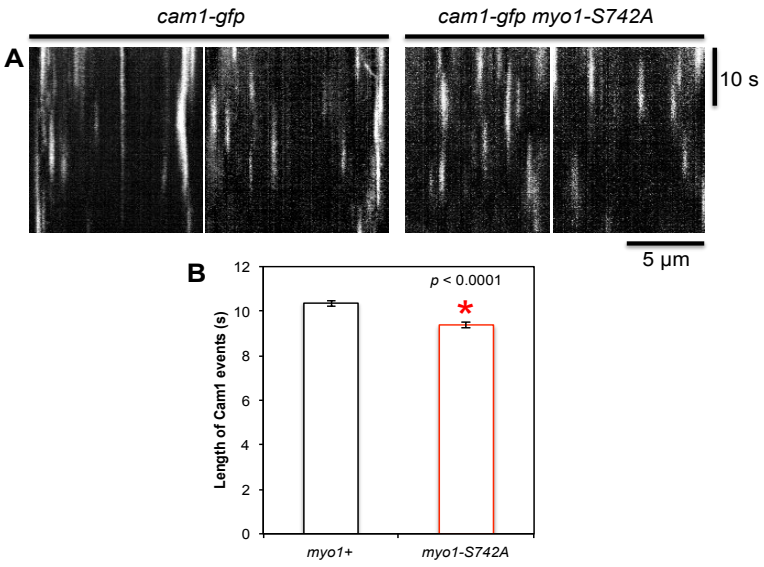

Figure 5.12. Analysis of Cam1-GFP dynamics in *myo1*$^{+}$ and *myo1-S742A* strains.

(A) Typical kymographs generated from single z-plane timelapse images of *cam1-gfp* and *cam1-gfp myo1-S742A* cells. The average measurements of the duration of >250 of these Myo1 events in each strain are shown in the histogram in (B).

These data show that Cam1 binds less strongly to the un-phosphorylated form of the Myo1 IQ domains *in vitro*, and that in the cell, this results in smaller foci, formed of less Cam1 protein, which associates with endocytic patches for a reduced period of time. It was next determined what effect mimicking a constitutively phosphorylated form of the Myo1 IQ domains, has on Cam1 localisation in the cell.

Cam1-GFP foci were detected from mix images of *cam1-gfp myo52-tdTomato* and *cam1-gfp myo1-S742D* cells (Figure 5.13). There are not the reciprocal increases in foci fluorescence, which may be expected as a contrast to the *myo1-S742A* data. When compared to *myo1*$^{+}$ cells, there is a 15% reduction in the size of Cam1 foci, which reduces the total Cam1-GFP being incorporated into foci. However this decrease in Cam1 incorporation into foci, is not as large as the 30% reduction in the size of Cam1-GFP foci seen in *myo1-S742A* cells.

A

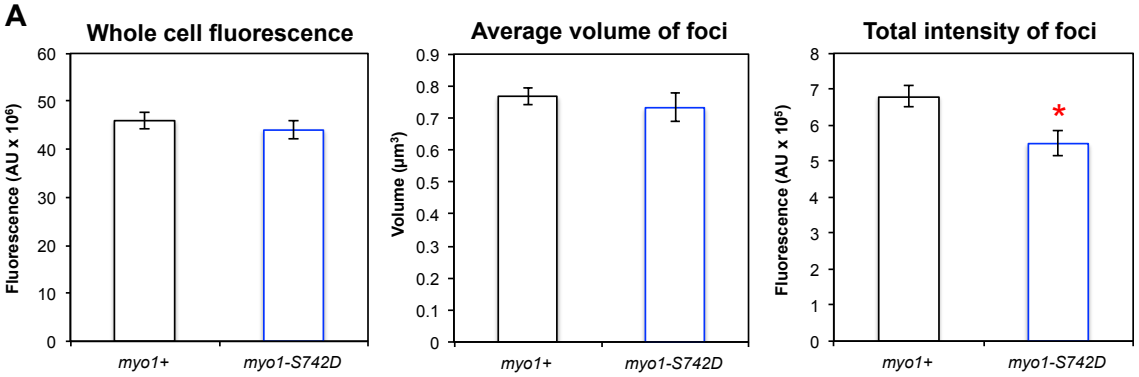

B

	cam1-gfp (myo1⁺)	*cam1-gfp myo1-S742D (myo1-S742D)*	Statistical significance (*P* value)
Whole cell fluorescence (AU)	45,979,000	44,024,800	0.4338
Cell size (µm²)	85.7	88.1	0.7899
Maximum intensity (AU)	221,350	202,100	0.1967
Number of foci	15.4	14.2	0.2376
Average foci volume (µm³)	0.77	0.73	0.5052
Total foci volume (µm³)	11.65	9.95	0.0261
Total foci fluorescence (AU)	680,500	549,010	0.0061
n =	25	22	

Figure 5.13. Analysis of Cam1-GFP foci in *myo1*⁺ and *myo1-S742D* strains.

(A-B) Summary of analysis of Cam1-GFP foci from *cam1-gfp myo52-tdTomato* (*myo1*⁺) and *cam1-gfp myo1-S742D* cells. Error bars indicate standard error values. ‘ * ‘ Denotes statistical significance of $p < 0.05$.

The effect of the *myo1-S742A* mutation on Cam2-GFP localisation and dynamics was also explored. There were no significant differences in the Cam2-GFP fluorescence or foci distribution in mid-log cultures of *cam2-gfp myo1-S742A* cells analysed (Figure 5.14). There was also no apparent effect on the oscillating lateral movements of Cam2-GFP as it is internalised with endocytic vesicles.

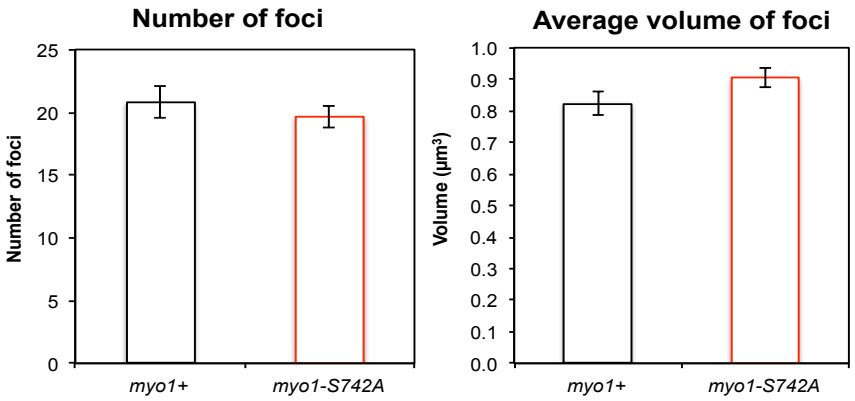

	Cam2-GFP (myo1⁺)	*cam2-GFP myo1-S742A (myo1-S742A)*	Statistical significance (*P* value)
Whole cell fluorescence (AU)	39,259,937	39,779,825	0.8063
Cell size (µm²)	79.3	70.7	0.2385
Maximum intensity (AU)	267,547	261,782	0.6339
Number of foci	20.8	19.6	0.4155
Average foci volume (µm³)	0.82	0.91	0.0737
Total foci volume (µm³)	16.53	17.35	0.4287
Total foci fluorescence (AU)	859,161	914,811	0.3374
n =	20	31	

Figure 5.14. Analysis of Cam2-GFP foci in *myo1*⁺ and *myo1-S742A* strains.

A summary of analysis of Cam2-GFP foci from *cam2-gfp myo52-tdTomato* (*myo1*⁺) and *cam2-gfp myo1-S742D* cells. Error bars indicate standard error values.

5.7. Effect of *myo1-742* mutations on other components of the cytoskeleton.

Following observations of small changes in Myo1 dynamics at endocytic patches, next, any changes in actin localisation were investigated. Cells containing an *mCherry-Lifeact* actin marker or *acp1-gfp* labelled actin capping protein, were crossed with *myo1-S742A* and *myo1-S742D* strains.

Analysis of Lifeact foci detected in these strains are summarised in Figure 5.15. These data show that, as for calmodulin, disruption of *myo1-S742* by either alanine or aspartic acid, both result in similar changes in Lifeact fluorescence, although these are small. In both *myo1-S742A* and *myo1-S742D* cells, there are slightly less foci, which have a significantly larger volume. In both strains, this is the only significant change in Lifeact fluorescence caused by changing the phosphorylation state of the Myo1 serine-742 residue.

The fluorescence of Acp1-GFP was also compared in *myo1*$^{+}$, *myo1-S742A* and *myo1-S742D* strains. The results of this analysis are summarised in Tables 5.1. and 5.2. In contrast to the small increase in actin patch fluorescence, *myo1-S742A* and *myo1-S742D* mutations did not cause any significant changes in Acp1-GFP fluorescence. As Acp1 forms part of the capping complex at branched ends of actin filaments, this data would suggest that the increases in Lifeact fluorescence are a result of longer actin filaments rather than an increased number of filaments.

A

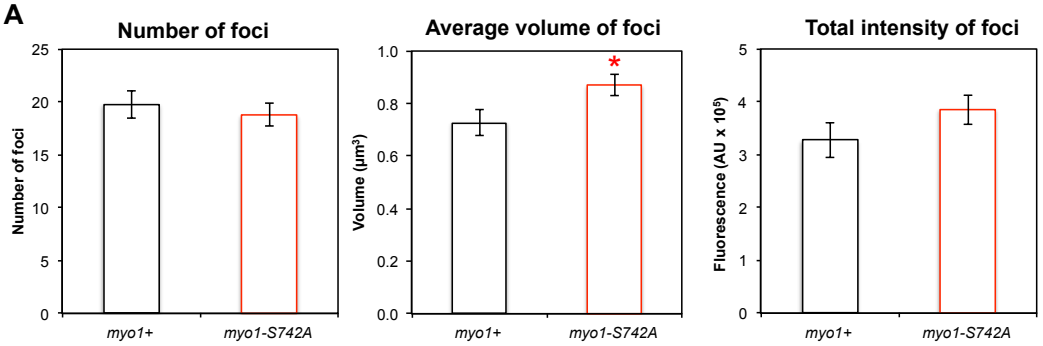

B

	Lifeact (myo1⁺)	*Lifeact myo1-S742A (myo1-S742A)*	Statistical significance (*P* value)
Whole cell fluorescence (AU)	17,116,300	19,474,850	0.0936
Cell size (µm²)	84.5	85.7	0.8787
Maximum intensity (AU)	94,671	100,487	0.4403
Number of foci	19.8	18.7	0.5502
Average foci volume (µm³)	0.73	0.87	0.0346
Total foci volume (µm³)	13.96	16.01	0.1771
Total foci fluorescence (AU)	327,017	385,243	0.1832
n =	23	23	

C

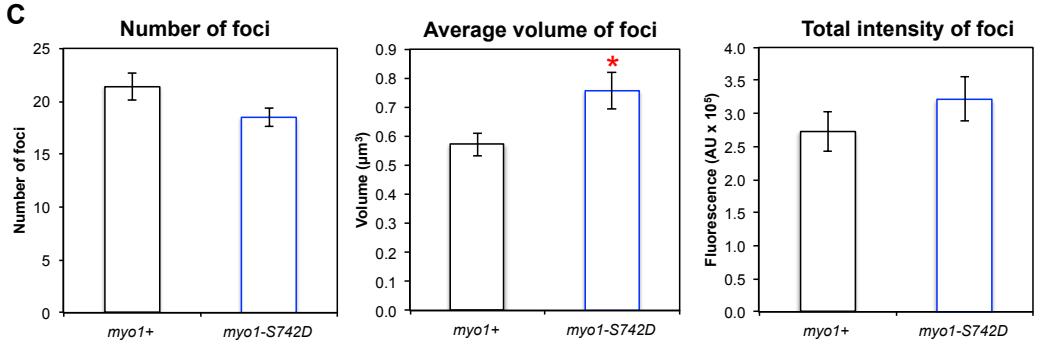

D

	Lifeact (myo1⁺)	*Lifeact myo1-S742D (myo1-S742D)*	Statistical significance (*P* value)
Whole cell fluorescence (AU)	16,420,220	17,524,450	0.4230
Cell size (µm²)	81.5	86.8	0.4370
Maximum intensity (AU)	78,103	84,872	0.3309
Number of foci	21.4	18.5	0.0606
Average foci volume (µm³)	0.57	0.76	0.0195
Total foci volume (µm³)	12.30	14.02	0.3191
Total foci fluorescence (AU)	273,100	321,540	0.2920
n =	20	23	

Figure 5.15. Analysis of Lifeact foci in *myo1*⁺, *myo1-S742A* and *myo1-S742D* strains.

Analysis of Lifeact foci from mix images of *Lifeact mNeongreen-myo1* (labelled *myo1*⁺) and *Lifeact myo1-S742A* or *Lifeact myo1-S742D* cells. Error bars indicate standard error values. ‘ * ‘ Denotes statistical significance of $p < 0.05$.

Table 5.1. Analysis of Acp1-GFP in *myo1*$^{+}$ and *myo1-S742A* cells.

	***acp1-gfp* (*myo1*$^{+}$)**	***acp1-gfp myo1-S742A* (*myo1-S742A*)**	Statistical significance (*P* value)
Whole cell fluorescence (AU)	20,347,500	21,988,300	0.2441
Cell size (μm^2)	73.1	73.8	0.9298
Maximum intensity (AU)	126,000	123,700	0.7297
Number of foci	16.3	17.4	0.4722
Average foci volume (μm^3)	0.54	0.53	0.8073
Total foci volume (μm^3)	8.30	8.85	0.4101
Total foci fluorescence (AU)	289,400	305,200	0.5322
n =	22	26	

Table 5.2. Analysis of Acp1-GFP in *myo1*$^{+}$ and *myo1-S742D* cells.

	***acp1-gfp* (*myo1*$^{+}$)**	***acp1-gfp myo1-S742D* (*myo1-S742D*)**	Statistical significance (*P* value)
Whole cell fluorescence (AU)	18,507,350	19,519,600	0.3272
Cell size (μm^2)	68.5	72.1	0.2957
Maximum intensity (AU)	115,400	120,700	0.4275
Number of foci	15.0	15.6	0.6092
Average foci volume (μm^3)	0.52	0.51	0.7132
Total foci volume (μm^3)	7.68	7.63	0.9245
Total foci fluorescence (AU)	257,690	260,970	0.8597
n =	26	36	

5.8. NETO is inhibited in cells expressing the phosphorylation-null Myo1-S742A.

Data in this chapter so far shows that a *myo1-S742A* mutation results in Myo1 and its associated light chain, Cam1, localising to endocytic patches for a shorter time. Less Myo1 and Cam1 are incorporated into these foci, but there is an increase in the amount of actin associated with these endocytic patches. Figure 5.11.C shows that the overall distribution of these patches – reported by Cam1-GFP – is not significantly affected in interphase cells. However to investigate this further, the localisation of endocytic patches was determined in newly divided cells, and followed as cells grew in length. In *S. pombe* cells, growth at the 'new' cell end created after cell division, begins once the cell reaches a length of ~9.5 µm (Mitchison & Nurse 1985). Initiation of growth at the new cell end is called 'new end take-off', (NETO). Endocytic patches localises to sites of cell growth, and have been shown to redistribute from the 'old' cell end, to the 'new' cell end once the cell reaches this critical length (J. Marks et al. 1986).

The method of analysis for NETO is detailed in Section 2.7.4. Maximum projections of 31 z-plane images taken at 3 minute intervals were used for this analysis, no single cell was imaged for more than 1 hour. Fluorescence at 'new' and 'old' cell ends was measured, along with cell length, throughout these timelapse images. The fluorescence intensity at the 'new' cell end was divided by the fluorescence intensity at the 'old' cell end to give a ratio, which was plotted against the cell length.

Firstly, the distribution of Cam1-GFP was measured in *myo1*$^{+}$ and *myo1-S742A* cells, the fluorescence ratio of new to old cell ends was plotted from the combined data of 10 growing cells (Figure 5.16). In *myo1*$^{+}$ cells (black line labelled WT), the fluorescence ratio >1 indicates that Cam1-GFP is initially localised at the 'new' cell end immediately after cell division. This is due to Cam1 concentrating at the cell equator at division. As cells elongate, Cam1-GFP fluorescence redistributes towards the old end. Once cells reach a length of ~ 10 µm, there is a distinct increase in the 'new' to 'old' end fluorescence ratio. The length at which there is a switch of Cam1 localisation to the new cell end is consistent with the reported

length of NETO (Mitchison & Nurse 1985). This suggests that Cam1 redistribution is co-ordinated with the sites of new growth associated with NETO.

In contrast, Cam1-GFP distribution in *myo1-S742A* cells (red line in Figure 5.16), does not show this same distinct pattern. The fluorescence ratio remains around 1 as cells grow, indicating a bi-polar localisation of Cam1 protein. The relatively small amount of data combined to plot the graph in Figure 5.16, along with Cam1-GFP bleaching during the time-course of the experiment, other strains were imaged and analysed to verify the trend in this data.

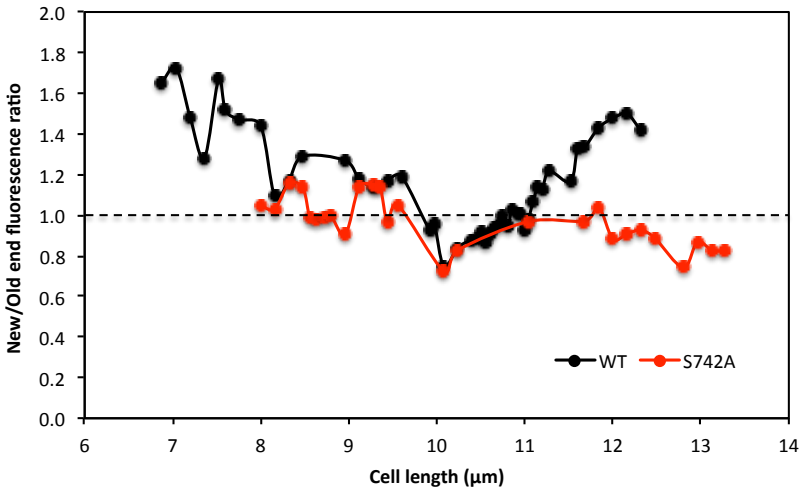

Figure 5.16. Effect of *myo1-S742A* mutation in Cam1-GFP distribution in growing *S. pombe* cells.

'New' / 'Old' cell end fluorescence ratios averaged from 10 growing mid-log *cam1-gfp myo52-tdTomato* (black line) and *cam1-gfp myo1-S742A* (red line) cells.

Figure 5.17. shows the equivalent data from *Lifeact* (black line – WT) and *Lifeact myo1-S742A* cells (red line), plotted from averaged data acquired from 12 cells. This graph shows actin localisation follows the same trends seen for Cam1-GFP. In *myo1*$^{+}$ cells, actin is concentrated at the cell equator immediately after cell division, resulting in a high fluorescence ratio. Actin then localises to the 'old' cell end, indicated by the New/Old end ratio of <1. Soon after cells reach the critical length of 9.5 µm, at which NETO takes place (Mitchison and Nurse 1985), Lifeact fluorescence begins to redistribute to the 'new' cell end. As for Cam1-GFP, in *myo1-S742A* cells, this significant increase in the Lifeact fluorescence ratio at ~ 9.5 µm is not seen.

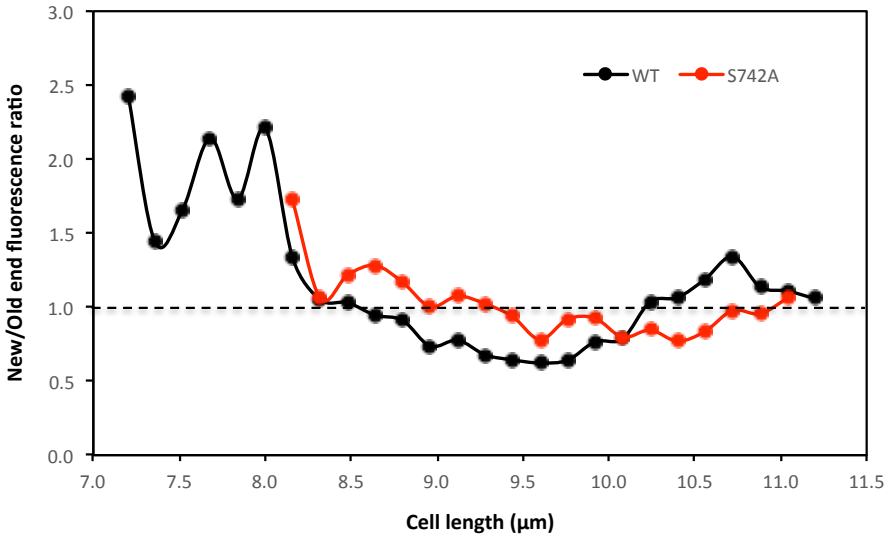

Figure 5.17. Effect of *myo1-S742A* mutation in Lifeact distribution in growing *S. pombe* cells.

'New' / 'Old' cell end fluorescence ratios averaged from 12 growing mid-log *lifeact mNeongreen-myo1* (black line) and *lifeact myo1-S742A* (red line) cells.

Finally, it was determined whether the lack of Cam1 and actin re-distribution in *myo1-S742A* cells was due to a change in the normal localisation of endocytic patches. In order to do this, the distribution of the early endocytic patch marker, Sla2 was observed. A *sla2-mCherry* strain was crossed with the *myo1-S742A* strain, and >30 cells imaged across a wide range of cell lengths. From the timelapse images of mix experiments with *sla2-mCherry YFP-myo1* cells, the same 'new' and 'old' cell end measurements were made as described previously (Figure 5.18).

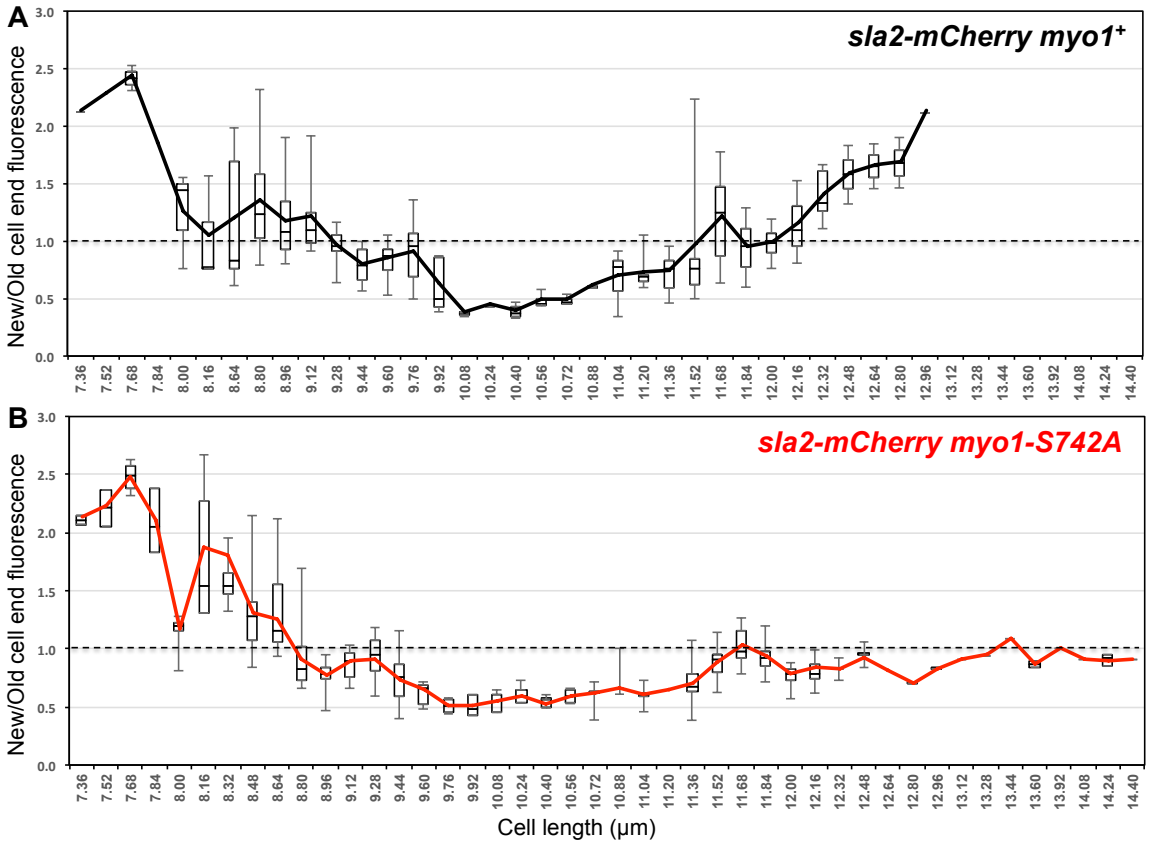

Figure 5.18. Effect of *myo1-S742A* mutation in Sla2 distribution in growing *S. pombe* cells.

'New' / 'Old' cell end fluorescence ratios averaged from >30 growing mid-log (A) *sla2-mCherry YFP-myo1* and (B) *sla2-mCherry myo1-S742A*. Boxes plot median and quartile for each length measured, lines are plotted from the mean average value at each length measured.

Figure 5.18.A shows the averaged data for *sla2-mCherry myo1*$^{+}$ cells. This again shows the movement of endocytic patches, away from the new cell end immediately after cell division, followed by re-distribution back to the new cell end after the cell reaches ~ 10 µm in length. Figure 5.18.B shows the equivalent data for Sla2-mCherry distribution in *myo1-S742A* cells. This confirms the inability of *myo1-S742A* cells to re-distribute the endocytic patches required at sites of cell growth during NETO. Sla2 localises to the cell equator during cell division, resulting in a 'new' to 'old' end fluorescence ration >1 in newly divided cells. Endocytic patches are able to accumulate at the old cell end, but when the cell reaches ~ 10 µm, Sla2 does not re-distribute to the new cell end. However the growth curves in Figure 5.6. would suggest that this does not impact on overall cell growth in *myo1-S742A* cells.

5.9. Myo1 serine residue S742 is phosphorylated prior to NETO.

To determine the phosphorylation status of Myo1 serine-742 in cultures of growing *S. pombe* cells, phosphospecific antibodies with generated against the following phosphorylated Myo1 IQ peptide sequence: RSYVRRR-S(PO3H2)-EAAAC (Eurogentec). Initial use of these anti-Myo1-S742 phospho-specific antibodies (α-Myo1-S742P*) in western blots of asynchronous mid-log *S. pombe* cultures did not result in a detectable band. Having shown that *myo1-S742A* cells appear to be unable to undertake NETO, it was next explored whether phosphorylation of Myo1 at serine-742, is dependent on the stage of the cell cycle. In order to do this, western blots of cell extracts from synchronous cultures, were probed with α-Myo1-S742P* antibodies. For these experiments, *cdc10-v50* and *cdc25-22* temperature sensitive mutants were used (Nurse 1975; J. Marks et al. 1992). Following arrest of these cells by a 4 hour incubation at 36 ºC, *cdc10-v50* cells were arrested at the G1-S transition point, before NETO, and *cdc25-22* cells arrested in G2 prior to entry into mitosis.

TCA extracts of cells from arrested synchronous cultures was used for a western blot along with asynchronous pre-arrest samples and wild type cells (Figure 5.19). These western blots show that the only band detected by α-Myo1-S742P* antibodies is in *cdc10-v50* arrested cell extracts. This implies that phosphorylation

of the serine-742 residue of Myo1 is required in a phosphorylated state prior to cells passing through the G1-S transition point and initiating NETO.

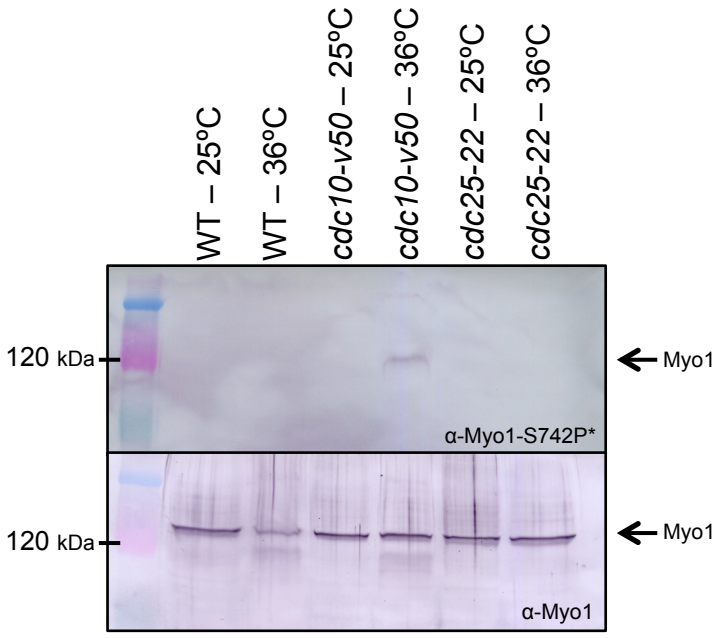

Figure 5.19. Western blot of synchronous *S. pombe* cell cultures.

TCA extracts of WT, *cdc10-v50* and *cdc25-22* cell cultures before and after incubation at 36 ºC for 4 hours. The top membrane was probed with α-Myo1-S742P* primary antibodies, the same extracts were also probed with α-Myo1 antibodies (bottom membrane).

To further explore the cell cycle control of Myo1-S742 phosphorylation, *cdc10-v50* cells were arrested, and the level of Myo1-S742 phosphorylation followed in the released synchronous culture. The culture of *cdc10-v50* cells were grown at 36ºC for 4 hours and quickly cooled to 25 ºC to generate a synchronous culture of cells proceeding through NETO and cell division.

From when the culture was released at 25 ºC (T=0), samples were taken every 20 minutes to make TCA extracts for western blotting, and a fixed cell sample for determining the septation index by Calcofluor staining. TCA extracts were made

as described in section 2.4.8. and a western blot carried out using the method described for a phospho-specific antibodies in section 2.3.2. Membranes labelled (A) in Figure 5.20. show the anti-Myo1-S742P* detected band in samples from the synchronous culture at each time point indicated.

Alkaline phosphatase detection method provides a quantitative measurement of the protein detected on a western blot. The density of each band on the western blot was calculated using ScnImage software. The solid red line in the graph in Figure 5.20.C shows that the level of Myo1 phosphorylation at serine-742 remains constant until around 160 minutes after *cdc10-v50* cells were released from the cell cycle arrest. The drop in levels of phosphorylation after 160 minutes, corresponds with an increase in the % of septating cells (black line).

The same membrane was then probed with anti-Myo1 antibodies, recognizing all Myo1 protein, (panels labelled (B) in Figure 5.20) Two bands can be seen, the upper band corresponds to the phosphorylated form of Myo1, also detected by the phophospecific Myo1-S742P* antibodies. The faster migrating band detected by anti-Myo1 antibodies, is the remaining population of un-phosphorylated Myo1. The density of the bands recognized by these anti-Myo1 antibodies are shown in Figure 5.20.C (dashed red line). This shows that the total levels of Myo1 in the cell do not fluctuate throughout the cell cycle.

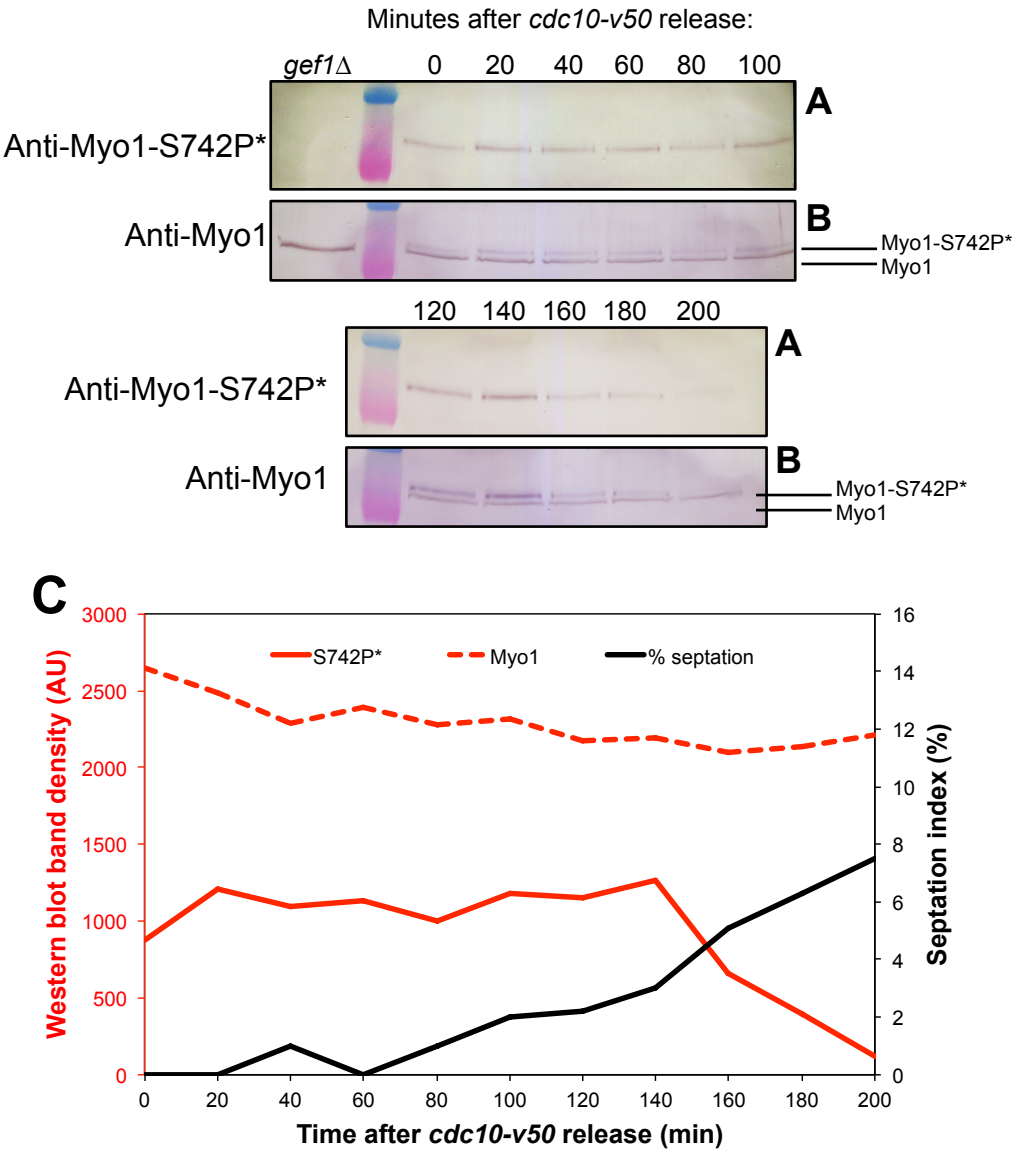

Figure 5.20. Western blots of TCA extracts from a synchronous culture of *cdc10-v50 S. pombe* cells.

Western blots of samples taken every 20 minutes after release of a *cdc10-v50* arrested synchronous culture. The blot was first probed with anti-Myo1-S742P* antibodies (A), and then anti-Myo1 antibodies (B). (C) Densitometry measurements of the bands in these blots are plotted along with the % of cells in the culture with septa.

These data show that a large proportion of Myo1 is phosphorylated at residue serine-742 when *S. pombe* cells are in G1 phase of the cell cycle. This also suggests that Myo1-S742 remains phosphorylated once cells pass through G1-S and begin NETO. Once NETO has occurred and the cell enters mitosis, Myo1-S742 is de-phosphorylated, (the increasing septation index at ~140 minutes would indicate the majority of cells are mitotic). Together with the observations of *myo1-S742A* cells not initiating NETO, it would appear that the Myo1-S742 residue must be phosphorylated for cells to carry out NETO.

5.10. Investigation of potential kinases for Myo1-S742 phosphorylation.

Having shown that Myo1-S742 is likely to be phosphorylated and de-phosphorylated at defined points of the cell cycle, it was investigated what kinases and phosphatases may be involved in this process.

The Myo1-S742 sequence forms part of a conserved AGC kinase consensus sequence (Figure 5.21.A) (Pearson & Kemp 1991). Gad8 is an AGC kinase which is phosphorylated by TORC2 (Section 1.5) a known regulator of the cytoskeleton and essential for cell survival under stress conditions (Matsuo et al. 2003). To investigate if Gad8, or any TORC2 dependent protein kinases were responsible for phosphorylation of Myo1, TCA cell extracts were made from *gad8*Δ and *ste20*Δ cells (*ste20*Δ specifically abolishes TORC2 function). Extracts from these cells were run on a PhosTag SDS-PAGE gel (Figure 5.21.B) which separates proteins based on molecular weight and relative to phosphorylation (Kinoshita et al. 2009). In wild type cell extracts probed with anti-Myo1 antibodies, three distinct bands can be visualised. In *myo1-S742A* cells, it would be expected that one of these bands was absent, which appears to be the fastest migrating band (Figure 5.21.B). This band is also absent in extracts of both *gad8*Δ and *ste20*Δ cells, with an additional band also absent in the *gad8*Δ strain.

A AGC kinase consensus:

```
   RxRxxS
WRSYVRRRSEAAACIQK   Sp Myo1   742
LLSRKRVRSFQAVAHGF   Sp Myo52  798
YIQRKRYLSLIKCAIVI   Sp Myo51  822
WLARRRFQSIRRFVLNI   Hs MyoVc  877
```

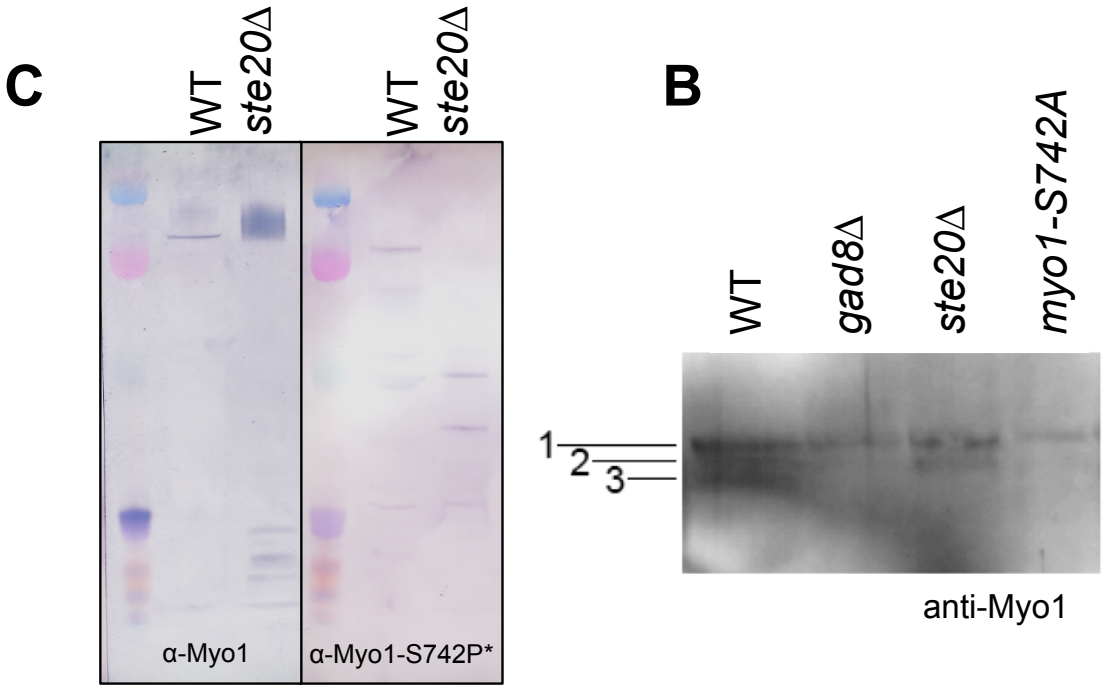

Figure 5.21. Investigation of Myo1 phosphorylation in *S. pombe* cells.

(A) Myo1-S742 is a partially conserved AGC kinase consensus site (RXRXXS). (B) anti-Myo1 probed western blot of TCA cell extracts run on a PhosTag gel. (C) Anti-Myo1 and anti-Myo1-S742P* western blots of TCA cell extracts from wild type and *ste20*Δ.

The potential TORC2 dependent regulation of Myo1-S742 phosphorylation was further explored using phospho-specific anti-Myo1-S742P* antibodies. Western blots of extracts from wild type and *ste20*Δ (Figure 5.21.C) cells also suggest that phosphorylation of this Myo1 residue is dependent on TORC2. Anti-Myo1 antibodies detected a smeared band of Myo1 protein, potentially indicating differential phosphorylation at multiple sites on the protein. None of these bands were detected by the anti-Myo1-S742P* antibodies. These data suggest that phosphorylation of Myo1-S742 is dependent on the TORC2 signalling pathway.

5.11. Investigation of potential phosphatases for Myo1-S742 de-phosphorylation.

Myo1-S742 is de-phosphorylated before cells enter mitosis. Potential phosphatases which may be involved in this process were explored. One key regulator of polarized cell growth in fission yeast, is the Rho-family GTPase, Cdc42. Cdc42 is known to interact with multiple effector proteins, which are involved in organization of the actin cytoskeleton (Zhao and Manser 2005). Guanine nucleotide exchange factor (Gef1) is responsible for the exchange of GDP-to-GTP, required for activation of Cdc42. If a Cdc42 regulated phosphatase, such as the Type I phosphatase (PP1), is involved in de-phosphorylation of Myo1-S742, in a *gef1*Δ cell, an increase in phosphorylated Myo1 would be expected.

Therefore a western blot of TCA extracts, made from *gef1*Δ cells, was probed with the phospho-specific, anti-Myo1-S742P* antibodies. This sample is shown in the first lane of the western blot in Figure 5.18. No phosphorylated Myo1 band was detected, despite a significant amount of total Myo1 protein in the cell extract. This is typical of the western blots observed from asynchronous cultures of wild type cells, and suggests that Gef1 activated Cdc42 is not part of the mechanism by which Myo1-S742 is de-phosphorylated.

Summary:

Statement	Evidence
Phosphorylation between the Myo1 IQ1 and IQ2 domains does not change the flexibility of the IQ region.	Myo1-IQ12 and Myo1-IQ12-S742D FRET proteins have similar spectra.
Myo1 IQ12-S742D phosphorylation does not significantly change Cam1 affinity for the IQ domains.	A K_d of 0.87 μM for Cam1 binding to the Myo1IQ12-S742D FRET protein compared to 0.80 μM to the Myo1IQ12 FRET protein.
Cam2 binds 4-fold more tightly to the Myo1 IQ12-S742D FRET protein.	A K_d of 0.28 μM for Cam2 binding to the Myo1IQ12-S742D FRET protein compared to 1.16 μM to the Myo1IQ12 FRET protein.
A *myo1-S742A* mutant does not cause any visual phenotypic effects.	No morphological defects and no significant differences in the growth rates of *myo1-S742A* or *myo1-S742D* cells.
myo1-S742A cells in the mitotic cell cycle incorporate less Myo1 protein into endocytic patches.	Analysis of mNeongreen-Myo1 and mNeongreen-Myo1-S742A fluorescence.
Less Cam1 is recruited to endocytic foci in *myo1-S742A* cells.	Analysis of Cam1-GFP fluorescence in *myo1*$^+$ and *myo1-S742A* cells.
The lifetimes of Myo1 and Cam1 foci are reduced in *myo1-S742A* cells.	Analysis of the lifetime of mNeongreen-Myo1 and Cam1-GFP foci in *myo1*$^+$ and *myo1-S742A* cells.
myo1-S742D mutation does not affect the localisation of Cam1.	Analysis of Cam1-GFP fluorescence in *myo1*$^+$ and *myo1-S742D* cells.
myo1-S742A and *myo1-S742D* mutations both result in small increases in the sizes of Lifeact labelled actin patches.	Analysis of Lifeact fluorescence in *myo1*$^+$, *myo1-S742A* and *myo1-S742D* cells.
myo1-S742A cells are unable to redistribute endocytic patches to the new cell end during NETO.	Distribution of Lifeact, Cam1-GFP and Sla2-mCherry endocytic patch proteins in growing cells following cell division.
Myo1-S742 is differentially phosphorylated during the cell cycle.	Anti-Myo1-S742P* antibodies do not detect Myo1-S742 phosphorylation in asynchronous cell cultures, but do in arrested *cdc10-v50* cell lysates.
Myo1-S742 is phosphorylated prior to NETO, but is de-phosphorylated prior to cells entering mitosis.	Anti-Myo1-S742P* western blots of *cdc10-v50* and *cdc25-22* arrested cells and *cdc10-v50* released synchronous culture.
Myo1-S742 phosphorylation is dependent on the TORC2 signalling pathway.	Absence of phosphorylation in *ste20*Δ and *gad8*Δ cells.
De-phosphorylation of Myo1-S742 is not under the control of Cdc42.	Anti-Myo1-S742P* antibodies do not detect phosphorylated Myo1 in *gef1*Δ cells (inactive Cdc42).

Summary:

Data presented in this chapter investigates the potential role of phosphorylation of the Myo1 neck region, in regulating Myo1 function and light chain binding. *In vitro* analysis shows that phosphorylation of Myo1-S742 results in Cam2 having a higher affinity for the Myo1 IQ domains than Cam1. This suggests a potential mechanism for 'switching' light chain binding, as Cam1 has a higher affinity for the un-phosphorylated form of the Myo1 IQ domain. Phosphorylation mutant strains suggest that during the mitotic cell cycle, this phosphorylation event results in only subtle defects. *myo1-S742A* cells appear unable to correctly re-distribute cell growth to the new cell end during NETO, however this does not affect the overall growth rates of cells.

This study shows that phosphorylation of Myo1-S742 is regulated during the cell cycle, in a TOR signalling dependent manner. The timing of phosphorylation appears to peak around the G1-S transition point, it is at this stage of the cell cycle when cells exit into meiosis under nitrogen starvation conditions. With TOR signalling regulating growth in response to nutrient availability (Matsuo et al 2007; Kawai et al 2001), and the reported function of Cam2 and Myo1 during meiosis (Itadani et al 2006), these data suggest a possible function of this phosphorylation event during meiosis.

Chapter 6: TOR dependent regulation of actin dynamics via Acp1 phosphorylation.

Introduction:

The Target of Rapamycin (TOR) signalling acts as the 'master switch' of cellular processes, regulating cell growth and metabolism, in response to external stimuli (Zhou & Huang 2010). Both TORC1 and TORC2 have been implicated in the control of F-actin organization and cell migration (Liu & Parent 2011). TORC2 deficient mutants in budding yeast, *Dictyostelium* and mammalian cells, all exhibit defects in actin polarization. Dependent on cell type, these defects result in reduced cell migration and chemotaxis, or in some cases increases in stress fibre formation (Jacinto et al. 2004; Lee et al. 2005; Schmidt et al. 1996). The molecular mechanism of TORC2 mediated actin reorganization has been studied in budding yeast and mammalian cell lines. There is evidence to suggest that TORC2 activates PKC through GTP-binding proteins (Jacinto et al. 2004). Active PKC influences polarization of the actin cytoskeleton by a MAPK signalling cascade (Matsuo et al. 2003). Studies in fission yeast have shown TORC2 dependent regulation of the actin cytoskeleton, with thicker F-actin cables observed in *tor1*-deficient mutants, and cortical actin accumulating asymmetrically at cell ends (Ikai et al. 2011; Matsuo et al. 2007).

In collaboration with Janni Petersen's group (University of Adelaide), the role of TORC2 during reorganization of the actin cytoskeleton during cytokinesis was explored. This followed the observation that *ste20*Δ cells display cytokinesis defects. Ste20 is the fission yeast homologue of the mammalian Rictor protein, a regulator of TORC2. Deletion of *ste20* from the fission yeast genome, specifically disrupts TORC2 function. This has considerable advantages over deletion of the TORC2 kinase component, Tor1, in that cells lacking Tor1 are able to incorporate Tor2 into TORC2 to restore its function.

The Petersen group went on to show that the TOR kinase, Tor1 physically interacts with components of the CAR. A proteomic-based analysis of Tor1 immuno-precipitates, identified that myosin heavy chains Myp2 and Myo51 interact with the TORC2 component, Tor1.

6.1. A summary of the timings of CAR constriction, and recruitment of CAR components.

In order to explore whether TORC2 affects regulation of cell division, distinct phases of cytokinesis were characterised in wild type and mutant strains, relative to timings of spindle dynamics and contractile actomyosin ring (CAR) formation. Strains were generated containing a CAR component Myo2-mCherry and either Sid4-tdTomato or Cut12-GFP, both components of the spindle pole body (SPB). During metaphase the SPBs begin to separate, as foci of Myo2-mCherry accumulate at the cell equator. From the moment the two SPBs separate until the onset of anaphase, where the Myo2 foci coalesce to form the CAR is defined as Phase I. Phase II corresponds to the SPBs continuing to separate as the spindle elongates, until the CAR begins to constrict. Constriction of the CAR occurs at the end of anaphase, and is defined as Phase III, the end of which is identified when the diameter of the ring reaches < 1 μm. Phase IV represents the final stage of ring constriction and subsequent CAR disassembly.

Time-lapse microscopy was used to determine the lengths of these phases, firstly in a *myo2-mCherry sid4-tdTomato* strain and then subsequently in strains deficient of TORC2 or CAR components. Images were taken every three minutes, with mCherry illumination and emission filters capturing both Myo2-mCherry and Sid4-tdTomato signal (see Movie 9 – Appendix 2). For each frame, distances between SPBs and the diameter of the Myo2 ring were measured in μm using Metamorph software. For all strains, more than 20 dividing cells were used to determine the average length of each phase.

Selected timelapse images of a typical dividing *myo2-mCherry sid4-tdTomato* cell (Figure 6.1) correspond to the spindle and ring dynamics at the transition points from one phase to the next. A graph was plotted from the measurements of Myo2 ring diameter during constriction and distance of SPB separation (Figure 6.1). The length of each phase was determined from an average of these measurements in 20 dividing cells. The same methods of imaging and analysis were used for all mutant strains described later in this chapter. Figure 6.2. and Table 6.1. summarise the timings of the phases of cytokinesis, in each mutant background

analysed. The rationale of analyzing these particular deletion strains and the significance of the results are discussed in the following sections of this chapter.

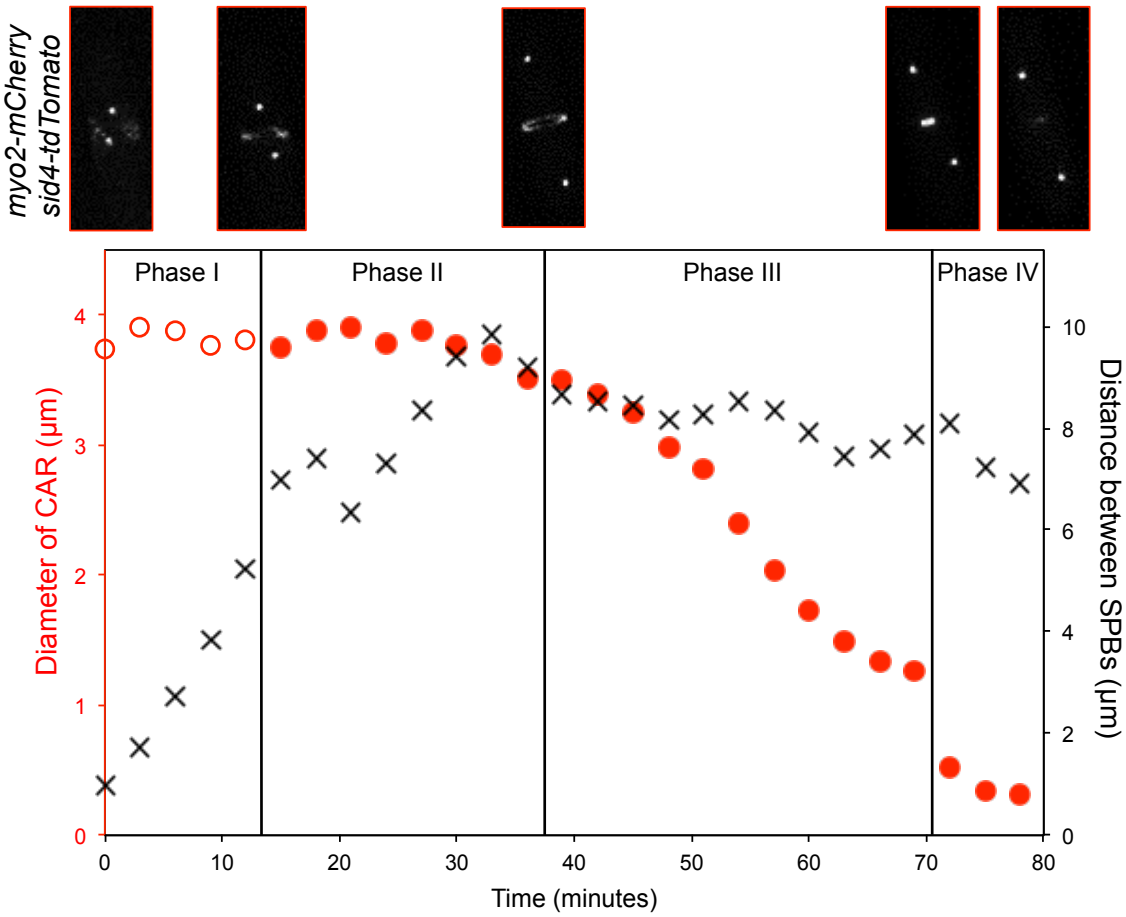

Figure 6.1. Defining phases of cytokinesis.

Aligned with the graph are images of a dividing *myo2-mCherry sid4-tdTomato* cell at the transitions between phases of cytokinesis. The empty circles in Phase I represent foci of Myo2, before they coalesce into a complete ring (filled circles). During Phase II, the SPBs move apart, before the CAR constricts during Phase III. Phase IV includes the last 1 µm diameter of ring constriction and CAR disassembly.

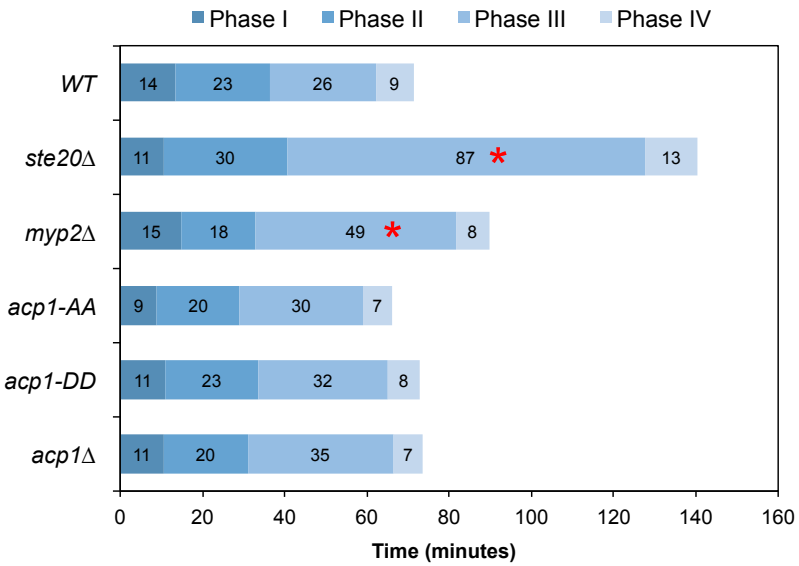

Figure 6.2. Average timings of cytokinesis.

Timings of the phases of cytokinesis in wild type and mutant backgrounds. Each phase for all strains was calculated from an average of at least 20 cells. Timings are annotated in the bar chart in minutes.

Table 6.1. Summary of cytokinesis phase timings.

Strain	Phase I (mins)		Phase II (mins)		Phase III (mins)		Phase IV (mins)		Cells failing to complete CAR constriction (%)
	Mean	SEM	Mean	SEM	Mean	SEM	Mean	SEM	
WT	**13.6**	±2.3	**22.8**	±1.5	**25.7**	±1.3	**9.2**	±1.5	0
ste20Δ	**10.5**	±1.5	**30.0**	±6.9	**87.0 ***	±13.1	**13.0**	±3.6	50
myp2Δ	**15.0**	±0.0	**18.0**	±4.6	**48.5 ***	±3.7	**8.3**	±1.4	40
acp1-AA	**9.0**	±1.2	**20.0**	±3.0	**30.0**	±2.7	**7.1**	±1.0	13
acp1-DD	**11.0**	±1.0	**22.5**	±1.0	**31.5**	±5.0	**7.8**	±2.6	0
acp1Δ	**10.5**	±1.0	**20.5**	±1.2	**35.4**	±4.0	**7.4**	±0.6	0

* Denotes a statistical significance of $p < 0.05$

WT – *myo2-mCherry sid4-tdTomato* cells

To summarise the observations in Figure 6.2 and Table 6.1, firstly disruption of Acp1 protein, by either complete deletion, or change in phosphorylation status (*acp1-AA* and *acp1-DD* mutants described in section 6.6), did not significantly affect the length of any phase of CAR organization and dynamics. In contrast, the overall time of mitosis was greatly increased in cells lacking either the Class II myosin, Myp2 or the TORC2 regulatory component, Ste20, with Phase III being most significantly affected. Compared to wild-type cells, Phase III constriction of the CAR took on average twice as long in a *myp2*Δ strain, and over three times longer in a *ste20*Δ strain.

Following characterisation of the timings of cytokinesis, the timings of recruitment of each protein component to the CAR was then determined. In order to achieve this, strains were generated containing *myo2-mCherry* and a GFP / YFP labelled protein if interest. Strains were again imaged every 3 minutes, and the timing of protein arrival at the CAR determined in relation to the phases of cytokinesis described above. Table 6.2. and Figure 6.3. summarise the timings of these proteins arriving at the CAR in wild type and deletion backgrounds.

Table 6.2. Summary of protein recruitment to the CAR.

Strain	Timing of protein arrival to CAR after start of Phase II (min)		
	Ste20-GFP	**YFP-Myp2**	**Acp1-GFP**
WT	4.36	10.33	7.50
***ste20*Δ**	-	**21.00 ***	4.80
***myp2*Δ**	4.80	-	7.00
acp1-AA	N.D.	N.D.	-
***acp1*Δ**	N.D.	8.63	-

* Denotes a statistical significance of $p < 0.05$

WT – *myo2-mCherry ste20-gfp, myo2-mCherry YFP-myp2 or myo2-mCherry acp1-gfp* cells.

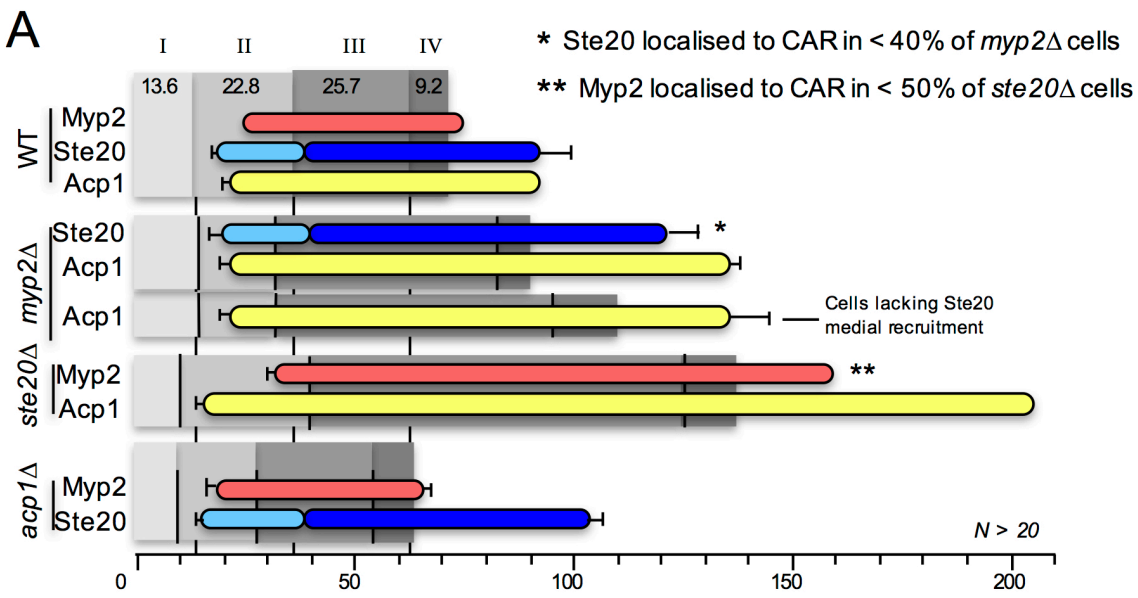

Figure 6.3. Recruitment of proteins to the CAR.

Histogram showing timings of the arrival and disappearance of fluorescently labelled proteins (YFP-Myp1, Ste20-GFP, Acp1-GFP) to the Myo2-mCherry labelled CAR. The dynamics of protein recruitment in 'wild-type' cells are followed by those in the deletion backgrounds (*myp2*Δ, *ste20*Δ and *acp1*Δ). These timings are made from averages of cells which correctly recruited proteins to the CAR, while asterisks indicate strains in which only a percentage of cells recruited protein to the CAR.

These results show that there is a significant delay in the recruitment of Myp2 to the CAR in the absence of Ste20, arriving 10 minutes later than seen in wild type cells. There is not a significant delay in the timing of Ste20 arrival at the CAR in the absence of Myp2, however all of the data shown in this section is taken from cells that completed all phases of mitosis. This therefore does not take account of the significant numbers of cells which did not form a fully functional, constricting CAR. The percentages of mitotic cells imaged which showed an aberrant or collapsed CAR are summarised in Table 6.1. and discussed further in the following sections.

6.2. TORC2 localises to the CAR and maintains its integrity during constriction.

In order to determine any effect that TORC2 may have on controlling cell division, timings of cytokinesis were first compared in wild type and *ste20*Δ backgrounds. Ste20 is the *S. pombe* Rictor homologue and an essential component of TORC2. The absence of Ste20 results in the loss of TORC2 function specifically.

In *ste20*Δ strains the timing of the constriction phase (III) was over three times longer than in *ste20*$^{+}$ cells (Figure 6.2). However it is important to note that this average is made only from those cells which completed CAR constriction. In 55 % of the mitotic *ste20*Δ cells imaged, the CAR was not located at the cell equator, a phenotype not seen in any of the wild-type cells imaged. In 39 % of all mitotic *ste20*Δ cells imaged, the CAR was observed to either split or collapse, and in a further 11 % of cells, remain un-constricted and slide along the cortex.

Typical examples of these phenotypes are shown in micrographs from *myo2-mCherry cut12-gfp ste20*Δ cells (Figure 6.4.B-C). The micrograph in the top panel of this figure shows typical constriction of the cytokinetic ring in a *myo2-mCherry sid4-tdTomato ste20*$^{+}$ cell for comparison. Figure 6.4.B. shows the Myo2-mCherry ring of a *ste20*Δ cell forming, but then collapsing (indicated with arrow) before constriction has occurred. The second example (Figure 6.4.C) shows a Myo2-mCherry ring remaining un-constricted for an extended period of time, but also sliding away from the cell equator (marked with arrows). This indicates that TORC2 may have a role in anchoring the CAR at the middle of the cell and possibly mediates CAR interactions with the membrane (see movie 10 – Appendix 2).

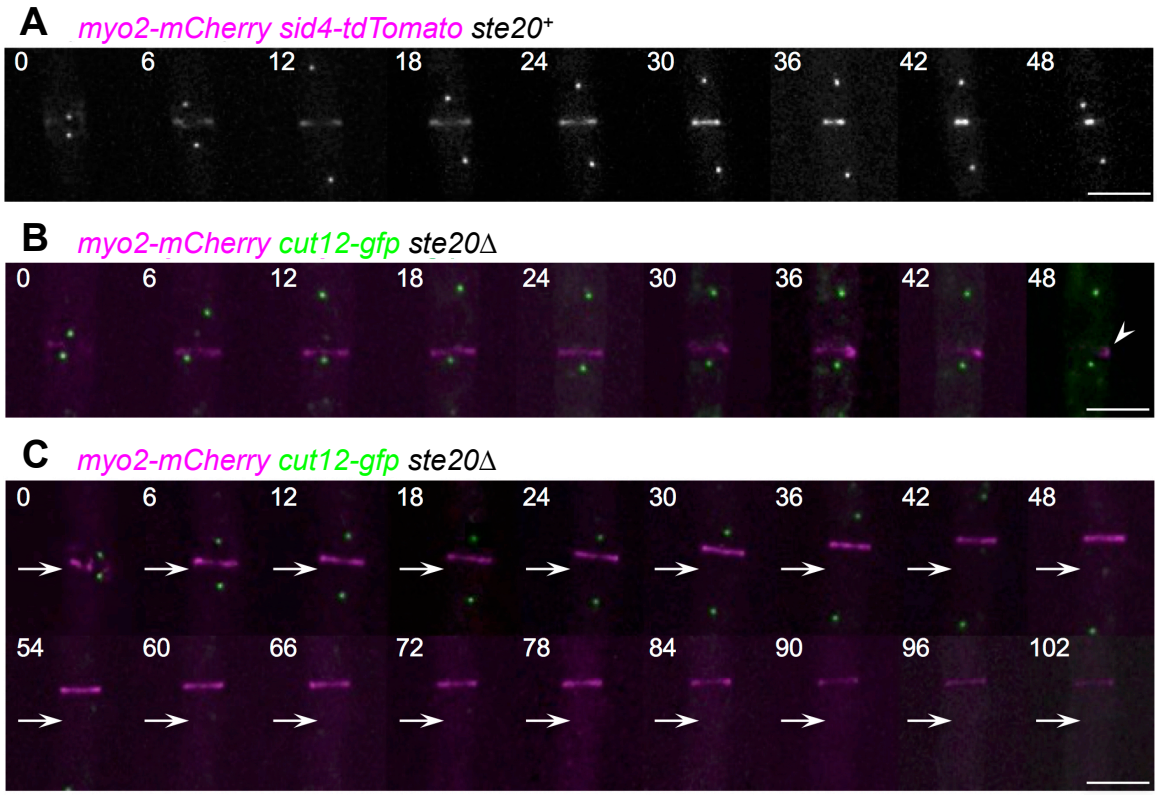

Figure 6.4. CAR constriction in *ste20*$^{+}$ and *ste20*Δ cells.

The micrograph in (A) shows images of a *myo2-mCherry sid4-tdTomato ste20*$^{+}$ cell taken at 3 minute intervals. The CAR formation and constriction can be seen along with separation of the SPBs. (B) shows the formation of the CAR in a *myo2-mCherry cut12-gfp ste20*Δ cell, followed by its collapse, indicated with an arrow. (C) shows an example of an un-constricted CAR sliding along the length of a *ste20*Δ cell, from its initial position at the cell equator, indicated with arrows. Scale Bar represents 5 μm.

Having determined that Ste20 plays an important role in facilitating CAR constriction and cytokinesis, the cellular localisation of TORC2 was determined using a strain in which the endogenous Ste20 protein was labelled with a C-terminal 3-GFP fusion. In a maximum projection of 31 Z-plane images (Figure 6.5.A), Ste20 can be seen to co-localise with a constricting Myo2 ring. In order to correlate the timings of Ste20 localisation to the CAR with the phases of cell division, timelapse images were taken of *myo2-mCherry sid4-tdTomato ste20-gfp*. Ste20 can be seen to recruit to the Myo2 ring throughout cytokinesis (Figure 6.5.C). Foci of Ste20 (shown as light blue bars in Figure 6.3.) first arrive at the cell

equator just over 4 minutes after the start of phase II, once foci of Myo2 coalesce to form the CAR. These foci of Ste20-GFP also coalesce to form a complete ring (dark blue bars in Figure 6.3.) as the Myo2 ring begins to constrict at the beginning of phase III. Figure 6.5.B shows co-localisation of Ste20 and Myo2 in a constricting ring at the cell equator. Ste20 remains at the CAR throughout constriction and is seen at the ensuing new cell end.

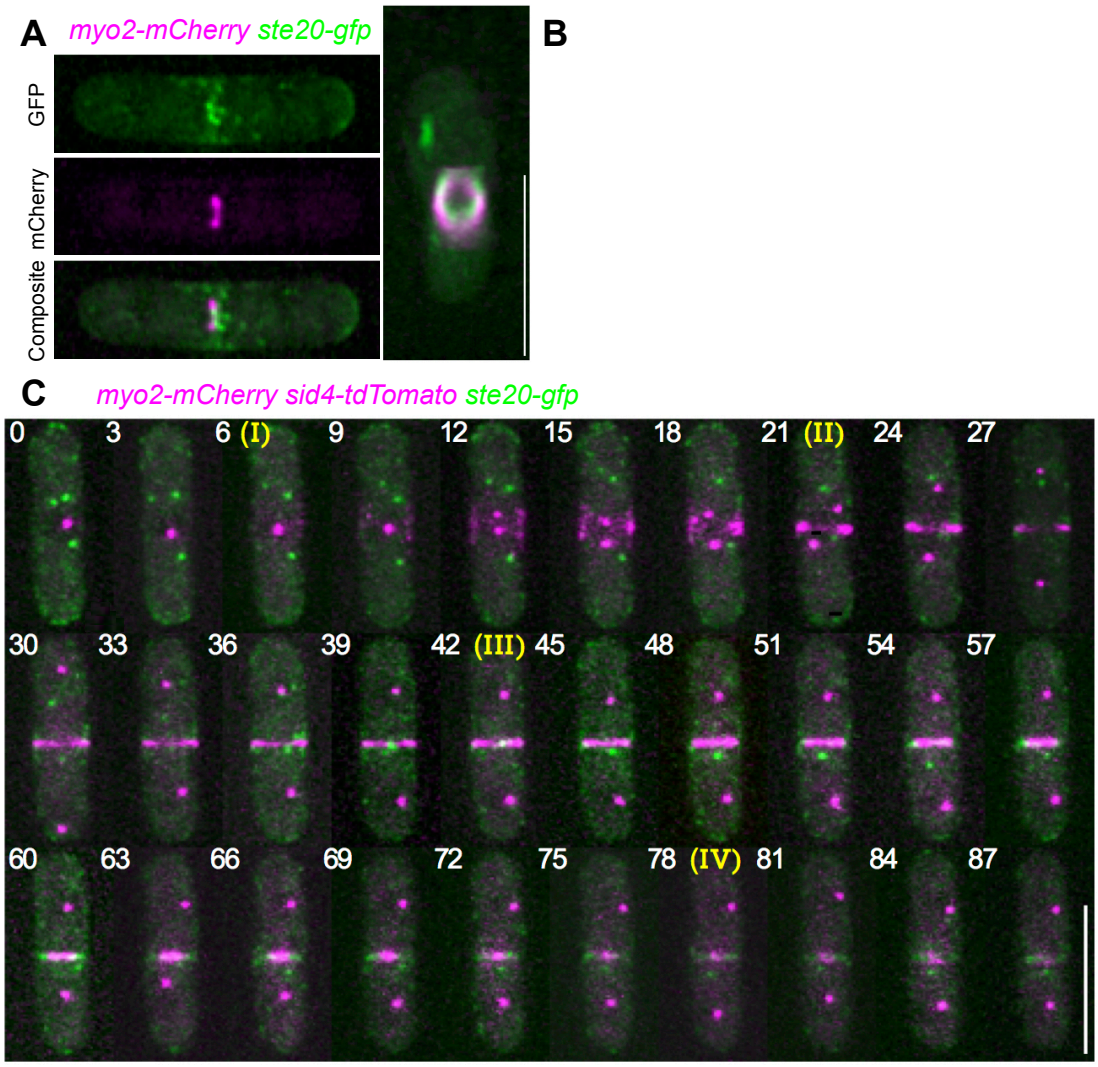

Figure 6.5. Ste20 co-localisation with Myo2 at the CAR.

(A) is a maximum projection of 31 z-plane images of a *myo2-mCherry ste20-* cell, showing co-localisation of Ste20 and Myo2. (B) is a 3D view of the cell showing both Ste20 and Myo2 form a ring structure. (C) A micrograph of images taken every 3 mintues of a myo2-mCherry sid4-tdTomato ste20-gfp cell throughout all stages of cytokinesis. The time in minutes and beginning of each stage are annotated. Scale bar represents 10 μm.

6.3. Myosin II regulates Ste20 recruitment to the CAR.

Having shown that Ste20 localises to the CAR and is critical for normal ring constriction, we next explored what other proteins may be involved in controlling TORC2 recruitment and function. Deletion of the Class II myosin, Myp2 has previously been shown to cause cytokinesis defects (Bezanilla et al. 1997; Mulvihill et al. 2000) similar to those seen with *ste20*Δ, this led to further investigation of the involvement of Myp2 in cytokinesis. In a screen of Tor1 immuno-precipitates carried out by the Petersen group, Myp2 was identified as a protein interacting with the Tor1 component of TORC2.

In order to determine if Myp2 interaction with TORC2 components is required for TORC2 recruitment to the CAR, a *ste20-gfp myo2-mCherry myp2*Δ strain was generated. Firstly it was observed that 40 % of *myp2*Δ cells had aberrant rings which did not constrict, and of those that did, the constriction phase of the CAR (Phase III) was almost twice as long as that seen in *myp2*$^{+}$ cells, (Figure 6.2.). As seen in *ste20*Δ cells, in the absence of Myp2, Myo2 rings either did not form, collapsed, or slid along the length of the cell. There were also instances of Myo2-mCherry ring structures splitting into two before constricting separately (Figure 6.6.B - highlighted by an asterisk).

Ste20 was only recruited to the CAR in 40% of dividing *myp2*Δ cells compared to 100 % of *myp2*$^{+}$ cells. In this proportion of cells where Ste20 was recruited to the CAR, constriction was 10 minutes longer than that observed in wild type cells. However in the 60% of cells where Ste20 did not localise to the CAR, phase III was over 25 minutes longer compared to wild type (Figure 6.6.A). Figure 6.6.B. shows a typical example of a *myp2*Δ cell in which Ste20 does not localise to the CAR, and results in aberrant CAR formation. Together these data indicate that Myp2 plays a role in regulating TORC2 localisation to the CAR, and therefore the timing of cytokinesis. The observation of Ste20 localisation to the CAR in some *myp2*Δ cells, is likely to be due to alternative proteins being involved in Ste20 recruitment. One possible protein responsible for TORC2 recruitment to the CAR is Myo51, another protein identified in Tor1 immuno-preciptates (Petersen personal communication).

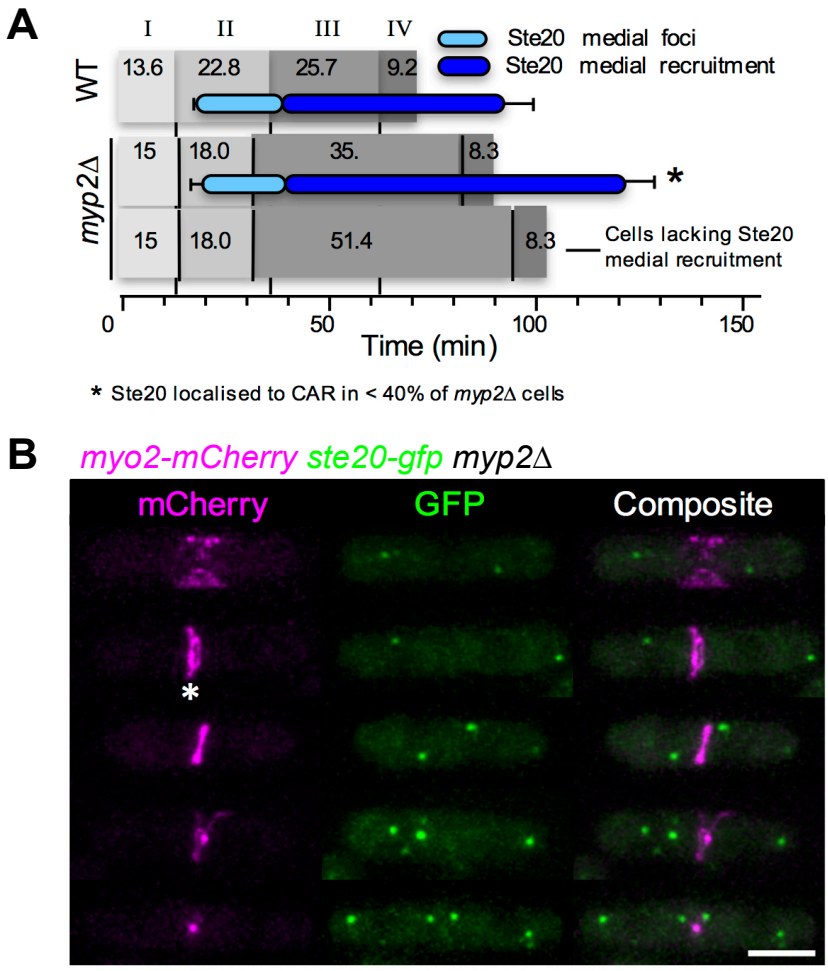

Figure 6.6. Effect of *myp2*Δ on recruitment of Ste20 to the CAR.

(A) Timings of recruitment of Ste20-GFP to the CAR. Timings of Ste20 recruitment in wild type cells, are compared to those in *myp2*Δ cells. In *myp2*Δ cells where Ste20 is not recruited to the CAR (60 % of cells imaged) a further delay in cytokinesis was observed. (B) Images taken every 14 minutes of a *myo2-mCherry ste20-gfp myp2*Δ cell in which Ste20 does not localise to the CAR. The * indicates the CAR splitting in two. Scale bar represents 5 μm.

6.4. Ste20 regulates Myp2 localisation and the timing of CAR constriction.

Following the observation that Myp2 affects the localisation of the TORC2 component Ste20 to the CAR, this link was further explored by looking at the effect *ste20*Δ has on Myp2 localisation. As seen with Myo2, Myp2 rings were frequently aberrant in *ste20*Δ cells, with YFP-Myp2 rings collapsing, remaining un-constricted

or sliding along the length of the cell in the majority of cells imaged. In *ste20*$^{+}$ cells, Myp2 arrived at the CAR 10.3 minutes after Myo2 forms a complete ring. In more than 50 % of *ste20*Δ cells, Myp2 recruitment to the CAR was extremely transient. Figure 6.7.B-D. shows typical examples of aberrant Myp2 ring formation and constriction in *ste20*Δ cells compared with that of wild type cells. In *ste20*Δ cells where Myp2 did form a complete ring, constriction was significantly impaired, with the CAR either not constricting or often seen to slide along the length of the cell. These observations indicate that there is a co-dependency between Myp2 and Ste20 localisation and function at the CAR.

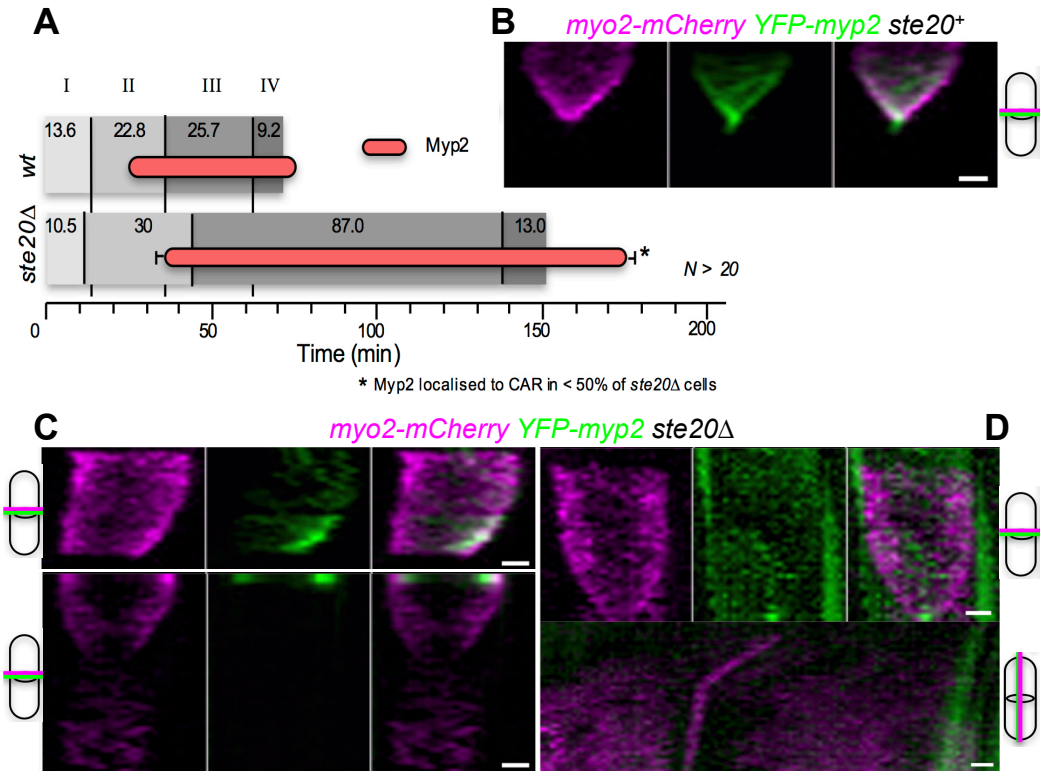

Figure 6.7. Effect of *ste20*Δ on recruitment of Myp2 to the CAR.

(A) Histogram showing the prolonged phase III CAR constriction and delayed recruitment of Myp2 in *ste20*Δ cells. (B) Kymographs of Myo2-mCherry and YFP-Myp2 ring constriction in a *ste20*$^{+}$ cell. Kymographs of *myo2-mCherry YFP-myp2 ste20*Δ cells show (C) two examples of transient YFP-Myp2 interaction with the CAR, resulting in slow constriction and expansion. (D) kymographs generated in two axes show transient YFP-Myp2 association with the CAR which results in the Myo2-mCherry ring sliding along the length of the cell – seen in the bottom panel. Scale bars: 1 μm.

6.5. Acp1 localises to the CAR, and has a depolarized distribution in *ste20*Δ cells.

These data show that the Class II myosin, Myp2 and Myo51 interact with the TORC2 component, Tor1, and are required for recruitment of TORC2 to the CAR. Having identified that TORC2 is involved in controlling the timing of CAR constriction, studies by the J. Petersen and colleagues identified TOR-dependent phosphorylation events on proteins potentially involved in regulating the actomyosin ring and cytokinesis.

Using Torin1 treatment to specifically target TOR kinase activity (Thoreen et al. 2009), it is possible to identify phosphorylation events that are dependent on the TOR signalling pathway (Atkin et al. 2014). A TOR-phosphorylation-dependent SILAC screen showed that neither Myp2 nor Myo51 are substrates of TORC2. However, two serine residues on the actin capping protein Acp1 (Serine 172 and 189), were identified as having differential phosphorylation following addition of Torin1. There is also evidence of cytokinesis defects in *acp* mutants, under conditions of elevated temperature and osmotic stress (Kovar et al. 2005). We therefore proceeded to investigate the role that Acp1 may have during cytokinesis, and the effect that blocking TORC2 function has on Acp1 localisation and dynamics.

Acp1-GFP is recruited to the cell equator soon after CAR formation is completed (Figure 6.8). On average, Acp1 is recruited to the CAR 7.5 minutes after the start of phase II, which is shortly after the arrival of Ste20 (Table 6.2). Also shown in Table 6.2. is that the timing of Acp1 recruitment is not significantly altered in *ste20*Δ and *myp2*Δ backgrounds. However in the absence of Ste20, Acp1 localises to the cell equator throughout the delayed phase III and remains at the new cell ends for a prolonged period when compared to wild type cells.

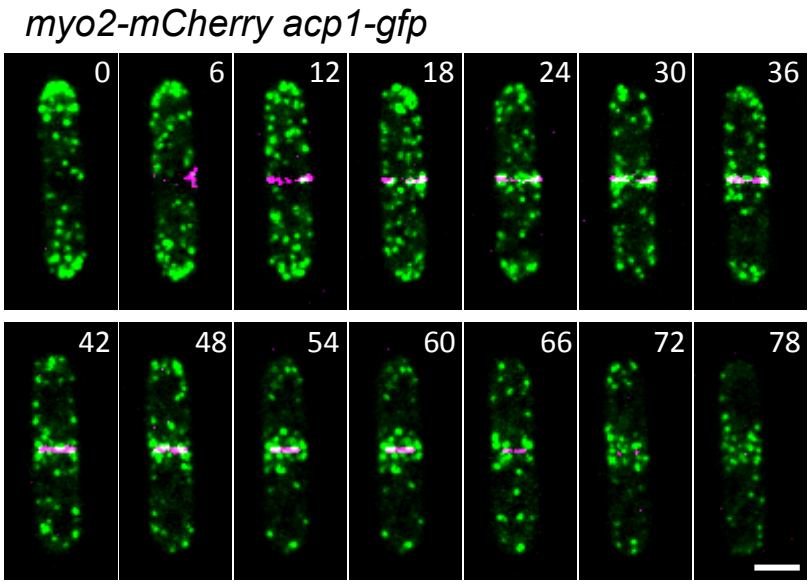

Figure 6.8. Localisation of Acp1 to the cell equator during cell division.

Images taken every 3 minutes of a dividing *myo2-mCherry acp1-gfp* cell. Foci of Acp1-GFP are localised to the growing tips of interphase cells. After the formation of a complete Myo2 ring, Acp1 foci re-distribute to the cell equator where they remain throughout CAR constriction. Foci of Acp1-GFP can be seen at the ensuing new cell end in the final image. Time intervals of each image are shown in minutes and the scale bar represents 5 μm.

Acp1 is a very dynamic protein that localises to the barbed ends of branched actin filaments (Wear et al. 2003; T. Kim et al. 2010). The localisation and dynamics are therefore very similar to those seen with actin markers such as Lifeact (Figure 6.9.A). These kymographs show that both proteins have the same oscillating lateral movements associated with the internalisation of endocytic vesicles (described in Chapter 4). Figure 6.9.B shows kymographs generated from timelapse images of *acp1-gfp lifeact-mCherry* cells, where both wavelengths were acquired simultaneously using an Optosplit. From these kymographs it is possible to identify that Acp1 arrives at the actin patch about a second after the patch forms. Acp1 is internalised with the actin patch and remains co-localised with actin as the patch disassembles. This is highlighted in the individual foci shown in Figure 6.9.C. where patches are initially Lifeact (magenta) alone, then joined by Acp1-GFP throughout the majority of its lifetime (white co-localisation), before actin is disassembled after internalisation, leaving Acp1 (green).

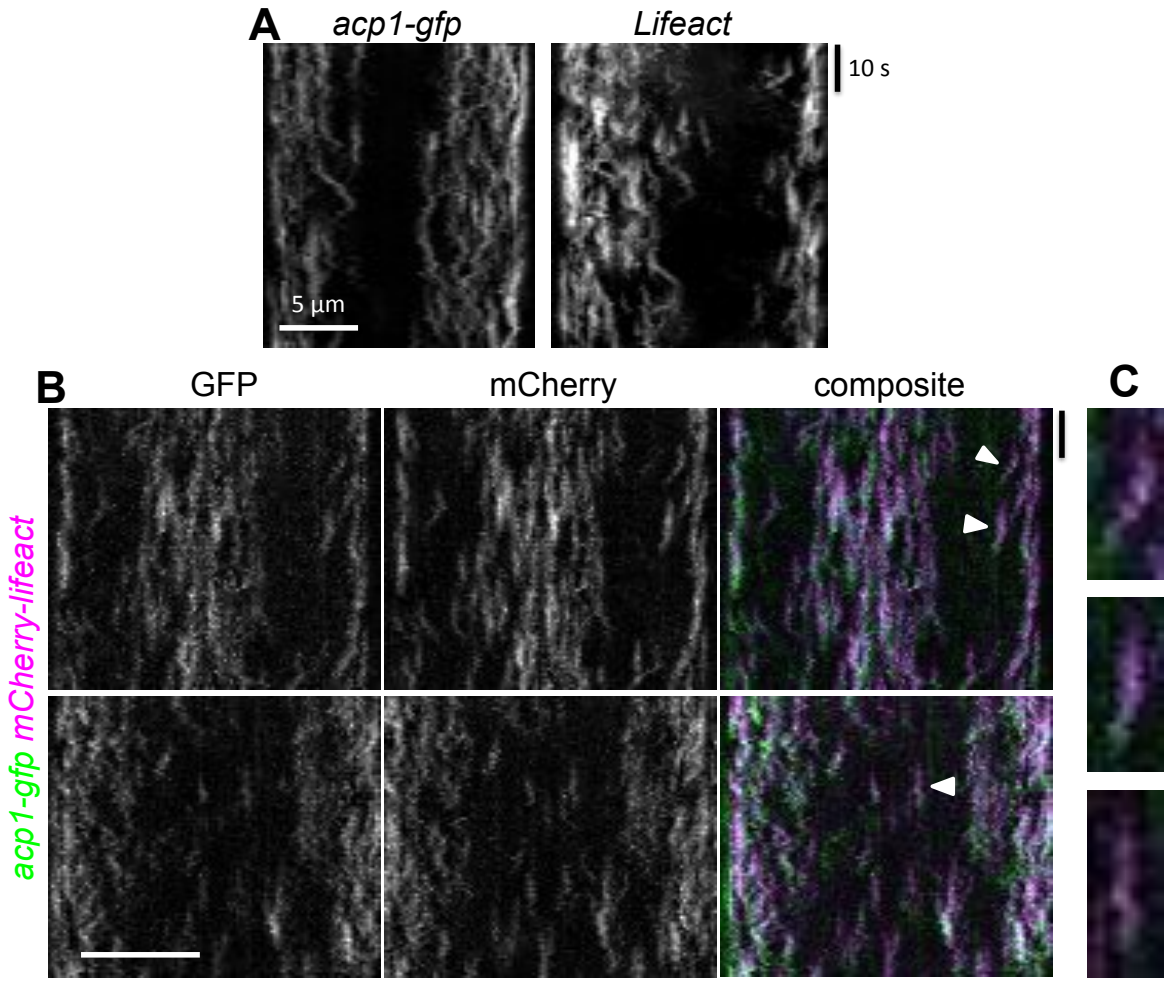

Figure 6.9. Dynamics and co-localisation of actin and Acp1.

(A) Kymographs generated from maximum projections of 13 z-plane images. (B) GFP and mCherry kymographs generated from maximum projections of 7 z-plane images captured simultaneously using an Optosplit. Kymographs in the top panel are made from a mitotic cell and show actin and Acp1 foci co-localising at the cell equator. The bottom panel is from an interphase cell and shows actin and Acp1 at the cell tips. (C) Expanded views of the individual foci highlighted by arrows in the composite images. Horizontal scale bars represent 5 µm and vertical bars 10 s.

The possible effect of TORC2 function on the localisation and dynamics of Acp1 was investigated by imaging and analysis of Acp1-GFP in a *ste20*Δ background. In the absence of Ste20, the localisation of Acp1 still mirrors that of Lifeact labelled actin patches (Figure 6.10.A). The dynamic oscillating movements of Acp1 and actin seen in *ste20*$^{+}$ cells, are still present in *ste20*Δ cells (Figure 6.10.B).

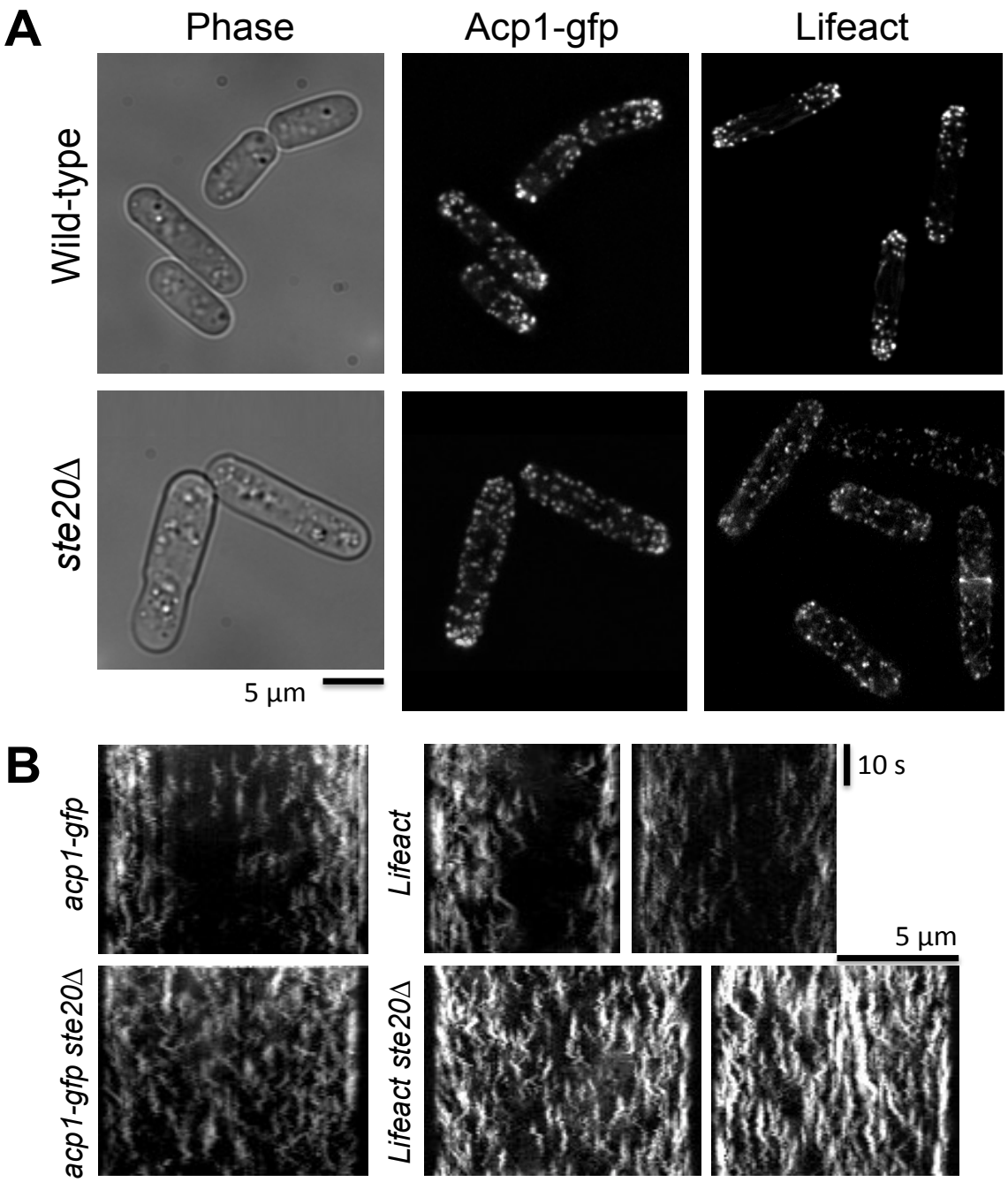

Figure 6.10. Effect of *ste20*Δ on Acp1 and Lifeact localisation and dynamics

(A) A single plane phase image of *ste20*$^{+}$ and *ste20*Δ cells, showing typical *ste20*Δ phenotype. Maximum projections of 31 z-plane fluorescent images, showing Acp1-GFP and mCherry-Lifeact localisation in *ste20*$^{+}$ and *ste20*Δ backgrounds. (B) Kymographs generated from 13 z-plane images showing the dynamics of Acp1-GFP and Lifeact in wild type and *ste20*Δ backgrounds. The intensities of the kymographs are relative to one another.

Although the overall dynamics of Acp1-GFP do not appear to be affected in the absence of functioning TORC2, the cellular distribution of both Acp1 and cortical actin patches is depolarized. In both maximum projection images and kymographs (Figure 6.10) foci of both Acp1 and Lifeact are distributed throughout the cell in *ste20*Δ strains. This is in contrast to wild type cells in the top panel, in which Acp1 and Lifeact localise predominantly to the cell ends.

6.6. Phosphorylation-null Acp1-AA strains have aberrant CAR morphology.

Having identified that Acp1 localises to the CAR during cytokinesis and TORC2 influences the polarized distribution of actin and the capping protein Acp1, next the effect of phosphorylation at serines 172 and 189 were explored. We received strains from the Petersen group in which the two serine residues identified as sites of TORC2 dependent phosphorylation – 172 and 189, were mutated to alanine or aspartate. In this chapter these strains are referred to as *acp1-AA-HA / acp1-AA-gfp* or *acp1-DD-HA* respectively. These two serine residues are conserved in the mammalian homologue of Acp1, CAPZA, and are located at the binding interface with Acp2. This Acp1-Acp2 actin capping heterodimer complex was shown by co-immuno-precipitation experiments by J. Petersen and colleagues to be more stable in the *acp1-AA* mutant strain when compared to wild type. These *acp1* mutant alleles were crossed with strains expressing fluorescently labelled CAR components in order to investigate possible effects of these mutations on localisation and dynamics of the CAR.

As previously shown (Figure 6.2) the timings of cytokinesis in Acp1 mutant strains were not significantly altered. Deletion of the *acp1* gene did not affect the length of any phase of cytokinesis. Neither the phosphorylation-null *acp1-AA-HA* strain or the equivalent phosphomimic *acp1-DD-HA* strain had any significant effect on the overall timings of cytokinesis. However these timings are an average from cells which completed CAR constriction. Although deletion of the *acp1* gene did not result in the appearance of aberrant cytokinetic rings, 13% of all Myo2-mCherry rings visualised in *acp1-AA* cells did not complete constriction. These aberrant Myo2 rings either only partially formed or collapsed during constriction. Figure

6.11. shows typical examples *acp1-AA* cells not forming complete cytokinetic rings.

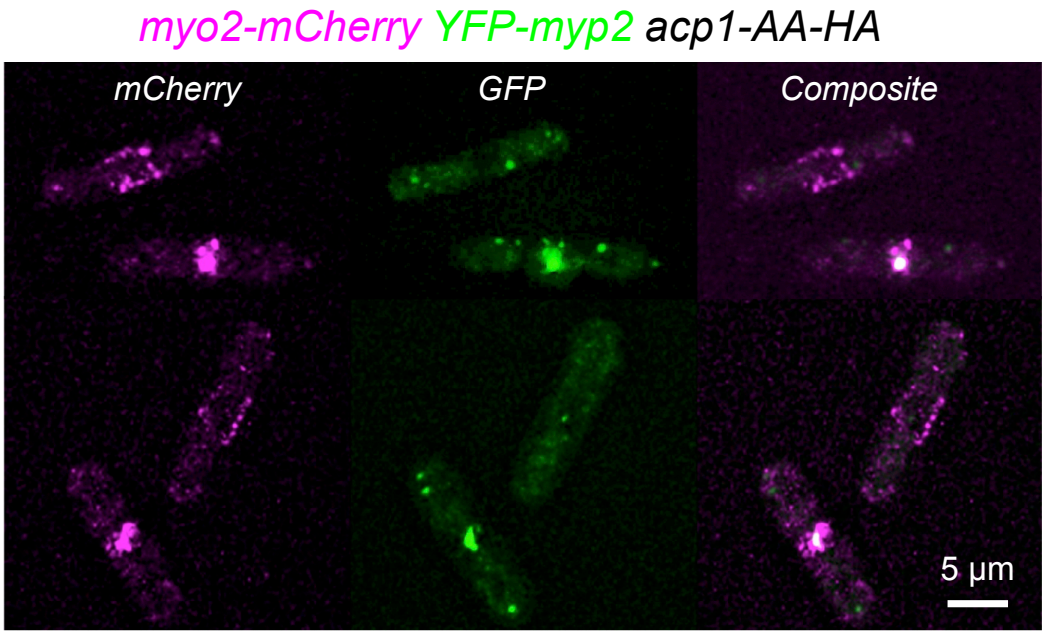

Figure 6.11. Aberrant formation of the CAR in *acp1-AA* cells.

Maximum projections of 31 z-plane images, illustrating examples of aberrant Myo2-mCherry and YFP-myp2 ring formation in an *acp1-AA-HA* mutant strain.

Having identified that a number of *acp1-AA* cells are unable to form a stable, constricting CAR, it was investigated how the absence of phosphorylation on Acp1 may impact the actin composition at the CAR. In order to specifically examine the actin filaments which incorporate into the CAR, Tropomyosin, Cdc8, was visualised using anti-Tropomyosin^{Cdc8} immunofluorescence. Cdc8 only associates with formin nucleated actin filaments, and gives a clear readout of actin incorporated in the CAR. Visualising Tropomyosin allows quantitative analysis of actin at the CAR. This is not possible in Lifeact labelled strains, in which actin filaments in the CAR are indistinguishable from the patches which also associate at the cell equator. Fluorescently labelling Cdc8 seriously impacts its function *in vivo* and therefore immunofluorescence of fixed cell samples from wild-type and *acp1-AA-HA* cells was compared.

Figure 6.12.A. shows typical images of anti-Cdc8 immunofluorescence samples imaged using a spinning disk confocal microscope (Cairn Research Ltd). Analysis of these images from wild type and *acp1-AA-HA* cells identified that there is a reduction in the amount of Cdc8 at the CAR in *acp1-AA* cells. This reduction in Cdc12 nucleated actin filaments incorporated into the CAR is a potential explanation for collapsing Myo2 rings in acp1-AA cells.

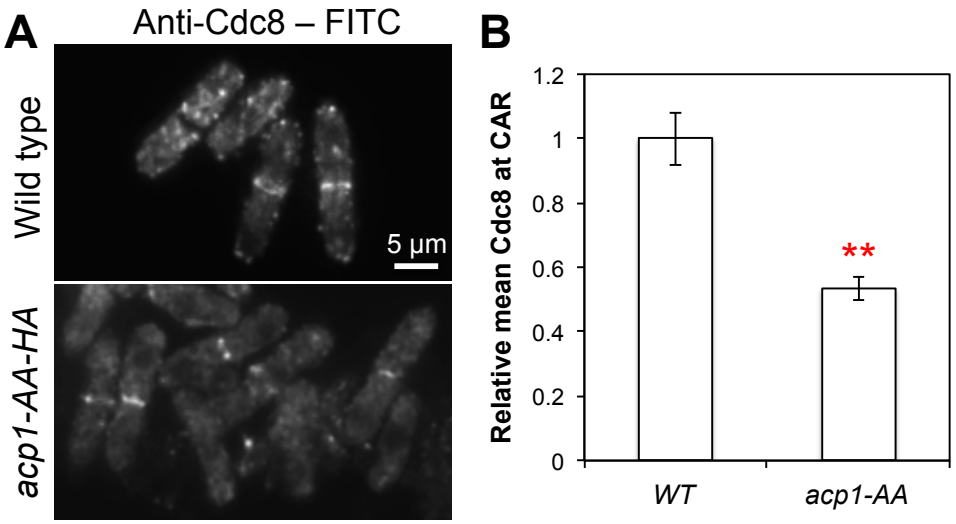

Figure 6.12. Anti-Cdc8 immunofluorescence.

(A) Typical maximum projections of 31 z-plane spinning disk confocal images of FITC labelled anti-Cdc8 immunofluorescence samples. (B) Histogram showing relative amounts of Cdc8 incorporated into the CAR, based on the average fluorescence intensity of the CAR in >30 dividing cells. ‘ ** ‘ Denotes statistical significance $p < 0.0001$.

6.7. Acp1-AA stabilises cortical actin patches.

Within the cell there is a finite pool of actin polymers, which are incorporated into specific actin structures dependent on the actin nucleator (Chesarone & Goode 2009; Gao & Bretscher 2008; Burke et al. 2014). As immunofluorescence imaging of *acp1-AA* cells indicated a decrease in the amount of Cdc12 formin nucleated actin filaments at the CAR, the organization of Arp2/3 nucleated cortical patches was explored using the Lifeact actin marker. The overall distribution of actin was compared in *Lifeact, Lifeact ste20*Δ and *Lifeact acp1-AA* strains.

Having previously observed that disruption of TORC2 by deletion of *ste20* results in a depolarized distribution of actin, (Figure 6.10), we next looked to see if blocking Tor-dependent phosphorylation of Acp1 specifically caused a similar effect. When compared to *Lifeact acp1*$^{+}$ (Figure 6.13.A) Lifeact fluorescence in a typical *Lifeact acp1-AA* cell (Figure 6.13.B) is depolarized. This loss of polarized actin distribution is similar to that seen in *ste20*Δ cells (Figure 6.10). Analysis of Lifeact foci in these strains confirmed a loss in polarized distribution. Figure 6.13.C shows that in *acp1-AA* cells, Lifeact foci are distributed equally throughout the cell and not localised to the cell ends as seen in *acp1*$^{+}$ cells. This depolarized actin localisation is also reflected in the overall distribution of Lifeact signal in the cell (Figure 6.13.D). This data indicates that actin distribution is not only affected by the overall disruption of TORC2 (by *ste20*Δ), but also by specific prevention of phosphorylation at serines 172 and 189 on Acp1.

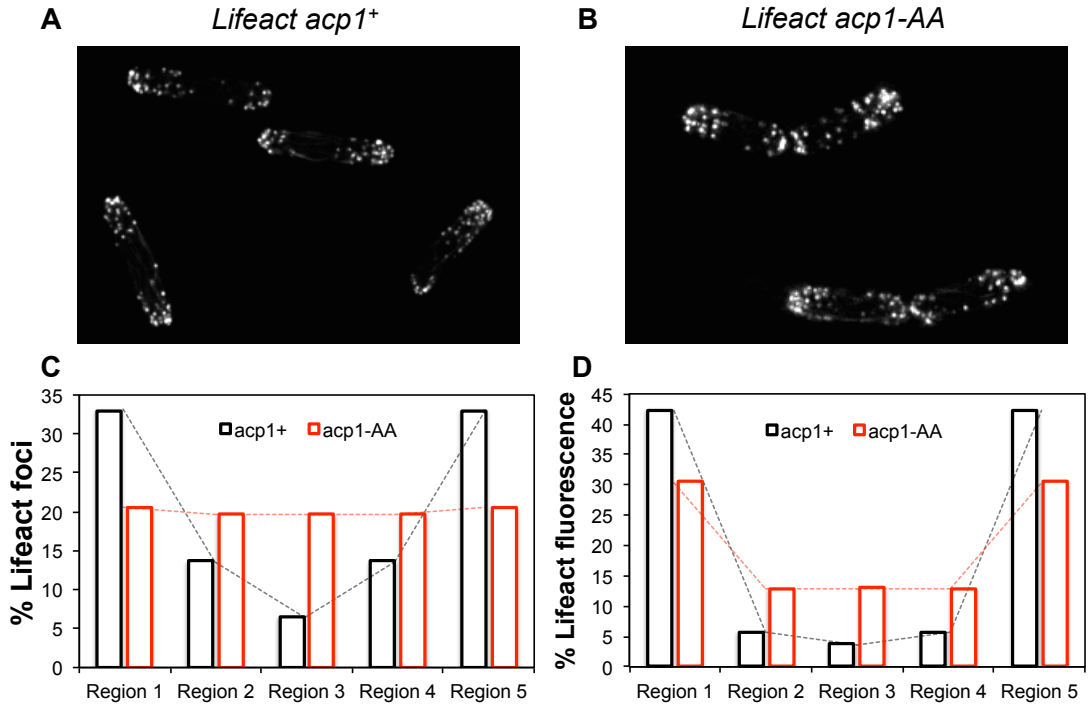

Figure 6.13. Effect of *acp1-AA* mutation on Lifeact distribution.

Maximum projections of 31 z-plane images of Lifeact in (A) an *acp1*$^{+}$ strain and (B) an *acp1-AA* strain. The cellular localisation of Lifeact foci was determined in >30 interphase *acp1*$^{+}$ and *acp1-AA* cells. (C) shows the average distribution of Lifeact foci in each region of the cell (1 & 5 – cell tips, 3 – cell equator). (D) Average Lifeact fluorescence detected in each region.

To further investigate the role of Acp1 phosphorylation in regulating actin polymerization, the dynamics of Lifeact labelled actin was observed in *acp1*$^{+}$ and *acp1-AA* cells (Figure 6.14.A). Images were captured under identical conditions, and the intensities of these kymographs are relative to one another. Although the lateral dynamics are not affected, cortical actin patches in *acp1-AA* cells have significantly higher intensities than those seen in wild type cells. This difference in Lifeact intensity is also shown in images from mix experiments (Figure 6.14) of *Lifeact acp1-gfp* cells imaged simultaneously with (B) *Lifeact ste20*Δ or (C) *Lifeact acp1-AA-HA* cells. These images confirm the relative increase in Lifeact signal in both *ste20*Δ and *acp1-AA* backgrounds.

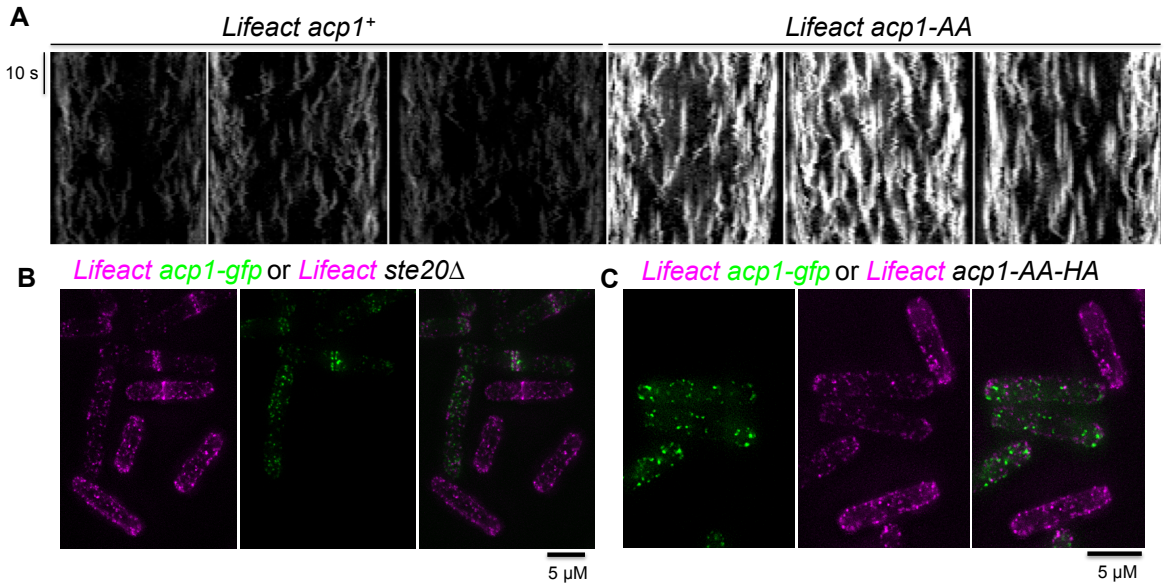

Figure 6.14.Comparison of Lifeact in *acp1*$^{+}$ and *acp1-AA* cells.

Kymographs generated from 13 z-plane images of *Lifeact acp1*$^{+}$ or *Lifeact acp1-AA* cells. Maximum projections of 31 z-plane images from mix experiments of *Lifeact acp1-gfp* cells with *Lifeact ste20*Δ (B) or *Lifeact acp1-AA-HA* (C) cells.

Lifeact fluorescence and foci were analysed from images of *acp1*$^{+}$ and *acp1-AA* cells using the methods described in materials and methods (section 2.7.1). A summary of the analysis of Lifeact foci in these strains indicates total Lifeact signal in the cell is increased three fold in *acp1-AA-gfp* cells compared to *acp1*$^{+}$ (Figure 6.15.A,C). Despite the increase in total Lifeact signal, there was no significant

difference in the number of Lifeact foci detected in each cell. However in *acp1-AA-gfp* cells there was a 4-fold increase in the volume of each Lifeact foci detected and a 5.5-fold increase in the amount of Lifeact incorporated into each patch.

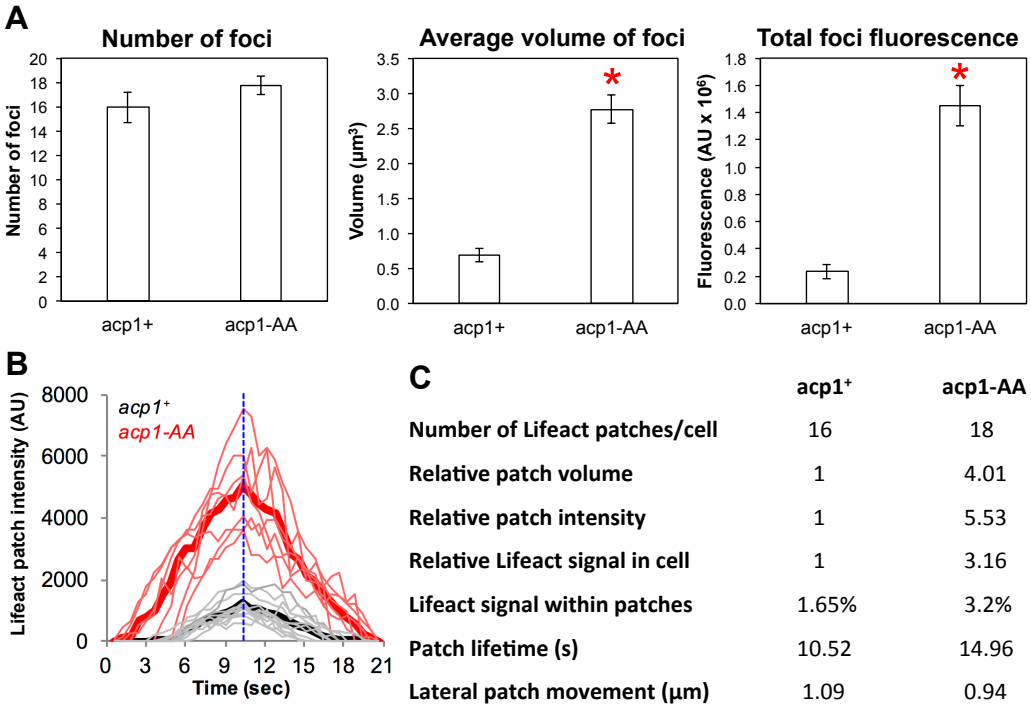

Figure 6.15. Analysis of Lifeact patches in *acp*$^{+}$ and *acp1-AA* cells.

(A) Histograms showing results from analysis of Lifeact foci in >30 *acp1*$^{+}$ (*Lifeact acp1-gfp*) and *acp1-AA* (*Lifeact acp1-AA-gfp*) cells. Error bars represent standard error of the mean, and asterisks highlight statistically significant differences in the mean values, determined by an unpaired *t*-test. (B) Graph showing Lifeact intensity over the lifetime of patches. Faint lines represent individual patches, and thick lines the overall average. (C) A summary of relative Lifeact patch dynamics in *acp1*$^{+}$ and *acp1-AA* cells. ' ** ' Denotes statistical significance $p < 0.0001$.

Analysis of individual foci was also carried out from raw images of these strains, using Metamorph software, to assess the length of time Lifeact foci persist and their lateral dynamics. The average Lifeact fluorescence intensity of individual

cortical actin patches was tracked over their lifetime (Figure 6.15.B). In *acp1-AA* cells, Lifeact signal was 5 times brighter, consistent with analysis of single time-point images (Figure 6.15.A,C). In *acp1-AA* cells, actin patches had increased average lifetimes of 15.0 seconds compared to 10.5 seconds in wild type cells. Lateral movements of Lifeact foci were also determined for each strain, this was slightly reduced in *acp1-AA* cells to 0.94 µm compared to 1.09 µm of patched in wild type cells.

Summary:

Statement	**Evidence**
TORC2 localises to the CAR and is required for cytokinesis.	Co-localisation of Ste20-GFP with Myo2-mCherry. * Myo2 immuno-precipitates with Tor1.
Myp2 is required for Ste20 localisation to the CAR.	Ste20-GFP only localised to the CAR in 40% of *myp2*∆ cells imaged.
Ste20 is required for Myp2 localisation to the CAR.	YFP-Myp2 only localised to the CAR in 50% of *ste20*∆ cells imaged.
Acp1 and actin are depolarized in *ste20*∆ cells.	Analysis of the distribution of Acp1-GFP and Lifeact in *ste20*∆ cells.
TORC2 dependent phosphorylation of Acp1 is required to maintain correct CAR formation.	CAR collapses in 13 % of *acp1-AA-HA* cells imaged.
Less actin is incorporated into the CAR in *acp1-AA-HA* strains.	Immunofluorescence shows less Cdc8 tropomyosin at the CAR of *acp1-AA-HA* cells compared to wild-type.
Acp1-AA stabilises cortical actin patches.	More dense, stabilised cortical actin Lifeact patches observed in *ste20*∆ and *acp1-AA-HA* cells. * Acp1-AA-HA forms a more stable heterodimer with Acp2.

‘ * ‘ Supporting evidence provided from studies by the J. Petersen group.

This study is published and included in Appendix 1.

K. Baker, S. Kirkham, L. Halova, J. Atkin, M. Franz-Wachtel, D. Cobley, K. Krug, B. Maček, Daniel P. Mulvihill and Janni Petersen (2016)
“TOR Complex 2 localises to the Cytokinetic Actomyosin ring and controls the fidelity of cytokinesis.”
Journal of Cell Science. Jul 1;129(13):2613-24. doi: 10.1242/jcs.190124.

Chapter 7: Discussion:

This study explored the signalling dependent regulation of the *S. pombe* actomyosin cytoskeleton. Calmodulin light chains bind to IQ motifs in the neck region of myosin heavy chains. Fission yeast express two calmodulin-like light chains, Cam1 and Cam2. This study explored the association of these proteins with myosin heavy chains *in vivo*, and their function in regulating the Myo1 driven endocytic mechanism. *In vitro* analysis of calmodulin binding to the IQ domains of Myo1 was combined with cell biological techniques to explore how these proteins regulate Myo1 function. Cam1 protein is acetylated in *S. pombe* cells by the NatA complex, the importance of this post-translational modification on Cam1 function was also investigated.

Phosphorylation is a ubiquitous method of regulating protein function in all eukaryotic cell types. Multiple phosphoproteomic screens have been carried out in fission yeast to identify residues of proteins that are phosphorylated. This study investigated the potential function of one of these phosphorylation events – at serine-742 of Myo1 – in regulating the localisation and function of Myo1 protein during the mitotic cell cycle. As this residue is between the two IQ motifs in the neck region of Myo1, the effect of phosphorylation on binding of calmodulin light chains was explored *in vitro* and *in vivo*. Indications suggest that this phosphorylation event is controlled in a cell cycle dependent manner.

The TOR signalling network regulates the cytoskeleton in order to control cell growth and division in response to changes in environment. This study explores a novel interaction of the fission yeast TOR Complex 2 (TORC2) with the CAR, and investigates the role of TORC2 and CAR proteins in maintaining normal cytokinesis. Following identification of TORC2 dependent phosphorylation events on Acp1, the function of these post-translational modifications in regulating the actin cytoskeleton were explored.

7.1. *In vitro* analysis of Cam1 function as a Myo1 light chain.

7.1.1. Calcium dependency:

Calmodulin light chains bind to the neck region of unconventional myosin motor proteins to regulate their function (Heissler & Sellers 2014). *S. pombe* calmodulin, Cam1, contains the conserved EF-hand domains (Figure 1.32) required for binding of calcium ions (Zhou et al. 2006). To study direct interactions between Cam1 and the IQ motifs of myosin heavy chains, recombinant proteins were designed and expressed (Figure 3.8) for use in FRET based binding assays (Figure 3.9.). Data shows that Cam1 binds to the IQ domains of Myo1 in a calcium dependent manner (Figure 3.12) with the presence of calcium resulting in no detectable binding of Cam1 to the Myo1IQ12 FRET protein. This is consistent with previous observations that Cam1 protein does not co-immunoprecipitate with Myo1 in the presence of calcium (Toya et al. 2001). Quin-2 calcium dissociation data suggests that all four EF-hand motifs of Cam1 are able to bind calcium ions which dissociate from Cam1 at different rates (Figure 4.1.B). This is consistent with previous studies investigating the functional importance of each calcium binding site (Moser et al. 1995). These data suggest that Cam1 is a conventional calmodulin light chain, in which binding of calcium results in an open conformation of the protein (Trybus et al. 2007) that dissociates from the Myo1 IQ domains.

Analysis of Cam1 binding to the Myo1 IQ domains was made in the presence of 4 mM EGTA, (pCa > 8.0) providing a buffer solution in which Cam1 binds the IQ domains most efficiently. Increasing the calcium concentration of the buffer solution dissociates Cam1 from the Myo1 IQ domains (Figure 3.16.B). The pCa_{50} value for this calcium dependent binding of Cam1 to the Myo1 IQ domains was calculated at 5.87 for acetylated Cam1. The cellular calcium concentration in resting yeast cells is reported to be ~ pCa 7 (Halachmi & Eilam 1993), this would indicate that under normal cellular growth conditions Cam1 association with Myo1 is favourable.

However, calcium concentrations are known to fluctuate during the cell cycle, activating multiple calcium signalling pathways to regulate many processes such

as entry of fertilised eggs into mitosis (Fontanilla & Nuccitelli 1998), and progression through multiple cell cycle checkpoints (Kahl & Means 2003). Increases in cellular calcium concentrations are likely to result in weakening of interactions between Cam1 and Myo1. The pCa_{50} value of Cam1 association with Myo1 is within the range of cellular fluctuations in calcium concentrations, suggesting that Cam1 may have a function in regulating Myo1 in response to calcium signalling. Calcium-induced release of Cam1 from Myo1 may be a mechanism of modulating Myo1 function, as described for vertebrate myosin I proteins (Whittaker & Milligan 1997; Manceva et al. 2007). In addition, calcium induced changes in the lever arm of myosins have been shown to affect the activity of the motor domain (Adamek et al. 2008). Calcium induced weakening or dissociation of the Cam1 – Myo1 interaction may serve to regulate Myo1 driven processes such as endocytosis in response to cell signalling.

7.1.2. Measurement of Calmodulin binding to Myo1.

Binding of calmodulin to the Myo1 IQ domains was explored using a Myo1IQ12 FRET protein (Figure 3.13). The emission spectra of this protein following excitation at 435 nm (Cypet), shows a large Ypet fluorescence peak and very little Cypet fluorescence, indicating high levels of FRET. A large proportion of this Ypet FRET signal is lost after addition of very small amounts of Cam1 in the first titration addition of Cam1 (Figure 3.13.A). This quench of fluorescence is too large to account for Cam1 binding to the IQ motifs alone. One possibility is that the FRET proteins interact with one another in solution as a dimer which strongly quenches the Cypet signal. On addition of small amounts of Cam1 it may not only be a binding event that is measured but in addition, forced dissociation of these dimers, amplifying the observed changes in FRET signal. Such large changes are not seen on addition of Cam2, possibly due to the weaker binding to the IQ domains, and a more gradual dissociation of FRET dimers.

Large decreases in Ypet signal of the Myo1IQ12 FRET protein when CaM binds do not result in a proportional increase in Cypet fluorescence, (compared to the restoration of Cypet fluorescence observed in Myo1IQ1 FRET spectra – Figure

4.3.A). This could indicate that the Myo1IQ12 FRET protein does not fully extend, and FRET still occurs once CaM is bound. However, upon binding of Cam1, the increases in Cypet fluorescence are smaller than those observed for Cam2 (Figure 4.1.A). This suggests that Cypet fluorescence may be directly affected by binding of CaM. Although the FRET protein has a flexible linker between the Cypet protein and IQ domains, binding of calmodulin to the IQ1 region may impact folding of the fluorophore.

If as suggested (Sammons et al. 2011), Cam2 binds only to the second IQ motif it may not have the same steric effect on the Cypet fluorophore compared to Cam1 binding to the IQ1 domain adjacent to the Cypet molecule. Without being able to asses the binding of each CaM to IQ1 and IQ2 individually (Figure 4.3), it was not possible to determine whether each CaM binds preferentially to either IQ motif. However, data showing that Cam2 binds efficiently to the Myo1IQ1 protein suggests that IQ2 is not the sole Cam2 binding site.

Although affinities of CaM binding to Myo1 IQ domains were calculated using a single quadratic equation, Scatchard plots (Figure 4.4) show that not all binding events consist of a single phase. As would be expected for a protein with a single binding site, CaM binding to Myo1IQ1 FRET protein was a single phase. Cam1, but not Cam2 binding to the two IQ domains of Myo1 is a bi-phasic event (Figure 4.4.A-B). This would suggest that Cam1 binds to one IQ domain of Myo1 with a higher affinity than the other. If Cam2 were to only bind one IQ domain, it would be predicted that the change in FRET signal would half that seen for binding of Cam1. As this is not the case, and Cam2 results in larger changes in FRET, this may indicate that Cam2 binds both IQ domains but with the same affinity, or that binding of Cam2 results in a different conformation of the IQ domains.

7.2. Cam1 function as a Myo52 light chain.

Co-localisation of Cam1 with Myo52 in *S. pombe* cells (Figure 3.4) and analysis of protein dynamics (Figure 3.7) is consistent with Cam1 functioning as a light chain for the Class V myosin. However, using the *in vitro* methods described (Figure 3.9), it was not possible to directly investigate these interactions in the same way as for Myo1.

Observations of low levels of FRET in Myo52 IQ12 FRET proteins (Figure 3.10 & Figure 3.11) suggest that the first two IQ domains of Myo52 have a more extended conformation without binding of a calmodulin light chain. It is possible that the linker sequence used in the FRET protein does not take on the native structure found in full length Myo52 protein. However, a semi-rigid structure of the first pair of IQ motifs would be consistent with some models of myosin V neck structure which suggest that IQ domains function in pairs, with bending occurring primarily at 'hinge' points between pairs (Terrak et al. 2005; Craig & Linke 2009).

A relatively stiff neck region without the requirement of calmodulin light chain binding may provide an explanation for why deletion of the IQ domains of Myo52 in *S. pombe* does not effect cellular localisation and movement (Grallert et al. 2007). However, the reported velocities of Myo52ΔIQ proteins vary, indicating that Cam1 may play a role in regulating the step length of Myo52. To explore this *in vitro*, a FRET based approach described in this study is not suitable. *In vitro* motility assays, as described for vertebrate myosin V motors (Nguyen & Higuchi 2005) may provide a better approach to study the function of Cam1 in regulating Myo52.

7.3. *In vivo* analysis of Cam1 function as a Myo1 light chain.

Observation of similar cellular localisation patterns and dynamics for Cam1 and Myo1 (Figure 3.3), combined with evidence of binding *in vitro* suggests that Cam1 acts as the Myo1 light chain, consistent with immuno-precipitation data (Toya et al. 2001). The dependency of Cam1 on Myo1 for localisation to endocytic foci suggests Cam1 is recruited to these patches by Myo1 (Figure 3.7).

The lifetime of Cam1 foci at the membrane is 3.6 seconds shorter than that measured for Myo1 (Section 3.2). Without simultaneously observing the recruitment of these two proteins to the membrane, it is not possible to determine the significance of shorter Cam1 patch lifetimes. These differences could be due to methods of detection, Cam1 was observed using a GFP fusion protein, while Myo1 was fused to an mNeongreen fluorophore. Differences in fluorescent protein intensities could influence the measurement of event duration.

Both Myo1 and Cam1 foci disassemble at the membrane as the endocytic vesicle is internalised (Figure 3.6). This is consistent with previous observations of Myo1 recruitment to endocytic patches in fission yeast (Sirotkin et al 2010). From the strains generated and imaged in this study it is not possible to determine whether the shorter lifetimes of Cam1 patches indicate that Cam1 is recruited to the membrane after, or disassociates prior to Myo1.

Due to the essential and ubiquitous roles of Cam1 in cellular processes, it is not possible to generate a *cam1*Δ strain or use temperature sensitive mutants to explore the role of Cam1 in regulating Myo1 *in vivo*. Due to possible redundancy in function between Cam1 and the second calmodulin-like protein, Cam2, use of specific IQ mutants (such as those in Sammons 2011) may also not provide accurate information about the role of Cam1.

7.4. Function of N-terminal acetylation of Cam1.

7.4.1. Structure and stability.

The N-terminus of *S. pombe* Cam1, and mammalian calmodulin proteins, are predicted to be acetylated by the NatA acetylation complex (Starheim et al. 2012). During this study, the process for expressing acetylated recombinant Cam1 protein was optomised to produce a 100 % yield of Nt-acetylated Cam1 (Figure 3.14).

The role of Cam1 acetylation was characterised *in vitro* by comparison of acetylated (Cam1-ACE) and unacetylated Cam1 proteins. Nt-acetylation appears to have a significant effect on the overall structure and stability of the Cam1 protein measured by CD (Figure 3.15). This could be due to the acetyl group affecting interactions of the N-terminal turn (residues 2-5) which are not part of the first α-helix. Cartoon diagrams from the crystal structure of chicken calmodulin show the location of the N-terminal residues (Figure 7.1.B), the sequence of structured regions are well conserved between *S. pombe* and chicken (Figure 7.1.A). The N-terminal turn is likely to be flexible due to its unstructured nature, allowing possible interactions with other regions on the protein, or with ligands.

It is possible that acetylation of the N-terminus affects the stability of the first α-helix, or modulates interactions of the N-terminus with other regions such as the hydrophobic surface of the 4th α-helix. Although well conserved, a significant sequence difference between *S. pombe* Cam1 and vertebrate calmodulins is in the 2nd and 3rd amino acid residues. *S. pombe* Cam1 has a threonine and arginine residue providing a positive change, while vertebrate calmodulins have a conserved negatively charged aspartate residue. How this change in charge affects the N-terminus of calmodulin and whether it has an effect on the function of Nt-acetylation is difficult to predict.

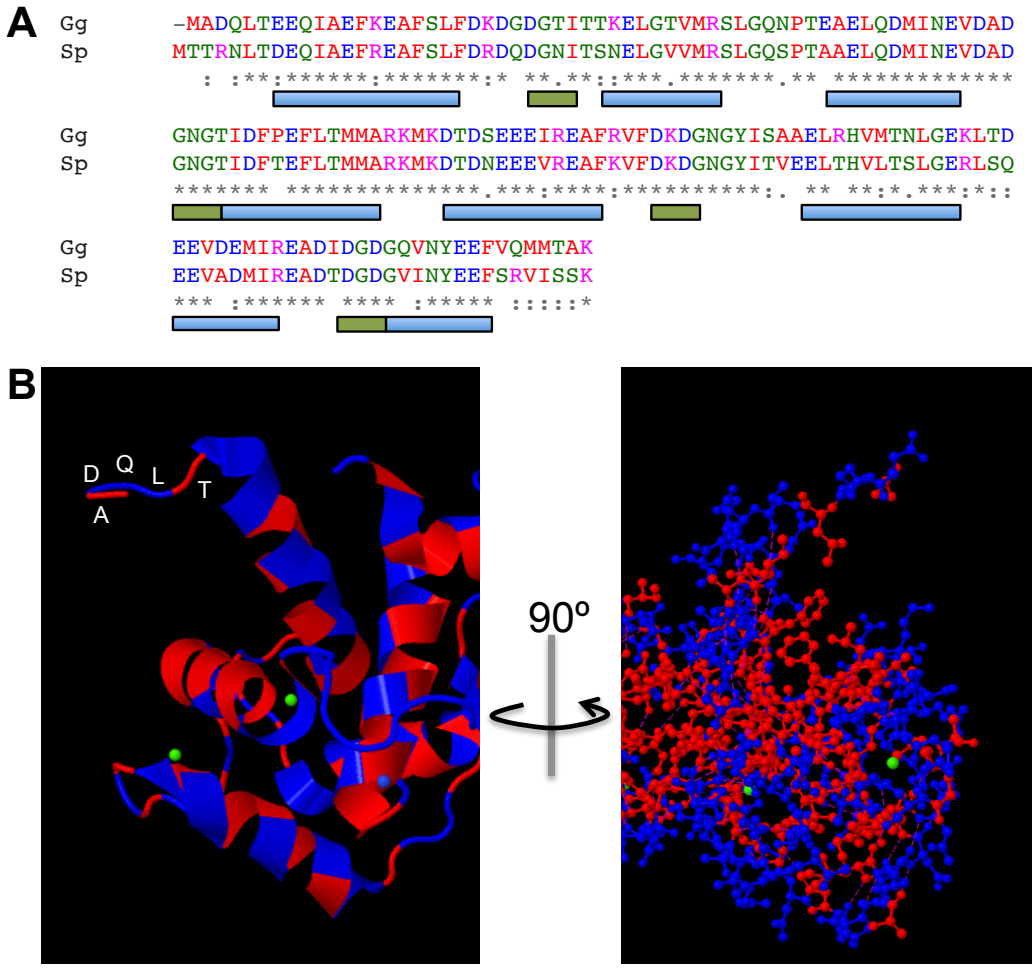

Figure 7.1. Sequence and structure of calmodulin.

(A) Sequence alignment of S. *pombe* (Sp) and chicken (Gg) calmodulin sequences indicating regions of α-helix (blue) and β-sheet (green). (B) Crystal structure of chicken calmodulin (PDB 2O60) highlighting the positions of N-terminal residues.

Acetylation of *S. pombe* calmodulin functions to protect the protein from irreversible unfolding at higher temperatures (Figure 3.15.B), possibly by protecting the N-terminal α-helix from denaturation. However, the irreversible denaturation seen in these experiments was after exposure to 70 ºC, and the calculated T_m values for both Cam1 proteins were above 40 ºC. These temperatures are above the physiological conditions encountered by yeast cells. Both forms of Cam1 are likely to be stable within the cell, this is supported by no overall changes in Cam1-GFP fluorescence levels in *naa15*Δ cells (Figure 3.18.F).

7.4.2. Calcium sensitivity.

IAANS labelled Cam1 proteins provide evidence that acetylation of *S. pombe* Cam1 affects its calcium sensitivity (Figure 3.16.A). The higher pCa_{50} value of acetylated Cam1, 6.54 compared to 6.03 for unacetylated Cam1, suggests that Cam1-ACE binds calcium more efficiently. One possibility is that acetylation may have an effect on the structure of the first α-helix, in turn changing the orientation or flexibility of the loops involved in calcium ion binding. The positioning of these regions (highlighted in Figure 7.2 - crystal structure of chicken calmodulin), illustrates how changes in stability or position of the N-terminus could be relayed to the calcium binding loops by the 1st α-helix. Despite acetylation resulting in changes in calcium sensitivity, determined by changes in conformation of IAANS labelled Cam1 proteins, this did not result in a change in the calcium sensitivity of Cam1 binding to the IQ domains of the Myo1IQ12 FRET protein (Figure 3.16.B).

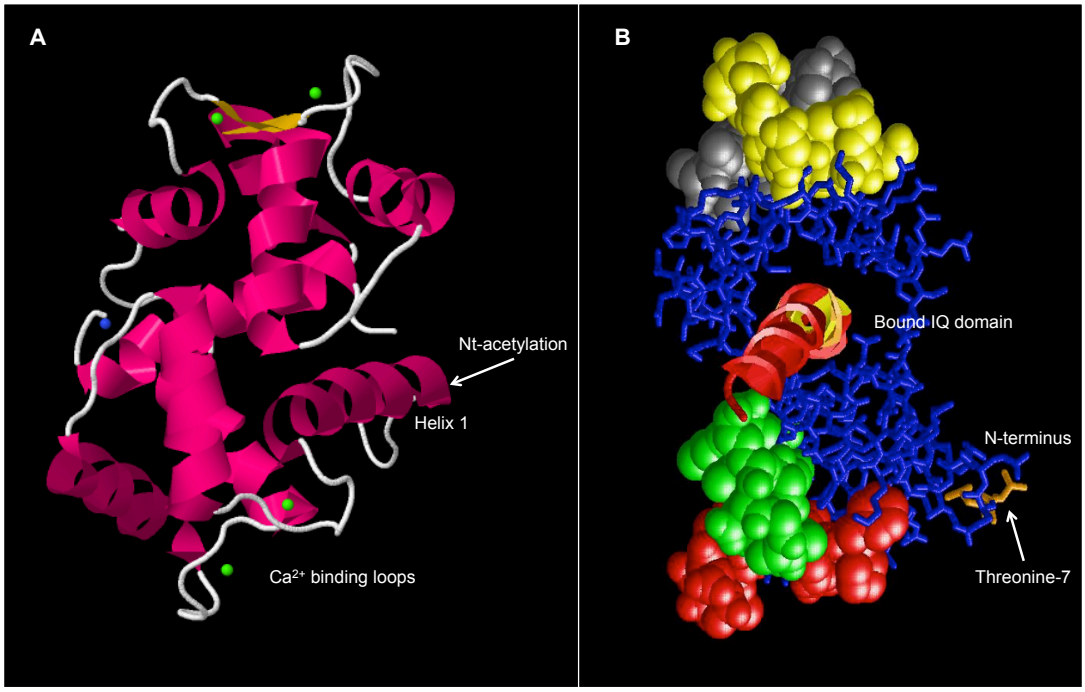

Figure 7.2. Structure of calmodulin.

(A) Location of the calcium binding loops in relation to acetylation at the N-terminus of (chicken) calmodulin (PDB 2O60). Crystal structure of human calmodulin with a bound helical IQ peptide (PDB 3EWT), highlighting the location of the IQ binding site and threonine-7. Equivalent Thr-7 in Cam1 mutated to cysteine and labelled with an IAANS molecule.

7.4.3. Interaction with Myo1 – *in vitro*.

The effect of Cam1 Nt-acetylation on its interaction with Myo1 IQ domains was firstly investigated *in vitro*. FRET binding assays show that Nt-acetylation results in a 3-fold increase in the affinity of Cam1 for Myo1 IQ domains (Figure 3.17). These measurements were made in the absence of calcium, meaning that this change in affinity is not due to the possible changes in calcium sensitivity of Cam1 upon acetylation. It is possible that the structural changes observed from CD measurement (also made in the absence of calcium) are sufficient to alter the IQ binding site in the centre of the calmodulin protein (Figure 7.2.B).

7.4.4. Interaction with Myo1 – *in vivo*.

Following these observations *in vitro*, the effect of acetylation was investigated in the cell (Figure 3.18). Cam1-GFP fluorescence was analysed in *naa15*Δ cells, in which function of the NatA acetylation complex was abolished. These results suggest that in the absence of acetylation, Cam1 is distributed between more, smaller foci. The mechanism of endocytosis still functions in *naa15*Δ cells, but the lifetimes of Cam1 patches at the membrane are 30 % longer, suggesting that the rate of endocytosis is slowed (Figure 3.18.B-C).

It is possible that a weaker interaction of unacetylated Cam1 with the IQ domains of Myo1 could result in reduced Myo1 activity. Calmodulin light chain binding to vertebrate Myo1c has been shown to influence myosin motor activity (Adamek et al. 2008). This would explain the slower rates of endocytosis, as Myo1 motor activity is required for efficient vesicle internalisation (Figure 4.19) (J. Bi et al. 2015; Attanapola et al. 2009). However, it is not clear how acetylation of Cam1 alone regulates its localisation to more, smaller foci.

Deletion of the *naa15* gene results in a subset of unacetylated proteins in the cell with ~30 % of all proteins in yeast predicted to be acetylated by the NatA complex (Starheim et al. 2012). Among these proteins is Myo1, also predicted to be acetylated by the NatA complex (Figure 7.3). Therefore observations of Cam1-GFP fluorescence in a *naa15*Δ cell could also report changes in Myo1 protein

localisation and function. Myo1 localisation to sterol rich regions of the plasma membrane is dependent on the TH1 domain (Takeda & Chang 2005) located in the tail region of the protein. It is unlikely that Nt-acetylation would effect the function of this distal domain in the protein, especially considering that addition of a fluorescent molecule at the N-terminus does not significantly impair Myo1 function.

It is therefore possible that changes in binding of acetylated Cam1 to Myo1, predicted by *in vitro* data, could result in changes in the localisation of Myo1. However, using a *naa15*Δ background in which the function of many proteins may be altered, it is not possible to determine what affect Nt-acetylation has directly on Cam1-Myo1 interactions or their localisation. In order to specifically investigate the function of Cam1 acetylation *in vivo*, a strain could be made in which the N-terminal sequence is mutated in order to prevent acetylation For example, N-terminal proline or MG- residues are not acetylated in yeast. This would allow more specific investigation of whether Nt-acetylation of Cam1 affects Myo1 localisation.

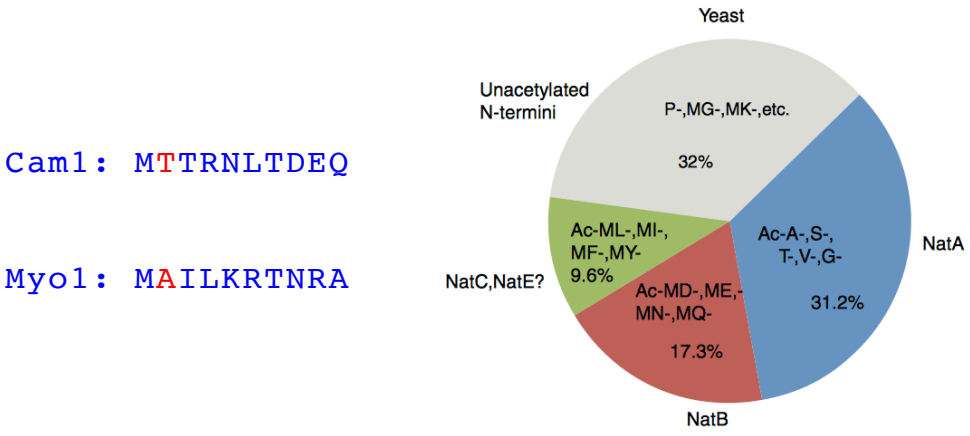

Figure 7.3. N-terminal sequence of *S. pombe* Cam1 and Myo1.
N-terminal protein sequences of *S. pombe* Cam1 and Myo1. Prediction of N-terminal acetylation in yeast (Starheim 2012).

7.5. *In vitro* analysis of Cam2 function.

Despite sequence similarities with myosin light chains (Lord & Pollard 2004), Cam2 has distinct biochemical properties and dynamics within the cell. Firstly, in contrast to Cam1, Cam2 binds to the IQ domains of Myo1 in a calcium independent manner (Figure 4.1.A). This is consistent with the absence of the conserved EF-hand residues required for calcium binding (Figure 1.32), and inability to bind calcium ions (Figure 4.1.B). This would suggest that Cam2, is constantly in a 'gripping' conformation (Trybus et al. 2007), able to bind IQ domains irrespective of calcium concentration.

The affinity of Cam2 for the IQ domains of Myo1 was determined by binding to the Myo1IQ12 FRET protein, and was calculated to be 1.5-fold weaker than Cam1 in the absence of calcium (Figure 4.2). A possible explanation is that Cam2 is able to function as a light chain for Myo1, but may only be required under elevated calcium conditions when the interaction of Cam1 and Myo1 would be weakened. As discussed, it would appear that binding of Cam2 results in different flexibility of the Myo1 IQ domains when compared to Cam1 binding. One explanation could be that changes in calcium concentration during the cell cycle cause a switch in binding of Cam1 or Cam2 to the Myo1 neck region, resulting in differential regulation of Myo1.

7.6. *In vivo* analysis of Cam2 function during the mitotic cell cycle.

Data from this study suggests that during the mitotic cell cycle, Cam2 has a non-essential function in improving the efficiency of endocytosis. This is consistent with previously reported data showing that Cam2 enhances Myo1-driven actin filament motility (Sammons et al. 2011). Cam2 recruits to endocytic patches later than Cam1 and Myo1, as the vesicle is internalised (Figure 4.16.B), consistent with *in vitro* data which suggests that Cam2 binds preferentially to a Myo1-Cam1 complex (Figures 4.5 & 4.9). The interaction of Cam2 at the endocytic patch is more dynamic compared to Cam1.

The precise function of Cam2 during endocytosis is not clear, as although impaired, endocytosis still occurs in *cam2*Δ cells (Figure 4.20.C), resulting in no major growth defects at 25 ºC. One hypothesis is that Cam2 binds to Myo1-Cam1 complexes at endocytic patches, dissociating Cam1, and regulating Myo1 activity to prepare for vesicle scission. The nature of this interaction would be transient as Myo1 remains at the membrane while Cam2 is internalised with the vesicle. Consistent with this hypothesis is the longer lifetimes and less compact Cam1 foci (Figure 4.23). This suggests that Cam1 remains associated with Myo1 for longer and is still able to facilitate vesicle scission, but less efficiently than in the presence of Cam2. To further explore the function Cam2 has in regulating Myo1, the dynamics of Myo1 could be investigated in an *mNeongreen-myo1 cam2*Δ strain, not made during this study.

The localisation of Cam2 to patches in the absence of Myo1, indicates that Cam2 is recruited to the membrane by an alternative mechanism. Cam2 has been shown associate with Pik1 – a PI 4-kinase – *in vivo* (Sammons et al. 2011). This protein localises throughout the cell and concentrates at the Golgi (Park et al. 2009) and contains a partially conserved IQ domain at the C-terminus. Proteins such as Pik1 may be responsible for the localisation of Cam2 to the membrane.

However, Pik1 is not enriched at endocytic patches and the observation of Cam2 internalising with the vesicle (Figure 4.16) suggests Cam2 has an alternative binding partner. One method to elucidate this binding partner would be through analysis of Cam2 immunoprecipitates. The co-localisation of Cam2 with the endocytic patch marker, Sla2, and similar dynamics to actin and actin binding proteins, suggest that Cam2 may associate with a protein component of the endocytic vesicle or surrounding coat.

The role of calcium influx in triggering synaptic vesicle fusion and scission at nerve terminals has been extensively studied in mammalian cells (Hosoi et al. 2009; X.-Wu et al. 2009). Calcium influx through calcium channels triggers vesicle fusion at the membrane. Calmodulin activates the phosphatase, calcineurin which is involved in dephosphorylation of endocytic proteins (Marks & McMahon 1998). Similar roles for the *S. pombe* calcineurin-like protein, Ppb1 have not been

reported (Yoshida et al. 1994) suggesting that a different mechanism exists in yeast for triggering endocytosis. However, calcium concentrations in the cell fluctuate throughout the cell cycle (Kahl & Means 2003; Whittaker & Milligan 1997; Hallermann 2014) and at different locations within the cell (Clapham 2007; Hallermann 2014). This could present a role for the calcium insensitive Cam2 protein in *S. pombe*, in maintaining Myo1 function at sites of endocytosis when calcium concentrations in the cell are elevated. This theory is supported by reports of a 5-fold increase in Cam2 expression during meiosis (Mata et al. 2002), when cellular calcium concentrations are higher (Suizu et al. 1995). Cam2 may therefore be required for function with Myo1 during mating and meiosis due to its insensitivity to calcium.

7.7. Fluorescent labelling of proteins *in vivo*.

7.7.1. Choosing fluorescent proteins

Throughout this study, the use of fluorescently labelled proteins for imaging was carefully considered. Labelling of Cam1 at the same terminus of the protein with a different fluorophore indicates how the function of a protein can be altered (Figure 3.2). Care must therefore be taken when choosing fluorescent markers. eGFP fluorescent molecules were used to label a large amount of proteins studied. This was due to a high relative brightness and stability of GFP compared to other fluorophores (Shaner et al. 2005), and the ease of introducing the cDNA as a C-terminal fusion (Section 2.4.7). mNeongreen was used in later experiments to label Myo1 proteins due to the increased intensity, photostability and folding of this fluorophore in comparison to YFP and GFP (Shaner et al. 2007).

When adding considerable extra mass to a protein it must be considered whether the function, localisation or interactions of the protein are affected. Labelling structures of the cytoskeleton appears particularly problematic due to the complexity of interactions each protein makes. The difficulty in labelling actin in live cells is well documented (Belin et al. 2014; Huang et al. 2012), with different markers preferentially incorporated into certain actin structure and effects on the

stability of actin polymers. During this study the Lifeact peptide fused to mCherry was used to visualise actin (Riedl et al. 2008; Huang et al. 2012).

7.7.2. Simultaneous fluorescent labelling of proteins

Multiple combinations of fluorescently labelled Myo1 and CaM are shown to result in abnormal localisation of one or both proteins (Figures 3.5 and 4.15). This indicates that the fluorescent molecules inhibit the normal interactions between these two proteins. The *mCherry-myo1 cam2-gfp* strain appeared to maintain normal localisation of both proteins. While no confident conclusions could be made of the relative dynamics of these proteins, this does suggest that Cam2 interacts with Myo1 in a different manner than Cam1, as the equivalent *mCherry-myo1 cam1-gfp* strain was disrupted.

The double tagged strains used to determine the localisation of Myo1, Cam1 and Cam2 to endocytic patches appeared fully functional (Figures 3.6 and 4.16). From these strains it was possible to conclude that Myo1 and Cam1 remain at the cell membrane, while Cam2 internalises with the endocytic vesicle. However, to determine the relative timings of Myo1, Cam1 and Cam2 to endocytic patches, more detailed analysis would need to be made, ideally in strains containing the same reference protein.

7.8. Function of phosphorylation of Myo1 in the neck region.

7.8.1. Effect of Myo1-S742 phosphorylation *in vitro*.

The phosphoproteome screen by Wilson-Grady (2007) identified the serine-742 residue of Myo1 as a potential site of phosphorylation in *S. pombe* cells. This residue is between the Myo1 IQ1 and IQ2 motifs (Figure 1.33). During this study, the potential effects of phosphorylation at this site on light chain binding and regulation of Myo1 function was investigated.

Firstly, the effect of mimicking phosphorylation at Myo1-S742 was explored *in vitro* using the Myo1IQ12-S742D FRET protein (Figure 3.9.D). When comparing binding of Cam1 with the phosphorylation-null Myo1IQ12 FRET protein, it was

observed that phosphorylation of this residue does not significantly affect the interaction of Cam1 (Figure 5.2). In contrast, data suggests that binding of Cam2 is 4-fold tighter to the phosphorylated Myo1 IQ domains (Figure 5.3). The relative affinities of Cam1 (K_d = 0.87 μM) and Cam2 (K_d = 0.28 μM) mean that Cam2 has a higher affinity for the phosphorylated Myo1 IQ domains *in vitro*. Due to limitations of the FRET assay and the unstructured nature of a phosphorylated IQ peptide, it was not possible to determine whether this increased affinity of Cam2 would displace Cam1 from the IQ domains. However, the calculated affinities would suggest that Cam2 would bind preferentially to the phosphorylated Myo1 IQ domains. This data suggests phosphorylation of Myo1-S742 may induce a switch of binding between the two calmodulin light chains, Cam2 and Cam1.

Phosphorylation inducing a switch in the binding of proteins to the Myo1 IQ domains is similar to that seen for mammalian Myo1c. Insulin induced phosphorylation of a serine residue at the beginning of the Myo1c neck region results in a 45 % decrease in calmodulin binding and promotes 14-3-3 binding (Yip et al. 2008). Phosphorylation in the IQ domains of myosins and potentially other IQ domain containing proteins, may be a conserved mechanism of regulating calmodulin binding.

7.8.2. Effect of Myo1-S742 phosphorylation *in vivo*.

Strains were generated to observe the *in vivo* effects of differential phosphorylation of Myo1 at serine-742 (Section 5.2). In the time available during this study, strains were generated in order to investigate the effect of blocking phosphorylation at Myo1-S742 in *myo1-S742A* strains. Some *myo1-S742D* phosphomimic strains were generated but time did not allow for these to be completely characterised.

Altering the phosphorylation state at Myo1-S742 does not result in any major changes in the phenotype of cells, and the growth rates of mitotic cells are not significantly changed (Figure 5.6). Phosphorylation at this residue may therefore result in only subtle changes during the mitotic lifecycle of the cell, but it is possible

that phosphorylation is required for cell cycle progression or growth under specific conditions.

Localisation of the 'wild type' Myo1 and phosphorylation-null Myo1-S742A were compared using live cell imaging of mNeongreen labelled fusion proteins (Figure 5.9) and STORM super-resolution imaging of fixed samples (Figure 5.9). These results indicate that un-phosphorylated Myo1-S742A protein is detected in fewer, less intense foci, suggesting that in the absence of phosphorylation at serine-742, Myo1 is less able to form compact foci at endocytic patches. The same localisation is seen for Cam1-GFP in *myo1-S742A* cells, with less Cam1 incorporated into fewer, smaller, less intense foci (Figure 5.11). The reduction in Cam1 fluorescence at foci was more significant than that seen for Myo1. This suggests that the *myo1-S742A* mutation effects both Myo1 localisation and also the ability of Cam1 to bind to the Myo1 present at foci. This may indicate that although the affinity of Cam1 for the two forms of Myo1 *in vitro* is unchanged (Figure 5.2), Cam1 binding to the Myo1-S742A protein in cells may be impaired.

Impaired NETO was observed in *myo1-S742A* cells by following the redistribution of multiple endocytic patch proteins as cells grew in length (Figures 5.16-5.18). The sites of endocytosis are known to reflect the sites of new cell growth and are therefore redistributed once cells begin NETO (Marks et al. 1986). In *myo1*$^{+}$ cells, analysis of actin and the early endocytic protein, Sla2 showed this characteristic growth at the new cell end once cells reached ~9-10 μm in length (Mitchison & Nurse 1985). In contrast *myo1-S742A* cells appeared to exhibit no redistribution of endocytic patches, suggesting that NETO in these cells was impaired. This prompted the investigation of a possible cell cycle dependent mechanism of regulation for the phosphorylation of Myo1-S742.

7.9. Cell cycle dependent regulation of Myo1-S742 phosphorylation.

Antibodies specifically raised against a phosphorylated peptide of the Myo1-S742 region were used to investigate the phosphorylation status of this Myo1 residue. The lack of detectable Myo1-S742 phosphorylation in asynchronous cell cultures suggests that this residue remains phosphorylated for only a short period during the cell cycle. This is consistent with the observation of only small changes in overall growth rates of *myo1-S742* mutant strains. Synchronous cultures of *cdc10-v50* and *cdc25-22* cells were used to determine the phosphorylation status of Myo1 at the G1-S and G2/M transition points respectively (Nurse 1975; Marks et al. 1992). No phosphorylation was detected in *cdc25-22* arrested cells, indicating that in cells just prior to entry into mitosis Myo1-S742 is likely to be in an un-phosphorylated state. In contrast Myo1-S742 phosphorylation was detected in *cdc10-v50* cells arrested prior to NETO (Figure 5.19). These data are consistent with the observations of *myo1-S742A* cells exhibiting defects in redistribution of endocytic patches during NETO. Due to time constraints, the specificity of anti-Myo1-S742P* antibodies were not confirmed. In order to test this, a western blot of cell extracts from arrested *cdc10-v50 myo1-S742A* cells should be checked for the absence of phosphorylated Myo1-S742 protein.

If the Myo1-S742 phosphorylation event is required prior to NETO, in *myo1-S742A* cells lacking this phosphorylation event, NETO is likely to be impaired or delayed. As there are no major growth defects in *myo1-S742A* cells, and endocytosis still occurs, it is likely that growth can proceed but only from the old end. In order to redistribute growth to the new cell end, Tea4 and Tea1 proteins are delivered to the new cell end by microtubules (Martin et al. 2005) in order to initiate formation of actin filaments, along which Myo52 is involved in delivering proteins to the new cell end (Martín-García & Mulvihill 2009). The NETO defects observed in *myo1-S742A* cells are not as severe as those seen in, for example, *tea1*Δ cells. This indicates a possibility that the major mechanisms of NETO are initiated, but complete redistribution growth is not possible.

Myo1 has an essential function in determining the polarized distribution of actin patches (Figure 4.19) and cell growth (Lee et al. 2000). Reduced levels of Myo1-

S742A protein at endocytic patches (Figure 5.9) may be sufficient to inhibit the polarized redistribution of actin patches during NETO. Polarised cell growth is thought to result from a combination of actin polymerization-driven movement of actin patches and initiation of new patch formation at sites of growth (Pelham & Chang 2001). Myo1 functions in both of these processes, associating with sterol-rich membrane regions early in patch formation, and activating Arp2/3 actin nucleation. Subtle changes in the localisation or function of Myo1 in the absence of phosphorylation at serine-742 may therefore disrupt NETO.

7.10. Towards a model for Myo1-S742 phosphorylation and the role of Cam2.

7.10.1. Function of Cam2 and Myo1-S742 phosphorylation during the mitotic cell cycle.

Data suggests that during the mitotic cell cycle, Cam2 functions to enhance the recruitment of Myo1 to endocytic patches (Figure 4.20), where it is involved in internalisation and scission of vesicles (Jonsdottir & Li 2004). The longer lifetimes of Cam1-GFP foci in *cam2*Δ cells are consistent with this model. In the absence of Cam2 the Myo1-driven internalisation mechanism is impaired, slowing the rate of endocytosis and increasing the lifetimes of patches.

In vitro binding data suggests that Myo1-S742 phosphorylation enhances the binding of Cam2 to Myo1. Therefore, if the Myo1-S742 phosphorylation event simply functioned to recruit Cam2 for internalisation, the lifetimes of patches in *myo1-S742A* cells would also be extended as Cam2 would not be recruited. However, this is not the case for either mNeongreen-Myo1 or Cam1-GFP patch lifetimes, which are both reduced in *myo1-S742A* cells (Figures 5.10 and 5.12). This, combined with an apparent cell cycle dependence of phosphorylation (Figure 5.19), and the observation of normal Cam2 localisation in *myo1-S742A* cells (Figure 5.14) suggests that although Cam2 may have a non-essential function during endocytosis, changes in affinity for the phosphorylated Myo1 IQ domains does not facilitate this mechanism. The function of Cam2 in enhancing endocytosis possibly occurs through its binding to Myo1-Cam1 at cortical actin

patches, while the mechanism of Myo1-S742 phosphorylation in switching Cam1 and Cam2 plays a distinct role.

7.10.2. A possible function of Cam2 and Myo1-S742 phosphorylation in meiosis.

Cam2 has been shown to function during meiosis, localizing to the forespore membrane and is essential for its correct formation at elevated temperatures (Itadani et al. 2006). Cam2 localisation during this process is dependent on Myo1 (Itadani et al 2006), this is in contrast to observations of mitotic *cam2-gfp myo1*Δ cells, in which Cam2 localisation is independent of Myo1 (Figure 4.17). This suggests Cam2 has separate functions dependent on the stage of the cell cycle. This is consistent with a model in which phosphorylation of Myo1 is a mechanism of switching Cam2 and Myo1 function.

Similar observations of Myo1 and Cam1 are made in both *cam2*Δ and *myo1-S742A* cells, of smaller foci containing less protein (Figures 4.20, 4.21, 5.9 and 5.11). However, data shows relatively subtle defects in both *cam2*Δ and *myo1-S742* phosphorylation mutants during the mitotic cell cycle, under normal growth conditions. This is in contrast to a significant 4-fold increase in Cam2 affinity for the phosphorylated Myo1 IQ domains *in vitro*. This suggests that the major function of this phosphorylation event, and the role of Cam2 is more specific to cell growth under specific conditions. Observation of cell cycle dependent phosphorylation of Myo1-S742 led to investigations of these possibilities.

Data suggests that Myo1 phosphorylation occurs prior to the G1-S transition point and NETO (Figure 5.19), and is dephosphorylated before cells enter mitosis (Figure 5.20). In addition, Myo1-S742 phosphorylation also appears dependent on TORC2 signalling, with no phosphorylated Myo1-S742 protein detected in *ste20*Δ cell extracts (Figure 5.21). Phosphorylation does not appear essential for progression through the G1-S transition point, with NETO impaired but overall cell growth not inhibited.

At the G1-S transition point, cells asses the availability of nutrients and growth conditions, and can exit the mitotic cell cycle (Murakami & Nurse 2000). In the

presence of mating pheromones and under nitrogen starvation conditions, cells enter the meiotic cell cycle from this checkpoint (Mochizuki & Yamamoto 1992). As Myo1-S742 is phosphorylated in *cdc10-v50* cells arrested at this transition point, this suggests a possible function of this phosphorylation event in entry to meiosis.

This hypothesis is supported by data showing the absence of Myo1-S742 phosphorylation in *ste20*Δ cells. Tor signalling is a well-studied mechanism of regulating cell growth in response to nutrient levels in the environment. The TORC1 complex is required for sexual development of *S. pombe* cells in response to nitrogen starvation (Matsuo et al. 2007). TORC2 is also required for the transient arrest in G1 and entry into mitosis under nutrient starvation conditions (Weisman & Choder 2001; Kawai et al. 2001). TORC2-dependent phosphorylation of Myo1 at the G1-S transition point may prime the cell for exit from the mitotic growth cycle if nutrient conditions are un-favourable.

7.10.3. A possible model for future investigation:

Myo1-S742 is phosphorylated at the G1-S transition point, where cells are able to enter the meiotic cell cycle in response to nutrient starvation. It is possible that this phosphorylation is TOR-dependent, allowing controlled regulation in response to the environmental conditions. Phosphorylation of Myo1-S742 results in an increase in the affinity of Cam2, possibly resulting in a ‘switch’ of light chain from Cam1 that is normally bound during the mitotic cell cycle. Cam2 bound Myo1 may result in changes in Myo1 activity or localisation required for function at the leading edge of fore-spore membranes during meiosis (Toya et al. 2001; Itadani et al. 2006). This role for Cam2 would be consistent with the five-fold increase in *cam2*$^{+}$ transcripts in meiotic cells (Mata et al. 2002), and the ability of Cam2 to function in increased cellular calcium conditions associated with a meiotic cell.

To investigate this hypothesis, the localisation and dynamics of Myo1 and Cam2 should be investigated in mating and meiotic cells. One possibility is that Cam2 regulates Myo1 function during the multiple re-organizations of F-actin patches during meiosis (Petersen et al. 1998). Currently the mechanism of Myo1-S742 de-phosphorylation is unclear, but is presumably in response to the presence of a

sufficient nutrient supply. As neither *cam2*Δ or *myo1-S742A* cells are sterile at the 25ºC growth conditions used in this study, it is possible that this mechanism functions to maintain meiotic entry under stress-conditions. This would be consistent with evidence that *cam2*Δ and *myo1*Δ cells are unable to sporulate at elevated temperatures (Itadani et al. 2006; Lee et al. 2000).

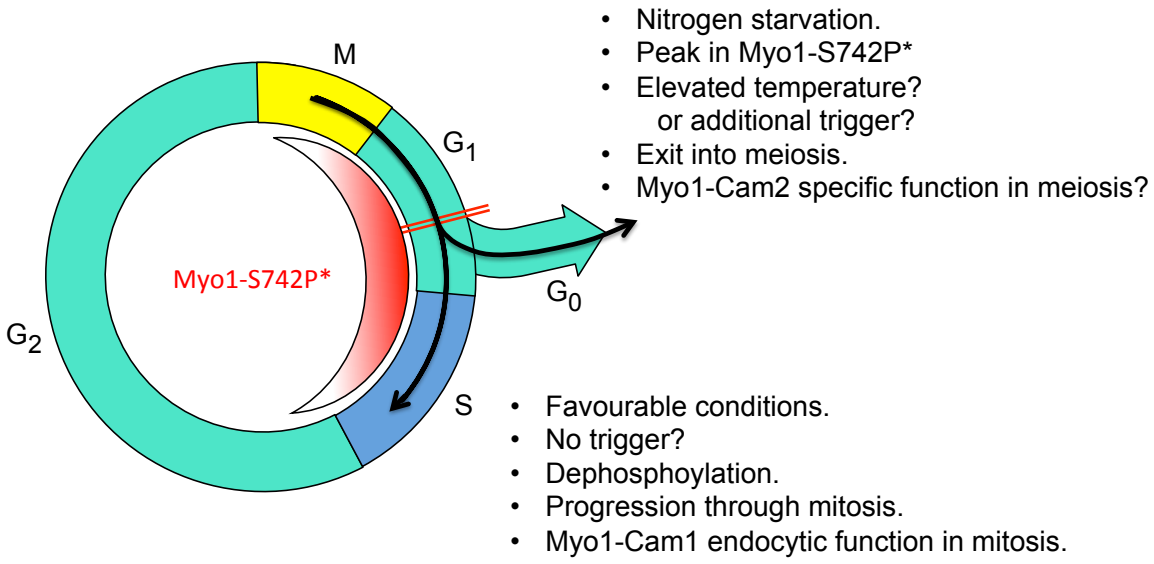

Figure 7.4. A possible model for Myo1-S742 phosphorylation and Cam2 in regulating cell cycle progression.

Cell cycle dependent phosphorylation of Myo1-S742 peaks around the G1-S transition point. Data suggests Cam2 binds more tightly to phosphorylated Myo1 IQ domains. Upon nitrogen starvation, a critical level of Myo1-S742 phosphorylation may induce a switch between Cam1 and Cam2 binding. Cam2 bound Myo1 may be required for a specific function during mating or meiosis, possibly due to its calcium insensitivity.

Table 7.1. Summary of *in vitro* binding data

	Cam1-ACE	Cam1 (unACE)	Cam2
Ca^{2+} off rate (s^{-1})	137 / 13 / 2	N.D.	0
pCa_{50}	6.54	6.03	N.A.
Myo1IQ12 FRET affinity (μM)	0.80	2.56	1.16
Myo1IQ1 FRET affinity (μM)	0.06	N.D.	0.39
Myo1IQ12-S742D FRET affinity (μM)	0.87	N.D.	0.28
Myo1IQ12 FRET affinity + 1 μM Cam1 (μM)	-	-	0.33
Myo1IQ12 FRET affinity + 0.2 μM Cam2 (μM)	1.98	N.D.	-

Table 7.2. Summary of *in vivo* fluorescence analysis

	Cam1-GFP	Cam1-GFP (*naa15Δ*)	Cam1-GFP (*cam2Δ*)	Cam1-GFP (*myo1-S742A*)	Cam2-GFP	Cam2-GFP (*myo1Δ*)	Cam2-GFP (*myo1-S742A*)
Relative whole cell fluorescence	1	1.1	0.97	0.89	1	1.48	1.01
Relative number of foci per cell	12.6	+ 7.8	- 1.0	- 0.6	20.4	+ 5.3	- 1.2
Relative foci volume	1	0.53	0.74	0.67	1	1.63	1.11
% of total fluorescence incorporated into foci	1.82	0.95	1.80	1.17	2.06	2.53	2.30
Patch lifetime (s)	10.2	13.2	13.3	9.4	11.0	17.0	N.D.
Patch lateral movement (μM)	N.A.	N.A.	N.A.	N.A.	1.2	0	N.D.

	Lifeact	Lifeact (*myo1Δ*)	Lifeact (*myo1-S742A*)	mNeongreen -Myo1	mNeongreen -Myo1-S742A	YFP-Myo1	YFP-Myo1 (*cam2Δ*)
Relative whole cell fluorescence	1	N.D.	1.14	1	0.86	1	0.90
Relative number of foci per cell	19.8	N.D.	- 1.1	15.9	- 2.8	13.4	- 2.1
Relative foci volume	1	N.D.	1.19	1	0.98	1	0.64
% of total fluorescence incorporated into foci	1.91	N.D.	1.98	1.48	1.31	1.56	0.78
Patch lifetime (s)	11.5	18.9	N.D.	13.9	10.9	N.D.	N.D.
Patch lateral movement (μM)	1.4	0	N.D.	N.A.	N.A.	N.D.	N.D.

Red numbers indicate statistically significant differences from 'wild-type' $p < 0.05$
'Wild type' data is averaged from multiple experiments presented in results.

7.11. TORC2 dependent regulation during cytokinesis.

Following observations that *ste20*Δ cells exhibit cytokinesis defects, this study explored the function of TORC2 during CAR formation and constriction. Multiple strains were generated and characterised to determine the relative timings of proteins to the CAR, and the effects of gene deletions on cytokinesis (Tables 6.1 and 6.2).

The yeast homologue of mammalian Rictor, Ste20, is an essential component of TORC2 and was used to determine the localisation of TORC2 in this study. Ste20 had previously been reported to localise the plasma membrane (Tatebe et al. 2010), therefore this study describes a novel localisation of TORC2 to the CAR. Observations that 50 % of *ste20*Δ cells imaged fail to complete CAR constriction indicates that TORC2 plays an important role in maintaining the fidelity of cytokinesis in fission yeast.

The Class II myosin CAR component, Myp2 was shown to function in recruiting Ste20 to the CAR. Ste20-GFP protein only localised to the CAR in less than 40 % of *myp2*Δ cells, and those cells which lacked Ste20 at the CAR displayed increased cytokinesis defects compared to those in which Ste20 was present (Figure 6.6). Those cells in which Ste20 does recruit to the cell equator indicate that Myp2 is not the only binding partner for Ste20 or TORC2 at the CAR. The Petersen group also identified that the Class V myosin, Myo51 interacts with TORC2, and Myo51 was also shown to recruit Ste20 to the CAR during the early stages of anaphase.

There is a co-dependency of Myp2 and Ste20 for recruitment to the CAR, with YFP-Myp2 protein absent from the CAR in 50 % of *ste20*Δ cells (Figure 6.7). Together, TORC2 and Myp2 are required to maintain the integrity and dynamics of the CAR (Table 6.1). In both *ste20*Δ and *myp2*Δ cells, un-constricted CAR structures are seen to slide along the cortex of the cell (Figure 6.4). This suggests that one or both of these proteins may function in anchoring the CAR at the cell equator. This is consistent with studies in budding yeast, in which the class II

myosin, Myo1 is involved in localising the CAR to septin proteins marking the division site (Bi et al. 1998; Roh et al. 2002).

7.12. TORC2 dependent regulation of the actin network.

Following studies by the Petersen group which showed that Myp2 and Myo51 were not substrates of TORC2, two TORC2-dependent phosphorylation sites were identified on the actin capping protein Acp1. Absence of phosphorylation at these sites was shown to stabilise the Acp1-Acp2 capping complex. This prompted the study of TORC2 involvement in regulating the stability and dynamics of actin structures in the cell.

Consistent with the observations of aberrant actomyosin rings in *ste20*Δ and *acp1-AA* strains, less tropomyosin labelled actin was incorporated into the CAR in the TORC2-dependent phosphorylation mutant, *acp1-AA-HA* (Figure 6.12). Consistent with models that suggest actin structures are nucleated from a finite pool of actin monomers (Burke et al. 2014; Rotty et al. 2015), reduced actin levels at the CAR were accompanied by increased actin incorporated into cortical actin patches in *ste20*Δ and *acp1-AA-HA* strains (Figure 6.14). This data suggests that TORC2 phosphorylation enhances CAR stability through modulation of the available pool of actin. Phosphorylation of the two serine residues, 172 and 189 on Acp1, destabilises the capping protein heterodimer, promoting recycling of actin monomers from cortical actin patches and allowing formin nucleated polymerization at the CAR. This provides an explanation for previous reports of stabilised actin polymers in *tor1*Δ cells (Ikai et al. 2011).

Despite a five-fold increase in the actin incorporated into cortical actin patches in *acp1-AA-HA* cells, the severity of cytokinesis defects in ste20Δ cells was significantly greater. This suggests that Acp1 is not the only TORC2 regulated protein involved in maintaining the integrity of cytokinesis. TORC2 is likely to regulate the function of multiple proteins in order to coordinate cell division. For example the SCYL family pseudo-kinase Ppk32 has been shown to regulate TOR

signalling, and concentrates at the cell equator in more than 60 % of dividing cells (Kowalczyk & Petersen 2016).

This TORC2 dependent control of actin distribution via destabilization of the Acp1-Acp2 heterodimer allows cells to couple growth and division in response to environmental signals. Many of the *S. pombe* TORC2 components are conserved in mammalian cells, highlighting the possibility of similar mechanisms to control cytokinesis. As in *S. pombe* cells, TORC2 knockouts also result in increases in actin fibres in mammalian cell lines (Sarbassov et al. 2004). In addition, as seen for *S. pombe* TORC2, the serine 2481 auto-phosphorylated form of mTOR is localised to the cleavage furrow in dividing cancer cells (Vazquez-Martin et al. 2012).

Bibliography

Adamek, N., Coluccio, L.M. & Geeves, M.A., 2008. Calcium sensitivity of the cross-bridge cycle of Myo1c, the adaptation motor in the inner ear. *Proceedings of the National Academy of Sciences of the United States of America*, 105(15), pp.5710–5715.

Aghamohammadzadeh, S. & Ayscough, K.R., 2009. Differential requirements for actin during yeast and mammalian endocytosis. *Nature cell biology*, 11(8), pp.1039–1042.

Akin, O. & Mullins, R.D., 2008. Capping Protein Increases the Rate of Actin-Based Motility by Promoting Filament Nucleation by the Arp2/3 Complex. *Cell*, 133(5), pp.841–851.

Alberts, B., et al., 2006. Molecular Biology of the Cell (4th edition). *New York: Garland Science.*

Arai, R. & Mabuchi, I., 2002. F-actin ring formation and the role of F-actin cables in the fission yeast *Schizosaccharomyces pombe*. *Journal of cell science*, 115(Pt 5), pp.887–898.

Arasada, R. & Pollard, T.D., 2011. Distinct roles for F-BAR proteins Cdc15p and Bzz1p in actin polymerization at sites of endocytosis in fission yeast. *Current biology : CB*, 21(17), pp.1450–1459.

Atkin, J. et al., 2014. Torin1-mediated TOR kinase inhibition reduces Wee1 levels and advances mitotic commitment in fission yeast and HeLa cells. *Journal of cell science*, 127(Pt 6), pp.1346–1356.

Attanapola, S.L., Alexander, C.J. & Mulvihill, D.P., 2009. Ste20-kinase-dependent TEDS-site phosphorylation modulates the dynamic localisation and endocytic function of the fission yeast class I myosin, Myo1. *Journal of cell science*, 122(Pt 21), pp.3856–3861.

Axelrod, D., 2001. Total internal reflection fluorescence microscopy in cell biology. *Traffic*, 2(11), pp.764–774.

Ayscough, K.R., 2000. Endocytosis and the development of cell polarity in yeast require a dynamic F-actin cytoskeleton. *Current Biology*, 10(24), pp.1587–1590.

Ayscough, K.R. et al., 1997. High rates of actin filament turnover in budding yeast and roles for actin in establishment and maintenance of cell polarity revealed using the actin inhibitor latrunculin-A. *The Journal of cell biology*, 137(2), pp.399–416.

Balasubramanian, M.K. et al., 1998. Isolation and characterisation of new fission yeast cytokinesis mutants. *Genetics*, 149(3), pp.1265–1275.

Balasubramanian, M.K., Bi, E. & Glotzer, M., 2004. Comparative analysis of cytokinesis in budding yeast, fission yeast and animal cells. *Current Biology*, 14(18), pp.R806–18.

Bartels, T. et al., 2014. N-Alpha-Acetylation of α-Synuclein Increases Its Helical Folding Propensity, GM1 Binding Specificity and Resistance to Aggregation A. Pastore, ed. *PLoS ONE*, 9(7), pp.e103727–10.

Barylko, B. et al., 1992. Purification and characterisation of a mammalian myosin I. *Proceedings of the National Academy of Sciences of the United States of America*, 89(2), pp.490–494.

Basu, R., Munteanu, E.L. & Chang, F., 2014. Role of turgor pressure in endocytosis in fission yeast. *Molecular biology of the cell*, 25(5), pp.679–687.

Bates, M. et al., 2007. Multicolor super-resolution imaging with photo-switchable fluorescent probes. *Science*, 317(5845), pp.1749–1753.

Bates, M., Huang, B. & Zhuang, X., 2008. Super-resolution microscopy by nanoscale localisation of photo-switchable fluorescent probes. *Current opinion in chemical biology*, 12(5), pp.505–514.

Bähler, J., Steever, A.B., et al., 1998. Role of polo kinase and Mid1p in determining the site of cell division in fission yeast. *The Journal of cell biology*, 143(6), pp.1603–1616.

Bähler, J., Wu, J.Q., et al., 1998. Heterologous modules for efficient and versatile PCR-based gene targeting in Schizosaccharomyces pombe. *Yeast*, 14(10), pp.943–951.

Bähler, M. & Rhoads, A., 2002. Calmodulin signalling via the IQ motif. *FEBS letters*, 513(1), pp.107–113.

Belin, B.J., Goins, L.M. & Mullins, R.D., 2014. Comparative analysis of tools for live cell imaging of actin network architecture. *Bioarchitecture*, 4(6), pp.189–202.

Bell, L. et al., 2014. A microfluidic device for the hydrodynamic immobilisation of living fission yeast cells for super-resolution imaging. *Sensors and actuators. B, Chemical*, 192, pp.36–41.

Bement, W.M. & Mooseker, M.S., 1995. TEDS rule: a molecular rationale for differential regulation of myosins by phosphorylation of the heavy chain head. *Cell motility and the cytoskeleton*, 31(2), pp.87–92.

Berg, J.S., Powell, B.C. & Cheney, R.E., 2001. A millennial myosin census. *Molecular biology of the cell*, 12(4), pp.780–794.

Berro, J., Sirotkin, V., & Pollard, T.D., 2010. Mathematical Modeling of Endocytic Actin Patch Kinetics in Fission Yeast: Disassembly Requires Release of Actin Filament Fragments. *Molecular biology of the cell*, 21, pp.2905–2915.

Bezanilla, M. & Pollard, T.D., 2000. Myosin-II tails confer unique functions in Schizosaccharomyces pombe: characterisation of a novel myosin-II tail. *Molecular biology of the cell*, 11(1), pp.79–91.

Bezanilla, M., Forsburg, S.L. & Pollard, T.D., 1997. Identification of a second myosin-II in Schizosaccharomyces pombe: Myp2p is conditionally required for cytokinesis. *Molecular biology of the cell*, 8(12), pp.2693–2705.

Bhattacharyya, A.M. & Horowitz, P., 2000. Alteration around the active site of rhodanese during urea-induced denaturation and its implications for folding. *The Journal of biological chemistry*, 275(20), pp.14860–14864.

Bi, E. et al., 1998. Involvement of an actomyosin contractile ring in Saccharomyces cerevisiae cytokinesis. *The Journal of cell biology*, 142(5), pp.1301–1312.

Bi, J. et al., 2015. Effects of FSGS-associated mutations on the stability and function of myosin-1 in fission yeast. *Disease models & mechanisms*, 8(8), pp.891–902.

Blanchoin, L., Pollard, T.D. & Hitchcock-DeGregori, S.E., 2001. Inhibition of the Arp2/3 complex-nucleated actin polymerization and branch formation by tropomyosin. *Current Biology*, 11(16), pp.1300–1304.

Bosch, M. et al., 2007. Analysis of the Function of Spire in Actin Assembly and Its Synergy with Formin and Profilin. *Molecular Cell*, 28(4), pp.555–568.

Bose, A. et al., 2002. Glucose transporter recycling in response to insulin is facilitated by myosin Myo1c. *Nature*, 420(6917), pp.821–824.

Brayford, S. et al., 2016. Tropomyosin Promotes Lamellipodial Persistence by Collaborating with Arp2/3 at the Leading Edge. *Current biology : CB*, 26(10), pp.1312–1318.

Bryce, N.S., et al., 2003. Specification of Actin Filament Function and Molecular Composition by Tropomyosin Isoforms. *Molecular biology of the cell*, 14, pp.1002–1016.

Brzeska, H. & Korn, E.D., 1996. Regulation of class I and class II myosins by heavy chain phosphorylation. *The Journal of biological chemistry*, 271(29), pp.16983–16986.

Burke, T.A. et al., 2014. Homeostatic actin cytoskeleton networks are regulated by assembly factor competition for monomers. *Current biology : CB*, 24(5), pp.579–585.

Cafferkey, R. et al., 1993. Dominant missense mutations in a novel yeast protein related to mammalian phosphatidylinositol 3-kinase and VPS34 abrogate rapamycin cytotoxicity. *Molecular and Cellular Biology*, 13(10), pp.6012–6023.

Campellone, K.G. & Welch, M.D., 2010. A nucleator arms race: cellular control of actin assembly. *Nature Reviews Molecular Cell Biology*, 11(4), pp.237–251.

Carballido-Lopez, R., 2006. The Bacterial Actin-Like Cytoskeleton. *Microbiology and Molecular Biology Reviews*, 70(4), pp.888–909.

Carnahan, R.H. & Gould, K.L., 2003. The PCH family protein, Cdc15p, recruits two F-actin nucleation pathways to coordinate cytokinetic actin ring formation in Schizosaccharomyces pombe. *The Journal of cell biology*, 162(5), pp.851–862.

Carpy, A. et al., 2014. Absolute proteome and phosphoproteome dynamics during the cell cycle of Schizosaccharomyces pombe (Fission Yeast). *Molecular & cellular proteomics : MCP*, 13(8), pp.1925–1936.

Chapman, E.R. et al., 1991. Characterisation of the calmodulin binding domain of neuromodulin. Functional significance of serine 41 and phenylalanine 42. *The Journal of biological chemistry*, 266(1), pp.207–213.

Cheney, R.E. & Mooseker, M.S., 1992. Unconventional myosins. *Current Opinion in Cell Biology*, 4(1), pp.27–35.

Cheng, Y. et al., 2007. Cryo-electron tomography of clathrin-coated vesicles: structural implications for coat assembly. *Journal of molecular biology*, 365(3), pp.892–899.

Chesarone, M.A. & Goode, B.L., 2009. Actin nucleation and elongation factors: mechanisms and interplay. *Current Opinion in Cell Biology*, 21(1), pp.28–37.

Chhabra, E.S., & Higgs, H.N., 2007. The many faces of actin: matching assembly factors with cellular structures. *Nature cell biology*, 9, pp.1110–1121.

Clapham, D.E., 2007. Calcium signalling. *Cell*, 131(6), pp.1047–1058.

Clayton, J.E. et al., 2010. Differential regulation of unconventional fission yeast myosins via the actin track. *Current biology : CB*, 20(16), pp.1423–1431.

Clos, J. & Brandau, S., 1994. pJC20 and pJC40--two high-copy-number vectors for T7 RNA polymerase-dependent expression of recombinant genes in Escherichia coli. *Protein expression and purification*, 5(2), pp.133–137.

Collins, K., Sellers, J.R. & Matsudaira, P., 1990. Calmodulin dissociation regulates brush border myosin I (110-kD-calmodulin) mechanochemical activity in vitro. *The Journal of cell biology*, 110(4), pp.1137–1147.

Conner, S.D., & Schmid, S.L., 2011. Regulated portals of entry into the cell. *Nature*, 422, pp.37–44.

Cooper, G.M., 2000. The Cell: A Molecular Approach (2nd edition). *Sinauer Associates Inc. U.S.*

Cooper, J.A. & Sept, D., 2008. New Insights into Mechanism and Regulation of Actin Capping Protein. In International Review of Cell and Molecular Biology. Elsevier, pp. 183–206.

Coulton, A., Lehrer, S.S. & Geeves, M.A., 2006. Functional homodimers and heterodimers of recombinant smooth muscle tropomyosin. *Biochemistry*, 45(42), pp.12853–12858.

Coulton, A.T. et al., 2010. The recruitment of acetylated and unacetylated tropomyosin to distinct actin polymers permits the discrete regulation of specific myosins in fission yeast. *Journal of cell science*, 123(Pt 19), pp.3235–3243.

Cox, S., 2015. Super-resolution imaging in live cells. *Developmental biology*, 401(1), pp.175–181.

Craig, E.M. & Linke, H., 2009. Mechanochemical model for myosin V. *Proceedings of the National Academy of Sciences of the United States of America*, 106(43), pp.18261–18266.

D'souza, V.M. et al., 2001. Interactions of Cdc4p, a myosin light chain, with IQ-domain containing proteins in Schizosaccharomyces pombe. *Cell structure and function*, 26(6), pp.555–565.

Das, M., et al., 2015. Phosphorylation-dependent inhibition of Cdc42 GEF Gef1 by 14-3-3 protein Rad24 spatially regulates Cdc42 GTPase activity and oscillatory dynamics during cell morphogenesis. *Molecular biology of the cell*, 26, pp.3520–3534.

Denessiouk, K. et al., 2014. Two structural motifs within canonical EF-hand calcium-binding domains identify five different classes of calcium buffers and sensors. M. Helmer-Citterich, ed. *PLoS ONE*, 9(10), p.e109287.

DesMarais, V. et al., 2002. Spatial regulation of actin dynamics: a tropomyosin-free, actin-rich compartment at the leading edge. *Journal of cell science*, 115(Pt 23), pp.4649–4660.

Doherty, G.J. & McMahon, H.T., 2009. Mechanisms of Endocytosis. *Annual Review of Biochemistry*, 78(1), pp.857–902.

Dominguez, R. & Holmes, K.C., 2011. Actin Structure and Function. *Annual Review of Biophysics*, 40(1), pp.169–186.

Doyle, A. et al., 2009. Fission yeast Myo51 is a meiotic spindle pole body component with discrete roles during cell fusion and spore formation. *Journal of cell science*, 122(Pt 23), pp.4330–4340.

East, D.A. & Mulvihill, D.P., 2011. Regulation and function of the fission yeast myosins. *Journal of cell science*, 124(Pt 9), pp.1383–1390.

Edamatsu, M. & Toyoshima, Y.Y., 2003. Fission yeast synaptobrevin is involved in cytokinesis and cell elongation. *Biochemical and biophysical research communications*, 301(3), pp.641–645.

Edwards, M. et al., 2014. Capping protein regulators fine-tune actin assembly dynamics. *Nature Reviews Molecular Cell Biology*, 15(10), pp.677–689.

Egel, R., et al., 1994. Assessment of pheromone production and response in fission yeast by a halo test of induced sporulation. *Yeast* 10(10), pp. 1347-54.

Engqvist-Goldstein, A.E. et al., 1999. An actin-binding protein of the Sla2/Huntingtin interacting protein 1 family is a novel component of clathrin-coated pits and vesicles. *The Journal of cell biology*, 147(7), pp.1503–1518.

Engqvist-Goldstein, A.E.Y. & Drubin, D.G., 2003. Actin assembly and endocytosis: from yeast to mammals. *Annual review of cell and developmental biology*, 19(1), pp.287–332.

Erickson, H.P., 2007. Evolution of the cytoskeleton. *BioEssays : news and reviews in molecular, cellular and developmental biology*, 29(7), pp.668–677.

Etienne-Manneville, S., 2004. Cdc42 - the centre of polarity. *Journal of cell science*, 117(8), pp.1291–1300.

Fededa, J.P. & Gerlich, D.W., 2012. Molecular control of animal cell cytokinesis. *Nature Publishing Group*, 14(5), pp.440–447.

Feierbach, B. & Chang, F., 2001. Roles of the fission yeast formin for3p in cell polarity, actin cable formation and symmetric cell division. *Current Biology*, 11(21), pp.1656–1665.

Firat-Karalar, E.N. & Welch, M.D., 2011. New mechanisms and functions of actin nucleation. *Current Opinion in Cell Biology*, 23(1), pp.4–13.

Flory, M.R. et al., 2004. An SMC-domain protein in fission yeast links telomeres to the meiotic centrosome. *Molecular Cell*, 16(4), pp.619–630.

Fontanilla, R.A. & Nuccitelli, R., 1998. Characterisation of the sperm-induced calcium wave in Xenopus eggs using confocal microscopy. *Biophysical journal*, 75(4), pp.2079–2087.

Forte, G.M.A., Pool, M.R. & Stirling, C.J., 2011. N-terminal acetylation inhibits protein targeting to the endoplasmic reticulum. P. Walter, ed. *PLOS Biology*, 9(5), p.e1001073.

Gachet, Y., 2005. Endocytosis in fission yeast is spatially associated with the actin cytoskeleton during polarised cell growth and cytokinesis. *Journal of cell science*, 118(18), pp.4231–4242.

Gao, L. & Bretscher, A., 2008. Analysis of unregulated formin activity reveals how yeast can balance F-actin assembly between different microfilament-based organizations. *Molecular biology of the cell*, 19(4), pp.1474–1484.

Garrod, D. & Chidgey, M., 2008. Desmosome structure, composition and function. *Biochimica et biophysica acta*, 1778(3), pp.572–587.

Gillespie, P.G., 2004. Myosin I and adaptation of mechanical transduction by the inner ear. *Philosophical transactions of the Royal Society of London. Series B, Biological sciences*, 359(1452), pp.1945–1951.

Goley, E.D. & Welch, M.D., 2006. The ARP2/3 complex: an actin nucleator comes of age. *Nature Reviews Molecular Cell Biology*, 7(10), pp.713–726.

Goode, B.L. & Eck, M.J., 2007. Mechanism and Function of Formins in the Control of Actin Assembly. *Annual Review of Biochemistry*, 76(1), pp.593–627.

Gould, K.L. & Simanis, V., 1997. The control of septum formation in fission yeast. *Genes & Development*, 11(22), pp.2939–2951.

Grallert, A. et al., 2012. Centrosomal MPF triggers the mitotic and morphogenetic switches of fission yeast. *Nature cell biology*, 15(1), pp.88–95.

Grallert, A. et al., 2007. In vivo movement of the type V myosin Myo52 requires dimerisation but is independent of the neck domain. *Journal of cell science*, 120(Pt 23), pp.4093–4098.

Greenfield, N.J., 2006. Using circular dichroism spectra to estimate protein secondary structure. *Nature protocols*, 1(6), pp.2876–2890.

Grosshans, B.L. et al., 2006. TEDS site phosphorylation of the yeast myosins I is required for ligand-induced but not for constitutive endocytosis of the G protein-coupled receptor Ste2p. *The Journal of biological chemistry*, 281(16), pp.11104–11114.

Gunning, P., O'neill, G. & Hardeman, E., 2008. Tropomyosin-Based Regulation of the Actin Cytoskeleton in Time and Space. *Physiological Reviews*, 88(1), pp.1–35.

Gunning, P.W. et al., 2015. The evolution of compositionally and functionally distinct actin filaments. *Journal of cell science*, 128(11), pp.2009–2019.

Gunning, P.W. et al., 2005. Tropomyosin isoforms: divining rods for actin cytoskeleton function. *Trends in cell biology*, 15(6), pp.333–341.

Hachet, O. & Simanis, V., 2008. Mid1p/anillin and the septation initiation network orchestrate contractile ring assembly for cytokinesis. *Genes & Development*, 22(22), pp.3205–3216.

Hachet, O. et al., 2011. A phosphorylation cycle shapes gradients of the DYRK family kinase Pom1 at the plasma membrane. *Cell*, 145(7), pp.1116–1128.

Hagan, I., et al., 2016. Fission Yeast: A Laboratory Manual. *Cold Spring Harbour Laboratory Press.*

Halachmi, D. & Eilam, Y., 1993. Calcium homeostasis in yeast cells exposed to high concentrations of calcium. Roles of vacuolar H(+)-ATPase and cellular ATP. *FEBS letters*, 316(1), pp.73–78.

Hall, A. & Nobes, C.D., 2000. Rho GTPases: molecular switches that control the organization and dynamics of the actin cytoskeleton. *Philosophical transactions of the Royal Society of London. Series B, Biological sciences*, 355(1399), pp.965–970.

Hallermann, S., 2014. Calcium channels for endocytosis. *The Journal of physiology*, 592(16), pp.3343–3344.

Hart, M.C. & Cooper, J.A., 1999. Vertebrate isoforms of actin capping protein beta have distinct functions In vivo. *The Journal of cell biology*, 147(6), pp.1287–1298.

Hartman, M.A. & Spudich, J.A., 2012. The myosin superfamily at a glance. *Journal of cell science*, 125(7), pp.1627–1632.

Hartmuth, S. & Petersen, J., 2009. Fission yeast Tor1 functions as part of TORC1 to control mitotic entry through the stress MAPK pathway following nutrient stress. *Journal of cell science*, 122(11), pp.1737–1746.

Hazard, A.L. et al., 1998. The kinetic cycle of cardiac troponin C: calcium binding and dissociation at site II trigger slow conformational rearrangements. *Protein science : a publication of the Protein Society*, 7(11), pp.2451–2459.

Heiss, S.G. & Cooper, J.A., 1991. Regulation of CapZ, an actin capping protein of chicken muscle, by anionic phospholipids. *Biochemistry*, 30(36), pp.8753–8758.

Heissler, S.M. & Sellers, J.R., 2014. Myosin light chains: Teaching old dogs new tricks. *Bioarchitecture*, 4(6), pp.169–188.

Hell, S.W. & Wichmann, J., 1994. Breaking the diffraction resolution limit by stimulated emission: stimulated-emission-depletion fluorescence microscopy. *Optics letters*, 19(11), pp.780–782.

Higgs, H., 2001. Branching out: cortactin stabilises actin networks generated by the Arp2/3 complex. *Trends in biochemical sciences*, 26(4), p.219.

Hoffman, C.S., Wood, V., & Fantes, P.A., 2015. An Ancient Yeast for Young Geneticists: A Primer on the Schizosaccharomyces pombe Model System. *Genetics*, 201, pp.403-423.

Holmes, K.C. & Lehman, W., 2008. Gestalt-binding of tropomyosin to actin filaments. *Journal of muscle research and cell motility*, 29(6-8), pp.213–219.

Hosoi, N., Holt, M. & Sakaba, T., 2009. Calcium dependence of exo- and endocytotic coupling at a glutamatergic synapse. *Neuron*, 63(2), pp.216–229.

Houdusse, A., Sliver, M., Cohen, C., 1996. A model of Ca2+-free calmodulin binding to unconventional myosins reveals how calmodulin acts as a regulatory switch. *Structure*, 4(12). pp.1–16.

Houdusse, A. et al., 2006. Crystal structure of apo-calmodulin bound to the first two IQ motifs of myosin V reveals essential recognition features. *Proceedings of the National Academy of Sciences of the United States of America*, 103(51), pp.19326–19331.

Hsiao, J.Y. et al., 2015. Arp2/3 Complex and Cofilin Modulate Binding of

Tropomyosin to Branched Actin Networks. *Current Biology*, 25(12), pp.1573–1582.

Huang, J. et al., 2012. Nonmedially assembled F-actin cables incorporate into the actomyosin ring in fission yeast. *The Journal of cell biology*, 199(5), pp.831–847.

Huang, Y., Yan, H. & Balasubramanian, M.K., 2008. Assembly of normal actomyosin rings in the absence of Mid1p and cortical nodes in fission yeast. *The Journal of cell biology*, 183(6), pp.979–988.

Hwang, C.-S., Shemorry, A. & Varshavsky, A., 2010. N-terminal acetylation of cellular proteins creates specific degradation signals. *Science*, 327(5968), pp.973–977.

Ikai, N. et al., 2011. The reverse, but coordinated, roles of Tor2 (TORC1) and Tor1 (TORC2) kinases for growth, cell cycle and separase-mediated mitosis in Schizosaccharomyces pombe. *Open Biology*, 1(3), pp.110007–110007.

Ioannoni, R. et al., 2010. Copper-dependent trafficking of the Ctr4-Ctr5 copper transporting complex. G. Butler, ed. *PLoS ONE*, 5(8), p.e11964.

Itadani, A. et al., 2010. Schizosaccharomyces pombe calmodulin, Cam1, plays a crucial role in sporulation by recruiting and stabilizing the spindle pole body components responsible for assembly of the forespore membrane. *Eukaryotic cell*, 9(12), pp.1925–1935.

Itadani, A., Nakamura, T. & Shimoda, C., 2006. Localisation of type I myosin and F-actin to the leading edge region of the forespore membrane in Schizosaccharomyces pombe. *Cell structure and function*, 31(2), pp.181–195.

Jacinto, E. et al., 2004. Mammalian TOR complex 2 controls the actin cytoskeleton and is rapamycin insensitive. *Nature cell biology*, 6(11), pp.1122–1128.

James, P., Vorherr, T. & Carafoli, E., 1995. Calmodulin-binding domains: just two faced or multi-faceted? *Trends in biochemical sciences*, 20(1), pp.38–42.

Janke, C. et al., 2004. A versatile toolbox for PCR-based tagging of yeast genes: new fluorescent proteins, more markers and promoter substitution cassettes. *Yeast*, 21(11), pp.947–962.

Johnson, M. et al., 2010. Targeted Amino-Terminal Acetylation of Recombinant Proteins in E. coli C. Herman, ed. *PLoS ONE*, 5(12), pp.e15801–5.

Johnson, M., East, D.A. & Mulvihill, D.P., 2014. Formins Determine the Functional Properties of Actin Filaments in Yeast. *Current Biology*, 24(13), pp.1525–1530.

Jonsdottir, G.A. & Li, R., 2004. Dynamics of yeast Myosin I: evidence for a possible role in scission of endocytic vesicles. *Current Biology*, 14(17), pp.1604–1609.

Kabsch, W., & Holmes, K.C., 1995. The actin fold. *The FASEB journal*, 9(2),

pp.167–174.

Kahl, C.R. & Means, A.R., 2003. Regulation of cell cycle progression by calcium/calmodulin-dependent pathways. *Endocrine reviews*, 24(6), pp.719–736.

Kaksonen, M., Sun, Y., & Drubin, D.G., 2003. A Pathway for Association of Receptors, Adaptors, and Actin during Endocytic Internalization. *Cell*, 115 pp.475-487.

Kaksonen, M., Toret, C.P. & Drubin, D.G., 2005. A modular design for the clathrin- and actin-mediated endocytosis machinery. *Cell*, 123(2), pp.305–320.

Kaksonen, M., Toret, C.P. & Drubin, D.G., 2006. Harnessing actin dynamics for clathrin-mediated endocytosis. *Nature Reviews Molecular Cell Biology*, 7(6), pp.404–414.

Kaur, J., Sebastian, J. & Siddiqi, I., 2006. The Arabidopsis-mei2-like genes play a role in meiosis and vegetative growth in Arabidopsis. *The Plant cell*, 18(3), pp.545–559.

Kawai, M. et al., 2001. Fission yeast tor1 functions in response to various stresses including nitrogen starvation, high osmolarity, and high temperature. *Current genetics*, 39(3), pp.166–174.

Kawamura, S., et al., 2002. Confocal laser microscope & CCD camera. *Yokagowa Technical Report.*

Kelley, C.A. et al., 1991. Phosphorylation of vertebrate smooth muscle and nonmuscle myosin heavy chains in vitro and in intact cells. *Journal of cell science. Supplement*, 14, pp.49–54.

Kellogg, D.R., 2003. Wee1-dependent mechanisms required for coordination of cell growth and cell division. *Journal of cell science*, 116(Pt 24), pp.4883–4890.

Kelly, S.M., Jess, T.J. & Price, N.C., 2005. How to study proteins by circular dichroism. *Biochimica et Biophysica Acta (BBA) - Proteins and Proteomics*, 1751(2), pp.119–139.

Kim, S.V. & Flavell, R.A., 2008. Myosin I: from yeast to human. *Cellular and molecular life sciences : CMLS*, 65(14), pp.2128–2137.

Kim, T., Cooper, J.A. & Sept, D., 2010. The interaction of capping protein with the barbed end of the actin filament. *Journal of molecular biology*, 404(5), pp.794–802.

Kinoshita, E. et al., 2009. Two-dimensional phosphate-affinity gel electrophoresis for the analysis of phosphoprotein isotypes. *Electrophoresis*, 30(3), pp.550–559.

Klein, M.G. et al., 2004. Structure of the actin crosslinking core of fimbrin.

Structure (London, England : 1993), 12(6), pp.999–1013.

Kovelman, R., & Russell, P., 1996. Stockpiling of Cdc25 during a DNA Replication Checkpoint Arrest in *Schizosaccharomyces pombe*. *Molecular and cellular biology*, 16(1), pp.86–93.

Kovar, D.R., 2006. Molecular details of formin-mediated actin assembly. *Current Opinion in Cell Biology*, 18(1), pp.11–17.

Kovar, D.R. et al., 2003. The fission yeast cytokinesis formin Cdc12p is a barbed end actin filament capping protein gated by profilin. *The Journal of cell biology*, 161(5), pp.875–887.

Kovar, D.R., Sirotkin, V. & Lord, M., 2011. Three's company: the fission yeast actin cytoskeleton. *Trends in cell biology*, 21(3), pp.177–187.

Kovar, D.R., Wu, J.-Q. & Pollard, T.D., 2005. Profilin-mediated competition between capping protein and formin Cdc12p during cytokinesis in fission yeast. *Molecular biology of the cell*, 16(5), pp.2313–2324.

Kowalczyk, K.M. & Petersen, J., 2016. Fission Yeast SCYL1/2 Homologue Ppk32: A Novel Regulator of TOR Signalling That Governs Survival during Brefeldin A Induced Stress to Protein Trafficking. G. P. Copenhaver, ed. *PLoS genetics*, 12(5), p.e1006041.

Köhler, D., Struchholz, S. & Bähler, M., 2005. The two IQ-motifs and Ca2+/calmodulin regulate the rat myosin 1d ATPase activity. *The FEBS journal*, 272(9), pp.2189–2197.

Krendel, M., Osterweil, E.K. & Mooseker, M.S., 2007. Myosin 1E interacts with synaptojanin-1 and dynamin and is involved in endocytosis. *FEBS letters*, 581(4), pp.644–650.

La Cruz, De, E.M. & Ostap, E.M., 2004. Relating biochemistry and function in the myosin superfamily. *Current Opinion in Cell Biology*, 16(1), pp.61–67.

Laakso, J.M. et al., 2008. Myosin I can act as a molecular force sensor. *Science*, 321(5885), pp.133–136.

Lai, F.P.L. et al., 2009. Cortactin promotes migration and platelet-derived growth factor-induced actin reorganization by signalling to Rho-GTPases. *Molecular biology of the cell*, 20(14), pp.3209–3223.

Laor, D. et al., 2015. TORC1 Regulates Developmental Responses to Nitrogen Stress via Regulation of the GATA Transcription Factor Gaf1. *mBio*, 6(4), p.e00959.

Laplante, M. & Sabatini, D.M., 2012. mTOR signalling in growth control and disease. *Cell*, 149(2), pp.274–293.

Laporte, D., Zhao, R. & Wu, J.-Q., 2010. Mechanisms of contractile-ring assembly in fission yeast and beyond. *Seminars in Cell & Developmental Biology*, 21(9),

pp.892–898.

Lara-Gonzalez, P., Westhorpe, F.G. & Taylor, S.S., 2012. The Spindle Assembly Checkpoint Review. *Current Biology*, 22(22), pp.R966–R980.

Lau, S.Y.M., et al., 1984. Synthesis of a model protein of defined secondary structure and quaternary structure. *The journal of biological chemistry*, 259(21), pp.13253–13261.

Lee, S. et al., 2005. TOR complex 2 integrates cell movement during chemotaxis and signal relay in Dictyostelium. *Molecular biology of the cell*, 16(10), pp.4572–4583.

Lee, W.L., Bezanilla, M. & Pollard, T.D., 2000. Fission yeast myosin-I, Myo1p, stimulates actin assembly by Arp2/3 complex and shares functions with WASp. *The Journal of cell biology*, 151(4), pp.789–800.

Lehman, W. et al., 2000. Tropomyosin and actin isoforms modulate the localisation of tropomyosin strands on actin filaments. *Journal of molecular biology*, 302(3), pp.593–606.

Liu, L. & Parent, C.A., 2011. TOR kinase complexes and cell migration. *The Journal of cell biology*, 194(6), pp.815–824.

Looke, M., Kristjuhan, K., & Kristjuhan, A., 2011. Extraction of genomic DNA from yeasts for PCR-based applications. *Biotechniques*, 50(5), pp. 325-328.

Lord, M. & Pollard, T.D., 2004. UCS protein Rng3p activates actin filament gliding by fission yeast myosin-II. *The Journal of cell biology*, 167(2), pp.315–325.

Lord, M., Laves, E. & Pollard, T.D., 2005. Cytokinesis depends on the motor domains of myosin-II in fission yeast but not in budding yeast. *Molecular biology of the cell*, 16(11), pp.5346–5355.

Ma, H.T. & Poon, R.Y.C., 2011. How protein kinases co-ordinate mitosis in animal cells. *Biochemical Journal*, 435(1), pp.17–31.

Manceva, S. et al., 2007. Calcium regulation of calmodulin binding to and dissociation from the myo1c regulatory domain. *Biochemistry*, 46(42), pp.11718–11726.

Mandelkow, E. & Mandelkow, E.M., 1995. Microtubules and microtubule-associated proteins. *Current Opinion in Cell Biology*, 7(1), pp.72–81.

Marguerat, S. & Bähler, J., 2012. Coordinating genome expression with cell size. *Trends in genetics : TIG*, 28(11), pp.560–565.

Marks, B. & McMahon, H.T., 1998. Calcium triggers calcineurin-dependent synaptic vesicle recycling in mammalian nerve terminals. *Current Biology*, 8(13), pp.740–749.

Marks, J. et al., 1992. Cytoskeletal and DNA structure abnormalities result from

bypass of requirement for the cdc10 start gene in the fission yeast Schizosaccharomyces pombe. *Journal of cell science*, 101 (Pt 3), pp.517–528.

Marks, J., Hagan, I.M. & Hyams, J.S., 1986. Growth polarity and cytokinesis in fission yeast: the role of the cytoskeleton. *Journal of cell science. Supplement*, 5, pp.229–241.

Martin, S.G. & Chang, F., 2006. Dynamics of the Formin For3p in Actin Cable Assembly. *Current Biology*, 16(12), pp.1161–1170.

Martin, S.G. et al., 2007. Regulation of the formin for3p by cdc42p and bud6p. *Molecular biology of the cell*, 18(10), pp.4155–4167.

Martin, S.G. et al., 2005. Tea4p links microtubule plus ends with the formin for3p in the establishment of cell polarity. *Developmental Cell*, 8(4), pp.479–491.

Martín-García, R. & Mulvihill, D.P., 2009. Myosin V spatially regulates microtubule dynamics and promotes the ubiquitin-dependent degradation of the fission yeast CLIP-170 homologue, Tip1. *Journal of cell science*, 122(Pt 21), pp.3862–3872.

Mashanov, G.I. et al., 2003. Visualizing single molecules inside living cells using total internal reflection fluorescence microscopy. *Methods (San Diego, Calif.)*, 29(2), pp.142–152.

Mashanov, G.I. & Molloy, J.E., 2007. Automatic detection of single fluorophores in live cells. *Biophysical Journal*, 92(6), pp. 2199-2211.

Masino, L., Martin, S.R. & Bayley, P.M., 2000. Ligand binding and thermodynamic stability of a multidomain protein, calmodulin. *Protein science*, 9(8), pp.1519–1529.

Mata, J. et al., 2002. The transcriptional program of meiosis and sporulation in fission yeast. *Nature Genetics*, 32(1), pp.143–147.

Matsuo, T. et al., 2007. Loss of the TOR Kinase Tor2 Mimics Nitrogen Starvation and Activates the Sexual Development Pathway in Fission Yeast. *Molecular and Cellular Biology*, 27(8), pp.3154–3164.

Matsuo, T. et al., 2003. Schizosaccharomyces pombe AGC family kinase Gad8p forms a conserved signalling module with TOR and PDK1-like kinases. *The EMBO Journal*, 22(12), pp.3073–3083.

McCann, R.O. & Craig, S.W., 1997. The I/LWEQ module: a conserved sequence that signifies F-actin binding in functionally diverse proteins from yeast to mammals. *Proceedings of the National Academy of Sciences of the United States of America*, 94(11), pp.5679–5684.

McConnell, R.E. & Tyska, M.J., 2010. Leveraging the membrane – cytoskeleton interface with myosin-1. *Trends in cell biology*, 20(7), pp.418–426.

McConnell, R.E. et al., 2009. The enterocyte microvillus is a vesicle-generating organelle. *The Journal of cell biology*, 185(7), pp.1285–1298.

Mehta A.D., et al., 1999. Myosin-V is a processive actin-based motor. *Nature*, 400, pp.590–593.

Merrifield, C.J. et al., 2002. Imaging actin and dynamin recruitment during invagination of single clathrin-coated pits. *Nature cell biology*, 4(9), pp.691–698.

Minsky, M., 1988. Memoir on inventing the confocal scanning microscope. *Scanning*, 10, pp. 128-138.

Mishra, M., Huang, J. & Balasubramanian, M.K., 2014. The yeast actin cytoskeleton. *FEMS Microbiology Reviews*, 38(2), pp.213–227.

Mitchson, J.M., & Nurse, P., 1985. Growth in cell length in the fission yeast Schizosaccharomyces pombe. *Journal of cell science*, 75, pp.357–376.

Mochizuki, N. & Yamamoto, M., 1992. Reduction in the intracellular cAMP level triggers initiation of sexual development in fission yeast. *Molecular & general genetics : MGG*, 233(1-2), pp.17–24.

Monteiro, P.B. et al., 1994. Functional alpha-tropomyosin produced in Escherichia coli. A dipeptide extension can substitute the amino-terminal acetyl group. *The Journal of biological chemistry*, 269(14), pp.10461–10466.

Moreno, S., Klar, A., & Nurse, P., 1991. Molecular and genetic analysis of fission yeast *Schizosaccharomyces pombe*. Methods in Enzymology, 194, pp. 795-823.

Morgan, D.O., 2007. The Cell Cycle. *London: New Science Press*.

Moser, M.J. et al., 1995. Ca2+ binding to calmodulin and its role in Schizosaccharomyces pombe as revealed by mutagenesis and NMR spectroscopy. *The Journal of biological chemistry*, 270(35), pp.20643–20652.

Moser, M.J., Flory, M.R. & Davis, T.N., 1997. Calmodulin localises to the spindle pole body of Schizosaccharomyces pombe and performs an essential function in chromosome segregation. *Journal of cell science*, 110 (Pt 15), pp.1805–1812.

Motegi, F., Arai, R. & Mabuchi, I., 2001. Identification of two type V myosins in fission yeast, one of which functions in polarized cell growth and moves rapidly in the cell. *Molecular biology of the cell*, 12(5), pp.1367–1380.

Motegi, F., Nakano, K. & Mabuchi, I., 2000. Molecular mechanism of myosin-II assembly at the division site in Schizosaccharomyces pombe. *Journal of cell science*, 113 (Pt 10), pp.1813–1825.

Mulholland, J. et al., 1994. Ultrastructure of the yeast actin cytoskeleton and its association with the plasma membrane. *The Journal of cell biology*, 125(2),

pp.381–391.

Mulvihill, D.P. & Hyams, J.S., 2003. Role of the two type II myosins, Myo2 and Myp2, in cytokinetic actomyosin ring formation and function in fission yeast. *Cell motility and the cytoskeleton*, 54(3), pp.208–216.

Mulvihill, D.P. et al., 2000. Cytokinesis in fission yeast: a myosin pas de deux. *Microscopy research and technique*, 49(2), pp.152–160.

Mulvihill, D.P., Barretto, C. & Hyams, J.S., 2001. Localisation of fission yeast type II myosin, Myo2, to the cytokinetic actin ring is regulated by phosphorylation of a C-terminal coiled-coil domain and requires a functional septation initiation network. *Molecular biology of the cell*, 12(12), pp.4044–4053.

Mulvihill, D.P., Edwards, S.R. & Hyams, J.S., 2006. A critical role for the type V myosin, Myo52, in septum deposition and cell fission during cytokinesis inSchizosaccharomyces pombe. *Cell motility and the cytoskeleton*, 63(3), pp.149–161.

Mulvihill, D.P., Pollard, P.J., et al., 2001. Myosin V-mediated vacuole distribution and fusion in fission yeast. *Current biology : CB*, 11(14), pp.1124–1127.

Munn, A.L., 2001. Molecular requirements for the internalisation step of endocytosis: insights from yeast. *Biochimica et biophysica acta*, 1535(3), pp.236–257.

Murakami, H. & Nurse, P., 2000. DNA replication and damage checkpoints and meiotic cell cycle controls in the fission and budding yeasts. *Biochemical Journal*, 349(Pt 1), pp.1–12.

Murray, A., & Hunt, T., 1993. The Cell: An introduction. *Oxford University Press*.

Nakano, A., 2002. Spinning-disk confocal microscopy -- a cutting-edge tool for imaging of membrane traffic. *Cell structure and function*, 27(5), pp.349–355.

Nakano, K. & Mabuchi, I., 2006. Actin-capping protein is involved in controlling organization of actin cytoskeleton together with ADF/cofilin, profilin and F-actin crosslinking proteins in fission yeast. *Genes to cells : devoted to molecular & cellular mechanisms*, 11(8), pp.893–905.

Nambiar, R., McConnell, R.E. & Tyska, M.J., 2009. Control of cell membrane tension by myosin-I. *Proceedings of the National Academy of Sciences of the United States of America*, 106(29), pp.11972–11977.

Naqvi, N.I. et al., 2000. Type II myosin regulatory light chain relieves auto-inhibition of myosin-heavy-chain function. *Nature cell biology*, 2(11), pp.855–858.

Neil, M.A., Juskaitis, R. & Wilson, T., 1997. Method of obtaining optical sectioning by using structured light in a conventional microscope. *Optics letters*, 22(24), pp.1905–1907.

Nguyen, H. & Higuchi, H., 2005. Motility of myosin V regulated by the dissociation of single calmodulin. *Nature structural & molecular biology*, 12(2), pp.127–132.

Nielsen, O. & Davey, J., 1995. Pheromone communication in the fission yeast Schizosaccharomyces pombe. *Seminars in cell biology*, 6(2), pp.95–104.

Norbury, C. & Nurse, P., 1992. Animal cell cycles and their control. *Annual Review of Biochemistry*, 61(1), pp.441–470.

Nurse, P., 1975. Genetic control of cell size at cell division in yeast. *Nature*, 256(5518), pp.547–551.

Nurse, P., Thuriaux, P. & Nasmyth, K., 1976. Genetic control of the cell division cycle in the fission yeast Schizosaccharomyces pombe. *Molecular & general genetics : MGG*, 146(2), pp.167–178.

O'Connell, C.B. & Khodjakov, A.L., 2007. Cooperative mechanisms of mitotic spindle formation. *Journal of cell science*, 120(10), pp.1717–1722.

O'Day, D.H., 2003. CaMBOT: profiling and characterising calmodulin-binding proteins. *Cellular Signalling*, 15, pp.347-354.

Ono, S. & Ono, K., 2002. Tropomyosin inhibits ADF/cofilin-dependent actin filament dynamics. *The Journal of cell biology*, 156(6), pp.1065–1076.

Padte, N.N. et al., 2006. The cell-end factor pom1p inhibits mid1p in specification of the cell division plane in fission yeast. *Current Biology*, 16(24), pp.2480–2487.

Palmer, S.E. et al., 2015. A Dynamin-Actin Interaction Is Required for Vesicle Scission during Endocytosis in Yeast. *Current Biology*, 25(7), pp.868–878.

Paoletti, A. & Chang, F., 2000. Analysis of mid1p, a protein required for placement of the cell division site, reveals a link between the nucleus and the cell surface in fission yeast. *Molecular biology of the cell*, 11(8), pp.2757–2773.

Paoletti, A. & Tran, P.T., 2007. Anchoring microtubules at the spindle poles. *Nature cell biology*, 9(6), pp.619–621.

Pardee, J.D. & Spudich, J.A., 1982. Mechanism of K+-induced actin assembly. *The Journal of cell biology*, 93(3), pp.648–654.

Park, J.-S. et al., 2009. Essential Role for Schizosaccharomyces pombe pik1 in Septation A. S. Gladfelter, ed. *PLoS ONE*, 4(7), pp.e6179–21.

Pearson, R.B. & Kemp, B.E., 1991. Protein kinase phosphorylation site sequences and consensus specificity motifs: tabulations. *Methods in enzymology*, 200, pp.62–81.

Pelham, R.J. & Chang, F., 2002. Actin dynamics in the contractile ring during cytokinesis in fission yeast. *Nature*, 419(6902), pp.82–86.

Pelham, R.J. & Chang, F., 2001. Role of actin polymerization and actin cables in actin-patch movement in Schizosaccharomyces pombe. *Nature cell biology*, 3(3), pp.235–244.

Petersen, J. & Nurse, P., 2007. TOR signalling regulates mitotic commitment through the stress MAP kinase pathway and the Polo and Cdc2 kinases. *Nature cell biology*, 9(11), pp.1263–1272.

Petersen, J., Nielsen, O., Egel, R. & Hagan, I.M., 1998a. F-actin distribution and function during sexual differentiation in Schizosaccharomyces pombe. *Journal of cell science*, 111 (Pt 7), pp.867–876.

Petersen, J., Nielsen, O., Egel, R. & Hagan, I.M., 1998b. FH3, a domain found in formins, targets the fission yeast formin Fus1 to the projection tip during conjugation. *The Journal of cell biology*, 141(5), pp.1217–1228.

Pittenger, M.F., Kazzaz, J.A. & Helfman, D.M., 1994. Functional properties of non-muscle tropomyosin isoforms. *Current Opinion in Cell Biology*, 6(1), pp.96–104.

Purcell, T.J., et al., 2002. Role of the lever arm in the processive stepping of myosin V. *Proceedings of the National Academy of Sciences of the United States of America*, 99(22), pp.14159–14164.

Qin, Z., Kreplak, L. & Buehler, M.J., 2009. Nanomechanical properties of vimentin intermediate filament dimers. *Nanotechnology*, 20(42), p.425101.

Quinlan, M.E., et al., 2005. Drosophila Spire is an actin nucleation factor. *Nature*, 433, pp.382-388.

Rayment, I. et al., 1993. Structure of the actin-myosin complex and its implications for muscle contraction. *Science*, 261(5117), pp.58–65.

Rayment, I., 1996. The structural basis of the myosin ATPase activity. The journal of Biological Chemistry, 271(27), pp.15850-15853.

Redowicz, M.J., 2001. Regulation of nonmuscle myosins by heavy chain phosphorylation. *Journal of muscle research and cell motility*, 22(2), pp.163–173.

Remedios, Dos, C.G. et al., 2003. Actin Binding Proteins: Regulation of Cytoskeletal Microfilaments. *Physiological Reviews*, 83(2), pp.433–473.

Rhind, N. & Russell, P., 2012. Signalling Pathways that Regulate Cell Division. *Cold Spring Harbor Perspectives in Biology*, 4(10), pp.a005942–a005942.

Ridley, A.J., 2006. Rho GTPases and actin dynamics in membrane protrusions and vesicle trafficking. *Trends in cell biology*, 16(10), pp.522–529.

Riedl, J. et al., 2008. Lifeact: a versatile marker to visualise F-actin. *Nature methods*, 5(7), pp.605–607.

Roberts, R. et al., 2004. Myosin VI: cellular functions and motor properties. *Philosophical transactions of the Royal Society of London. Series B, Biological sciences*, 359(1452), pp.1931–1944.

Rogers, S.L. et al., 2003. Molecular requirements for actin-based lamella formation in Drosophila S2 cells. *The Journal of cell biology*, 162(6), pp.1079–1088.

Roh, D.-H. et al., 2002. The septation apparatus, an autonomous system in budding yeast. *Molecular biology of the cell*, 13(8), pp.2747–2759.

Roque, A. et al., 2008. Phosphorylation of the carboxy-terminal domain of histone H1: effects on secondary structure and DNA condensation. *Nucleic acids research*, 36(14), pp.4719–4726.

Roshak, A.K. et al., 2000. The human polo-like kinase, PLK, regulates cdc2/cyclin B through phosphorylation and activation of the cdc25C phosphatase. *Cellular signalling*, 12(6), pp.405–411.

Rotty, J.D. et al., 2015. Profilin-1 serves as a gatekeeper for actin assembly by Arp2/3-dependent and -independent pathways. *Developmental Cell*, 32(1), pp.54–67.

Ruff, C. et al., 2001. Single-molecule tracking of myosins with genetically engineered amplifier domains. *Nature structural biology*, 8(3), pp.226–229.

Russell, P. & Nurse, P., 1987. Negative regulation of mitosis by wee1+, a gene encoding a protein kinase homolog. *Cell*, 49(4), pp.559–567.

Sabry, J.H. et al., 1997. Myosin heavy chain phosphorylation sites regulate myosin localisation during cytokinesis in live cells. *Molecular biology of the cell*, 8(12), pp.2605–2615.

Sammons, M.R. et al., 2011. A calmodulin-related light chain from fission yeast that functions with myosin-I and PI 4-kinase. *Journal of cell science*, 124(14), pp.2466–2477.

Sarbassov, D.D. et al., 2004. Rictor, a novel binding partner of mTOR, defines a rapamycin-insensitive and raptor-independent pathway that regulates the cytoskeleton. *Current Biology*, 14(14), pp.1296–1302.

Schmidt, A., Kunz, J. & Hall, M.N., 1996. TOR2 is required for organization of the actin cytoskeleton in yeast. *Proceedings of the National Academy of Sciences of the United States of America*, 93(24), pp.13780–13785.

Schmidt, S. et al., 1997. The Spg1p GTPase is an essential, dosage-dependent inducer of septum formation in Schizosaccharomyces pombe. *Genes & Development*, 11(12), pp.1519–1534.

Schott, D.H., Collins, R.N. & Bretscher, A., 2002. Secretory vesicle transport velocity in living cells depends on the myosin-V lever arm length. *The Journal of cell biology*, 156(1), pp.35–40.

Scott, B.J., Neidt, E.M. & Kovar, D.R., 2011. The functionally distinct fission yeast formins have specific actin-assembly properties. *Molecular biology of the cell*, 22(20), pp.3826–3839.

Scott, D.C. et al., 2011. N-terminal acetylation acts as an avidity enhancer within an interconnected multiprotein complex. *Science*, 334(6056), pp.674–678.

Seki, A. et al., 2008. Bora and the kinase Aurora a cooperatively activate the kinase Plk1 and control mitotic entry. *Science*, 320(5883), pp.1655–1658.

Seki, N. et al., 1998. Cloning, expression analysis, and chromosomal localisation of HIP1R, an isolog of huntingtin interacting protein (HIP1). *Journal of human genetics*, 43(4), pp.268–271.

Sellers, J.R., 2000. Myosins: a diverse superfamily. *Biochimica et biophysica acta*, 1496(1), pp.3–22.

Shaner, N.C. et al., 2013. A bright monomeric green fluorescent protein derived from Branchiostoma lanceolatum. *Nature methods*, 10(5), pp.407–409.

Shaner, N.C., Patterson, G.H. & Davidson, M.W., 2007. Advances in fluorescent protein technology. *Journal of cell science*, 120(Pt 24), pp.4247–4260.

Shaner, N.C., Steinbach, P.A. & Tsien, R.Y., 2005. A guide to choosing fluorescent proteins. *Nature methods*, 2(12), pp.905–909.

Shih, Y.L. & Rothfield, L., 2006. The Bacterial Cytoskeleton. *Microbiology and Molecular Biology Reviews*, 70(3), pp.729–754.

Shimozono, S., & Miyawaki, A., 2008. Engineering FRET constructs using CFP and YFP. *Methods in cell biology*, 85, 381-393.

Simanis, V., 2015. Pombe's thirteen - control of fission yeast cell division by the septation initiation network. *Journal of cell science*, 128(8), pp.1465–1474.

Sirotkin, V. et al., 2005. Interactions of WASp, myosin-I, and verprolin with Arp2/3 complex during actin patch assembly in fission yeast. *The Journal of cell biology*, 170(4), pp.637–648.

Sirotkin, V. et al., 2010. Quantitative analysis of the mechanism of endocytic actin patch assembly and disassembly in fission yeast. *Molecular biology of the cell*, 21(16), pp.2894–2904.

Sjöblom, B., Salmazo, A. & Djinović-Carugo, K., 2008. α-Actinin structure and regulation. *Cellular and molecular life sciences : CMLS*, 65(17), pp.2688–2701.

Skoumpla, K. et al., 2007. Acetylation regulates tropomyosin function in the fission yeast Schizosaccharomyces pombe. *Journal of cell science*, 120(Pt 9), pp.1635–1645.

Sladewski, T.E., Previs, M.J. & Lord, M., 2009. Regulation of fission yeast myosin-II function and contractile ring dynamics by regulatory light-chain and heavy-

chain phosphorylation. *Molecular biology of the cell*, 20(17), pp.3941–3952.

Slupsky, C.M., 2000. Structure of Cdc4p, a Contractile Ring Protein Essential for Cytokinesis in Schizosaccharomyces pombe. *Journal of Biological Chemistry*, 276(8), pp.5943–5951.

Snaith, H.A. et al., 2010. New and old reagents for fluorescent protein tagging of microtubules in fission yeast; experimental and critical evaluation. *Methods in cell biology*, 97, pp.147–172.

Starheim, K.K., Gevaert, K. & Arnesen, T., 2012. Protein N-terminal acetyltransferases: when the start matters. *Trends in biochemical sciences*, 37(4), pp.152–161.

Stark, B.C. et al., 2010. Tropomyosin and myosin-II cellular levels promote actomyosin ring assembly in fission yeast. *Molecular biology of the cell*, 21(6), pp.989–1000.

Starr, C., et al. 2015. Evolution of Life. Biology: The unity and diversity of life (14th edition). *Brooks Cole*.

Stauffer, E.A. et al., 2005. Fast adaptation in vestibular hair cells requires myosin-1c activity. *Neuron*, 47(4), pp.541–553.

Steffen, A. et al., 2006. Filopodia formation in the absence of functional WAVE- and Arp2/3-complexes. *Molecular biology of the cell*, 17(6), pp.2581–2591.

Stöffler, H.E. & Bähler, M., 1998. The ATPase activity of Myr3, a rat myosin I, is allosterically inhibited by its own tail domain and by Ca2+ binding to its light chain calmodulin. *The Journal of biological chemistry*, 273(23), pp.14605–14611.

Suarez, C. et al., 2015. Profilin Regulates F-Actin Network Homeostasis by Favoring Formin over Arp2/3 Complex. *Developmental Cell*, 32(1), pp.43–53.

Suizu, T. et al., 1995. Calcium ion influx during sporulation in the yeast Saccharomyces cerevisiae. *Canadian journal of microbiology*, 41(11), pp.1035–1037.

Sun, Y. et al., 2007. PtdIns(4,5)P2 turnover is required for multiple stages during clathrin- and actin-dependent endocytic internalization. *The Journal of cell biology*, 177(2), pp.355–367.

Takeda, T. & Chang, F., 2005. Role of fission yeast myosin I in organization of sterol-rich membrane domains. *Current biology : CB*, 15(14), pp.1331–1336.

Takeda, T. & Yamamoto, M., 1987. Analysis and in vivo disruption of the gene coding for calmodulin in Schizosaccharomyces pombe. *Proceedings of the National Academy of Sciences of the United States of America*, 84(11), pp.3580–3584.

Tanaka, H., et al., 2002. The motor domain determines the large step of myosin-V.

Nature, 415, pp.192–195.

Tatebe, H. et al., 2010. Rab-family GTPase regulates TOR complex 2 signalling in fission yeast. *Current biology : CB*, 20(22), pp.1975–1982.

Tatsumi, R., Shimada, K. & Hattori, A., 1997. Fluorescence detection of calcium-binding proteins with quinoline Ca-indicator quin2. *Analytical biochemistry*, 254(1), pp.126–131.

Terrak, M. et al., 2005. Structure of the light chain-binding domain of myosin V. *Proceedings of the National Academy of Sciences of the United States of America*, 102(36), pp.12718–12723.

Thoreen, C.C. et al., 2009. An ATP-competitive mammalian target of rapamycin inhibitor reveals rapamycin-resistant functions of mTORC1. *The Journal of biological chemistry*, 284(12), pp.8023–8032.

Thuriaux, P., Sipiczki, M. & Fantes, P.A., 1980. Genetical analysis of a sterile mutant by protoplast fusion in the fission yeast Schizosaccharomyces pombe. *Journal of general microbiology*, 116(2), pp.525–528.

Toepfer, C. et al., 2013. Myosin Regulatory Light Chain (RLC) Phosphorylation Change as a Modulator of Cardiac Muscle Contraction in Disease. *The Journal of biological chemistry*, 288(19), pp.13446–13454.

Toomre, D. & Manstein, D.J., 2001. Lighting up the cell surface with evanescent wave microscopy. *Trends in cell biology*, 11(7), pp.298–303.

Torres, E. & Rosen, M.K., 2006. Protein-tyrosine kinase and GTPase signals cooperate to phosphorylate and activate Wiskott-Aldrich syndrome protein (WASP)/neuronal WASP. *The Journal of biological chemistry*, 281(6), pp.3513–3520.

Toya, M. et al., 2001. Identification and functional analysis of the gene for type I myosin in fission yeast. *Genes to cells : devoted to molecular & cellular mechanisms*, 6(3), pp.187–199.

Trybus, K.M., 2008. Myosin V from head to tail. *Cellular and molecular life sciences : CMLS*, 65(9), pp.1378–1389.

Trybus, K.M., 1991. Regulation of smooth muscle myosin. *Cell motility and the cytoskeleton*, 18(2), pp.81–85.

Trybus, K.M. et al., 2007. Effect of calcium on calmodulin bound to the IQ motifs of myosin V. *The Journal of biological chemistry*, 282(32), pp.23316–23325.

Uings, I.J. & Farrow, S.N., 2000. Cell receptors and cell signalling. *Molecular pathology : MP*, 53(6), pp.295–299.

Ullal, P. et al., 2015. The DYRK-family kinase Pom1 phosphorylates the F-BAR protein Cdc15 to prevent division at cell poles. *The Journal of cell biology*, 211(3), pp.653–668.

Uyeda, T.Q., Abramson, P.D. & Spudich, J.A., 1996. The neck region of the myosin motor domain acts as a lever arm to generate movement. *Proceedings of the National Academy of Sciences of the United States of America*, 93(9), pp.4459–4464.

Van der Voort, H., Scientific Volume Imaging (online resource).

Vavylonis, D. et al., 2008. Assembly mechanism of the contractile ring for cytokinesis by fission yeast. *Science*, 319(5859), pp.97–100.

Vazquez-Martin, A. et al., 2012. Ser2481-autophosphorylated mTOR colocalises with chromosomal passenger proteins during mammalian cell cytokinesis. *Cell Cycle*, 11(22), pp.4211–4221.

Vermeulen, K., et al., 2003. The cell cycle: a review of regulation, deregulation and therapeutic targets in cancer. Cell proliferation, 36(3), pp.131–149.

Vetter, S.W. & Leclerc, E., 2003. Novel aspects of calmodulin target recognition and activation. *European journal of biochemistry / FEBS*, 270(3), pp.404–414.

Volinsky, N. & Kholodenko, B.N., 2013. Complexity of Receptor Tyrosine Kinase Signal Processing. *Cold Spring Harbor Perspectives in Biology*, 5(8), pp.a009043–a009043.

Walch-Solimena, C. & Novick, P., 1999. The yeast phosphatidylinositol-4-OH kinase pik1 regulates secretion at the Golgi. *Nature cell biology*, 1(8), pp.523–525.

Walker, L.M. et al., 2000. Two-headed binding of a processive myosin to F-actin. *Nature*, 405, pp.804–807.

Wallace, W., Schaefer, L.H. & Swedlow, J.R., 2001. A workingperson's guide to deconvolution in light microscopy. *BioTechniques*, 31(5), pp.1076–8– 1080–1082 passim.

Wang, N. et al., 2016. Roles of the TRAPP-II Complex and the Exocyst in Membrane Deposition during Fission Yeast Cytokinesis F. Hughson, ed. *PLOS Biology*, 14(4), pp.e1002437–36.

Watanabe, T.M. et al. 2004. A one-headed class V myosin molecule develops multiple large (~32-nm) steps successively. *Proceedings of the National Academy of Sciences of the United States of America*, 101(24),pp.9630-9635.

Wawro, B. et al., 2007. Tropomyosin regulates elongation by formin at the fast-growing end of the actin filament. *Biochemistry*, 46(27), pp.8146–8155.

Wear, M.A. et al., 2003. How capping protein binds the barbed end of the actin filament. *Current Biology*, 13(17), pp.1531–1537.

Weisman, R. & Choder, M., 2001. The fission yeast TOR homolog, tor1+, is required for the response to starvation and other stresses via a conserved serine. *The Journal of biological chemistry*, 276(10), pp.7027–7032.

Whittaker, M. & Milligan, R.A., 1997. Conformational changes due to calcium-induced calmodulin dissociation in brush border myosin I-decorated F-actin revealed by cryoelectron microscopy and image analysis. *Journal of molecular biology*, 269(4), pp.548–557.

Wickstead, B. & Gull, K., 2011. The evolution of the cytoskeleton. *The Journal of cell biology*, 194(4), pp.513–525.

Willet, A.H. et al., 2015. The F-BAR Cdc15 promotes contractile ring formation through the direct recruitment of the formin Cdc12. *The Journal of cell biology*, 208(4), pp.391–399.

Williams, R. & Coluccio, L.M., 1994. Novel 130-kDa rat liver myosin-1 will translocate actin filaments. *Cell motility and the cytoskeleton*, 27(1), pp.41–48.

Wilson-Grady, J.T., Villén, J. & Gygi, S.P., 2008. Phosphoproteome Analysis of Fission Yeast. *Journal of Proteome Research*, 7(3), pp.1088–1097.

Win, T.Z. et al., 2001. Two type V myosins with non-overlapping functions in the fission yeast Schizosaccharomyces pombe: Myo52 is concerned with growth polarity and cytokinesis, Myo51 is a component of the cytokinetic actin ring. *Journal of cell science*, 114(Pt 1), pp.69–79.

Wolenski, J.S. et al., 1993. In vitro motilities of the unconventional myosins, brush border myosin-I, and chick brain myosin-V exhibit assay-dependent differences in velocity. *The Journal of experimental zoology*, 267(1), pp.33–39.

Wong, K.C.Y. et al., 2002. Importance of a myosin II-containing progenitor for actomyosin ring assembly in fission yeast. *Current Biology*, 12(9), pp.724–729.

Wood, V. et al., 2002. The genome sequence of Schizosaccharomyces pombe. *Nature*, 415(6874), pp.871–880.

Wu, J.-Q. et al., 2006. Assembly of the cytokinetic contractile ring from a broad band of nodes in fission yeast. *The Journal of cell biology*, 174(3), pp.391–402.

Wu, J.-Q. et al., 2003. Spatial and temporal pathway for assembly and constriction of the contractile ring in fission yeast cytokinesis. *Developmental Cell*, 5(5), pp.723–734.

Wu, X.-S. et al., 2009. Ca(2+) and calmodulin initiate all forms of endocytosis during depolarization at a nerve terminal. *Nature neuroscience*, 12(8), pp.1003–1010.

Wullschleger, S., Loewith, R. & Hall, M.N., 2006. TOR signalling in growth and metabolism. *Cell*, 124(3), pp.471–484.

Yamamoto, M., Imai, Y., & Watanabe, Y. 1997. Volume III: The molecular & cellular biology of the yeast Saccharomyces: Cell cycle and cell biology. *Cold Spring Harbour Laboratory Press.*

Yarar, D. et al., 2002. Motility determinants in WASP family proteins. *Molecular*

biology of the cell, 13(11), pp.4045–4059.

Ydenberg, C.A. et al., 2011. Cease-fire at the leading edge: New perspectives on actin filament branching, debranching, and cross-linking. *Cytoskeleton*, 68(11), pp.596–602.

Yip, M.F. et al., 2008. CaMKII-Mediated Phosphorylation of the Myosin Motor Myo1c Is Required for Insulin-Stimulated GLUT4 Translocation in Adipocytes. *Cell Metabolism*, 8(5), pp.384–398.

Yoshida, T., Toda, T. & Yanagida, M., 1994. A calcineurin-like gene ppb1+ in fission yeast: mutant defects in cytokinesis, cell polarity, mating and spindle pole body positioning. *Journal of cell science*, 107 (Pt 7), pp.1725–1735.

Young, K.G. & Copeland, J.W., 2010. Biochimica et Biophysica Acta. *BBA - Molecular Cell Research*, 1803(2), pp.183–190.

Zhou, Y. et al., 2006. Prediction of EF-hand calcium-binding proteins and analysis of bacterial EF-hand proteins. *Proteins*, 65(3), pp.643–655.

Zhou, H., & Huang, S., 2010. The complexes of mammalian target of rapamycin. *Current protein & peptide science*, 11(6), pp.409–424.

Zhu, T., Sata, M. & Ikebe, M., 1996. Functional expression of mammalian myosin I beta: analysis of its motor activity. *Biochemistry*, 35(2), pp.513–522.

Appendix 1.

K. Baker, S. Kirkham, L. Halova, J. Atkin, M. Franz-Wachtel, D. Cobley, K. Krug, B. Macek, Daniel P. Mulvihill and Janni Petersen (2016).

"TOR complex 2 localises to the Cytokinetic Actomyosin ring and controls the fidelity of cytokineis."

Journal of Cell Science. Jul 1;129(13):2613-24. Doi: 10.1242/jcs.190124.

Appendix 2.

Timelapse movies of fluorescently labelled *S. pombe* strains:

Movie 1:

mNeongreen-myo1.

50 frames taken at 0.67 s intervals. Each a 13 z-plane maximum projection.

Movie 2:

cam1-gfp

30 frames taken at 0.67 s intervals. Each a 13 z-plane maximum projection.

Movie 3:

*cam1-gfp myo1*Δ

100 frames taken at 0.67 s intervals. Each a 13 z-plane maximum projection.

Movie 4:

cam2-gfp

30 frames taken at 0.67 s intervals. Each a 13 z-plane maximum projection.

Movie 5:

Lifeact-mCherry

100 frames taken at 0.67 s intervals. Each a 13 z-plane maximum projection.

Movie 6:

*cam2-gfp myo1*Δ

50 frames taken at 0.67 s intervals. Each a 13 z-plane maximum projection.

Movie 7:

*Lifeact-mCherry myo1*Δ

100 frames taken at 0.67 s intervals. Each a 13 z-plane maximum projection.

Movie 8:

*cam1-gfp cam2*Δ

60 frames taken at 0.67 s intervals. Each a 13 z-plane maximum projection.

Movie 9:

myo2-mCherry sid4-tdTomato

30 frames taken at 3 minute intervals. Each a 31 z-plane maximum projection.

Movie 10:

*myo2-mCherry cut12-gfp ste20*Δ

40 frames taken at 3 minute intervals. Each a 31 z-plane maximum.

© 2016. Published by The Company of Biologists Ltd | Journal of Cell Science (2016) 129, 2613-2624 doi:10.1242/jcs.190124

RESEARCH ARTICLE

TOR complex 2 localises to the cytokinetic actomyosin ring and controls the fidelity of cytokinesis

Karen Baker[1,*], Sara Kirkham[2,*], Lenka Halova[2], Jane Atkin[2], Mirita Franz-Wachtel[3], David Cobley[2], Karsten Krug[3], Boris Maček[3], Daniel P. Mulvihill[1,‡] and Janni Petersen[2,4,5,‡]

ABSTRACT

The timing of cell division is controlled by the coupled regulation of growth and division. The target of rapamycin (TOR) signalling network synchronises these processes with the environmental setting. Here, we describe a novel interaction of the fission yeast TOR complex 2 (TORC2) with the cytokinetic actomyosin ring (CAR), and a novel role for TORC2 in regulating the timing and fidelity of cytokinesis. Disruption of TORC2 or its localisation results in defects in CAR morphology and constriction. We provide evidence that the myosin II protein Myp2 and the myosin V protein Myo51 play roles in recruiting TORC2 to the CAR. We show that Myp2 and TORC2 are co-dependent upon each other for their normal localisation to the cytokinetic machinery. We go on to show that TORC2-dependent phosphorylation of actin-capping protein 1 (Acp1, a known regulator of cytokinesis) controls CAR stability, modulates Acp1–Acp2 (the equivalent of the mammalian CAPZA–CAPZB) heterodimer formation and is essential for survival upon stress. Thus, TORC2 localisation to the CAR, and TORC2-dependent Acp1 phosphorylation contributes to timely control and the fidelity of cytokinesis and cell division.

KEY WORDS: Rictor, TOR, TORC2, Myosin II, Myosin V, Acp1, CAPZA, *Schizosaccharomyces pombe*

INTRODUCTION

Target of rapamycin (TOR) signalling plays a key role in modulating the spatial and temporal control of cell growth in response to different environmental conditions. The TOR kinase forms two functionally distinct protein complexes, TOR complex 1 (TORC1) and TORC2 (Laplante and Sabatini, 2012). TORC1 and TORC2 are defined by unique components that are highly conserved across species. TORC1 contains regulatory associated protein of mTOR (RAPTOR, also known as RPTOR), and TORC2 contains Sin1 and rapamycin-insensitive companion of mTOR (RICTOR) (Wullschleger et al., 2006). It is rapamycin-sensitive TORC1 that is the major nutrient sensor, which integrates environmental cues with cell growth. TORC2 is regulated by different cues and exerts distinct functions (Laplante and Sabatini, 2012). Both TORC1 and TORC2 have been implicated in the control of cell migration and F-actin organisation (Liu and Parent, 2011). Inhibition of TORC1 with rapamycin prevents lamellipodia formation through a reduced expression of the small GTPase RhoA in mammalian cells (Liu et al., 2010). Similarly, TORC2 has been shown to play a key role in regulating the organisation and polarity of the actin cytoskeleton in *Saccharomyces cerevisiae*, *Dictyostelium discoideum* and mammalian cells (Jacinto et al., 2004; Lee et al., 2005; Schmidt et al., 1996).

The fission yeast, *Schizosaccharomyces pombe*, contains two TOR protein kinases, Tor1 and Tor2. The majority of TORC2 contains the non-essential catalytic kinase component Tor1 (Alvarez and Moreno, 2006; Hayashi et al., 2007; Matsuo et al., 2007). Importantly, all the functional specificities of TORC1 and TORC2 are conserved in yeasts. Cells lacking TORC2 components, such as Tor1, Sin1 or the fission yeast RICTOR homolog Ste20 (which is not a homolog of the budding yeast PAK-like kinase of the same name, and is hereafter denoted RICTOR^{Ste20}) are larger than wild type, and are sensitive to heat, osmotic and oxidative stress. In addition these mutants are sterile as they are unable to undergo the G1 arrest that is an essential pre-requisite for mating in fission yeast (Kawai et al., 2001; Weisman and Choder, 2001). In fission yeast, F-actin cables are thicker than wild type and the cortical actin is atypically asymmetric in *tor1*-deficient mutants (Ikai et al., 2011; Matsuo et al., 2007). These distinctions prompted us to explore mechanisms by which TORC2 might impact upon actin cytoskeletal functions in fission yeast.

Here, we report a novel localisation of TORC2 to the cytokinetic actomyosin ring (CAR) where it has a role in moderating the successful completion of cytokinesis. We describe a mechanism by which TORC2 controls heterodimer formation between the actin-capping proteins Acp1 and Acp2 (the equivalent of mammalian CAPZA and CAPZB proteins, and are hereafter denoted CAPZA^{Acp1} and CAPZB^{Acp2}, respectively) to regulate the actin cytoskeleton, and thereby the timely control of cytokinesis, to ensure survival upon changes to the extracellular environment.

RESULTS

TORC2 controls the integrity of the CAR

In order to examine the potential roles that TORC2 might have during actin-dependent cell growth and division (Lancaster and Baum, 2014), we undertook a phenotypic analysis of fission yeast cells lacking RICTOR^{Ste20} (denoted *Rictor^{ste20}*Δ), the core TORC2-specific component. The main catalytic component of TORC2 is the Tor1 protein kinase (Alvarez and Moreno, 2006; Hayashi et al., 2007; Matsuo et al., 2007); however, cells lacking Tor1 are capable of incorporating Tor2 into the TORC2 complex (Matsuo et al.,

[1]School of Biosciences, University of Kent, Giles Lane, Canterbury, Kent CT2 7NJ, UK. [2]Faculty of Life Sciences, University of Manchester, Oxford Road, Manchester M13 9PT, UK. [3]Proteome Center Tübingen, Auf der Morgenstelle 15, Tübingen 72076, Germany. [4]Flinders Centre for Innovation in Cancer, School of Medicine, Flinders University, Adelaide, SA 5001, Australia. [5]South Australia Health and Medical Research Institute, North Terrace, PO Box 11060, Adelaide, SA 5000, Australia.
*These authors contributed equally to this work

‡Authors for correspondence (d.p.mulvihill@kent.ac.uk; Janni.Petersen@Flinders.edu.au)

D.P.M., 0000-0003-2502-5274

Received 30 March 2016; Accepted 6 May 2016

Journal of Cell Science

Journal of Cell Science (2016) 129, 2613-2624 doi:10.1242/jcs.190124

2007; Hartmuth and Petersen, 2009). In contrast, deleting RICTOR^{Ste20} from the genome specifically ablates TORC2 function within the cell. *Rictor^{ste20}*Δ cells are elongated and display an altered cell morphology, with a cell diameter significantly greater than otherwise isogenic wild-type controls (Matsuo et al., 2007; Hartmuth and Petersen, 2009; Fig. 1A,B; Fig. S1A). Increased cell diameter and cell length is normally associated with cells in the diploid lifecycle. Fluorescence-activated cell sorting (FACS) analysis of TORC2-deficient mutants or wild-type cells after an acute treatment with Tor inhibitor 1 (Torin1) (Atkin et al., 2014) revealed the major 2N peak that is normally associated with wild-type haploid fission yeast cells (Fig. 1C), along with an additional minor 4N peak (Fig. 1C). Cells in the diploid lifecycle have significantly larger nuclei than haploid cells (Neumann and Nurse, 2007). The nuclei diameter were equivalent in wild-type and *Rictor^{ste20}*Δ cells (Fig. 1D) indicating that the TORC2-deficient mutants are haploid cells with altered cell size. The minor 4N peak observed by FACS might be brought about by a small population of diploid cells. Alternatively, this small peak could represent cells in the haploid life cycle delayed in cell division but which have completed the next S-phase. Division septa were often aberrant and misplaced, with the septum located away from the cell equator in 55% of *Rictor^{ste20}*Δ cells [these included septa positioned more than 5% away from the cell equator (of the distance spanning the cell end to the cell equator)]. In contrast, none of the septa were misplaced in all observed wild-type cells. Finally, elevated levels of new cell wall material was observed at the cell equator in the absence of TORC2 function (Fig. 1A; Fig. S1A). Taken together, these data indicate that TORC2-deficient haploid cells display defects in cytokinesis and cell fission.

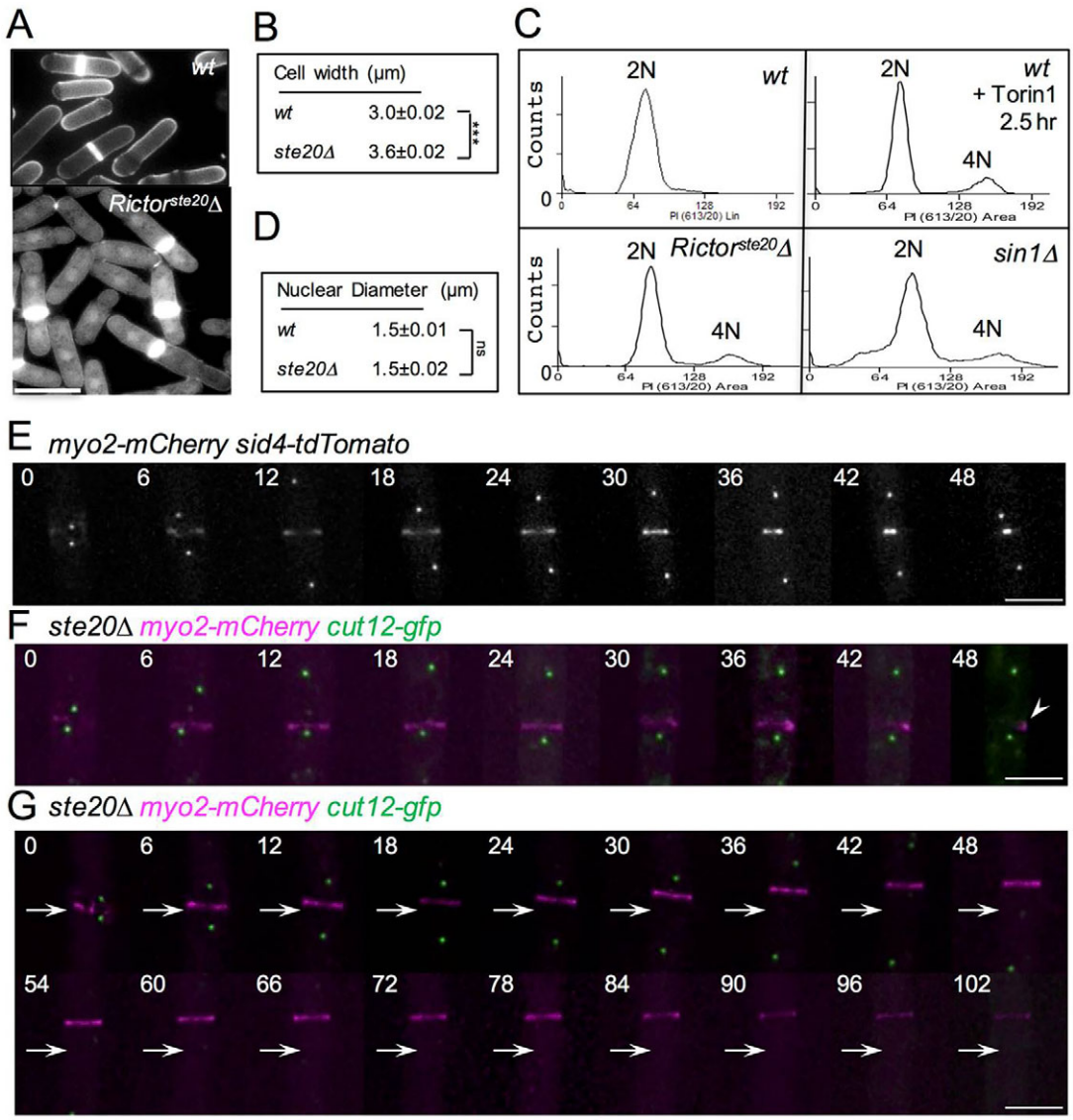

Fig. 1. TORC2-deficient mutants display defects in cytokinesis and cell fission. (A) Early exponential wild-type (*wt*) and *Rictor^{ste20}*Δ (*ste20*Δ) prototroph cells were stained with Calcofluor to visualise the division septa. Scale bar: 10 μm. These cells, as well as *sin1*Δ cells and cells treated with Torin1, were (C) processed for flow cytometry analysis to measure DNA content. Mean cell width (B) and nuclear diameter (D) were each determined from counting 300 wild-type and *Rictor^{ste20}*Δ cells in mid-log culture. ***P<0.001, ns, not significant (Student's *t*-test). (E) A montage of time-lapse images showing red fluorescence from *myo2–mCherry sid4–tdTomato* cells undergoing cell division. Cells illustrating timing of CAR formation and constriction in relation to SPB segregation in wild-type cells are shown. (F,G) Equivalent montages of time-lapse images of mCherry (magenta) and GFP (green) fluorescene from *myo2–mCherry cut12–gfp Rictor^{ste20}*Δ cells. In a large proportion of anaphase *Rictor^{ste20}*Δ cells the CAR was seen to either collapse (arrowhead, F) or drift along the cortex towards one end of the cell (arrows, G). Scale bars: 5 μm.

Journal of Cell Science (2016) 129, 2613-2624 doi:10.1242/jcs.190124

Visualisation of septal material in *Rictor*^{ste20}Δ cells revealed that a large proportion of cells had misplaced or aberrant septa (Fig. 1A; Fig. S1A). *myo2–mCherry* cells were used to follow CAR localisation and dynamics. *myo2–mCherry* cells containing functional TORC2 displayed growth characteristics and genetic interactions equivalent to the wild-type *myo2*$^{+}$ allele (Fig. 1E; Movie 1). In contrast, time-lapse imaging of *myo2–mCherry Rictor*^{ste20}Δ cells revealed that TORC2-deficient cells remained in the phase of the cell cycle dedicated to cytokinesis for a prolonged period. As well as displaying delayed constriction, the CAR was seen to either split or collapse (39% of cells) (Fig. 1F, Movie 2) or slide along the cortex (11% of cells) (Fig. 1G). This is consistent with our observation that a substantial proportion of septa in *Rictor*^{ste20}Δ cells formed septum that were more than 5% of the cell length away from the centre of the cell (Fig. S1A). In a small proportion (~2%) of these *Rictor*^{ste20}Δ cells, the spindle was seen to extend from one side of the misplaced CAR (Fig. S1B), these cells are likely to contribute to the 4N peak observed by FACS (Fig. 1C). In addition, *Rictor*^{ste20}Δ cells often failed to integrate medial Myo2 foci into a stable CAR over an extended period of several hours without inhibiting cell growth (<5% of cells) (Movie 3), and were also seen to complete CAR constriction, and then reform at the division site before dividing in two (7% of cells) (Movie 4). Consistent with this observation, anti-tropomyosin antibody immunofluorescence staining of actin filaments in *Rictor*^{ste20}Δ cells revealed defects in actin ring function during cytokinesis, with divided cells possessing an unconstructed CAR structure at the cell end at which cell division had just occurred (Fig. S1C). Thus, TORC2 function is not only required to maintain normal cell size, but also plays a crucial role in regulating the timing of CAR formation and maintaining its subsequent integrity during cell division.

TORC2 interacts with and localises to the CAR during ring constriction

In order to explore how TORC2 affects the integrity of the CAR, we undertook a proteomic-based analysis to identify proteins that co-purified with the main TORC2 catalytic component, Tor1. Mass spectrometry of Tor1 immuno-precipitates from 20 l of early-log phase culture identified three known core TORC2 components (RICTOR^{Ste20}, Sin1 and Pop3) as well as the TORC2 substrate Gad8 (Fig. 2A). Intriguingly, as well as co-purifying with Cdc12, a formin required for nucleation of tropomyosin-stabilised actin filaments within the CAR, in three independent experiments Tor1 co-purified with the class II and V myosin heavy chains, Myp2 and Myo51, both of which are core components of the actomyosin cytoskeleton and cytokinetic division machinery (Fig. 2A).

These links between TORC2 and control of cytokinesis prompted us to re-visit the localisation studies reporting GFP-tagged RICTOR^{Ste20} (RICTOR^{Ste20}–3GFP) recruitment to the plasma membrane (Tatebe et al., 2010). Live-cell imaging of *myo2–mCherry RICTOR*^{Ste20}*–3GFP* and *myo51–mCherry RICTOR*^{Ste20}*–3GFP* cells revealed that TORC2 colocalised with each myosin heavy chain at the CAR (Fig. 2B). To correlate the timing of TORC2 reorganisation and recruitment to the contractile apparatus with spindle dynamics and CAR formation, RICTOR^{Ste20}–3GFP dynamics was examined in cells expressing an mCherry-labelled allele of the essential class II myosin *myo2* and tdTomato-labelled version of the essential spindle pole body (SPB) component Sid4 (*myo2–mCherry sid4–tdTomato* cells) (Fig. 2C, Movie 5). Upon entry into mitosis, Myo2 was recruited to foci at the cell equator, and the two separate SPBs were juxtaposed the elongating mitotic spindle until metaphase (Fig. 2C–E, phase I; Fig. S1D). At the onset of anaphase, the spindle elongates and Myo2 foci coalesce to form the CAR (phase II) (Mulvihill and Hyams, 2002; Wu et al., 2003). It is at this time that foci of RICTOR^{Ste20}–3GFP localised to the CAR, where they remained through its subsequent constriction (phase III), and disassembly (phase IV), when they were recruited to the ensuing new cell end (Fig. 2C,F; Movie 5). Thus, TORC2 localises to the CAR during mitosis where it interacts with Cdc12, Myp2 and Myo51, key regulatory components of CAR formation and function.

Myosin V and myosin II regulate RICTOR^{Ste20} recruitment at the CAR

We next decided to investigate the physical interaction between RICTOR^{Ste20} and the myosins, Myp2 and Myo51, to explore whether these actin-associated motor proteins play a role in recruiting TORC2 to the cell equator during cytokinesis. The class V myosin, Myo51, plays key roles in regulating CAR function and dynamics (Bezanilla et al., 1997; Win et al., 2001). Fission yeast contains two myosin V proteins, Myo51 and Myo52. The minor myosin V isoform, Myo51, localizes to the CAR (Motegi et al., 2001; Win et al., 2001) and is required for correct CAR formation (Fig. S1E). Small-scale immunoprecipitation confirmed the physical association between TORC2 and the cargo-binding domain of Myo51, as Tor1 co-purified with the Myo51 tail fused to GFP (Doyle et al., 2009) (Fig. 3A). This confirmation, combined with our observation that Myo51–mCherry colocalised with RICTOR^{Ste20}–3GFP during cytokinesis (Fig. 2B) provides strong evidence that Myo51 interacts with TORC2 during cytokinesis. Consistent with this finding, RICTOR^{Ste20}–3GFP failed to localize to the ring in the absence of Myo51 (Fig. 3B,C), and localised instead to the septum as it forms around the outside edge of the constricting CAR (Fig. 3C). Removal of the second myosin V homologue through deletion of the *myo52*$^{+}$ gene had no discernible impact upon RICTOR^{Ste20}–3GFP distribution (data not shown). In contrast, RICTOR^{Ste20} function was not required for Myo51 recruitment to the CAR (Fig. 3D). Thus, the recruitment of TORC2 to the CAR is dependent upon the myosin V motor Myo51, with which it physically associates.

Like Myo51, the class II myosin Myp2 physically interacts with Tor1 (Fig. 2A) and plays a role in maintaining the integrity of the CAR during cytokinesis. Cells lacking Myp2 display cytokinesis defects (Bezanilla et al., 1997; Mulvihill et al., 2000) similar to those observed here for *Rictor*^{ste20}Δ cells. For example, the CAR sometimes split in two, and each half constricts independently of each other (Fig. 3E, asterisk) (Mulvihill and Hyams, 2003). Interestingly, in the majority (>60%) of cells lacking Myp2, RICTOR^{Ste20} did not localise to the cell equator (Fig. 3E,F). Intriguingly, Myp2 was also required for RICTOR^{Ste20}–3GFP localisation to cell poles (Fig. 3E, compare lack of cell pole localisation with that observed in *myp2*$^{+}$ cells, highlighted by arrowheads in Figs 2 and 3). Why this CAR component should affect the cortical TORC2 localisation is currently unclear; however, western blot analysis confirmed persistence of RICTOR^{Ste20} protein in the *myp2*Δ cells (data not shown). To further investigate and confirm the dependence of TORC2 upon Myp2 for localisation and interaction with the CAR, we used time-lapse imaging to characterise the relative timing of spindle dynamics, CAR formation and TORC2 localisation to the cell equator. Time-lapse imaging of more than 30 prototroph wild-type cells revealed CAR constriction (phase III) lasted 25 min (Fig. 3F). In contrast, this

Journal of Cell Science (2016) 129, 2613-2624 doi:10.1242/jcs.190124

A

Rictor^{ste20} immuno-precipitations

	Unique peptides						Unique Spectra						Unweighted spectum							
	Ctrl-1	Exp-1	Ctrl-2	Exp-2	Ctrl-3	Exp-3	Ctrl-1	Exp-1	Ctrl-2	Exp-2	Ctrl-3	Exp-3	Ctrl-1	Exp-1	Ctrl-2	Exp-2	Ctrl-3	Exp-3	Total Ctrl	Total Exp
Ste20	0	0	0	32	0	6	0	0	0	37	0	7	0	0	0	51	0	9	0	61
Mid1	0	0	2	26	0	2	0	0	2	27	0	2	0	0	2	34	0	2	2	36
Blt1	0	2	0	19	0	5	0	2	0	21	0	5	0	2	0	23	0	5	0	30
Ppk32	0	5	0	15	0	3	0	5	0	15	0	3	0	5	0	17	0	4	0	26
Myp2	0	7	2	4	2	5	0	7	2	4	2	5	0	8	2	7	2	8	4	23
Myo51	2	4	0	1	2	10	2	4	0	1	2	10	2	6	0	1	2	11	4	18
Pop3	1	6	2	8	0	2	1	6	2	12	0	2	1	7	2	15	0	2	3	18
Sin1	0	0	0	9	0	0	0	0	0	10	0	0	0	0	0	11	0	0	0	11
Gad8	0	2	0	0	0	3	0	2	0	0	0	3	0	2	0	0	0	3	0	5
Cdc12	0	0	0	3	0	0	0	0	0	3	0	0	0	0	0	3	0	0	0	3

Known interacting proteins

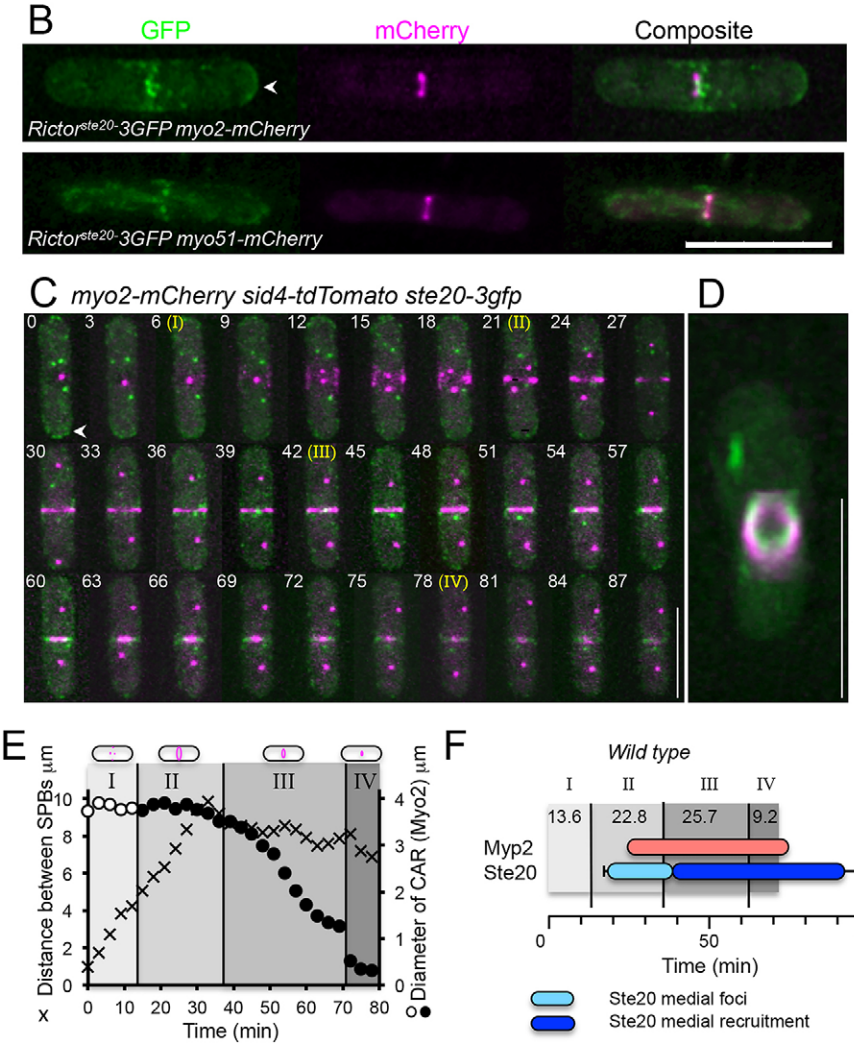

Fig. 2. TORC2 interacts with and localises to the CAR during ring constriction. (A) Summary of mass spectrometry analysis of three independent experiments of control (Ctrl, no anti-Tor1 antibodies added) and Tor1 immunoprecipitations (Exp), each purified from 20-l cell cultures. (B) Micrographs of RICTOR^{Ste20} (green) and Myo2 or Myo51 (magenta) signal from mitotic *RICTOR*^{Ste20}*–3GFP myo2–mCherry* cells or *RICTOR*^{Ste20}*–3GFP myo51–mCherry* cells. (C,D) Maximum projections of 21-slice *z*-stacks from a timecourse of mitotic *myo2–mCherry sid4–tdTomato RICTOR*^{Ste20}*–3GFP* cells reveals that RICTOR^{Ste20} foci (green) are recruited to the cell equator after SPB (magenta) separation and Myo2 ring (magenta) formation has occurred (frame 1–4 with non-separated SPBs represent interphase cells) (C) and coalesce to form a ring during CAR constriction. (D) Micrograph of mCherry and GFP signal from a *RICTOR*^{Ste20}*–3GFP myo2–mCherry* cell illustrating TORC2 association with the CAR. In B and C, arrowheads highlight RICTOR^{Ste20} localisation at cell tips. (E) The timing of key events during CAR formation and constriction [(I) Myo2 foci (empty circles) recruit to the cell equator; (II) Myo2 foci coalesce to form a CAR (filled circles); (III) the CAR constricts until, (IV) it reaches a diameter of 0.5 µm or less] were determined in relation to nuclear division (crosses, distance between SPBs) in wild-type. (F) The timing of the appearance of Myp2 ring (red bar) and RICTOR^{Ste20} medial foci (light blue bar) or RICTOR^{Ste20} ring recruitment (dark blue) were determined in wild-type strains in relation to the events determined in E. Scale bars: 10 µm.

event took twice as long in cells lacking Myp2 (50 min), confirming the role of this protein in modulating CAR constriction (Bezanilla et al., 1997; Mulvihill et al., 2000; Huang et al., 2012). RICTOR^{Ste20}–3GFP failed to localise to the cell equator in the majority (~60%) of *myp2*Δ cells, and these cells took almost twice as long as equivalent *myp2*$^{+}$ cells to complete CAR constriction (phase III) (Fig. 3F; Fig. S1D). However, RICTOR^{Ste20} localised correctly in the remaining ~40% of *myp2*Δ cells, and phase III took ~50% longer to complete than wild type (Fig. 3F; Fig. S1D). Taken together, our observations are consistent with both class II and V myosins co-purifying with TORC2, and playing a role in regulating TORC2 localisation to the CAR.

TORC2 regulate Myp2 CAR localisation and the timing of CAR constriction

We further explored the link between TORC2 and the timing of cytokinesis by visualising cytokinetic ring dynamics using the myosin II motor proteins, Myo2 and Myp2, in *Rictor*^{ste20}Δ cells. Time-lapse imaging of more than 30 *Rictor*^{ste20}Δ cells revealed that, of those cells which formed a CAR, constriction and disassembly (Fig. 4A, phase III and IV) took on average more than three times longer than in wild-type cells (Fig. 4A; Fig. S1A). RICTOR^{Ste20} only localised to the CAR in 40% of *myp2*Δ cells (Fig. 4), likewise Myp2 recruitment to the CAR was frequently aberrant in *Rictor*^{ste20}Δ cells (Fig. 4B,D) indicating a co-dependency.

Journal of Cell Science (2016) 129, 2613-2624 doi:10.1242/jcs.190124

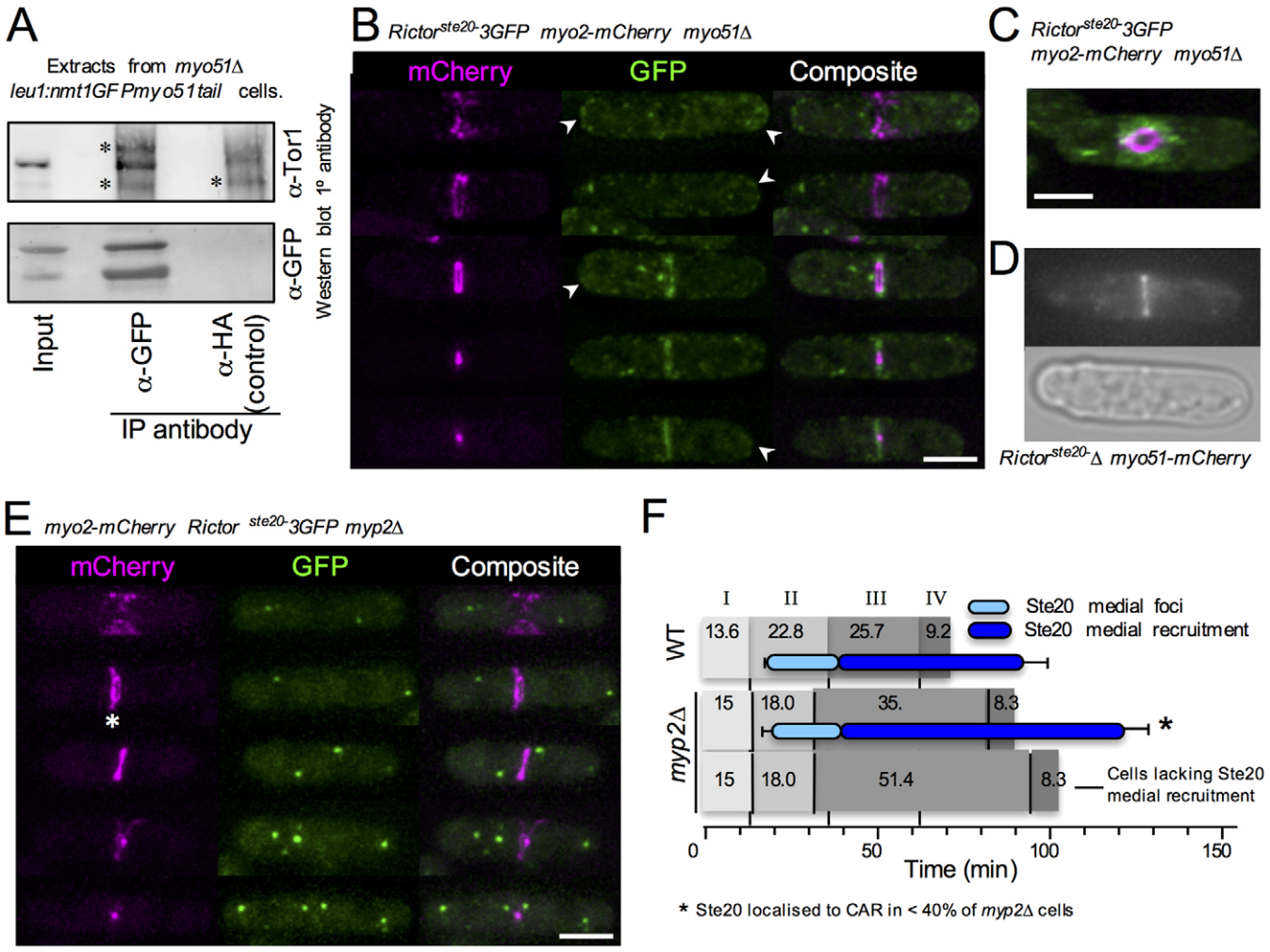

Fig. 3. Myosin II and V interact with and regulate RICTOR^{Ste20} localisation at the CAR. (A) Extract and subsequent anti-GFP and anti-HA (control) immunoprecipitates from *S. pombe* cells expressing a GFP-tagged Myo51 cargo-binding-tail domain fusion protein were subject to anti-Tor1 (upper panels) and anti-GFP (lower panels) antibody western blot analysis. The asterisks denote background bands. (B–E) Micrographs of mCherry and GFP signals in cells with the indicated genotype. The asterisk highlights rings split in two. Arrowheads highlight RICTOR^{Ste20} localisation at cell tips. (F) The timing of the appearance of RICTOR^{Ste20} medial foci (light blue bars) or RICTOR^{Ste20} ring recruitment (dark blue) were determined in wild-type and *myp2*Δ strains in relation to the events determined in Fig. 2E. Scale bars: 5 µm.

Although Myp2 was recruited to the CAR 10.3 min after its formation (phase II) in wild-type cells, and remained there throughout CAR constriction (Fig. 4A,C; Movie 6), Myp2 CAR recruitment was extremely transient in the majority of mitotic *Rictor*^{ste20}Δ cells lacking TORC2 function (Fig. 4D). Crucially, in *Rictor*^{ste20}Δ cells in which Myp2 localised to the CAR, the ring remained un-constricted for a long period (Fig. 4D,E), and the contractile apparatus was often observed sliding along the length of the cell (Fig. 4D,E). Therefore, TORC2 not only co-purifies with regulators of cytokinesis, but ablating TORC2 function leads to defects in CAR formation and severe delays in its constriction (Fig. 4A; Fig. S1A).

TOR-dependent phosphorylation on serine residues 172 and 189 of Acp1

To determine whether the TORC2-interacting CAR components (Fig. 2A) are substrates of the complex we examined data from a stable isotope labelling by amino acids in cell culture (SILAC) mass spectrometric screen for phospho-peptides that showed differential phosphorylation upon Torin1 inhibition of TOR function (Atkin et al., 2014). With the exception of Ppk32 and Myo51, phosphorylation sites were identified in all co-purifying proteins. Crucially, none of these sites were regulated by TOR signalling, as they remained unchanged following TOR inhibition by Torin1 (Fig. S1F).

Importantly, cytokinesis and the dynamics of actin polymers are regulated, in part, by a heterodimeric complex consisting of the actin-capping proteins Acp1 and Acp2 (homologues of human CAPZA and CAPZB proteins; hereafter denoted CAPZA^{Acp1} and CAPZB^{Acp2}, respectively), which binds to and stabilises the barbed end of actin structures (Yamashita et al., 2003). Interestingly, the TOR-phosphorylation-dependent SILAC screen revealed that CAPZA^{Acp1} displayed differentiation phosphorylation on serine residues 172 and 189 (Fig. 5A; Fig. S2A,B) in Torin1-treated cells. However, the sequence that serine 172 and 189 lies within does not conform to the TOR consensus phosphorylation site (Hsu et al., 2011), suggesting that phosphorylation of CAPZA^{Acp1} is dependent on TOR rather than being a direct target. The Psk1 and Gad8 kinases are two known TORC1 and TORC2 substrates and effector kinases (Pearson and Kemp, 1991). Both Gad8 and Psk1 are members of the

Journal of Cell Science (2016) 129, 2613-2624 doi:10.1242/jcs.190124

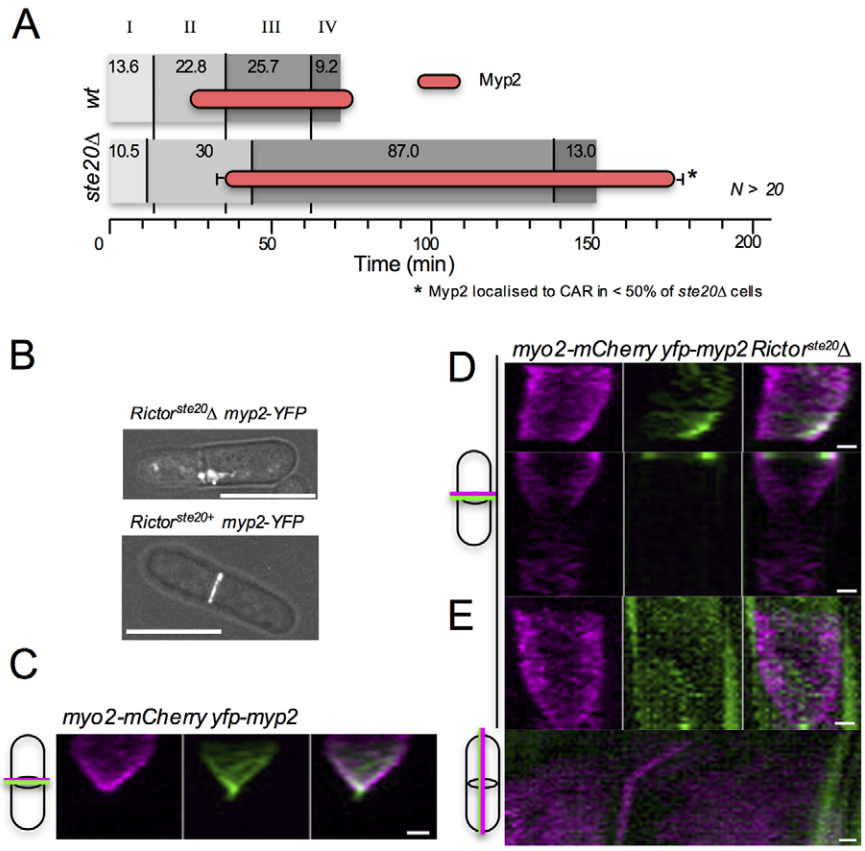

Fig. 4. Myp2 and TORC2 localisation to the actomyosin ring is co-dependent. (A) The timing of Myp2 ring recruitment (red bars) was determined in wild-type and *Rictor*^{ste20}Δ strains in relation to the events determined in Fig. 2E. (B) Composite micrographs of YFP and phase signal in *yfp–myp2 Rictor*$^{ste20+}$ and *yfp–myp2 Rictor*^{ste20}*Δ* cells. (C–E) Kymographs generated from 30 maximum projections of time-lapse images (3 min/frame) of (C) *myo2–mCherry YFP–myp2* and (D) *myo2–mCherry YFP–myp2 Rictor*^{ste20}Δ cells illustrating that TORC2 is required for Myp2 to remain at the CAR. (E) Time-lapse kymographs of the perpendicular (upper panels) and longitudinal (lower panels) axes of a *yfp–myp2 Rictor*^{ste20}Δ cell in which Myp2 signal is lost from the cell equator and the Myo2-containing CAR slides along the cell cortex before constricting. In C–E, cartoons illustrate orientation and origin of kymograph axes. Scale bars: 5 µm (B); 1 µm (C–E).

AGC family of kinases. However, the CAPZA^{Acp1} phosphorylation sites do not conform to the AGC kinase consensus site either. It is therefore possible that the TOR-dependent CAPZA^{Acp1} phosphorylation is regulated through an as yet unidentified signalling pathway. Interestingly, serine 189 is conserved in the mammalian CAPZA homologues (serine 208) (Fig. 5A), suggesting that TOR-dependent phosphorylation of CAPZA could be conserved in metazoan systems.

TORC2-dependent phosphorylation alters CAPZA^{Acp1}–CAPZB^{Acp2} heterodimer formation

The crystal structure of the human CAPZA–CAPZB heterodimer (Yamashita et al., 2003) reveals the CAPZA^{Acp1} serine 189 equivalent within human CAPZA maps to the CAPZA–CAPZB interface (Fig. 5A), and therefore its phosphorylation is likely to have an impact upon heterodimer formation and function. In order to assess the impact TOR-dependent CAPZA^{Acp1} phosphorylation had upon CAPZA^{Acp1}–CAPZB^{Acp2} heterodimer formation we undertook equivalent co-immunoprecipitation assays in wild-type cells treated with either Torin1, to inhibit TOR signalling (Atkin et al., 2014), or DMSO. Although CAPZA^{Acp1}–HA was seen to co-purify with CAPZB^{Acp2}–GFP in wild-type cells, this interaction was substantially enhanced by treatment with Torin1 (Fig. 5B). A conserved mutation within the ATP-binding pocket of genes encoding for either of the two fission yeast Tor kinases (*tor2.G2040D* *tor1.G2037D*; denoted *TORC1*^{R} and *TORC2*^{R}, respectively) specifically confers TORC1- or TORC2-dependent resistance to Torin1-induced inhibition (Atkin et al., 2014). These mutants can be used to establish whether the Torin1-induced effects are brought about by off-target effects. Torin1 enhanced CAPZA^{Acp1}–CAPZB^{Acp2} heterodimer formation in wild-type and the *TORC1*^{R} mutant (Fig. 5C). In contrast, heterodimer formation was not enhanced in the *TORC2*^{R} mutant upon Torin1 treatment. Therefore, as TORC2 activity in the *TORC2*^{R} mutant is resistant to the effects of Torin1, this result indicates that it is the specific inhibition of TORC2 that enhances the affinity between CAPZA^{Acp1} and CAPZB^{Acp2}.

To establish whether TORC2-dependent CAPZA^{Acp1} phosphorylation alters the stability of the CAPZA^{Acp1}–CAPZB^{Acp2} heterodimer we generated strains in which the endogenous *CAPZA*$^{acp1+}$ locus was mutated to encode for CAPZA^{Acp1} protein in which serine 172 and 189 had been replaced with alanine to mimic an unphosphorylated serine (denoted CAPZA^{Acp1}-AA). CAPZA^{Acp1}–CAPZB^{Acp2} co-immunoprecipitations were repeated using extracts from *CAPZA*^{acp1}*-AA* cells and the CAPZA^{Acp1}-AA mutant protein was seen to have an increased affinity for CAPZB^{Acp2} compared to wild type (Fig. 5D). Crucially, the Torin1-induced stabilisation of the CAPZA^{Acp1}–CAPZB^{Acp2} heterodimer was abolished with the *CAPZA*^{acp1}*-AA* allele (Fig. 5E). Thus, these data indicate that TORC2-dependent phosphorylation of CAPZA^{Acp1} serine 172 and 189 regulates CAPZA^{Acp1}–CAPZB^{Acp2} heterodimer formation.

The CAPZA^{acp1}-AA–CAPZB^{Acp2} complex stabilises cortical actin polymers

The fission yeast CAPZA^{Acp1}–CAPZB^{Acp2} complex regulates actin dynamics and cytokinesis (Kovar et al., 2005; Nakano and Mabuchi, 2006), and is recruited to the cell equator during cell division (Movie 7). CAPZA^{Acp1}–GFP remained localised at the cell equator at the end of cytokinesis for significantly longer in *Rictor*^{ste20}Δ and *myp2*Δ cells than in wild-type cells (Fig. 6A). In contrast, the timing of RICTOR^{Ste20}–3GFP CAR recruitment was unaffected in cells lacking the *CAPZA*^{acp1} gene (Fig. 6A).

Journal of Cell Science (2016) 129, 2613-2624 doi:10.1242/jcs.190124

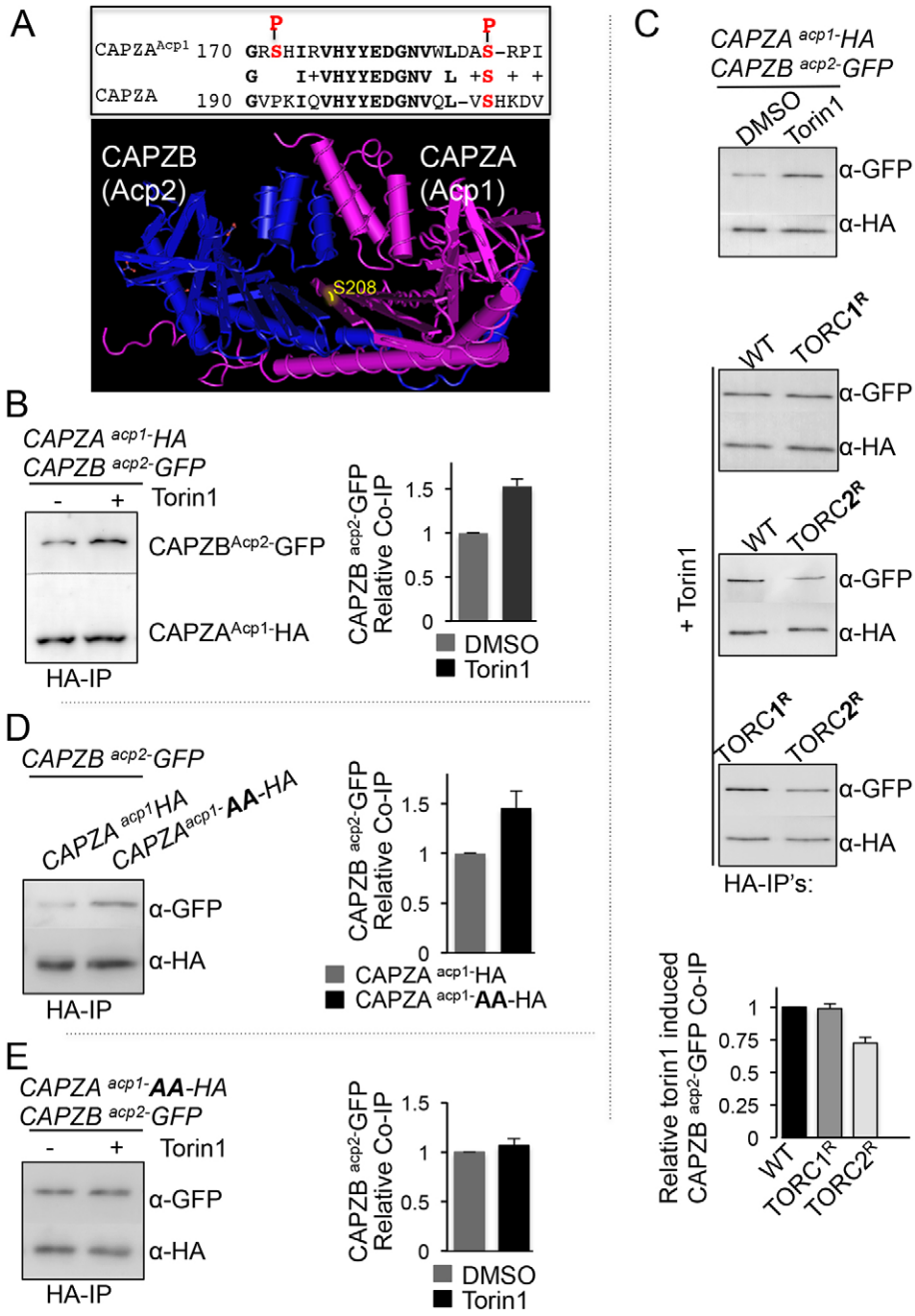

Fig. 5. TORC2 regulates CAPZA ^{Acp1}–CAPZB^{Acp2} heterodimer formation. (A) Alignment of the phosphorylated region of *S. pombe* Acp1 and the human CAPZA homologues. Conserved residues are highlighted in bold and the two TOR-dependent phosphorylation sites are shown in red. The position of the conserved phosphorylated serine 208 (in yellow) is shown on the crystal structure of CAPZA and CAPZB (Yamashita et al., 2003). (B–D) Anti-GFP (upper panels) and anti-HA (lower panels) antibody western blots of CAPZA^{Acp1}–HA immunoprecipitations (HA-IPs) from indicated strains in the absence or presence of the TOR inhibitor Torin1 (25 µM) (TORC1^{R}=*tor2.G2037D* TORC2^{R}=*tor1.G2040D*). (B–E) To ensure the measured relative levels of Acp1 and Acp2 within anti-HA immunoprecipitates were quantifiable, western blot membranes of immuno-precipitates were cut in half and the separate portions were subsequently probed with anti-GFP (upper panels) and anti-HA (lower panels) antibodies.

We next used LifeAct (Huang et al., 2012; Riedl et al., 2008) to compare actin dynamics in *CAPZA^{acp1+}* and *CAPZA^{acp1}-AA* mutant cells. Interestingly, the *CAPZA^{acp1}-AA* allele, which stabilises the CAPZA^{Acp1}–CAPZB^{Acp2} complex (Fig. 5D), had a substantial impact upon the stability of cortical filamentous actin patches (Fig. 6B–D). Actin patches were depolarised, had a longer lifetime, and increased polymerisation rates in *CAPZA^{acp1}-AA* cells when compared to wild type (growth rates: wild-type, 220.1 arbitrary units (AU) s^{-1}; *CAPZA^{acp1}-AA*, 573.8 AU s^{-1}; shrinkage rates: wild type, −167.5 AU s^{-1}; *CAPZA^{acp1}-AA*: −543.9 AU s^{-1}) (Fig. S3C). Cells possessing the *CAPZA^{acp1}-AA* allele had five times more LifeAct signal associated with cortical actin patches compared to wild type (Fig. 6B–D; Fig. S3C). In contrast, there was no significant difference in the number of cortical actin patches, patch-associated CAPZA^{Acp1} protein localisation or total CAPZA^{Acp1} protein within wild-type and mutant cells (Fig. S3C). This indicates the *CAPZA^{acp1}-AA* allele does not affect actin nucleation or stability of the CAPZA^{Acp1} protein, but that it remains associated with actin polymers longer than wild type, which continue to accumulate actin at the uncapped end.

CAPZA^{acp1}-AA has aberrant CAR morphology

It has been suggested that cells possess a finite pool of actin monomers, for which different actin nucleators (Arp2/3 and formins) compete (Burke et al., 2014; Suarez et al., 2015). Thus, increasing the proportion of the actin pool incorporated within Arp2/3-nucleated cortical actin patches would result in a reduction in the actin available for incorporation into formin-nucleated actin cables, which are essential for cytokinesis to occur. The amount of CAR-associated Cdc8 (the yeast tropomyosin) provides a

Journal of Cell Science (2016) 129, 2613-2624 doi:10.1242/jcs.190124

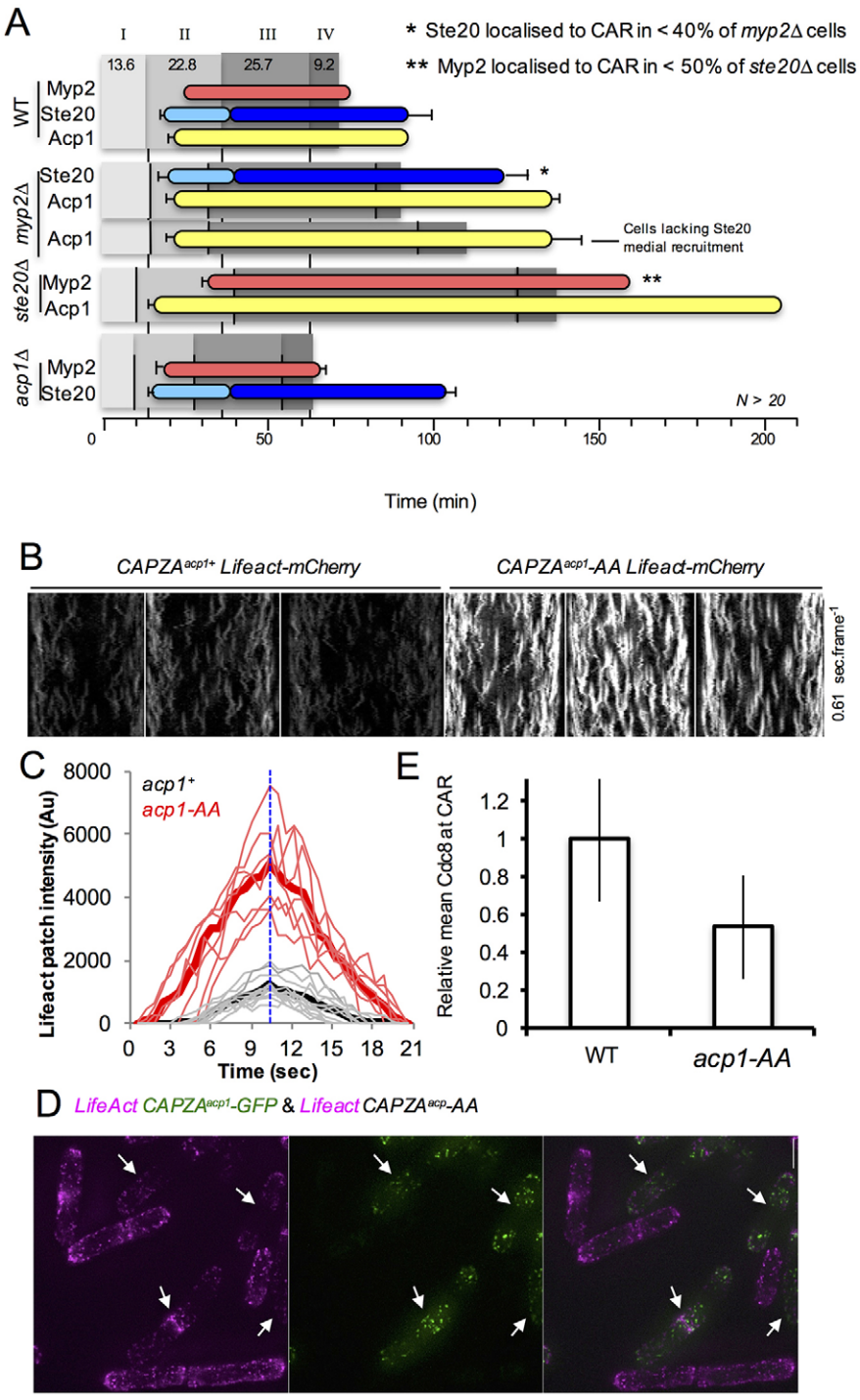

Fig. 6. *CAPZA*^{acp1}*-AA* mutants disrupt actin dynamics and cytokinesis. (A) The timing of the appearance of Myp2 ring (red bars), RICTOR^{Ste20} foci (light blue bars), Acp1 (yellow bars) medial recruitment and RICTOR^{Ste20} ring recruitment (dark blue) were determined in wild-type, *myp2*Δ, *Rictor*^{ste20}Δ (*ste20*Δ) and *acp1*Δ strains in relation to the events determined in Fig. 2E. Recruitment of these proteins to the CAR were observed in less than 40% (*) or 50% (**) of these deletion strains. CAR dynamics and composition were followed in >20 cells for each strain. Early exponential prototrophs were used in each experiment. (B) mCherry kymographs generated from 100 timeframe maximum projections from 13 *z*-plane images of *CAPZA*$^{acp1+}$ *Lifeact-mCherry* (left panels) and *CAPZA*^{acp1}*-AA Lifeact-mCherry* (right panels) cells (0.6 s/frame). (C) Graph showing lifetime kinetics of Lifeact signal from individual (faint lines) actin patches and overall averages (thick lines) of *CAPZA*$^{acp1+}$ *Lifeact-mCherry* (black lines) and *CAPZA*^{acp1}*-AA Lifeact–mCherry* (red lines) cells. (D) Maximum projections of a mixture of *CAPZA*^{acp1}*–GFP Lifeact–mCherry* and *CAPZA*^{acp1}*–AA Lifeact–mCherry cells*. Overlaying the GFP (green) and mCherry (magenta) signals demonstrate the increase in actin signal at cortical actin patches in the *CAPZA*^{acp1}*-AA* mutant compared to GFP-labelled wild type (arrows) cells. (E) Histograms illustrating mean±s.d. relative Cdc8 at the CAR in wild-type (WT) and *CAPZA*^{acp1}*-AA* cells (*n*>30 per strain).

specific measure of the amount of formin-nucleated actin cables (Skoumpla et al., 2007; Skau and Kovar, 2010). Consistent with the 'finite pool of actin monomers' model, quantification of the CAR-associated Cdc8 revealed a reduction in the amount of actin incorporated into Cdc12-nucleated (Cdc12 is a yeast formin) actin cables within the CAR in CAPZA^{acp1}*-AA* cells (Fig. 6E). Therefore, although cortical actin patches are more stable and persist for longer in the *CAPZA*^{acp1}*-AA* cells, there are fewer Cdc8-associated actin cables in the CAR. This might provide an explanation for the CAR instability in *CAPZA*^{acp1}*-AA* cells (Fig. 7A). Thus, the aberrant CAR morphology phenotype observed in *CAPZA*^{acp1}*-AA* mutant cells emulates that seen in *TORC2* deletion strains. Finally, in contrast to wild-type cells (Huang et al., 2012), and similar to with *CAPZA*^{acp1}*-AA*, the actin cytoskeleton was depolarised in *Rictor*^{ste20}Δ cells (Fig. 7B). This finding is consistent with the observed increased cell diameter of cells lacking TORC2 function (Fig. 1B), as cell growth might no longer be exclusively restricted to cell ends.

Finally, stress of wild-type cells at 37°C transiently disrupts actin organisation and dynamics, before a normal distribution is re-established and growth resumes within 90 min (Petersen and Hagan, 2005). TORC2 has a crucial role in responding to induced heat stress as TORC2-deficient cells are hypersensitive to transient increases in heat (Kawai et al., 2001; Weisman and Choder, 2001).

Journal of Cell Science (2016) 129, 2613-2624 doi:10.1242/jcs.190124

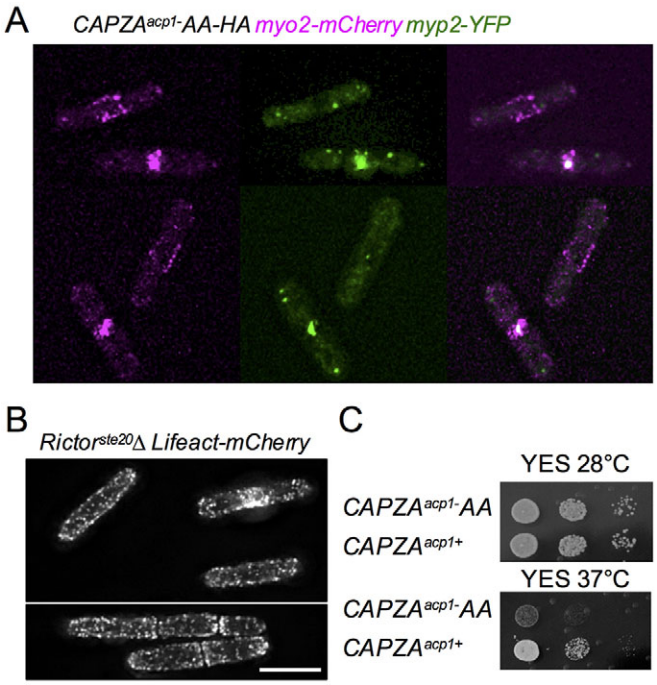

Fig. 7. TORC2 and CAPZA^{acp1}-AA mutants disrupt CAR and actin localisation. (A) Micrographs of Myo2 (magenta) and YFP (green) signal *CAPZA^{acp1}-AA–HA myo2–mCherry YFP–myp2* cells. (B) Micrograph of mCherry signal from *Rictor^{ste20}Δ Lifeact–mCherry* cells illustrating the cytokinesis defect and lack of polarised actin signal. Scale bar: 10 µm. (C) The CAPZA^{Acp1} phosphorylation site mutant *CAPZA^{acp1-}AA* is sensitive to heat stress at 37°C.

Intriguingly, *CAPZA^{acp1}-AA* cells also failed to recover from the stress imposed by a shift from 28°C to 37°C (Fig. 7C). CAPZA^{Acp1} protein levels did not change following heat stress of either wild-type or *CAPZA^{acp1}-AA* cells (Fig. S3A). Hence, the mutations did not affect CAPZA^{Acp1} stability, and the alteration in actin dynamics might cause the observed increased sensitivity to heat stress in *CAPZA^{acp1}-AA* cells.

In summary, we conclude that the TORC2-dependent phosphorylation of CAPZA^{Acp1} reduces the stability of the CAPZA^{Acp1}–CAPZB^{Acp2} heterodimer. This in turn modulates the stability of cortical actin patches and alters the concentration of free monomeric-actin within the cell, to affect the timing and fidelity of cytokinesis.

DISCUSSION

Here, we describe a novel TORC2 recruitment to the CAR that plays a role in maintaining the fidelity of cytokinesis in fission yeast. We describe a mechanism by which a myosin V and myosin II co-purify with TORC2 and play a role in its localisation to the CAR during cytokinesis. Each myosin appears to play a discrete role in affecting TORC2 CAR localisation. Myo51 ensures TORC2 is recruited to the CAR in the early stages of anaphase, whereas Myp2 maintains TORC2 at the CAR. Although TORC2 is required to maintain the CAR at the cell equator and prevent it from drifting along the cell cortex, both TORC2 and Myp2 maintain the integrity of a single CAR structure and prevent it from splitting in two during its constriction. It is currently unclear why RICTOR^{Ste20} only associates with the CAR in a subset of *myp2*Δ cells, however this might explain why cytokinesis defects are only observed in a subset of cells lacking this myosin II.

In the absence of TORC2 signalling, the stability and activity of the actomyosin ring and therefore cytokinesis are altered. These changes in actin dynamics arise in part from TORC2-dependent phosphorylation of the actin-capping protein CAPZA^{Acp1}. Perturbation of CAPZA^{Acp1} phosphorylation increases the stability of the CAPZA^{Acp1}–CAPZB^{Acp2} heterodimer (Fig. 5), significantly alters the cellular organisation of the actin cytoskeleton (Fig. 6) and disrupts CAR function (Fig. 7A). The increased severity in growth and cytokinesis phenotypes of *Rictor^{ste20}*Δ cells compared to the CAPZA^{acp1}*-AA* and *myp2*Δ mutants (Figs 1, 3 and 7) suggest that CAPZA^{Acp1} is very unlikely to be the sole protein with a key role in cytokinesis that is regulated in a TORC2-dependent manner. Consistent with this view, an increase in myosin II Myo2 levels was seen in the *Rictor^{ste20}*Δ cells but not in *acp1*Δ or *myp2*Δ cells (data not shown), thus TORC2 regulates Myo2 in an as yet unidentified manner. Multiple potential TORC2-regulated proteins involved in coordinating cell division co-purified with TORC2 (Fig. 2A). However, our SILAC analysis to date has not identified phospho-peptides that showed differential phosphorylation upon Torin1 inhibition of TOR function in any of the co-purifying proteins. Crucially, we recently demonstrated that the co-purifying SCYL family pseudo-kinase Ppk32 is a novel regulator of TOR signalling, and intriguingly Ppk32 concentrates at the cell equator during cell division in more than 60% of cells (Kowalczyk and Petersen, 2016). Thus, the TORC2-dependent regulation of CAPZA^{Acp1}–CAPZB^{Acp2} that we describe here is likely to be one of multiple TORC2-dependent mechanisms regulating the fidelity and timing of cytokinesis and cell division.

The TORC2 control of CAPZA^{Acp1}–CAPZB^{Acp2} heterodimer stabilisation enables cells to couple actin stability with changes in cell growth and division, which can be implemented in response to environmental stress. Crucially, this TORC2-dependent change in CAPZA^{Acp1}–CAPZB^{Acp2} affinity and actin stability provides an explanation for the enhanced F-actin cable stability observed in TORC2-deficient cells (Ikai et al., 2011; Matsuo et al., 2007), which appears to be key in ensuring cell survival following environmental stress. Similar controls are likely to underlie TORC2 control of actin dynamics and cytokinesis in mammalian cells, as knockout of TORC2 components in HeLa cells leads to similar increases in the abundance of actin fibres and increased cytoplasmic paxilin association (Sarbassov et al., 2004). Furthermore, serine 2481 auto-phosphorylated mTOR localises to the cleavage furrow at the onset of cytokinesis (Vazquez-Martin et al., 2009), suggesting that active mTOR plays a conserved role in cytokinesis and cell division.

MATERIALS AND METHODS

Strains and cell cultures

Strains used in this study are listed in Table S1. Unless otherwise specified, cells were cultured at 28°C in Edinburgh minimal media (EMM2) (Fantes, 1977) using 20 mM L-Glutamic acid as a nitrogen source (EMMG). Cells were grown exponentially for 48 h before being harvested or examined microscopically at early exponential phase of 1.5×10^6 cells/ml. *Rictor^{ste20}*Δ cells were frozen immediately after spore germination. Cells were tested for sensitivity to stress and sterility to ensure no suppressors had accumulated. All *Rictor^{ste20}*Δ cell cultures were maintained in exponential growth and never exposed to starvation.

FACS analysis

S. pombe DNA content was measured by flow cytometry as previously described (Costello et al., 1986).

Large scale Tor1 immunoprecipitation

Wild-type cells (JP350) were grown in EMMG to 2.5×10^6 cells/ml (5 l per immunoprecipitation condition) and harvested and disrupted using a freezer mill (SPEX 6870) in liquid nitrogen. The cell powder was thawed in immunoprecipitation buffer (50 mM HEPES pH 7.5, 150 mM NaCl, 0.1% CHAPS, 50 mM L-arginine, 50 mM L-glutamic acid, 0.05% Tween 20, 120 mM β-glycerophosphate di-sodium salt, 4 mM Na_3VO_4, 100 mM NaF, 2 mM PMSF, 10 mM N-ethylmaleimide, 2 mM dithiothreitol and 2×Roche EDTA-free protease inhibitor cocktail). The cleared supernatant was incubated with Invitrogen protein G Dynabeads, pre-incubated with anti-Tor1 antibodies (5 µg; Hálová et al., 2013) or no antibody for control, for 60 min at 4°C. Beads were then washed twice with immunoprecipitation buffer plus 50 mM NaCl (200 mM final concentration) and proteins were eluted by heating at 80°C for 10 min. The samples were loaded on to a NUPAGE Bis-Tris 4–12% gel (Life Technologies). The gel was fixed with 7% acetic acid and 25% methanol and stained with Coomassie Brilliant Blue. The entire lane was cut into small bands, before being sent for protein identification. Mass spectrometry data were analysed by Scaffold™ 3 software.

Immunoprecipitation of the Myo51 cargo-binding domain

Immunoprecipitation and cell lysis was performed in the following buffer – 50 mM HEPES pH7.5, 150 mM NaCl, 0.1% CHAPS, 50 mM L-arginine, 50 mM L-glutamic acid, 0.05% Tween, 50 mM NaF, 2 mM Na_3VO_4, 60 mM β-glycerophosphate di-sodium salt, 5 mM N-ethylmaleimide, 1 mM PMSF, 10 µM Z-LLF 1 mM DTT and 1× protease inhibitor without EDTA (Complete, Mini; Roche), with the addition of 150 mM NaCl (300 mM final concentration) and 100 mM KCl for washes. 6×10^8 cells, harvested at a density of 2×10^6/ml, were used per immunoprecipitation. Protein A dynal beads (Life Technologies) were used and the cell lysis solution was pre-cleared for 10 min with a bead-only slurry. Cleared extracts were incubated with GFP monoclonal antibody (clones 7.1 and 13.1, Roche) pre-coated dynal A beads for 30 min at 4°C and washed five times prior to elution from beads in loading buffer at 70°C for 15 min.

SILAC cell culture

car2::NAT lys1-131 arg3-d4 cells were inoculated in YES medium overnight and then washed into EMM-G containing 75 mg/l of either light [L-arginine monohydrochloride (Sigma) and L-lysine monohydrochloride (Sigma)] or medium [lysine-L, 2HCl 4.4.5.5-D4 (Cat code DLM-2640, Eurisotop), arginine-L, HCl, U-13C6 99%13C (cat. no. CLM-2265, Eurisotop)] amino acids. Cells were cultured in log phase for 48 h to ensure complete incorporation of labelled amino acids into the proteome. Light-labelled cultures were treated with DMSO and medium-labelled cultures were treated with a final concentration of 25 µM Torin1 at a density of 2.04×10^6 cells/ml. Approximately 4.8×10^9 cells were harvested for each sample. After 30 min cultures were harvested by centrifugation (3000 ***g*** for 5 min), washed in 20 ml of STOP buffer (10 mM EDTA, 1 mM sodium azide, 50 mM sodium fluoride, 0.9% NaCl), followed by washing with 10 ml of ice cold ddH_2O. The final pellets were then resuspended in an appropriate volume of ice cold ddH_2O and dropped directly into liquid nitrogen to produce frozen cell droplets.

SILAC protein extraction

Samples were processed using a SPEX Sample Prep LLC 6850 Freezer Mill in presence of liquid nitrogen. The resulting cell powder was resuspended in denaturation buffer (6 M urea, 2 M thiourea, 1% n-octyl glucoside) at a ratio of 500 mg powder to 500 µl denaturation buffer. Insoluble material was removed by centrifugation (13,000 ***g***, 10 min at 4°C) and the supernatant was designated supernatant I (soluble fraction). The pellet was then resuspended in 500 µl denaturation buffer, 500 µl glass beads were added and then subjected to 20 s shaking in a FastPrep machine (FP120, Qbiogene). The resulting suspension was again centrifuged (13,000 ***g***, 10 min at 4°C) and the supernatant retained (supernatant II). The pellet was then discarded. Protein concentrations were determined by Bradford assay according to the manufacturer's instructions.

Mass spectrometry for SILAC

Respective supernatants I and II derived from the 'light' and 'medium' labelled cell cultures were combined and proteins were precipitated at −20°C using ice-cold acetone in methanol left on ice overnight. The proteins were pelleted by centrifugation (2200 ***g***, 20 min, 4°C) and washed with 80% ice-cold acetone. Dried proteins were resolved in digestion buffer (6 M urea, 2 M thiourea, 10 mM Tris-HCl, pH 8.0) and mixed at a 1:1 ratio according to measured protein amounts. The mixtures were digested in solution with trypsin as described previously (Borchert et al., 2010). For proteome analyses, 100 µg of the mixtures were fractionated by isoelectric focusing on an OffGel 3100 Fractionator (Agilent) according to the manufacturer's instructions. Focusing was performed using 13-cm (12 well) Immobiline DryStrips pH 3–10 (Bio-Rad) at a maximum current of 50 µA for 24 kVh. Peptide fractions were collected and desalted separately using C18 StageTips (Rappsilber et al., 2007).

For phosphoproteome analyses, 8 mg of each peptide mixture was subjected to phosphopeptide enrichment as described previously (Olsen et al., 2005) with minor modifications: peptides were separated by strong cation-exchange (SCX) chromatography with a gradient of 0 to 35% SCX solvent B resulting in seven fractions that were subjected to phosphopeptide enrichment by TiO_2 beads. Elution from the beads was performed three times with 100 µl of 40% ammonia hydroxide solution in 60% acetonitrile (pH >10.5). Fractions rich in peptides were subjected to multiple TiO2 enrichment. Enrichment of phosphopeptides from the SCX flow-through was completed in five cycles.

Liquid chromatography tandem mass spectrometry (LC-MS/MS) analyses were performed on an EasyLC nano-HPLC (Proxeon Biosystems) coupled to an LTQ Orbitrap XL (Thermo Scientific) for phosphopeptide analyses, or an LTQ Orbitrap Elite mass spectrometer (Thermo Scientific) for proteome analyses as described previously (Koch et al., 2011). The peptide mixtures were injected onto the column in HPLC solvent A (0.5% acetic acid) at a flow rate of 500 nl/min and subsequently eluted with a 87-min (proteome) or a 127-min (phosphoproteome) segmented gradient of 5%, 33% and 90% HPLC solvent B (80% acrylonitrile in 0.5% acetic acid). During peptide elution, the flow rate was kept constant at 200 nl/min. For proteome analysis, the 20 most intense precursor ions were sequentially fragmented in each scan cycle. For the phosphoproteome analysis, the five most intense precursor ions were fragmented by multistage activation of neutral loss ions at −98, −49, and −32.6 Th relative to the precursor ion (Schroeder et al., 2004). In all measurements, sequenced precursor masses were excluded from further selection for 90 s. Full scans were acquired at resolution of 60,000 (Orbitrap XL), or 120,000 (Orbitrap Elite). The target values were set to 5000 charges for the LTQ (MS/MS) and 10^6 charges for the Orbitrap (MS), respectively; maximum allowed fill times were 150 ms (LTQ) and 1000 ms (Orbitrap). The lock mass option was used for real-time recalibration of mass spectrometry spectra (Olsen et al., 2005).

The mass spectrometry data of all SILAC experiments were processed using default parameters of the MaxQuant software (v1.2.2.9) (Cox and Mann, 2008). Extracted peak lists were submitted to database search using the Andromeda search engine (Cox et al., 2011) to query a target-decoy (Elias and Gygi, 2007) database of *S. pombe* proteome (http://www.pombase.org/, Protein Dataset in FASTA format, downloaded on the 6 April 2011), containing 5076 protein entries and 248 commonly observed contaminants.

Molecular manipulations and generation of single point mutations

The $CAPZA^{acp1}\Delta$ base strain was constructed from a DNA cassette for *acp1* deletion was prepared by PCR amplification. This construct was used to replace the $acp1^+$ gene at the native locus with the nat^+. To generate the *acp1-S172A-S189A* point mutation, standard site-directed mutagenesis was used. The mutant acp1 was then used to replace the *nat1 rpl42*$^+$ gene in JP2222 (Fennessy et al., 2014). The resulting strains were back-crossed and prototroph progeny was selected. The presence of the mutant *acp1* allele was verified by PCR. Thus, all *acp1* single point mutations used in this study are integrated into the *acp1* locus, and are all prototroph strains. C-terminal tagging method was performed as previously described (Bähler et al., 1998) using *acp1* C-terminal-specific primers.

Acp1–HA immunoprecipitations

Immunoprecipitation of Acp1–HA was carried out under non-denaturing conditions allowing for pulldown of any bound Acp2–GFP. Cell lysis buffer consisted of 50 mM HEPES pH 7.5, 100 mM KCl, 50 mM NaCl, 0.2% Tween 20, 0.1 mM EDTA, 1× protease inhibitors (Complete, Mini; Roche), 25 mM NaF, 2 mM Na_3VO_4, 25 mM β-glycerophosphate di-sodium salt, 5 mM N-ethylmaleimide, 0.5 mM PMSF, with the addition of a further 25 mM NaCl and 0.25% CHAPS in wash buffer. Briefly, anti-HA antibody (F7 clone, Santa Cruz Biotechnology) was dimethyl pimelimidate cross-linked to Dynal beads protein A (Life Technologies) and incubated with lysed *S. pombe* cells (3×10^8 cells per immunoprecipitation, harvested at 1.5×10^6cells/ml) for 1 hour at 4°C, followed by five washes with wash buffer. Bound proteins were eluted in loading buffer (100 mM Tris-HCl pH 6.8, 4% SDS, 0.2% Bromophenol Blue, 20% glycerol and 100 mM DTT) at 70°C for 15 min then loaded onto 12% tris-glycine PAGE gels, transferred to PVDF membrane and the membrane cut at ∼45 kDa enabling detection of both $CAPZA^{Acp1}$–HA and $CAPZB^{Acp2}$–GFP on the same gel.

Western blotting

The trichloroacetic acid (TCA) precipitation protocol was followed for total protein extracts (Caspari et al., 2000). The following dilutions of antibodies were used in this study: 1:1000 anti-Myo2 (Coulton et al., 2010) 1:100 anti-GFP (Roche, #11814460001), 1:2000 anti-HA (Santa Cruz Biotechnology, sc-7392 F7 clone). Alkaline-phosphatase-coupled secondary antibodies were used for all blots followed by direct detection with NBT/BCIP (VWR) substrates on PVDF membranes.

Microscopy

Samples were visualised using an Olympus IX71 microscope with a PlanApo 100× OTIRFM-SP 1.45 NA lens mounted on a PIFOC *z*-axis focus drive (Physik Instrumente, Karlsruhe, Germany), and were illuminated using LED light sources (Cairn Research Ltd, Faversham, UK) with appropriate filters (Chroma, Bellows Falls, VT). An Optosplit device (Cairn Research Ltd) was used to allow simultaneous acquisition of signals from two fluorophores that emitted light of different wavelengths. Samples were visualised using either a QuantEM (Photometrics) or ProEM 1024B (Princeton Instruments) EMCCD camera, and the system was controlled with Metamorph software (Molecular Devices). Each 3D-maximum projection of volume data was calculated from 21 *z*-plane images, each 0.2 µm apart, and analysed using Metamorph and Autoquant X software. During live-cell imaging, cells were cultured in EMMG. Cells were grown exponentially at 25°C for 48 h before being mounted (without centrifugation) onto lectin-coated (Sigma L2380; 1 mg/ml) coverslips with an a Bioptechs FCS2 (Bioptechs, Butler, PA), fitted onto an ASI motorised stage (ASI, Eugene, OR) on the above system, with the sample holder, objective lens and environmental chamber held at the required temperature. Cdc8 immunofluorescence was undertaken using conditions described previously (Skoumpla et al., 2007). Mean cell width, septa positioning and nuclear diameter was determined from measurements of ∼300 cells for each strain. In the determining of the timing of CAR formation and constriction, and protein recruitment in wild-type and mutant strains, time-lapse imaging and subsequently analysis was undertaken on >20 cells for each individual strain.

Acknowledgements

We thank Kazuhiro Shiozaki, David Kovar and Iain Hagan for reagents; Iain Hagan and members of the laboratories for stimulating discussions and valuable comments on the manuscript. We thank the Biological Mass Spectrometry Facility at the University of Manchester for protein identification.

Competing interests

The authors declare no competing or financial interests.

Author contributions

K.B., S.K., L.H, J.A., D.C. and D.P.M. performed the experiments. M.F-W., K.K. and B.M. identified the Acp1 phosphorylation sites. K.B., S.K., L.H, J.A., D.C, M.F-W, K.K, B.M., D.P.M. and J.P. analyzed the data. D.P.M. and J.P. conceived and designed the experiments, and wrote the manuscript.

Funding

This work was supported by the University of Kent; the University of Manchester; the University of Flinders; and funding from the Biotechnology and Biological Sciences Research Council [grant number BB/J012793/1]; a Royal Society Industry Fellowship to D.M.; a CASE industrial bursary from Cairn Research Ltd to K.B.; Wellcome Trust funded studentships to J.A. and D.C.; and a Cancer Research UK Senior Fellowship to J.P. [grant number C10888/A11178]. Deposited in PMC for immediate release.

Supplementary information

Supplementary information available online at
http://jcs.biologists.org/lookup/doi/10.1242/jcs.190124.supplemental

References

Alvarez, B. and Moreno, S. (2006). Fission yeast Tor2 promotes cell growth and represses cell differentiation. *J. Cell Sci.* **119**, 4475-4485.

Atkin, J., Halova, L., Ferguson, J., Hitchin, J. R., Lichawska-Cieslar, A., Jordan, A. M., Pines, J., Wellbrock, C. and Petersen, J. (2014). Torin1-mediated TOR kinase inhibition reduces Wee1 levels and advances mitotic commitment in fission yeast and HeLa cells. *J. Cell Sci.* **127**, 1346-1356.

Bähler, J., Wu, J.-Q., Longtine, M. S., Shah, N. G., McKenzie, A., III, Steever, A. B., Wach, A., Philippsen, P. and Pringle, J. R. (1998). Heterologous modules for efficient and versatile PCR-based gene targeting in Schizosaccharomyces pombe. *Yeast* **14**, 943-951.

Bezanilla, M., Forsburg, S. L. and Pollard, T. D. (1997). Identification of a second myosin-II in Schizosaccharomyces pombe: Myp2p is conditionally required for cytokinesis. *Mol. Biol. Cell* **8**, 2693-2705.

Borchert, N., Dieterich, C., Krug, K., Schutz, W., Jung, S., Nordheim, A., Sommer, R. J. and Macek, B. (2010). Proteogenomics of Pristionchus pacificus reveals distinct proteome structure of nematode models. *Genome Res.* **20**, 837-846.

Burke, T. A., Christensen, J. R., Barone, E., Suarez, C., Sirotkin, V. and Kovar, D. R. (2014). Homeostatic actin cytoskeleton networks are regulated by assembly factor competition for monomers. *Curr. Biol.* **24**, 579-585.

Caspari, T., Dahlen, M., Kanter-Smoler, G., Lindsay, H. D., Hofmann, K., Papadimitriou, K., Sunnerhagen, P. and Carr, A. M. (2000). Characterization of Schizosaccharomyces pombe Hus1: a PCNA-related protein that associates with Rad1 and Rad9. *Mol. Cell. Biol.* **20**, 1254-1262.

Costello, G., Rodgers, L. and Beach, D. (1986). Fission yeast enters the stationary phase g0 state from either mitotic G1 or G2. *Curr. Genet.* **11**, 119-125.

Coulton, A. T., East, D. A., Galinska-Rakoczy, A., Lehman, W. and Mulvihill, D. P. (2010). The recruitment of acetylated and unacetylated tropomyosin to distinct actin polymers permits the discrete regulation of specific myosins in fission yeast. *J. Cell Sci.* **123**, 3235-3243.

Cox, J. and Mann, M. (2008). MaxQuant enables high peptide identification rates, individualized p.p.b.-range mass accuracies and proteome-wide protein quantification. *Nat. Biotechnol.* **26**, 1367-1372.

Cox, J., Neuhauser, N., Michalski, A., Scheltema, R. A., Olsen, J. V. and Mann, M. (2011). Andromeda: a peptide search engine integrated into the MaxQuant environment. *J. Proteome Res.* **10**, 1794-1805.

Doyle, A., Martín-García, R. Coulton, A. T., Bagley, S. and Mulvihill, D. P. (2009). Fission yeast Myo51 is a meiotic spindle pole body component with discrete roles during cell fusion and spore formation. *J. Cell Sci.* **122**, 4330-4340.

Elias, J. E. and Gygi, S. P. (2007). Target-decoy search strategy for increased confidence in large-scale protein identifications by mass spectrometry. *Nat. Methods* **4**, 207-214.

Fantes, P. (1977). Control of cell size and cell cycle time in *Schizosaccharomyces pombe*. *J. Cell Sci.* **24**, 51-67.

Fennessy, D., Grallert, A., Krapp, A., Cokoja, A., Bridge, A. J., Petersen, J., Patel, A., Tallada, V. A., Boke, E., Hodgson, B. et al. (2014). Extending the Schizosaccharomyces pombe Molecular Genetic Toolbox. *PLoS ONE* **9**, e97683.

Hálová, L., Du, W., Kirkham, S., Smith, D. L. and Petersen, J. (2013). Phosphorylation of the TOR ATP binding domain by AGC kinase constitutes a novel mode of TOR inhibition. *J. Cell Biol.* **203**, 595-604.

Hartmuth, S. and Petersen, J. (2009). Fission yeast Tor1 functions as part of TORC1 to control mitotic entry through the stress MAPK pathway following nutrient stress. *J. Cell Sci.* **122**, 1737-1746.

Hayashi, T., Hatanaka, M., Nagao, K., Nakaseko, Y., Kanoh, J., Kokubu, A., Ebe, M. and Yanagida, M. (2007). Rapamycin sensitivity of the Schizosaccharomyces pombe tor2 mutant and organization of two highly phosphorylated TOR complexes by specific and common subunits. *Genes Cells* **12**, 1357-1370.

Hsu, P. P., Kang, S. A., Rameseder, J., Zhang, Y., Ottina, K. A., Lim, D., Peterson, T. R., Choi, Y., Gray, N. S., Yaffe, M. B. et al. (2011). The mTOR-regulated phosphoproteome reveals a mechanism of mTORC1-mediated inhibition of growth factor signaling. *Science* **332**, 1317-1322.

Huang, J., Huang, Y., Yu, H., Subramanian, D., Padmanabhan, A., Thadani, R., Tao, Y., Tang, X., Wedlich-Soldner, R. and Balasubramanian, M. K. (2012). Nonmedially assembled F-actin cables incorporate into the actomyosin ring in fission yeast. *J. Cell Biol.* **199**, 831-847.

Ikai, N., Nakazawa, N., Hayashi, T. and Yanagida, M. (2011). The reverse, but coordinated, roles of Tor2 (TORC1) and Tor1 (TORC2) kinases for growth, cell cycle and separase-mediated mitosis in Schizosaccharomyces pombe. *Open Biol.* **1**, 110007.

Jacinto, E., Loewith, R., Schmidt, A., Lin, S., Rüegg, M. A., Hall, A. and Hall, M. N. (2004). Mammalian TOR complex 2 controls the actin cytoskeleton and is rapamycin insensitive. *Nat. Cell Biol.* **6**, 1122-1128.
Kawai, M., Nakashima, A., Ueno, M., Ushimaru, T., Aiba, K., Doi, H. and Uritani, M. (2001). Fission yeast tor1 functions in response to various stresses including nitrogen starvation, high osmolarity, and high temperature. *Curr. Genet.* **39**, 166-174.
Koch, A., Krug, K., Pengelley, S., Macek, B. and Hauf, S. (2011). Mitotic substrates of the kinase aurora with roles in chromatin regulation identified through quantitative phosphoproteomics of fission yeast. *Sci. Signal.* **4**, rs6.
Kovar, D. R., Wu, J.-Q. and Pollard, T. D. (2005). Profilin-mediated competition between capping protein and formin Cdc12p during cytokinesis in fission yeast. *Mol. Biol. Cell* **16**, 2313-2324.
Kowalczyk, K. M. and Petersen, J. (2016). Fission yeast SCYL1/2 homologue Ppk32: a novel regulator of TOR signalling that governs survival during Brefeldin A induced stress to protein trafficking. *PLoS Genet* **12**, e1006041.
Lancaster, O. M. and Baum, B. (2014). Shaping up to divide: coordinating actin and microtubule cytoskeletal remodelling during mitosis. *Semin. Cell Dev. Biol.* **34**, 109-115.
Laplante, M. and Sabatini, D. M. (2012). mTOR signaling in growth control and disease. *Cell* **149**, 274-293.
Lee, S., Comer, F. I., Sasaki, A., McLeod, I. X., Duong, Y., Okumura, K., Yates, J. R., III, Parent, C. A. and Firtel, R. A. (2005). TOR complex 2 integrates cell movement during chemotaxis and signal relay in Dictyostelium. *Mol. Biol. Cell* **16**, 4572-4583.
Liu, L. and Parent, C. A. (2011). Review series: TOR kinase complexes and cell migration. *J. Cell Biol.* **194**, 815-824.
Liu, L., Luo, Y., Chen, L., Shen, T., Xu, B., Chen, W., Zhou, H., Han, X. and Huang, S. (2010). Rapamycin inhibits cytoskeleton reorganization and cell motility by suppressing RhoA expression and activity. *J. Biol. Chem.* **285**, 38362-38373.
Matsuo, T., Otsubo, Y., Urano, J., Tamanoi, F. and Yamamoto, M. (2007). Loss of the TOR kinase Tor2 mimics nitrogen starvation and activates the sexual development pathway in fission yeast. *Mol. Cell. Biol.* **27**, 3154-3164.
Motegi, F., Arai, R. and Mabuchi, I. (2001). Identification of two type V myosins in fission yeast, one of which functions in polarized cell growth and moves rapidly in the cell. *Mol. Biol. Cell* **12**, 1367-1380.
Mulvihill, D. P. and Hyams, J. S. (2002). Cytokinetic actomyosin ring formation and septation in fission yeast are dependent on the full recruitment of the polo-like kinase Plo1 to the spindle pole body and a functional spindle assembly checkpoint. *J. Cell Sci.* **115**, 3575-3586.
Mulvihill, D. P. and Hyams, J. S. (2003). Role of the two type II myosins, Myo2 and Myp2, in cytokinetic actomyosin ring formation and function in fission yeast. *Cell Motil. Cytoskeleton* **54**, 208-216.
Mulvihill, D. P., Win, T. Z., Pack, T. P. and Hyams, J. S. (2000). Cytokinesis in fission yeast: a myosin *pas de deux*. *Microsc. Res. Tech.* **49**, 152-160.
Nakano, K. and Mabuchi, I. (2006). Actin-capping protein is involved in controlling organization of actin cytoskeleton together with ADF/cofilin, profilin and F-actin crosslinking proteins in fission yeast. *Genes Cells* **11**, 893-905.
Neumann, F. R. and Nurse, P. P. (2007). Nuclear size control in fission yeast. *J. Cell Biol.* **179**, 593-600.
Olsen, J. V., de Godoy, L. M. F., Li, G., Macek, B., Mortensen, P., Pesch, R., Makarov, A., Lange, O., Horning, S. and Mann, M. (2005). Parts per million mass accuracy on an Orbitrap mass spectrometer via lock mass injection into a C-trap. *Mol. Cell Proteomics* **4**, 2010-2021.
Pearson, R. B. and Kemp, B. E. (1991). Protein kinase phosphorylation site sequences and consensus specificity motifs: tabulations. *Methods Enzymol.* **200**, 62-81.
Petersen, J. and Hagan, I. M. (2005). Polo kinase links the stress pathway to cell cycle control and tip growth in fission yeast. *Nature* **435**, 507-512.
Rappsilber, J., Mann, M. and Ishihama, Y. (2007). Protocol for micro-purification, enrichment, pre-fractionation and storage of peptides for proteomics using StageTips. *Nat. Protoc.* **2**, 1896-1906.
Riedl, J., Crevenna, A. H., Kessenbrock, K., Yu, J. H., Neukirchen, D., Bista, M., Bradke, F., Jenne, D., Holak, T. A., Werb, Z. et al. (2008). Lifeact: a versatile marker to visualize F-actin. *Nat. Methods* **5**, 605-607.
Sarbassov, D. D., Ali, S. M., Kim, D.-H., Guertin, D. A., Latek, R. R., Erdjument-Bromage, H., Tempst, P. and Sabatini, D. M. (2004). Rictor, a novel binding partner of mTOR, defines a rapamycin-insensitive and raptor-independent pathway that regulates the cytoskeleton. *Curr. Biol.* **14**, 1296-1302.
Schmidt, A., Kunz, J. and Hall, M. N. (1996). TOR2 is required for organization of the actin cytoskeleton in yeast. *Proc. Natl. Acad. Sci. USA* **93**, 13780-13785.
Schroeder, M. J., Shabanowitz, J., Schwartz, J. C., Hunt, D. F. and Coon, J. J. (2004). A neutral loss activation method for improved phosphopeptide sequence analysis by quadrupole ion trap mass spectrometry. *Anal. Chem.* **76**, 3590-3598.
Skau, C. T. and Kovar, D. R. (2010). Fimbrin and tropomyosin competition regulates endocytosis and cytokinesis kinetics in fission yeast. *Curr. Biol.* **20**, 1415-1422.
Skoumpla, K., Coulton, A. T., Lehman, W., Geeves, M. A. and Mulvihill, D. P. (2007). Acetylation regulates tropomyosin function in the fission yeast Schizosaccharomyces pombe. *J. Cell Sci.* **120**, 1635-1645.
Suarez, C., Carroll, R. T., Burke, T. A., Christensen, J. R., Bestul, A. J., Sees, J. A., James, M. L., Sirotkin, V. and Kovar, D. R. (2015). Profilin regulates F-actin network homeostasis by favoring formin over Arp2/3 complex. *Dev. Cell* **32**, 43-53.
Tatebe, H., Morigasaki, S., Murayama, S., Zeng, C. T. and Shiozaki, K. (2010). Rab-family GTPase regulates TOR complex 2 signaling in fission yeast. *Curr. Biol.* **20**, 1975-1982.
Vazquez-Martin, A., Oliveras-Ferraros, C., Bernadó, L., López-Bonet, E. and Menendez, J. A. (2009). The serine 2481-autophosphorylated form of mammalian Target Of Rapamycin (mTOR) is localized to midzone and midbody in dividing cancer cells. *Biochem. Biophys. Res. Commun.* **380**, 638-643.
Weisman, R. and Choder, M. (2001). The fission yeast TOR homolog, tor1+, is required for the response to starvation and other stresses via a conserved serine. *J. Biol. Chem.* **276**, 7027-7032.
Win, T. Z., Gachet, Y., Mulvihill, D. P., May, K. M. and Hyams, J. S. (2001). Two type V myosins with non-overlapping functions in the fission yeast Schizosaccharomyces pombe: Myo52 is concerned with growth polarity and cytokinesis, Myo51 is a component of the cytokinetic actin ring. *J. Cell Sci.* **114**, 69-79.
Wu, J.-Q., Kuhn, J. R., Kovar, D. R. and Pollard, T. D. (2003). Spatial and temporal pathway for assembly and constriction of the contractile ring in fission yeast cytokinesis. *Dev. Cell* **5**, 723-734.
Wullschleger, S., Loewith, J. and Hall, M. (2006). TOR signaling in growth and metabolism. *Cell* **124**, 471-484.
Yamashita, A., Maeda, K. and Maéda, Y. (2003). Crystal structure of CapZ: structural basis for actin filament barbed end capping. *EMBO J.* **22**, 1529-1538.